UNIVERSITY OF NAPOLI FEDERICO II

DEPARTMENT OF STRUCTURES FOR ENGINEERING AND ARCHITECTURE

PH.D. IN STRUCTURAL, GEOTECHNICAL ENGINEERING AND SEISMIC RISK
XXXIV CYCLE

TWO-DIMENSIONAL AMPLIFICATION OF SEISMIC MOTION IN ALLUVIAL VALLEYS

Giorgio Andrea Alleanza

A dissertation submitted in partial fulfillment of the
requirements for the degree of
Doctor of Philosophy
In
Structural, Geotechnical Engineering and Seismic Risk
2022

Supervisors
Prof. Anna d'Onofrio
Prof. Francesco Silvestri

Ph.D. Coordinator
Prof. Iunio Iervolino

TABLE OF CONTENTS

LIST OF TABLES

LIST OF FIGURES

NOTATION

VAF	Valley Amplification Factor
H	thickness of the valley
B	half-width of the valley
H/B	shape ratio
C_v	ratio between shear wave velocity of the bedrock and the soil
V_S	shear wave velocity of the soil
$V_{S,r}$	shear wave velocity of the bedrock
$f_{0,1D}$	1D resonance frequency of the soil column of the centre valley
$f_{0,2D}$	2D resonance frequency of the valley
$T_{0,1D}$	1D resonance period of the soil column of the centre valley
$T_{0,2D}$	2D resonance period of the valley
I	impedance ratio
α	slope of the edge
f_m	mean frequency of the reference input motion
f_p	predominant frequency of the reference input motion
T_m	mean period of the reference input motion
T_p	predominant period of the reference input motion
λ_m	mean wavelength of the reference input motion
AG_{1D}	1D spectral aggravation factor
AG_{2D}	2D spectral aggravation factor
$AG_{2D/1D}$	2D geometrical aggravation factor
x	distance from the centre of the valley
γ	unit weight of the soil
γ_r	unit weight of the bedrock
ρ	mass density of soil

ρ_r	mass density of the bedrock
D_0	initial damping of the soil
$D_{0,r}$	initial damping of the bedrock
PGA	peak ground acceleration
$S_a(T)$	spectral acceleration
VAF(0)	VAF value at the centre of the valley
f_1	function of the VAF for the central zone of the valley
f_2	function of the VAF for the lateral zone of the valley
$V_{S,eq}$	equivalent shear velocity
G_0	initial shear modulus
p'	actual confinement stress
p_r	reference confinement stress
p_a	atmospheric pressure
S	stiffness index
PI	plasticity index
$G(\gamma)/G_0$	shear modulus decay curve
$D(\gamma)$	damping variation curve with strain
PGA_o	outcrop peak ground acceleration
$f\left(\frac{x}{B}, PGA_o\right)$	function for accounting the nonlinearity and inhomogeneity
SRA	site response analysis
DH	Down Hole test
MASW	Multichannel Analysis of Surface Waves test
HVSR	Horizontal to Vertical Spectral Ratio test

ACKNOWLEDGEMENTS

First of all, I would like to express my deepest gratitude to Professors Anna d'Onofrio and Francesco Silvestri who, as modern Virgilio, drove me through the dark forest of billions of numerical data, in which I was more or less consciously involved during my PhD. Indeed, I think that the synthesis of all these results has been achieved mainly thanks to the continuous and constructive discussions during all these years, which also allowed me (I hope) to develop a critical view in the interpretation of data related engineering problems.

I would also like to thank Professor Achilleas Papadimitriou for his guidance, endless encouragement, and enthusiasm during my internship at the National Technical University of Athens.

Special thanks to all my PhD friends who, like souls in trouble, now or in the past crowd the second floor of Edificio 8 of Via Claudio 21. Thanks to them I enjoyed one of the best aspects of my Ph.D. experience, sharing with them pleasures and difficulties and establishing friendship that (I hope) will continue over time.

ABSTRACT

The alluvial valleys have historically been a preferable location for human settlements, for exploiting the proximity to transportation routes and waterways. However, the position of a settlement with respect to the valley can sensibly affect the degree of environmental risk with respect to natural phenomena such as floods, landslides, and earthquakes. In particular, alluvial valley deposits affect seismic site response by changing the frequency content, duration and amplitude of ground motion. Therefore, it is of the greatest importance for earthquake engineering to understand the relevant mechanisms and to quantify the most significant effects. Indeed, in this way it is possible to improve the prediction of seismic actions for the design of new constructions and the assessment of existing ones. At present, even the most advanced technical standards allow to take into account in a simplified way only the effects of topographic and stratigraphic amplification, while in the presence of valleys it is in principle necessary to carry out complex and time-consuming 2D or 3D numerical analyses.

In this study, the results obtained from extensive parametric two-dimensional analyses of the seismic response of shallow alluvial valleys are reported, synthesized, and discussed. They allowed to highlight the influence of the most significant

parameters and to define a valley amplification factor, VAF, which expresses the average ratio between the response spectrum all along the valley surface and that predictable by one-dimensional seismic response analyses at the valley centre. Analytical relationships are formulated for expressing the amplification factor as a function of the geometrical and mechanical properties of the valleys. Simplified charts are generated from them, which can be used for a quick estimate of the ground motion amplification. In addition, two different engineering approaches are proposed, in order to update the technical codes for considering valley effects in a simple way. Then, several case studies of real valleys located in Central Italy are analysed, comparing the results obtained with complete numerical analyses to those of the proposed simplified approaches. It is verified that the proposed simplified methods approximate satisfactorily the results obtained from 2D numerical analyses, provided that the geometrical and mechanical model of the real valley is compatible with the cases considered in the parametric analyses.

I. INTRODUCTION

From the beginning of time until today, alluvial valleys have been one of the most favourite locations for human civilisations to build their settlements. As a matter of fact, they are typically created and crossed by rivers, which provide an abounding and reliable source of water as well as a fast way of communication. Also, the valley morphology usually favours the construction of transportation routes. Nevertheless, from an engineering point of view, it is of great importance to assess the safety of these locations with respect to several natural hazards, such floods, landslides, and earthquakes, by analysing the physical phenomena affecting valleys from the geological, hydraulic and geotechnical viewpoints. For instance, a number of significant observations of earthquake-induced damage, in Italy and worldwide, proved that the combination of lithological and morphological properties of alluvial valley deposits influence their seismic response, by modifying the amplitude, duration and frequency content of the ground motion, compared to the conventional case of one-dimensional upward propagation of shear waves. Therefore, it is necessary to take into account such modifications when evaluating which seismic actions should be used to assess the seismic performance of buildings and infrastructures located along and across alluvial valleys. At present, even the most advanced technical codes provide simplified tools for the evaluation of stratigraphic and topographic effects on seismic motion, while the prediction of valley amplification phenomena is, in principle, affordable only through non-trivial dynamic analyses on two- or three-dimensional subsoil models.

I.1 Research objectives

Following the above considerations, the aim of the present work is to develop a reliable yet simplified methodology, to be ideally implemented in technical codes to estimate the valley effects. An extensive parametric study on the two-dimensional seismic response of trapezoidal alluvial valleys was required, in order to assess the influence of the most significant geometrical and mechanical factors. As a result, analytical formulae and graphical tools were developed, to evaluate the 2D amplification of the ground motion, which were then applied to several real case studies of Italian alluvial valleys.

The study is carried out as part of WP16.1 *"Seismic response analysis and liquefaction"* in the framework of the research programme funded by Italian Civil Protection through the ReLUIS Consortium (DPC-ReLuis 2019-2021).

I.2 Organization of the text

This dissertation comprises of 6 Chapters and 2 Appendices, which can be divided into 3 main parts.

The first part consists of Chapter II, where a summary of the state-of-the-art on the seismic response of alluvial valleys is presented. First, the physical phenomenon is discussed, then the dominating parameters are highlighted and, finally, the most recent proposals of simplified approaches are introduced.

In the second part (Chapters III and IV), the results obtained from an extensive parametric study are reported and discussed. The numerical data allow for defining an analytical relationship expressing a ‘Valley Amplification Factor’, as a function of the geometrical and mechanical parameters of the basin considered. Such a formulation is then used to obtain simplified charts, which enable a simplified estimation of the amplification along the valley. It should be noted that the results of Chapter III are achieved considering that the soil filling the basin is homogeneous and assuming a visco-elastic behaviour. In Chapter IV these two simplified hypotheses are lifted, aiming at investigating the effect on the ground motion of the inhomogeneity of the mechanical properties with depth and of the non-linear soil behaviour. The methodology used to obtain the analytical expression of the ‘Valley Amplification Factor’ is described in the two Appendices.

In Chapter V, the previous achievements are adopted as a simplified methodology to take into account valley effects in practical applications, by comparing the amplification predicted through the analytical and graphical tools to those numerically simulated for several case studies of alluvial valleys in Central Italy.

Finally, in Chapter VI the main conclusions of the study are summarised, and the perspectives of possible research developments are outlined.

II. BACKGROUND

The site seismic response can be defined as the totality of changes in amplitude, duration, and frequency content that the seismic reference motion has during the travel through the soil from the bedrock to the surface (Kramer, 1996; Lanzo & Silvestri, 1999).

The changes in seismic motion are mainly due to:

- Stratigraphic effects, associated with the soil layers and depending on the mechanical properties and the non-linear and dissipative behaviour of the soils and the bedrock (Idriss, 1991);
- Geometric effects, connected to the topographical surface pattern and to the geometry of the interfaces between the different layers of soils and bedrock (Bard 1982; Geli et al., 1988; Sanchez-Sesma, 1990; Bouckovalas & Papadimitriou, 2005; Papadimitriou, 2019);

In the case of an alluvial valley there are further phenomena, the so-called "valley effects", that are mainly related to buried 2D or 3D morphology of the interface between the bedrock and the overlaying soil deposit. Indeed, at the edge of the valley the complex interaction among the direct, reflected and refracted waves may cause a wave focalization at surface and the generation of surface waves. In particular, incident SH waves lead to Love surface waves (Aki & Larner, 1970; Bard & Bouchon, 1980a) while the combination of incident P and SV waves generates Rayleigh waves (Bard & Bouchon, 1980b). Moreover, due to the two-dimensional morphology of the valley and to the impedance ratio between the bedrock and the overlaying soil these waves get trapped within the valley, thus inducing an increase in the amplitude and duration of the seismic motion (Bard & Bouchon, 1980a, 1980b, 1985). For these reasons, in an alluvial basin, the ground motion at surface is significantly influenced by its geometry, i.e. shape of the valley (Bard & Bouchon, 1985) and inclination of the edges (Zhu & Thambiratnam, 2016; Zhu, Chávez-García, et al., 2018), and by the mechanical and non-linear properties of the soil filling the valley (Gelagoti et al., 2010, 2012; Iyisan & Khanbabazadeh, 2013; Riga et al., 2018).

In recent years, numerous studies have been carried out to quantify the amplification of the seismic motion in alluvial valleys and to define an appropriate Valley Aggravation Factor, VAF (Riga et al., 2016; Zhu, Chávez-García, et al., 2018; Zhu, Riga, et al., 2018; Zhu, Thambiratnam, et al., 2018; Papadimitriou, 2019; Pitilakis et al., 2019), such as that typically adopted by the codes of practice to quantify topographic amplification (NTC 2018). However, an easily calculated VAF that can adequately consider the influence of geometry, mechanical and non-linear soil properties on the seismic response has not been defined yet. Usually, to isolate the geometric 2D effects from the stratigraphic ones an aggravation factor is defined, as the ratio between the results obtained from 2D and 1D analyses. Generally, a visco-elastic model is adopted in the analyses assuming that the geometric aggravation factor is not significantly affected by the non-linear properties of the soil.

In the following, a basic state of the art of valley seismic response is outlined, beginning with the physical phenomena of seismic wave transmission, both body and surface, within the valley. Then the key parameters regulating the dynamics of alluvial basins are examined, finally the more recent factors used to describe and synthesise the amplification of reference seismic motion are discussed.

II.1 Theoretical studies

The first research on the seismic response of valleys begins at the end of the XIX century, but it is only since the mid XX century that the phenomenon is studied systematically and instrumentally, using the first seismographs. For example, Gutemberg (1957) compares the different response of several seismographs placed by the California Technology Institute in various locations in the Los Angeles valley, both on outcropping bedrock and on sediments of different thickness. Gutemberg (1957) shows that the surface response varies according to the thickness of the sediment and the position in the valley with respect to the bedrock. In the following years the research progresses until the first studies allow to understand the physical phenomena that rule the valley effects. As a matter of fact, first Aki & Larner (1970) followed by Trifunac (1971), Wong & Trifunac (1974) and Hong & Helmberger (1978) provide the theoretical bases that allow Bard & Bouchon (1980a, 1980b) to identify the main mechanisms governing the seismic response of valleys affected by SH waves and by the combination of P and SV.

Indeed, Bard & Bouchon (1980a), using the numerical technique developed by Aki & Larner (1970), study the effects that the propagation of SH waves has on ground motion. The authors conclude that at the edges, the inclined interface between the deformable sediment and the bedrock modifies the direction of the seismic waves. They do not propagate in a vertical direction but in an inclined one, which generates Love waves at the surface that travel inside the basin. In addition, usually in alluvial basins the impedance ratio between the bedrock and the filling material is high, which causes the trapping of these waves within the basin, that are reflected several times from the edges, and travel back and forth through the valley. This phenomenon leads to an increase in the amplitude and duration of seismic motion at the surface. In the case of P-waves and SV-waves, Bard & Bouchon (1980b) find that the same effects as for SH-waves occur, but the surface waves generated are Rayleigh waves.

II.2 Shape ratio

The influence of valley shape has been studied in depth by Bard & Bouchon (1985). The authors define the shape ratio, H/B, as the ratio between the thickness, H, and the half-width, B, of the valley (Figure II.2.1).

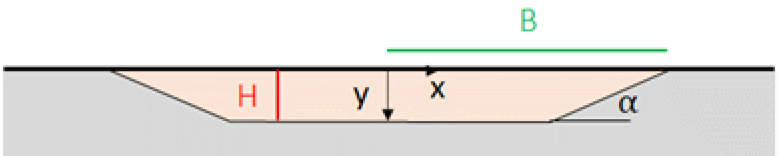

Figure II.2.1 – Simplified scheme of the valley.

The authors also give a critical value for the shape ratio of:

$$\left(\frac{H}{B}\right)_c = \frac{0.65}{\sqrt{C_v - 1}} \qquad \text{II.2.1}$$

where C_v is the ratio between the shear wave velocity, V_s, of the bedrock and the soil. If the shape ratio is lower than the critical one, then the valley is considered 'shallow', otherwise 'deep' (Figure II.2.2). In the first case, the ground motion within the valley is mainly due to the combination of the one-dimensional resonance and the propagation of the surface waves, while in the other case a two-dimensional resonance phenomenon is developed (Bard & Bouchon, 1985).

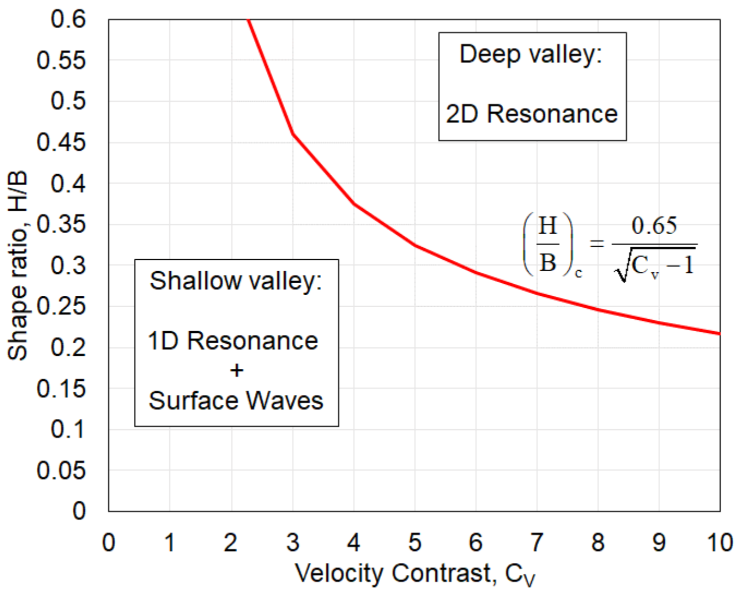

Figure II.2.2 – Critical shape ratio (Bard & Bouchon, 1985)

The shape ratio also affects the two-dimensional resonance frequency, $f_{0,2D}$, which is higher than the one-dimensional one of the soil column in the centre of the valley, $f_{0,1D}$, and increases with H/B. Bard & Bouchon (1985) provide the following equations, shown in Figure II.2.3, for the evaluation of resonance frequencies for the different wave types:

$$\begin{cases} f^{P}_{0,2D} = f^{P}_{0,1D} \cdot \sqrt{1+\left(\frac{H}{B}\right)^2} \\ f^{SV}_{0,2D} = f^{SV}_{0,1D} \cdot \sqrt{1+\left(2.9 \cdot \frac{H}{B}\right)^2} \\ f^{SH}_{0,2D} = f^{SH}_{0,1D} \cdot \sqrt{1+\left(2 \cdot \frac{H}{B}\right)^2} \end{cases} \quad \text{II.2.2}$$

Therefore, in the case of shallow valleys H/B is small and the 2D resonance frequency, is close to the 1D one for most of the basin, except for the lateral zone. On the other hand, in the case of deep basins H/B is large and a pure 2D resonance pattern is developed, with $f_{0,2D}$ greater than $f_{0,1D}$ and constant along the basin, with the highest amplification in the centre of the valley that decrease towards the edges. Furthermore, the motion is in phase for most of the basin and is characterised by a longer duration (Bard & Bouchon, 1985).

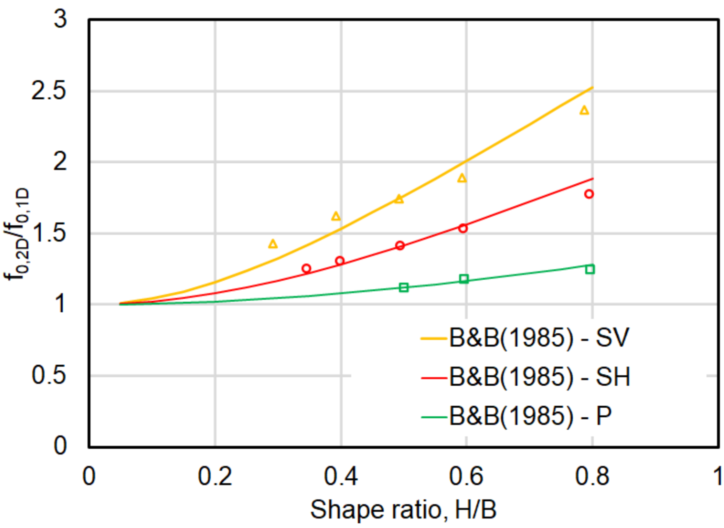

Figure II.2.3 – Variation of the $f_{0,2D}/f_{0,1D}$ with the shape ratio (Bard & Bouchon, 1985)

II.3 Impedance ratio

The impedance ratio between the bedrock and the overlaying soil, I, is another key parameter influencing the seismic response at surface. As a matter of fact, it regulates the amount of energy transmitted from the bedrock to the valley and the radiation damping. Indeed, seismic waves propagating from depths towards the surface hit the alluvial deposit interface where part of the energy is reflected to the half-space, while the remaining portion is transmitted to the basin. The transmitted energy increases with the impedance ratio while the reflected one and then the radiative damping decreases. For these reasons, generally the amplitude and duration of the seismic motion increase with the impedance ratio (Bard & Bouchon, 1980b, 1980a, 1985).

II.4 Slope of the edge

The influence of the edges slope, α, of a trapezoidal valley is studied by Zhu & Thambiratnam (2016) and Zhu, Chávez-García, et al. (2018). The authors identified two different waves pattern depending on the value of α. In the case of high angle values (Figure II.4.1a) most of the waves transmitted at the edges (red arrows) are directed towards the centre of the valley, where they interfere with the direct waves (blue arrows). Instead, for low inclinations (Figure II.4.1b) a non-negligible amount of energy gets trapped within the edges (dark yellow arrows) thus resulting in an amplification of the motion at the borders of the valley.

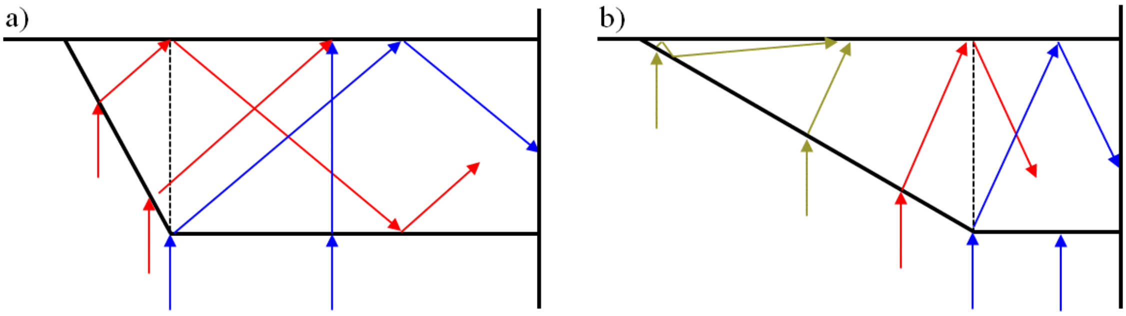

Figure II.4.1 – Ray path in case of a) high; b) low inclination of the edge (modified from Zhu & Thambiratnam, 2016).

II.5 Input frequency content

The seismic response of the alluvial valleys also depends on the frequency content of acceleration input motion, more precisely on the ratio between the mean frequency of the reference motion (Rathje et al., 1998), f_m, and the resonance frequency of the valley, $f_{0,2D}$, this latter proportional to $f_{0,1D}$. This ratio is proportional to the ratio between the thickness of the valley and the mean wavelength ($\lambda_m = V_S/f_m$). If f_m is much lower than $f_{0,1D}$, the amplification is negligible, because λ_m is much greater than H and the seismic waves do not interact with the deformable layer. If f_m is close to $f_{0,1D}$, λ is close to 4H and the amplification is mainly due to the 1D resonance. Finally, if f_m is greater than $f_{0,1D}$, the amplification is affected by to 2D effects and is greater than the 1D case (Alleanza et al., 2019).

II.6 Non linearity

The effect of nonlinear and dissipative properties of soils is investigated in detail by Gelagoti et al. (2010, 2012), Iyisan & Khanbabazadeh, (2013) and Riga et al. (2018). If 2D motion is taken into account, it is generally found that it decreases when considering nonlinearity with respect to the visco-elastic case. However, it is usually preferable to consider the ratio between the surface motion obtained from 2D analysis and the 1D motion of the valley centre. In this case the prediction of the effects of the nonlinearity is more difficult, and in general at the valley centre the nonlinearity reduces the ground motion with respect to the visco-elastic case, while at the edges there is a behaviour that depends on the reference motion and non-linear properties of the soils. This is due to the fact that in these areas there is a concentration of shear strains due to the heavy interaction between the different wave fronts (direct, indirect and surface). This leads to a decay of the shear modulus and an increase of damping which results in an additional trapping effect of the seismic waves, both volume and surface, in the side zone of the valley. This effect is dependent on the non-linear properties of the soils and the duration and frequency content of the reference seismic motion. Indeed, as the duration increases, the load cycles and therefore the strain will increase, with a consequent rise in both deformability and damping (Gelagoti et al., 2010, 2012; Iyisan & Khanbabazadeh, 2013; Riga et al., 2018).

II.7 Valley Amplification Factor

In recent years, the aim of the most part of the research has been to go beyond the phenomenological study of the effects of the seismic response of valleys, and provide an easy and reliable method to take into account the amplification of seismic ground motion in engineering applications (Chávez-García & Faccioli, 2000; Vessia et al., 2011; Riga et al., 2016; Zhu, Riga, et al., 2018; Zhu, Thambiratnam, et al., 2018; Papadimitriou, 2019; Pitilakis et al., 2019). Just like for the topographic amplification, in order to quantify 2D geometrical effects as decoupled from the stratigraphic amplification, a Valley Amplification Factor, VAF, can be defined as the ratio between peak or integral ground motion parameters computed by 2D and 1D analyses. Generally, 2D visco-elastic analyses are carried out assuming that VAF is not significantly affected by non-linear soil properties, that are deemed to be included in 1D stratigraphic amplification. Nevertheless, it has not yet been definitely stated if it is possible to decouple geometric from stratigraphic effects and to quantify them separately.

One of the first approaches to define a method for introducing valley effects into technical codes is the study of Chávez-García & Faccioli (2000). The authors consider a sinusoidal, symmetrical valley with homogeneous, visco-elastic soil. They take into account both shallow and deep valleys by varying the shape ratio between 0.16 and 0.41 and velocity ratios between 1.75 and 5.25. Chávez-García & Faccioli (2000) are one of the first to define an aggravation factor, $AG_{2D/1D}$, as the ratio between the spectral ordinates obtained on the surface in the 2D case and the 1D ones, the latter calculated from a soil column similar to the centre of the valley. They also propose to consider valley effects in the technical codes by introducing an additional amplification factor. Therefore, the design spectrum is given by the product of the reference spectrum, obtained for outcropping horizontal bedrock, and the stratigraphic and topographic amplification factors and this new valley amplification factor. Due to the lack of a systematic study, they suggest to adopt for the latter a value between 2 and 3 for the whole valley, neglecting for the sake of safety the variability of the response along the basin.

Vessia et al. (2011) extend the conclusions of Chávez-García & Faccioli (2000), considering valleys of sinusoidal shape, with homogeneous soil and non-linear behaviour. They always use the ratio between the 2D and 1D spectra, $AG_{2D/1D}$, as the aggravation factor and find that it is greater than 1 for periods below a certain value, T_S, above which it becomes less than 1. Then they define a geometric amplification factor, S_G, as:

$$S_{G(0.01-T_S)} = \frac{\int_{0.01s}^{T_S} AG_{2D/1D}(T)dT}{(T_S - 0.01)} \qquad \text{II.7.1}$$

In other words, S_G is nothing more than a measure of how much on average the 2D spectrum is amplified compared to the 1D spectrum, taking into account a period interval that neglects any attenuation effects. Vessia et al. (2011) give S_G and T_S values for subsoil classes B and C, as defined by Italian technical codes (NTC 2018), for both shallow and deep valleys, as a function of distance from the valley centre, x, divided by the valley half-width, B (Table II.7.1). T_S is in practice equal to about twice the one-dimensional resonance period of the valley centre, $T_{0,1D}$. The latter is calculated considering a column of 30m thickness and a V_S mean between ones that are the threshold of the relative subsoil class. For shallow valleys it is found that the maximum S_G is localised at the edges, while for deep valleys at the centre of the valley. In both cases there are two amplifying peaks, one in the centre of the valley and one near the edges. Indeed, in the centre it is equal to 1.35 (1.6), then it decreases up to 1.3 (1.35) for x/B=0.3 and hence it increases up to 1.5 (1.4) for x/B=0.6. Moreover, the authors suggest not to magnify all the spectrum of S_G, but to use it only for periods lower than T_S assuming for the higher ones that it is equal to 1.

Table II.7.1 – Summary of the geometrical correction factors suggested by Vessia et al. (2011).

	x/B	S_G(B,C)	T_S(B) (s)	T_S(C) (s)
Shallow valley (H/B≤0.2)	0	1.35	0.35	0.85
	0.3	1.3	0.2	0.6
	0.6	1.5	0.15	0.35
Deep valley (H/B≥0.4)	0	1.6	0.28	0.65
	0.3	1.35	0.25	0.6
	0.6	1.4	0.15	0.4

Riga et al. (2016) carried out an extensive parametric analysis considering trapezoidal valleys with homogeneous and visco-elastic soil and again computed the aggravation factor as the ratio between the 2D and 1D response spectra. The authors divided the valley into several sections and provided the maximum of this factor for them, based on the period $T_{0,1D}$, identifying a threshold value for this period of 3s. They note that, if this value is exceeded, the amplification is greater than for shorter periods. In general, at the border of the valley there are attenuation effects and the ratio between the spectra is less than 1. On the other hand, in the area of the valley with constant thickness the amplification increases with H/B and I, varying between 1 and 2.3.

Lastly, Zhu, Thambiratnam et al. (2018) analyses the trapezoidal valley case by assuming a visco-elastic behaviour of the soil, with V_S both constant and increasing with depth. In that study, the authors take as their starting point a valley spectral aggravation factor, SAG($T/T_{0,1D}$; x/B), defined as the ratio between 2D and 1D spectra, dependent on the period and position in the valley. Then they calculate a second amplification factor, SAG(x/B), at each point in the basin as the maximum of SAG($T/T_{0,1D}$; x/B) over the period between 0s and $T_{0,1D}$, thus removing the period dependence. Therefore, they identify along the valley a zone where SAG(x/B) is higher than a predefined threshold value, and hence calculate in this zone a further amplification factor obtained as the average of SAG(x/B). Therefore, this latter factor is an index of the mean of the maximum values of the ratio between the 2D and 1D spectra. It ranges between 1 and 3 depending on the V_S and the geometry of the deposit.

In conclusion, in the literature there are several valley amplifications factors, VAF, obtained in a slightly different way but all of them representing an index of how much, on average or at maximum, the 2D response spectrum is greater than the 1D one. Particularly when considering mean values (e.g. Vessia et al., 2011) it varies between 1 and 1.6, while at the maximum (e.g. Chávez-García & Faccioli, 2000; Riga et al., 2016; Zhu, Thambiratnam, et al., 2018) it ranges between 1 and 3.

III. PARAMETRIC LINEAR ANALYSES ON HOMOGENEOUS VALLEYS

The following chapter describes the details and summarise the results of an extensive parametric study carried out to analyse the seismic response of trapezoidal shallow valleys: 2160 different models are analysed, obtained considering five different shape ratios, six different impedance ratios, six different edge slope angles and twelve input motions. All the analyses are carried out considering homogeneous soil deposits characterised by a linear visco-elastic behaviour. Chapter IV is then devoted to the critical evaluations of the analyses results obtained adopting the above-mentioned simplified model, and to the proposal of a possible methodology to extend the results obtained to inhomogeneous non-linear soil deposits.

III.1 Subsoil models

An extensive set of 2D numerical seismic response analyses of symmetrical trapezoidal valley (Figure III.1.1) is carried out to evaluate the influence of the geometrical and mechanical parameters on the seismic response at surface.

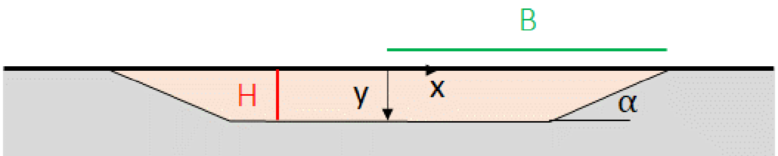

Figure III.1.1 – Geometric scheme of the valley.

The geometrical characteristics of the models adopted are summarised in Table III.1.1 while the mechanical properties are reported in Table III.1.2. All the geometrical models are characterised by the same thickness, H, equal to 100 m and by a variable width, 2B, to obtain a shape ratio, H/B, ranging between 0.05 and 0.25. For each value of H/B six different edge slopes, α, are considered varying between 90° and the one corresponding to the wedge geometry (arctan(H/B)). Analyses are carried out assuming a linear visco-elastic behaviour of soil, assigning an initial damping ratio, D_0, constant for both bedrock and homogeneous soil deposit. For this latter D_0 varies between 5% and 1%, in a way inversely proportional to the assigned shear wave velocity, V_S, indeed, according to Riga et al. (2016), it is assumed that $D_0 = 10/(2 \cdot V_S)$. The shear wave velocity of the bedrock is fixed to 800 m/s, while that of the deformable soil varies between 100 and 580 m/s, to model the response of subsoil belonging to the categories B, C and D, as defined by the Italian technical building standards (NTC 2018). Following the indications by Bard & Bouchon (1985), all the analysed models can be classified as shallow valleys, as shown by the black dots reported on the chart in Figure III.1.2. It is worth highlighting that the resonance frequency reported in Table III.1.2 is referred to the 1D vertical profile corresponding to the centre of the valley, and it is calculated as:

$$f_{0,1D} = \frac{V_S}{4H} \qquad \text{III.1.1}$$

Table III.1.1 – Geometrical properties

Thickness H (m)	Width 2B (m)	Shape ratio H/B	Slope of the edge α (°)
100	4000	0.05	90/60/45/30/15/Wedge
	2000	0.10	
	1340	0.15	
	1000	0.20	
	800	0.25	

Table III.1.2 – Mechanical properties

Shear wave velocity		Unit weight		Poisson ratio		Initial Damping		1D Resonance Frequency $f_{0,1D}$ (Hz)	Impedance ratio I
Bedrock $V_{S,r}$ (m/s)	Soil V_S (m/s)	Bedrock γ_r (kN/m^3)	Soil γ (kN/m^3)	Bedrock ν_r	Soil ν	Bedrock $D_{0,r}$ (%)	Soil D_0 (%)		
800	100	22	19	0.33	0.33	0.5	5.0	0.25	9.26
	130						3.8	0.32	7.13
	180						2.8	0.45	5.15
	270						1.9	0.67	3.43
	360						1.4	0.90	2.57
	580						1.0	1.45	1.60

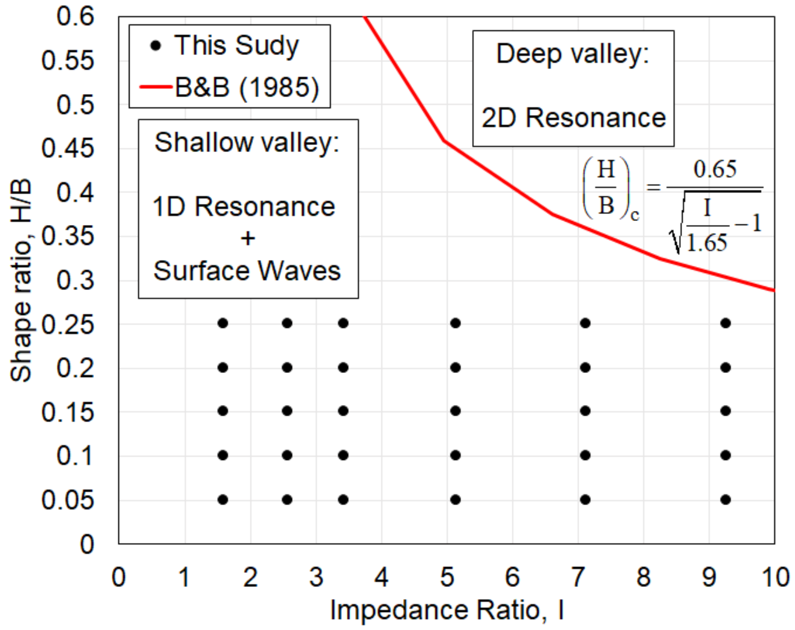

Figure III.1.2 – Valley considered in the analysis (modified from Bard & Bouchon, 1985)

The 2D numerical simulations are carried out with the finite difference code FLAC 8.0 (Itasca Consulting Group, 2016). The code adopts the Rayleigh formulation with a single-frequency approach to model the viscous damping. Since it is less accurate than the double-frequency approach, the method of Verrucci et al. (2022) is used in this study, which allows to obtain an equivalent single-frequency approach by defining two control frequencies: the first of them is set equal to the $f_{0,1D}$ while the second is inferred from the predominant frequency of input motion, f_p. This latter is the inverse of the predominant period, T_p, defined as the one at which the maximum spectral acceleration occurs in an acceleration response spectrum calculated for 5% viscous damping (Rathje et al., 1998).

For each 2D model, a 1D analysis is also carried out along the vertical corresponding to the centre of the valley, using the well-known code STRATA (Kottke & Rathje, 2008). The output of this analysis is then compared with that obtained from 2D analysis with the aim of isolating the geometric effects from the stratigraphic ones.

As these codes work in the time domain and the frequency domain respectively, it is checked that, for 1D visco-elastic analysis, considering the same models in terms of boundary conditions and geometric discretization, the two codes provide the same results (Alleanza & Chiaradonna, 2018).

III.2 Reference input motion

The influence of the input motion is studied considering twelve Ricker wavelets (Figure III.2.1a) with variable mean frequency, f_m, whose properties are shown in Table III.2.1. The adoption of wavelet as input in the analyses allows to better recognise the influence of the frequency content of motion on the response at surface. The acceleration mean frequency is defined in accordance with Rathje et al. (1998) as:

$$f_m = \frac{\sum_i C_i^2 \cdot f_i}{\sum_i C_i^2} \qquad \text{III.2.1}$$

with C_i the Fourier amplitude of the entire accelerogram and f_i the discrete Fourier frequencies between 0.01 and 20 Hz, this latter frequency interval is different from that of Rathje et al. (1998), which ranges between 0.25 and 20 Hz. This change is due to the fact that for some reference input motions most of the frequency content is lower than 0.25 Hz.

In the following all the time histories are represented considering a normalized time, $t \cdot f_m$, obtained by multiplying the time, t, by the mean frequency of the reference input motion. In this way it is possible to compare accelerograms with very different frequencies because the shape of the Ricker becomes independent of them. Figure III.2.1b,c show the response and Fourier spectra of the input motions, respectively: in Figure III.2.1b the spectral acceleration, $S_a(T)$, is normalised respect to the peak ground acceleration, PGA, and represented as a function of the period, T, normalised respect to the one-dimensional resonance values, $T_{0,1D}$, computed at the centre of the valley as inverse of $f_{0,1D}$. While Figure III.2.1c shows the normalised Fourier amplitude, i.e. the Fourier amplitude divided by its maximum amplitude, as a function of a normalised frequency, $f/f_{0,1D}$. This normalization allows to easily represent the spectral shapes of all inputs motion. Note that in the present study a wide frequency range has been investigated, with accelerograms that can be representative of both impulsive sources (c.f. Figure III.2.1a #9-12) and signals with a wider frequency content (c.f. Figure III.2.1a #1-3). Furthermore, the use of wavelets as reference input motions makes it easier to study ground motions and identify direct, indirect and surface waves, which allows for a better understanding of ray paths within the valley.

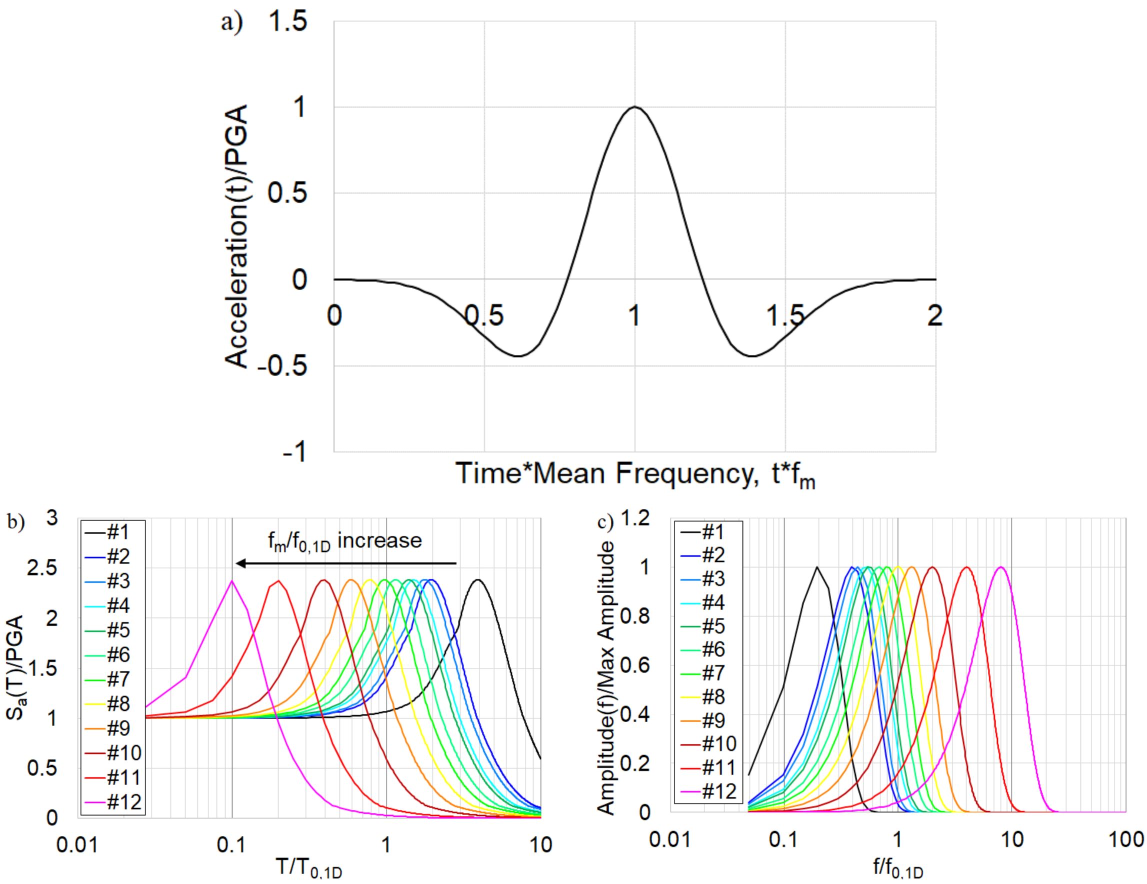

Figure III.2.1 – Reference input motions: a) shape of accelerogram; b) response spectra; c) Fourier spectra

Table III.2.1 – Properties of the input motions

#	Mean Frequency f_m (Hz)	Predominant Frequency f_p (Hz)	Mean Wavelength λ_m (m)	λ_m/H	B/λ_m	f_m / $f_{0,1D}$	$T_m/T_{0,1D}$
1	0.05-0.29	0.06-0.37	2000.00	20.00	1.00	0.20	5.00
2	0.10-0.58	0.13-0.74	1000.00	10.00	2.00	0.40	2.50
3	0.11-0.64	0.14-0.82	909.09	9.00	2.20	0.45	2.25
4	0.13-0.73	0.17-0.93	769.23	8.00	2.50	0.50	2.00
5	0.14-0.83	0.18-1.06	714.29	7.00	2.90	0.58	1.75
6	0.17-0.97	0.22-1.23	588.24	6.00	3.30	0.67	1.50
7	0.20-1.16	0.26-1.49	500.00	5.00	4.00	0.80	1.25
8	0.25-1.45	0.32-1.85	400.00	4.00	5.00	1.00	1.00
9	0.33-1.93	0.42-2.50	303.03	3.00	6.70	1.30	0.75
10	0.50-2.90	0.64-3.70	200.00	2.00	10.00	2.00	0.50
11	1.00-5.80	1.28-7.14	100.00	1.00	20.00	4.00	0.25
12	2.00-11.60	2.56-14.30	50.00	0.50	40.00	8.00	0.12

III.3 Numerical model

The numerical model adopted in the analyses should reproduce the scheme of a trapezoidal valley with a horizontal ground surface, filled with a homogeneous visco-elastic soil, laying on a deformable bedrock. To this aim the first step has been the definition of the boundary conditions.

The bedrock can be modelled as a visco-elastic half-space adopting a quiet (or absorbing) boundary at the base. FLAC code comply with this requirement using the viscous boundary developed by Lysmer & Kuhlemeyer, (1969), implemented with independent dashpot in the vertical and horizontal directions. The use of dashpots requires applying the input reference motion to the base as a time history of shear stresses, τ, defined as:

$$\tau = 2 \cdot (\rho_r \cdot V_{s,r}) \cdot v(t) \qquad \text{III.3.1}$$

With:

- $(\rho_r \cdot V_{s,r})$ the impedance of the bedrock, obtained by multiplying the mass density, ρ_r, and the shear wave velocity, $V_{s,r}$, of the bedrock;
- $v(t)$ the velocity time history of the half-space.

The simulation of a lateral semi-infinite medium is achieved by placing the so-called free-field lateral boundaries. They are obtained placing a one-dimensional soil column, characterised by the same stratigraphic sequence of the 2D model, linked to the mesh grid through viscous dashpots, so that 1D conditions of propagation are established along the lateral borders of the domain.

The mesh grid consists of quadrilateral elements whose maximum thickness is calculated through the Kuhlemeyer & Lysmer (1973) relationship, considering a maximum frequency of 20 Hz.

The second step into the creation of the numerical model is the definition of the size of the domain, that has been set based on the results of a sensitivity analysis. The latter is aimed to establish the minimum distance, between the valley and the borders of the numerical domain, to avoid any undesired boundary effect on the computed ground motion at surface. Figure III.3.1 shows the scheme of the numerical model adopted in these preliminary analyses, while Table III.3.1 summarises the geometrical and mechanical properties out of the analysed models.

Table III.3.1 – Characteristic of the models used in sensitivity analysis

<table>
<tr><th>b/B</th><th>h/H</th><th>H/B</th><th>$f_m/f_{0,1D}$</th><th>I</th></tr>
<tr><td>0.1</td><td rowspan="4">5</td><td rowspan="8">0.05-0.25</td><td rowspan="8">0.2-2</td><td rowspan="8">9.26-1.60</td></tr>
<tr><td>0.5</td></tr>
<tr><td>1</td></tr>
<tr><td>2</td></tr>
<tr><td rowspan="4">0.5</td><td>0.1</td></tr>
<tr><td>0.5</td></tr>
<tr><td>1</td></tr>
<tr><td>2</td></tr>
</table>

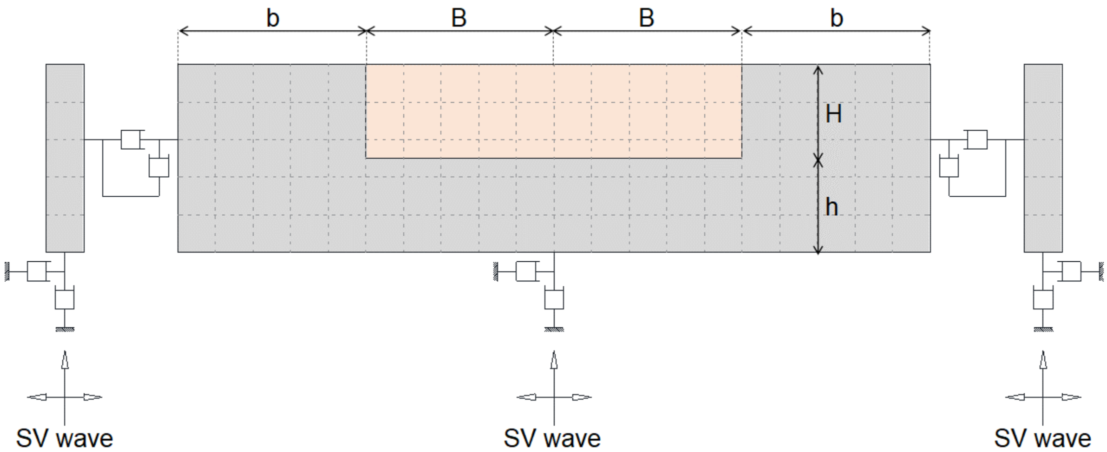

Figure III.3.1 – Schematic representation of the numerical model

Two values of shape ratio, H/B (0.05 and 0.25), impedance ratio, I (9.26 and 1.6), and frequency ratio, $f_m/f_{0,1D}$ (0.2-2) are considered. The thickness of the bedrock below the valley, h, is initially set equal to 5H, since this value is considered high enough to ensure that it does not affect the ground motion at surface. While the distance between the edge of the valley and the lateral boundary of the analysed domain, b, has varies between 0.1B and 2B.

The time histories of the acceleration computed at the lateral boundary of the model are shown Figure III.3.2 while those evaluated at the centre of the valley are reported in Figure III.3.3 for both H/B, $f_m/f_{0,1D}$ and I=9.26.

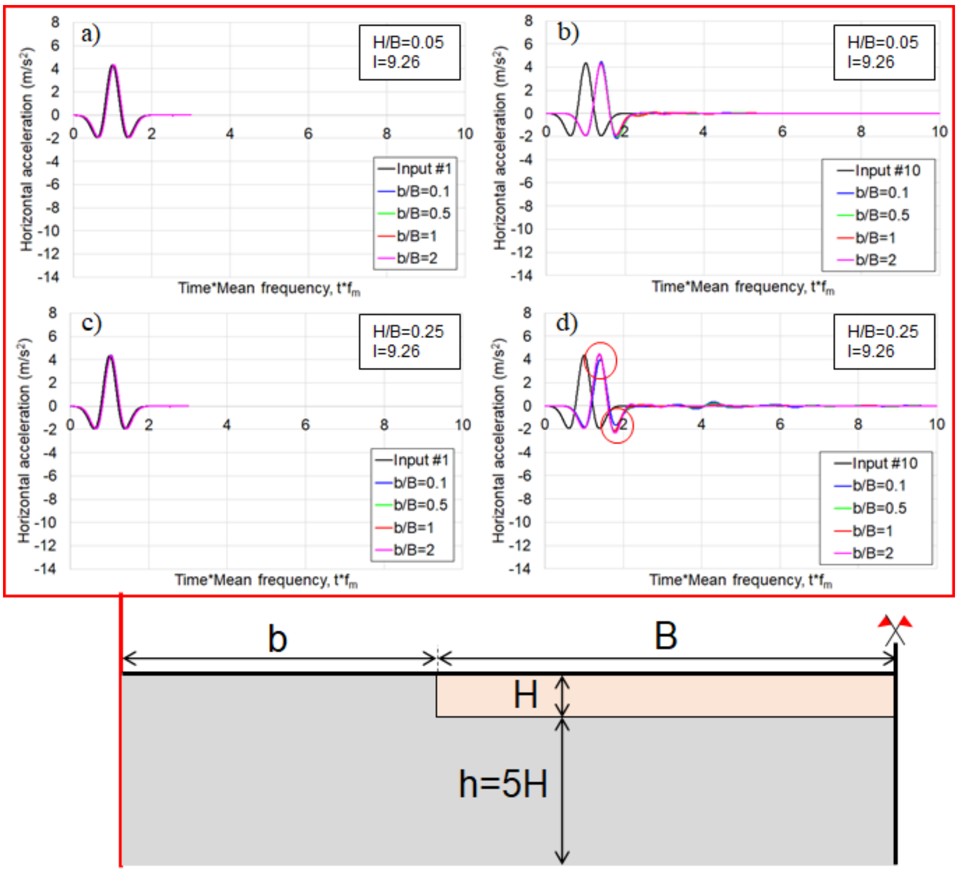

Figure III.3.2 – Accelerograms at the lateral boundary of the model for I=9.26, H/B=0.05-0.25, #1-10 varying b/B

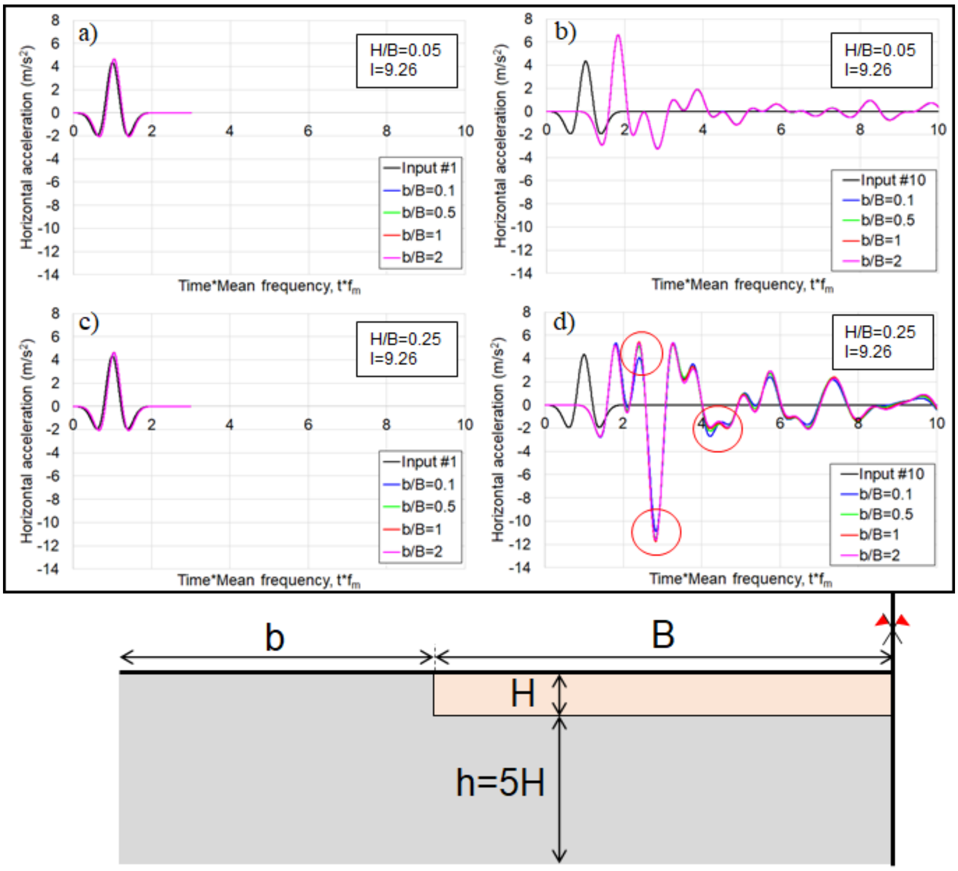

Figure III.3.3 – Accelerograms at the centre of the valley for I=9.26, H/B=0.05-0.25, #1-10 varying b/B

In details, when the mean frequency of the input motion is significantly lower than $f_{0,1D}$ ($f_m/f_{0,1D}$=0.2 in Figure III.3.2a,c - Figure III.3.3a.c) the ground motion at surface is not influenced by the shape ratio or more precisely, by presence of the deformable valley, since the wavelength of the input is much larger than the thickness of the valley, this behaviour is extensively studied in the following (c.f. §III.4.4). For higher frequencies (Figure III.3.2b,d - Figure III.3.3b,d), however, the amplitude of the acceleration at surface is not affected by the border if b/B≥0.5, while it slightly decreases when the border of the domain are closer to the edge of the valley (b/B=0.1). Furthermore, in the case of I=9.26 and H/B=0.25 at the centre of the valley (Figure III.3.3d), the maximum acceleration depends non-negligibly on the width of the model, indeed, for b/B=0.1 the PGA is a 10% lower than for larger values of b/B.

Figure III.3.4 shows the contour of PGA obtained for H/B=0.25, I=9.26 and $f_m/f_{0,1D}$=2 as b/B varies. The wave propagation inside the bedrock at the lateral sides of the valley is almost 1D for b/B≥0.5, while slight disturbances can be observed for lower values of b.

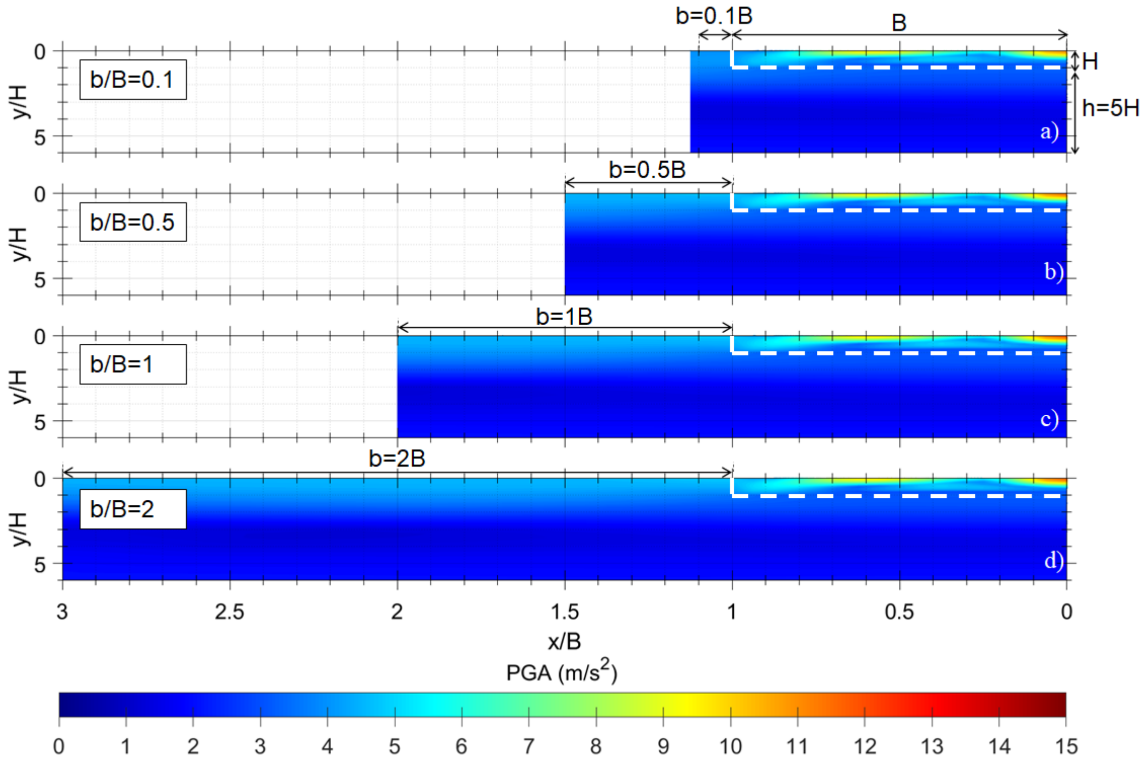

Figure III.3.4 – PGA contour for H/B=0.25, I=9.26, #10 varying b/B

Once evaluated the optimal value of the ratio b/B equal to 0.5, another set of analyses is carried out varying the thickness of the bedrock, ranging the ratio h/H between 0.1 and 5. Figure III.3.5 reports the contour of the PGA for different values of h/H showing that a bedrock thickness comparable to that of the valley (h/H=1) is enough to guarantee that the lower border of the domain does not influence the ground motion at surface.

In the following all the analysed models are characterised by a ratio b/B=0.5 and h/H=1.

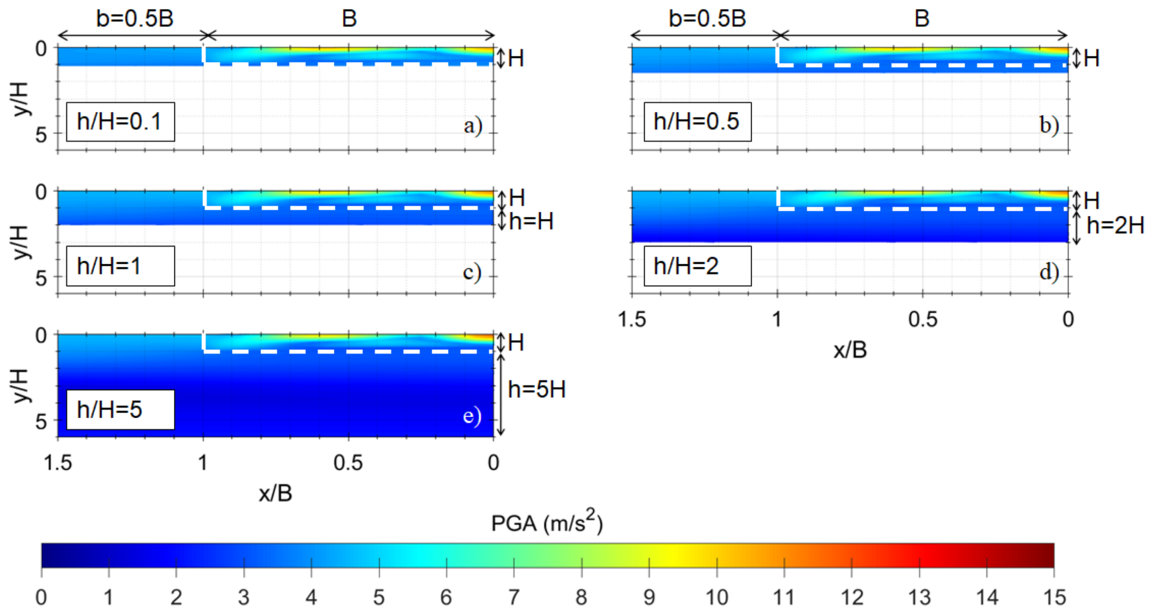

Figure III.3.5 – PGA contour for H/B=0.25, I=9.26, #10 varying h/H

III.4 Influence of factors on surface ground motion

The results of the parametric analyses have been preliminarily represented in terms of time histories of acceleration at surface comparing the results obtained from 2D and 1D analyses. Furthermore, the same results are then synthesized in terms of spectral amplification factor, AG:

$$AG\left(T,\frac{x}{B}\right)=\frac{S_{a,s}\left(T,\frac{x}{B}\right)}{S_{a,r}(T)} \qquad \text{III.4.1}$$

where:

— $S_{a,s}\left(T,\frac{x}{B}\right)$: spectral acceleration of ground motion at the surface;

— $S_{a,r}(T)$: spectral acceleration of the input.

and finally, a geometrical aggravation factor is computed as:

$$AG_{2D/1D}\left(T,\frac{x}{B}\right)=\frac{AG_{2D}\left(T,\frac{x}{B}\right)}{AG_{1D}(T,0)} \qquad \text{III.4.2}$$

where AG_{2D} and AG_{1D} are the amplification factor obtained with 2D and 1D analysis, respectively. Note that $AG_{2D/1D}$ is in practice the same aggravation factor as defined by Chávez-García & Faccioli (2000). Indeed, AG_{1D} and AG_{2D} are calculated as the ratio of the 1D or 2D spectra at the surface and at the bedrock, and thus $AG_{2D/1D}$ is simply the ratio of the 2D and 1D surface spectra.

In the following a synthesis of the numerical results is reported with the aim of highlighting the influence of the geometric and mechanical properties on the 2D amplification at surface. For each of the analysed factor some typical and most significant results are shown. Firstly, the results obtained for trapezoidal valleys are reported (§§III.4.1-III.4.4), then the case of wedge-type geometry is analysed (§III.4.5).

III.4.1 Shape ratio

The influence of shape ratio, H/B, on the seismic response is here illustrated comparing the time histories of the horizontal and vertical acceleration at surface, computed considering two valley models characterized by the same impedance ratio (I=9.26), and edge slopes (α=45°) and by two different shape ratio respectively equal to 0.05 (Figure III.4.1c) and 0.25 (Figure III.4.1d), subjected to the same input motion, in such a way as to obtain a frequency ratio, $f_m/f_{0.1D}$, equal to 2 in both cases. It is worth to highlight that the results reported in Figure III.4.1 are drawn in a normalised plot where the abscissa is the ratio between the distance from the centre and the half width of the basin, x/B, and the ordinate is a normalised time obtained by multiplying the time by the mean frequency of the reference input motion. In the same figure the time history of the input motion is shown in Figure III.4.1a while the 1D response at surface obtained along the vertical profile corresponding to the centre of both valleys is reported in Figure III.4.1b.

In the case of very shallow valley (H/B=0.05) (Figure III.4.1c) the ground motion at surface is close to the 1D response computed at the centre of the valley (Figure III.4.1b) except for a limited zone close to the edges, where Rayleigh waves generated at the edges of the valleys interfere with the vertical propagating direct waves, sensibly modifying the amplitude and the frequency content of the signal. Conversely, for the high values of shape ratio (H/B=0.25) (Figure III.4.1d) the seismic motion at surface along the valley profile is clearly different from 1D response, since in this case it is significantly affected by the propagation of Rayleigh waves that interact with direct waves along the whole basin. The value of the amplification peak near the edge does not depend on the shape ratio, H/B, while its relative position x/B varies, approaching the centre of the valley as the shape ratio increases. The abscissa of the peak amplification can be computed as a function of the thickness, H and the slope angle, α, as $B - H \cdot \left(\tan(\alpha) + \cot(\alpha)\right)$, confirming the finding by Zhu & Thambiratnam (2016) who studied the geometry and the interference of wave paths. As a matter of fact, for edge slopes greater than 30°, the zone of maximum interference between the direct, reflected, and refracted waves is external to the edge zone and extends for a length of $H \cdot \tan(\alpha)$ toward the centre of the valley. The portion of the valley where the ground motion at surface is affected by 2D effects increases with the shape ratio extending from the edges towards the centre.

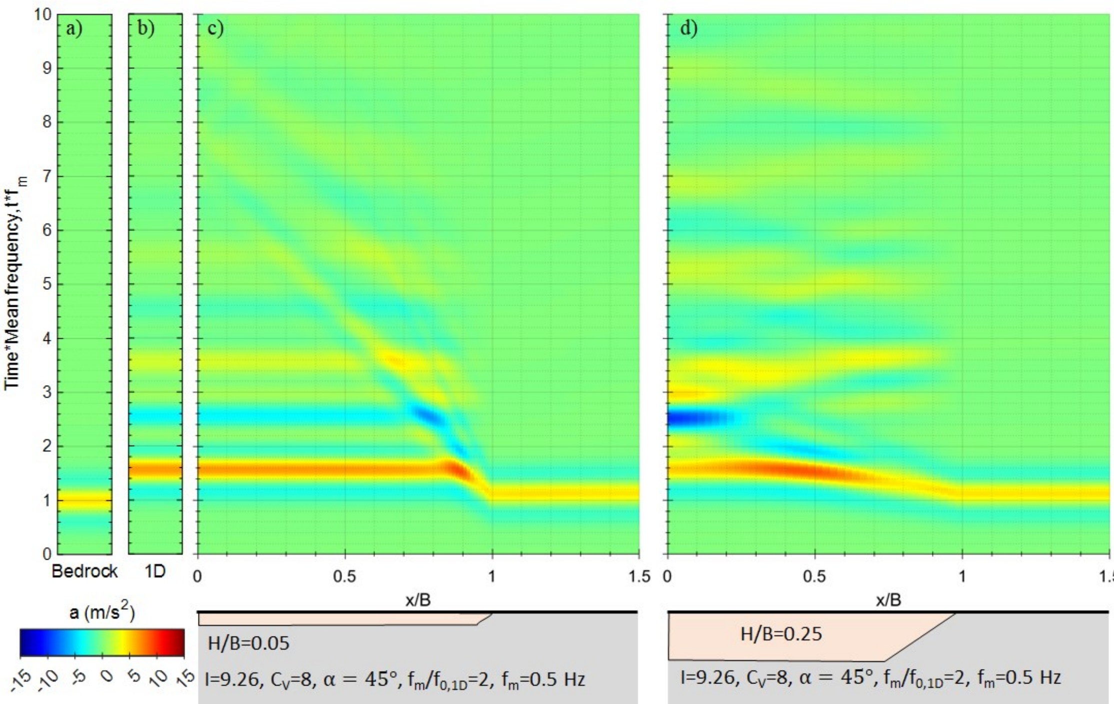

Figure III.4.1 – Horizontal accelerograms: a) input motion, b) at the surface of the 1D profile at the centre of the valley, c) at surface of the valley with H/B=0.05; d) at surface of the valley with H/B=0.25

These trends are confirmed also by the vertical accelerations at surface, reported in Figure III.4.2, which become relevant (with a magnitude comparable to the horizontal component) at the centre of the valley characterised by a high shape ratio (H/B=0.25), while in the case of the shallowest valley (H/B=0.05) the vertical accelerations can be detected only at the edge of the basin. The interference between Rayleigh and direct waves also produces clearly asynchronous seismic motion along the basin, as shown by the time histories reported in Figure III.4.1d which should be accounted in the design of infrastructures (e.g. bridge, pipeline). In the case of shallower valley, instead, the motion is in phase along most of the basin except for the zone near the edges (see Figure III.4.1c).

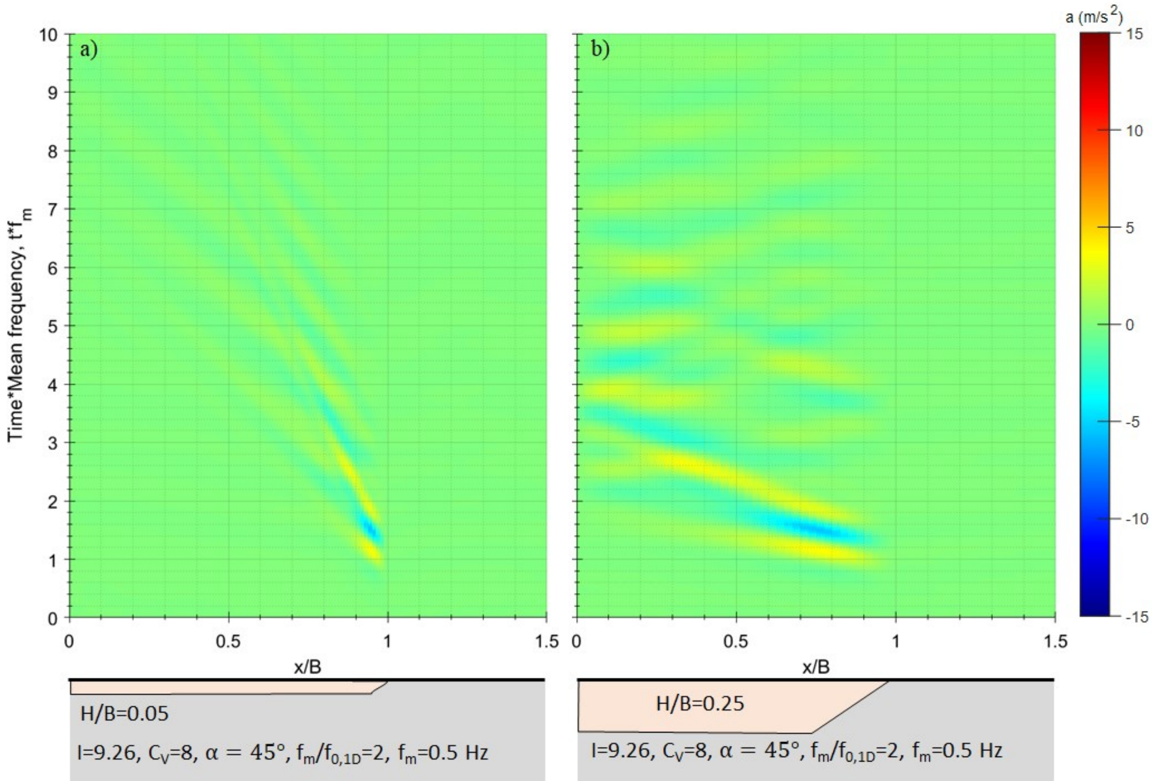

Figure III.4.2 – Vertical acceleration at surface for H/B: a) 0.05; b) 0.25

To better highlight the different behaviour of the two valleys Figure III.4.3 - Figure III.4.5 show the reference input motion (grey line), the 1D ground motion (green line) and the horizontal and vertical accelerograms obtained in correspondence of the centre of the valley (black line), for x/B=±0.5 (blue and cyan lines) and x/B=±0.95 (red and magenta lines), respectively.

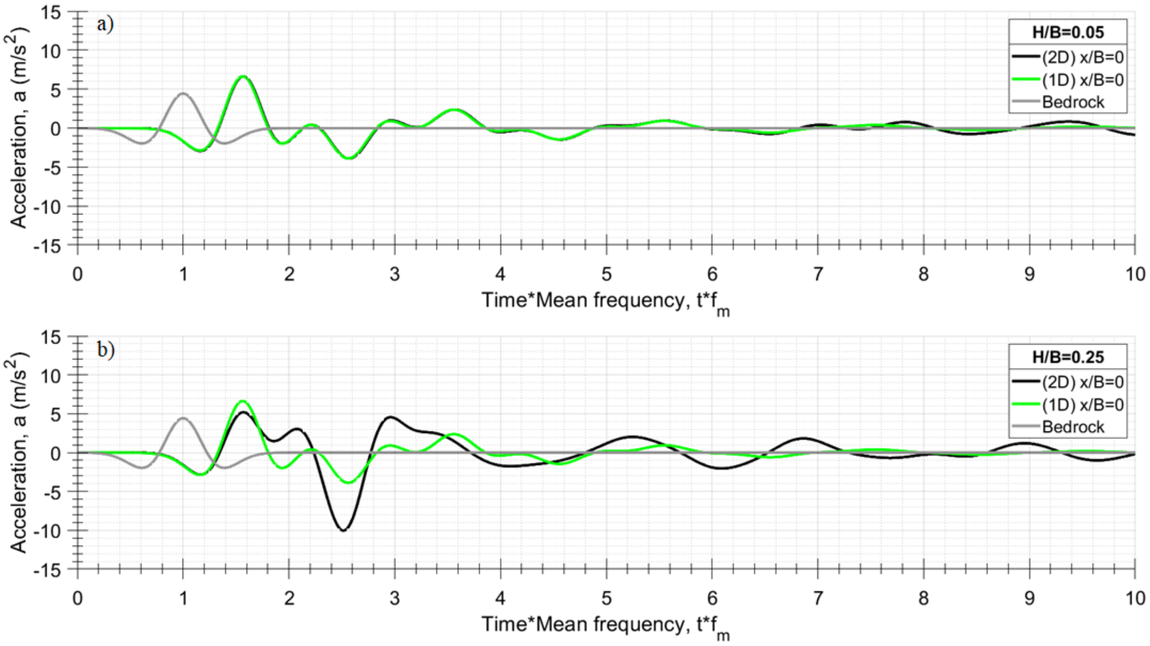

Figure III.4.3 – Comparison between horizontal accelerograms obtained at the centre of the valley (x/B=0) with 2D (black line), 1D (green line) and the reference input motion (grey line) for H/B: a)0.05; b) 0.25

The plot of Figure III.4.3a clearly confirms that there are no 2D effects at the centre of the valley characterised by a low shape ratio (H/B=0.05). On the other hand, in the case of the valley with high shape ratio, the comparison between the time histories of acceleration, computed at the centre of the valley by 2D and 1D analyses (Figure III.4.3b), shows that initially the 2D motion is not influenced by the Rayleigh waves which take a finite time to travel through the valley and reach the centre. When this occurs, the 2D accelerogram change significantly from the 1D one both in amplitude and frequency content. This is confirmed also by the results obtained for x/B=±0.5 for both shape ratios, as shown in Figure III.4.4. Indeed, for the very shallow valley, H/B=0.05 (Figure III.4.4a,c), the 1D and 2D time histories overlap until the time at which the Rayleigh wave arrives ($t \cdot f_m = 4$) when an increase of vertical acceleration takes place and the 2D horizontal acceleration tends to differ from 1D case. On the other hand, for H/B=0.25 (Figure III.4.4b,d), the arrival time of Rayleigh waves is comparable to that of direct ones thus influencing the whole 2D time history of accelerations. In this case, there is a constructive interference between the different wave fields causing an increase in the maximum horizontal acceleration.

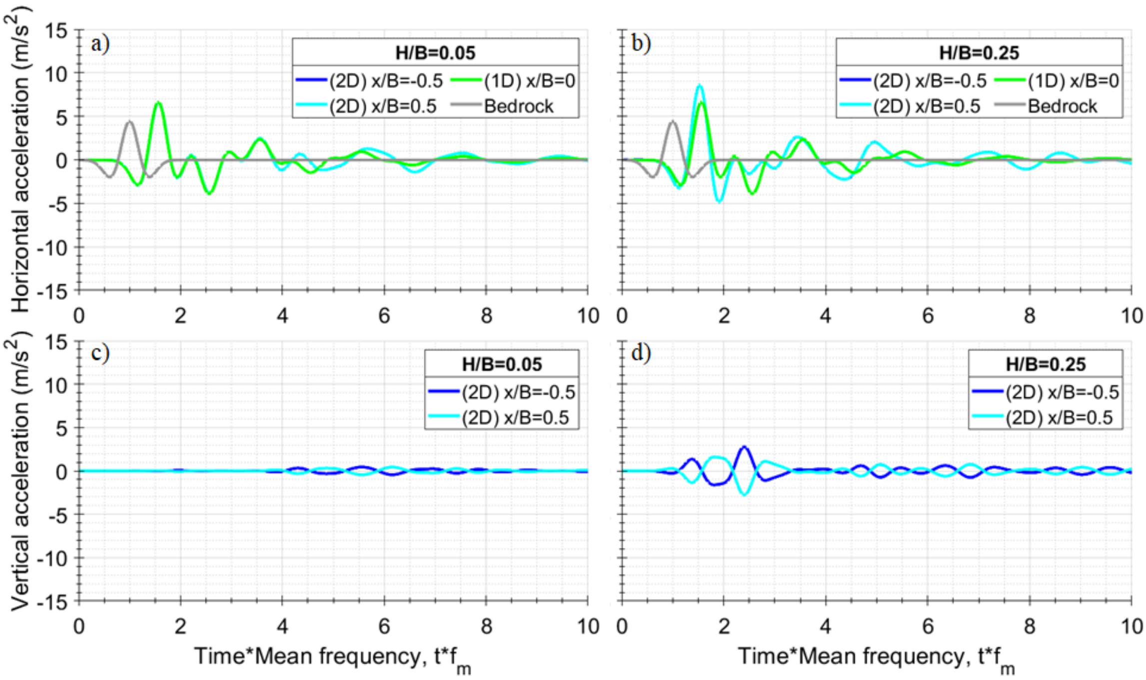

Figure III.4.4 – Comparison between horizontal and vertical accelerograms obtained at x/B=0.5 of the valley with 2D (blue and cyan lines), 1D (green line) and the reference input motion (grey line) for H/B: a,c)0.05; b,d) 0.25

At x/B=±0.95 (Figure III.4.5), instead, an attenuation of 2D seismic motion respect to the 1D case takes place, whatever the shape ratio is.

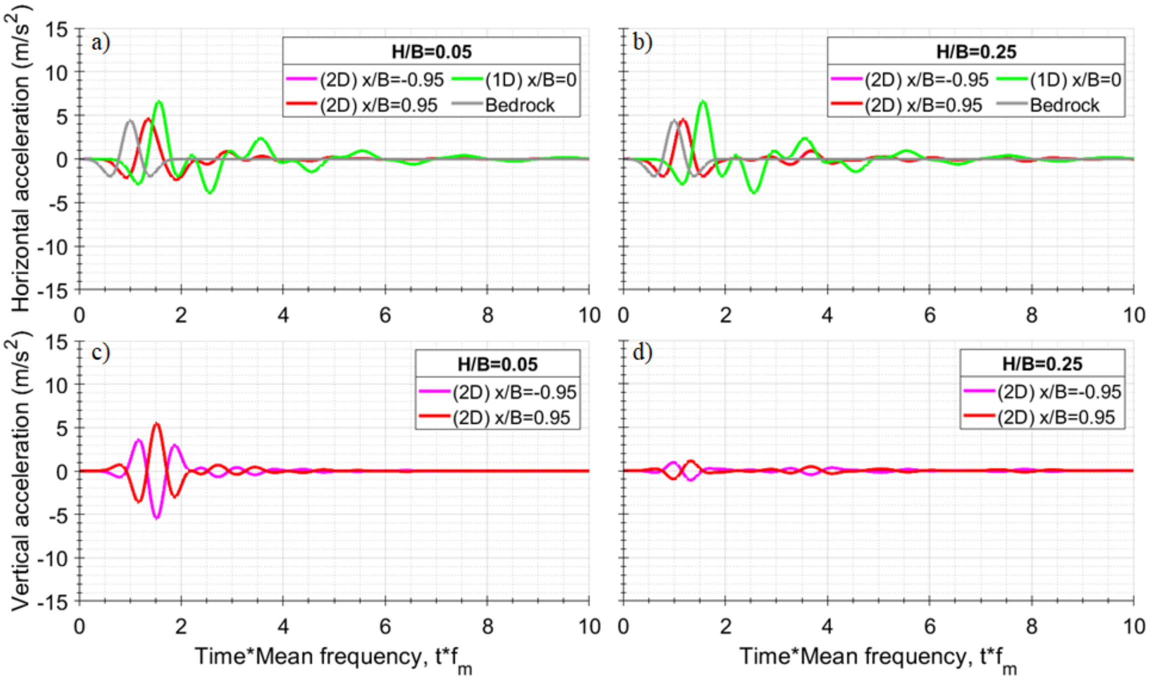

Figure III.4.5 – Comparison between horizontal and vertical accelerograms obtained at x/B=0.95 of the valley with 2D (red and magenta lines), 1D (green line) and the reference input motion (grey line) for H/B: a,c) 0.05; b,d) 0.25

Note that representing the results adopting the normalised abscissa, x/B, may cause a misunderstanding of the wave propagation phenomena close to the edges. The phenomena appear clearer if an absolute abscissa is considered. As a matter of fact, in Figure III.4.6 the time histories of acceleration computed at a distance of 20 m from the valley edge are plotted for both shape ratios (x/B=±0.9875 for H/B=0.05 and x/B=±0.95 for H/B=0.25): the horizontal and vertical component of ground motion computed for both values of shape ratios are similar (Figure III.4.6). This is since the surface waves move with a velocity that does not depend on H/B but only on the f_m and V_s, which are equal for the two analysed models. Therefore, for the same I, α, $f_m/f_{0,1D}$ and different shape ratios, H/B, points at equal distance from the edge have different x/B but the same ground motion due to the combination of body and surface waves.

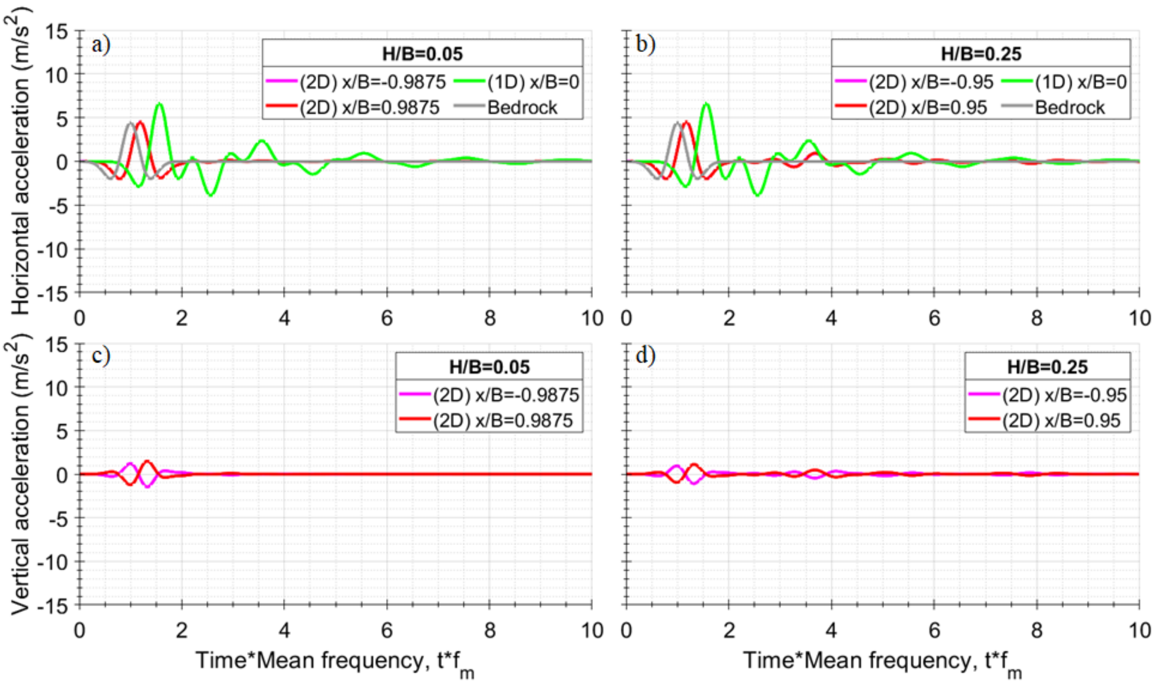

Figure III.4.6 – Comparison between horizontal and vertical accelerograms obtained at 20m from the edge with 2D (red and magenta lines), 1D (green line) and the reference input motion (grey line) for H/B: a,c) 0.05; b,d) 0.25.

The influence of shape ratio on the response at the ground surface has been also evaluated in terms of amplification function (ratio between the Fourier spectra of acceleration at surface and at bedrock): in Figure III.4.7 the amplification function computed at the surface of the 1D profile corresponding to the centre of the valley (Figure III.4.7a), is compared to those evaluated along the valleys characterised by H/B=0.05 (Figure III.4.7b) and 0.25 (Figure III.4.7c). The results confirm what has been already observed in terms of time histories of accelerations. In the case of H/B=0.05 the amplification function computed within the central part of the valley is very similar to that of the 1D column, while at the edge a slight increase in the fundamental frequency occurs. Instead, the amplification function of the valley with H/B=0.25 is characterized by a 2D resonance frequency, $f_{0,2D}$, equal to 1.1-1.2 $f_{0,1D}$ in the central area and 1.8-2 $f_{0,1D}$ at the edge.

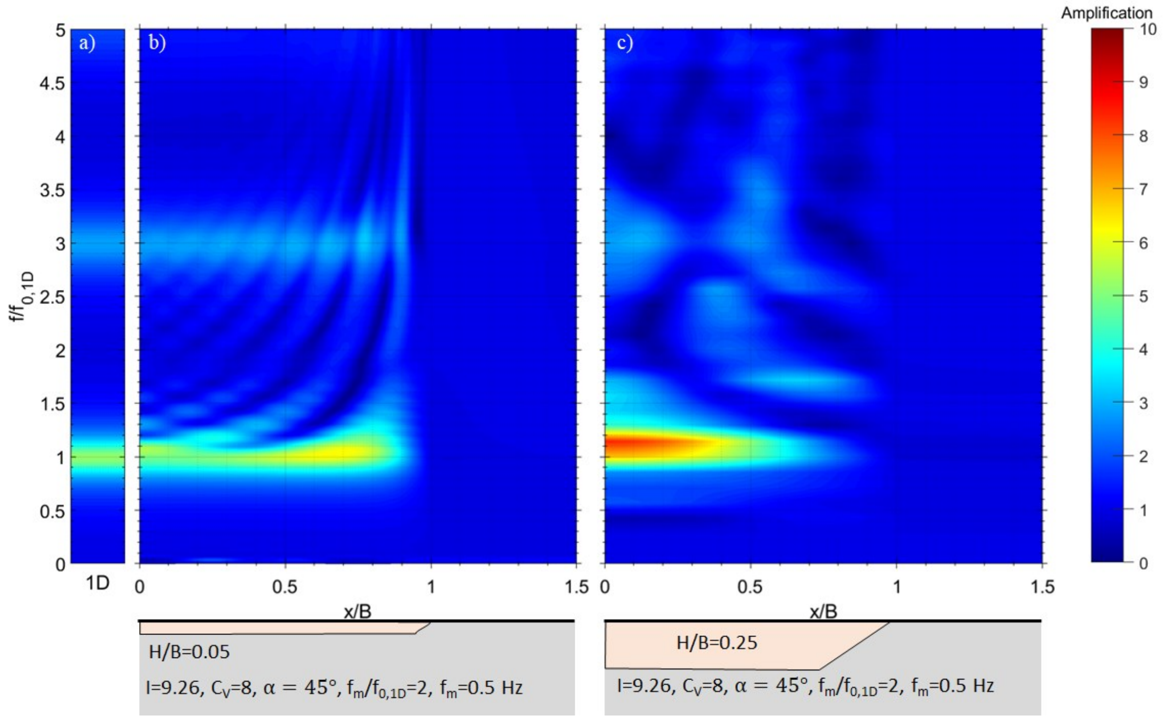

Figure III.4.7 – Ratio between Fourier spectra at the surface and bedrock for a) 1D analysis and b,c) 2D analysis.

For further confirmation, Figure III.4.8 shows the comparison between the amplification functions computed at the valley centre by 1D and 2D analyses for the two different shape ratios. In the case of very shallow valley, H/B=0.05 (Figure III.4.8a), the amplification functions computed by 1D and 2D analyses are almost identical. Both are similar to the theoretical one, obtained for a continuous deformable soil lying on a deformable bedrock. Indeed, the first two amplification peaks are obtained for frequencies equal to 1 and 3 $f_{0,1D}$ and maximum amplitude, A_{max}, equal to (Lanzo & Silvestri, 1999):

$$A_{max} \approx \frac{1}{\frac{1}{I}+\frac{\pi}{2}\cdot D_0} \approx \frac{1}{0.1+\frac{\pi}{2}\cdot 0.05} \approx 5.6 \qquad \text{III.4.3}$$

In the case of H/B=0.25 (Figure III.4.8b) the 2D amplification function at the valley centre is clearly different from the 1D one, $f_{0,2D}$ is around 1.1-1.2 $f_{0,1D}$ and the maximum amplification is about 8.5. Furthermore, the peak of the second mode of vibration occurs at a frequency of 3 times $f_{0,1D}$ but extends over a wider frequency range.

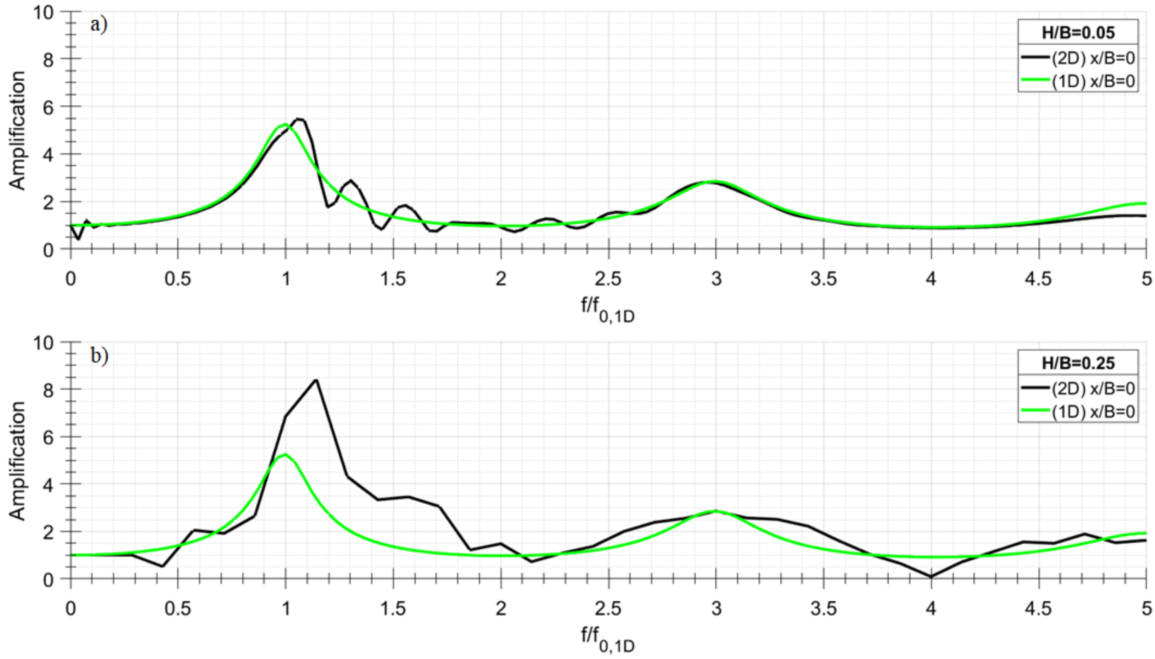

Figure III.4.8 – Comparison between the amplification functions obtained at centre of the valley with 2D (black lines), 1D (green line) analysis for H/B: a) 0.05; b) 0.25.

The results interpreted in terms of response spectra further confirm the observed trends. As a matter of fact, the spectral accelerations computed along the valleys, having different shape ratios, are plotted in Figure III.4.9c,d and compared with that of the input motion (Figure III.4.9a), and that computed at the surface of the 1D reference profile corresponding to the centre of the valley (Figure III.4.9b). The spectral response of the shallow valley, H/B=0.05, (Figure III.4.9c) does not differ from that of the 1D column all along the valley except for the edge zone. The maximum spectral accelerations correspond to a period next to the predominant period of the input motion ($T/T_{0,1D}$≈0.4), both at the centre and at the edge of the valley. A further peak amplification at higher periods can be detected at the edge of the valley (x/B=0.9-0.95) due to Rayleigh waves. On the other hand, for the basin characterised by H/B=0.25 (Figure III.4.9d), a marked spatial variability of the spectral response can be observed. At the centre of the valley the maximum spectral amplification occurs at two different periods, one close to the predominant one and another one corresponding to longer period ($T/T_{0,1D}$=0.6-0.7), probably related to the 2D resonance of the valley.

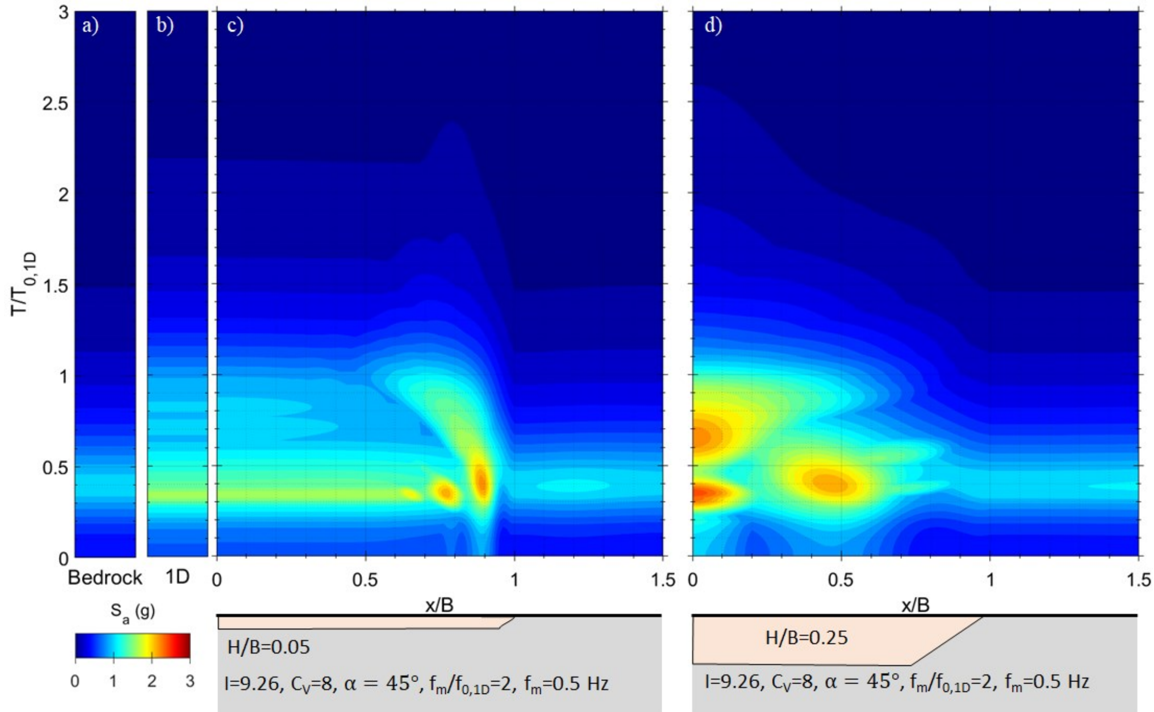

Figure III.4.9 – Acceleration response spectra for: a) input motion; b) 1D analysis; c,d) 2D analysis

Based on the analyses results expressed in terms of response spectra, a spectral amplification factor, AG, has been computed by applying the Eq. III.4.1. AG has been plotted in Figure III.4.10b,c with reference to the results obtained by 2D analyses, and compared to the spectral amplification computed by 1D analysis carried out at the centre of the valley (Figure III.4.10a). According to the response spectra, for H/B=0.05, AG_{2D} is close to AG_{1D} for most of the valley, while at the edges it is higher. On the other hand, for H/B=0.25, AG_{2D} is always greater and different from AG_{1D}.

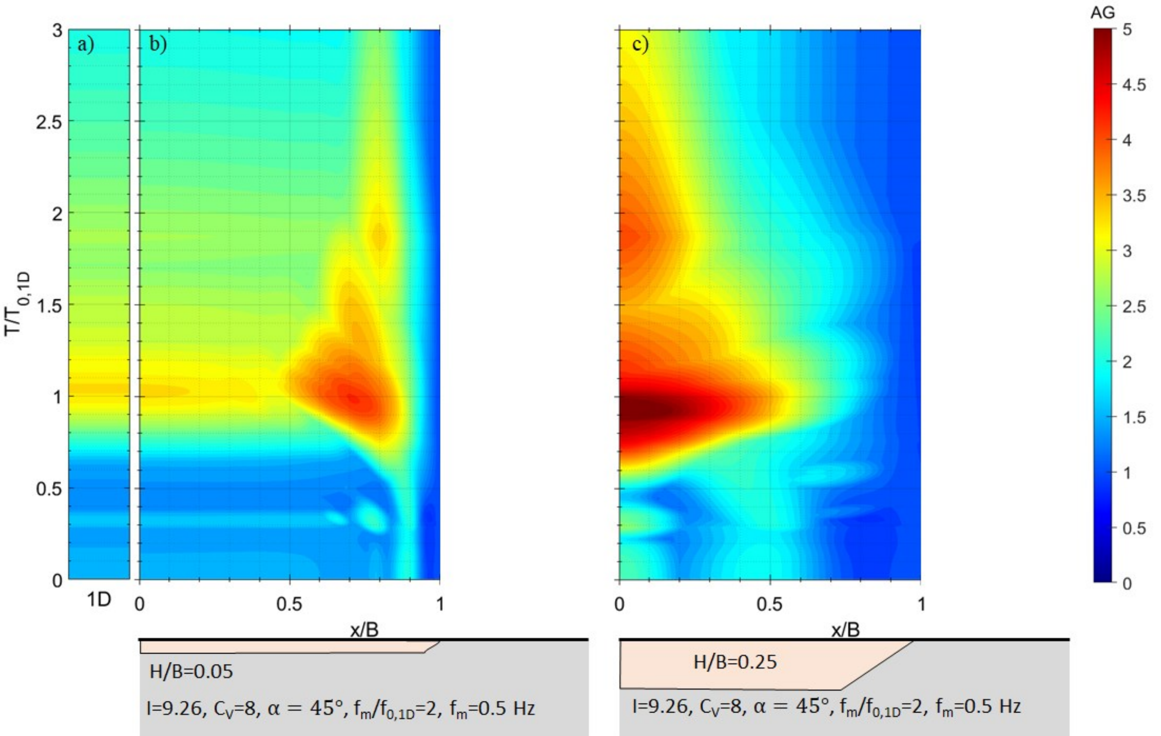

Figure III.4.10 – Spectral amplification factor for: a) 1D analysis; b,c) 2D analysis

To better highlight the role of 2D geometry on the seismic response at surface the analyses results are finally expressed in terms of $AG_{2D/1D}$, as defined by Eq. III.4.2. The results are here shown in Figure III.4.11a,b respectively for the two shape ratios selected. In the case of very shallow valley, H/B=0.05 (Figure III.4.11a), there is no geometrical effect on the response at ground surface computed along the valley except for the zone near the edge. As a matter of fact, the value of $AG_{2D/1D}$ is about one in the central zone of the valley and slightly increases at the edge due to 2D effects. On the other hand, for H/B=0.25 (Figure III.4.11b), the $AG_{2D/1D}$ is greater than 1 along the whole valley confirming that for high values of H/B (but lower than the critical value defined by the relationship suggested by Bard & Bouchon, 1985), the ground motion at surface is increasingly influenced by 2D effects.

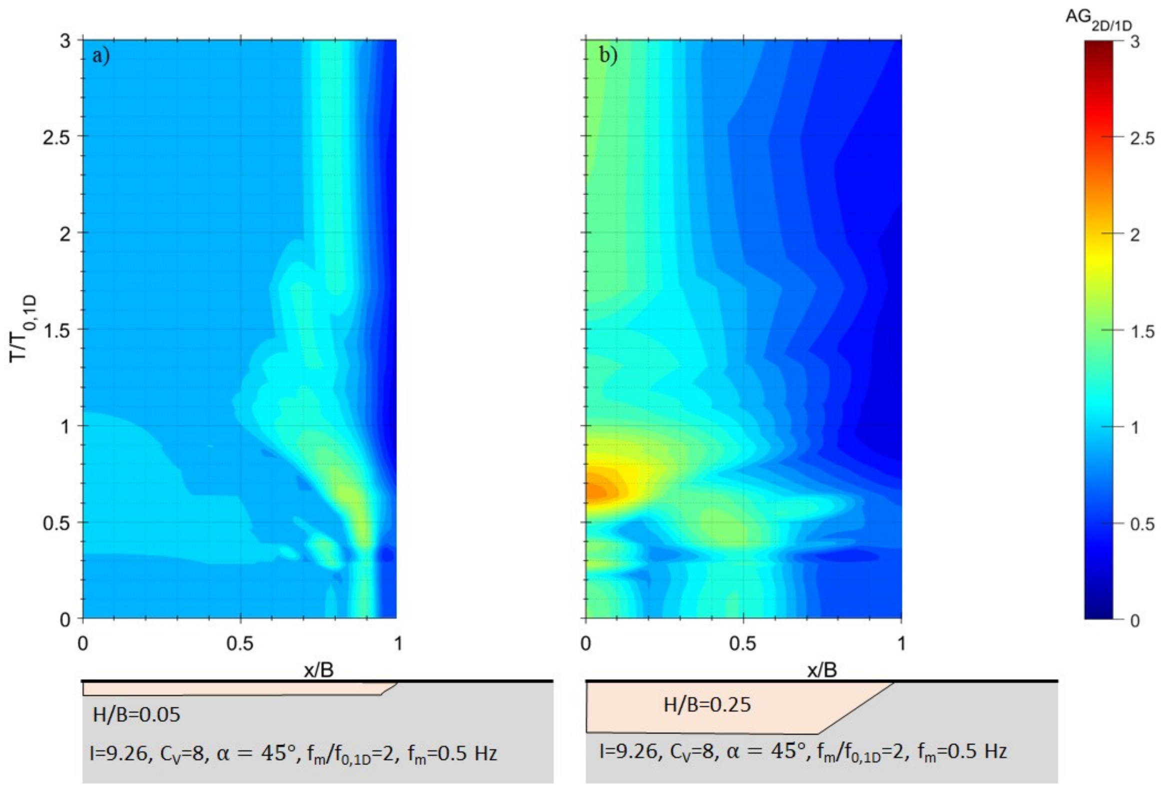

Figure III.4.11 – $AG_{2D/1D}$ for: a) H/B=0.05; b) H/B=0.25.

To better highlight the results obtained in terms of amplification factors, Figure III.4.12, Figure III.4.13 and Figure III.4.14 show the response spectra computed by 2D analyses at three relevant normalised abscissa (x/B=0, x/B=0.5, x/B=0.7) along the very shallow (H/B=0.05) and shallow valley (H/B=0.25), compared to that evaluated at the centre of the valley by 1D analysis and that corresponding to the input motion. In the same figures the amplification factors AG_{1D} and AG_{2D} as well as the ratio $AG_{2D/1D}$ are also reported.

In the case of the very shallow valley (H/B=0.05) the geometrical aggravation factor is equal to one both at the centre (Figure III.4.12a,c) and at x/B=0.5 (Figure III.4.13a,c), whatever the period considered. Near the edge (Figure III.4.14a,c), instead, the 2D S_a is greater than for 1D for $T/T_{0,1D}$=0.8-0.9 and tends to the value for 1D conditions for longer periods.

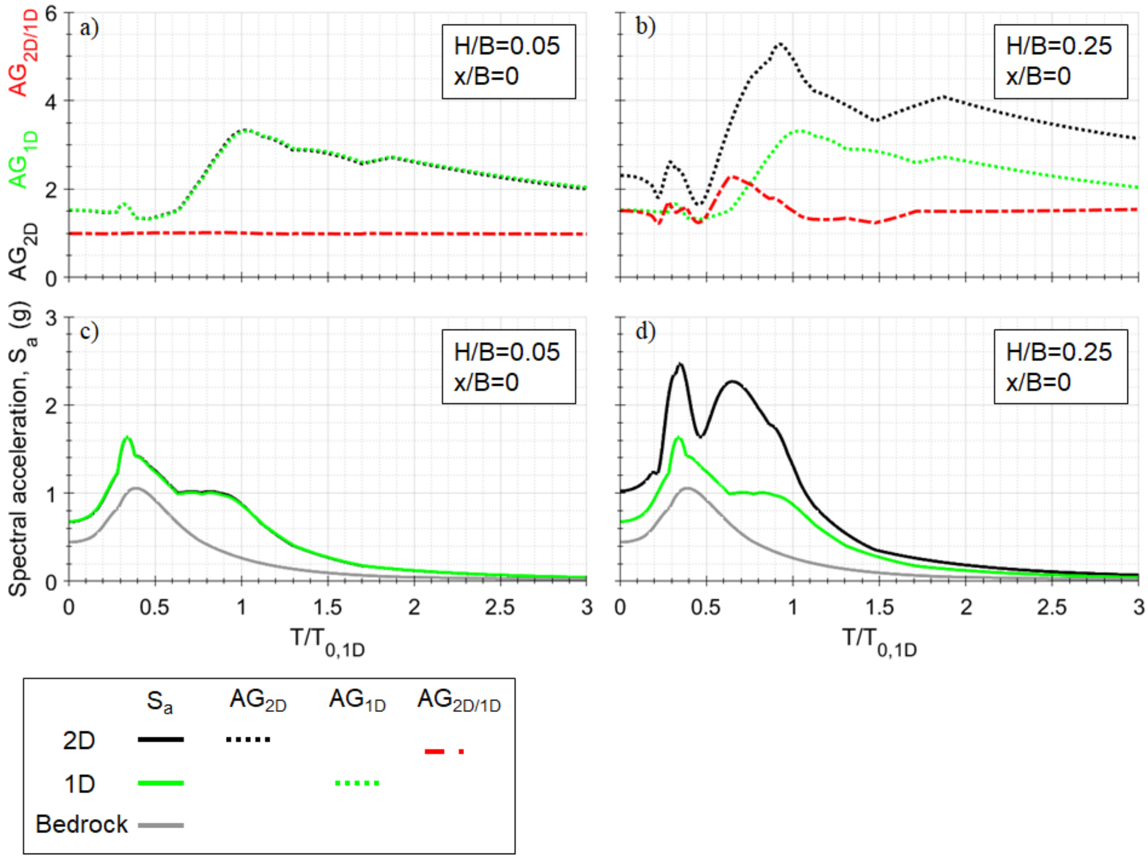

Figure III.4.12 – Comparison between the acceleration response spectra (c,d), AG and $AG_{2D/1D}$ (a,b) obtained at centre of the valley with 2D (black lines), 1D (green lines) analysis for H/B=0.05 and 0.25.

In the case of H/B=0.25 the 2D spectral acceleration at the centre of the valley (Figure III.4.12b,d) is higher than that computed by 1D analysis for periods lower than $T_{0,1D}$, while for longer periods the difference between the two spectra is almost negligible. As a consequence, $AG_{2D/1D}$ is higher than 1, it has a peak for $T/T_{0,1D}$=0.7, due to 2D resonance, while it is constant for greater periods.

Moving from the centre of the valley toward the edge, for x/B=0.5 (Figure III.4.13c,d) the spectral response is mainly ruled by the predominant period of the input, and 2D S_a is greater than 1D for periods close to the predominant one ($T/T_{0,1D}$=0.4). Moreover, for periods greater than $T_{0,1D}$ the 2D spectral ordinates are slightly lower than the 1D ones, hence $AG_{2D/1D}$ is greater than 1 for $T/T_{0,1D}$<1. Therefore, the 2D effects influence the spectral response for periods shorter than the resonance period while they become negligible at longer periods.

Finally, for x/B=0.7 and H/B=0.25 (Figure III.4.14b,d) the 2D response is mostly smaller than the 1D response.

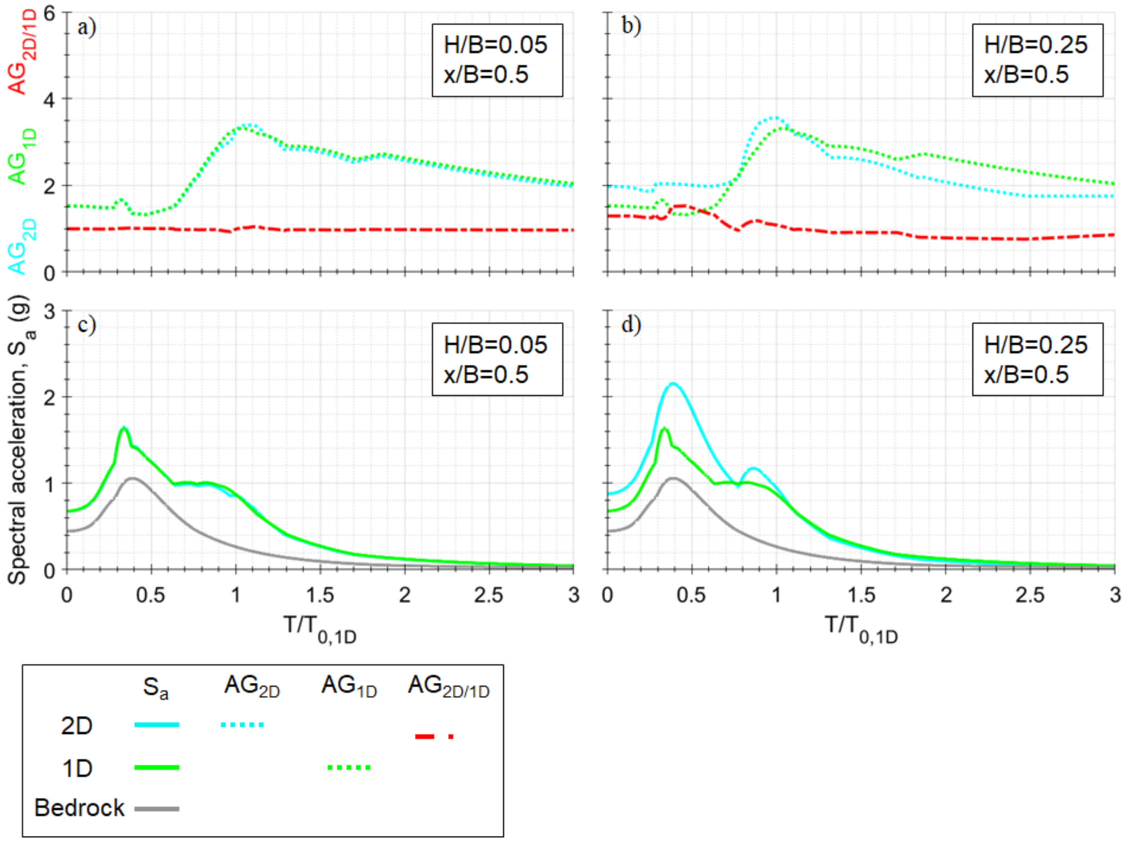

Figure III.4.13 – Comparison between the acceleration response spectra (c,d), AG and $AG_{2D/1D}$ (a,b) obtained at x/B=0.5 with 2D (cyan lines), 1D (green lines) analysis for H/B=0.05 and 0.25.

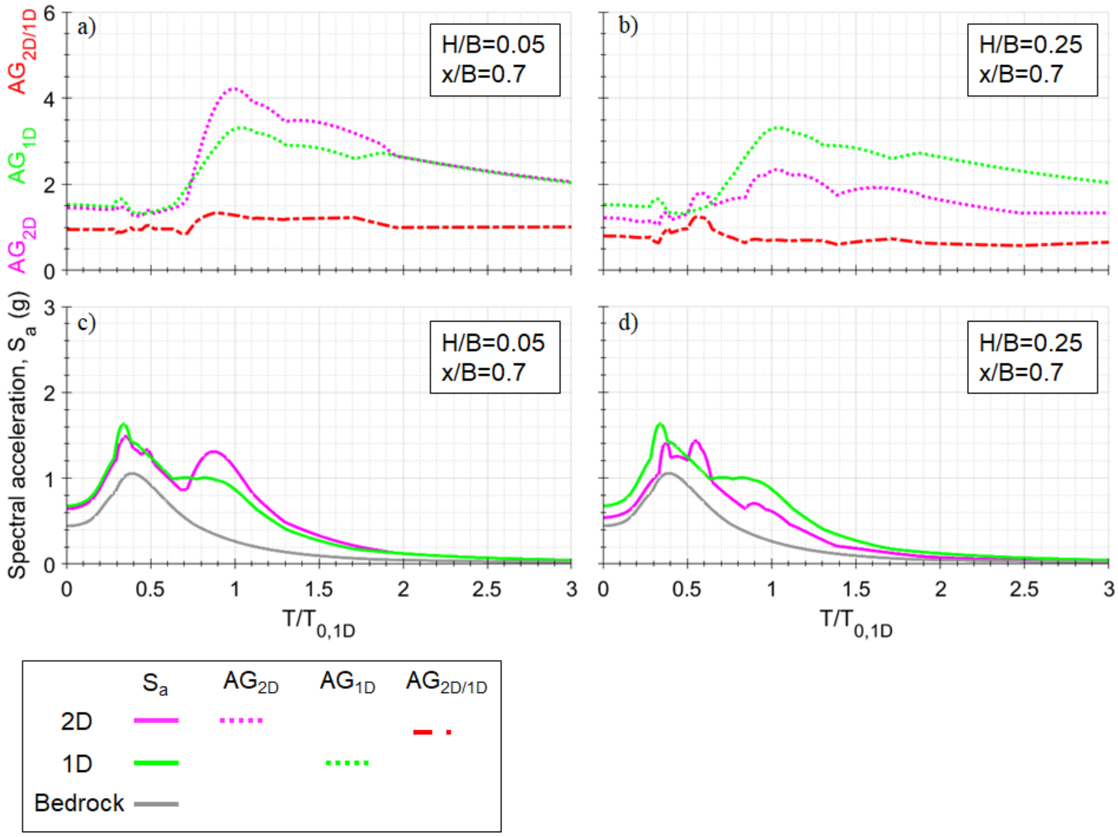

Figure III.4.14 – Comparison between the acceleration response spectra (c,d), AG and AG2D/1D (a,b) obtained at x/B=0.7 with 2D (magenta lines), 1D (green lines) analysis for H/B=0.05 and 0.25.

III.4.2 Impedance ratio

The role of impedance ratio on the seismic response at the ground surface of an alluvial valley is investigated assigning five different shear velocity values (listed in Table III.1.2) to the homogeneous soil deposit laying on a bedrock characterised by a constant shear wave velocity of 800 m/s. Here, a typical example, the response obtained from the numerical analyses applying the same reference input motion to valleys, characterised by the same geometrical model (H/B=0.25, α= 45°), and by two different impedance ratios (I= 1.60 and 9.26) are compared. Figure III.4.15 and Figure III.4.16 show the horizontal and vertical acceleration computed for both valleys.

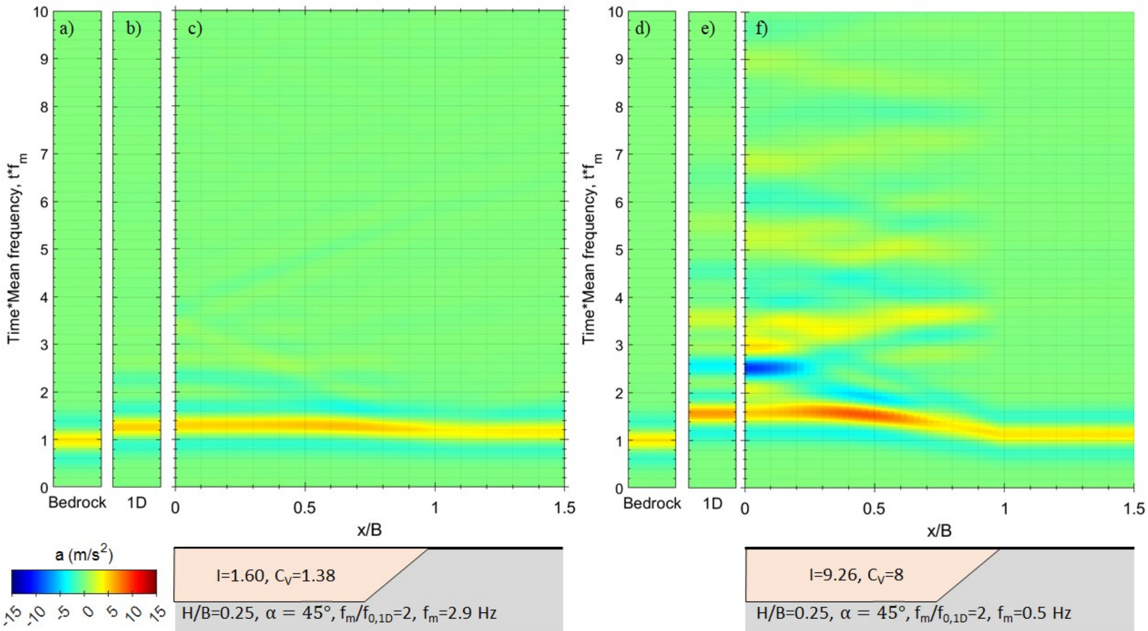

Figure III.4.15 – Horizontal accelerograms: a,d) input motion, b,e) at the surface of the 1D profile at the centre of the valley, c) at surface of the valley with I=1.60; d) at surface of the valley with I=9.26.

As expected, the amplification and the duration of the seismic motion are strongly influenced by the impedance ratio: the energy transmitted at the edge interface and the amplitude of the generated Rayleigh waves increase with I. The horizontal acceleration along the whole valley is poorly amplified in the case of low impedance ratio, as also happen in the case of the 1D response of the column at the centre of the valley (Figure III.4.15b,c), while the vertical accelerations are negligible (Figure III.4.16a). This is not the case of the soft valley, where both 2D and 1D amplification can be clearly detected, as already observed in the previous paragraph (Figure III.4.15d,e,f).

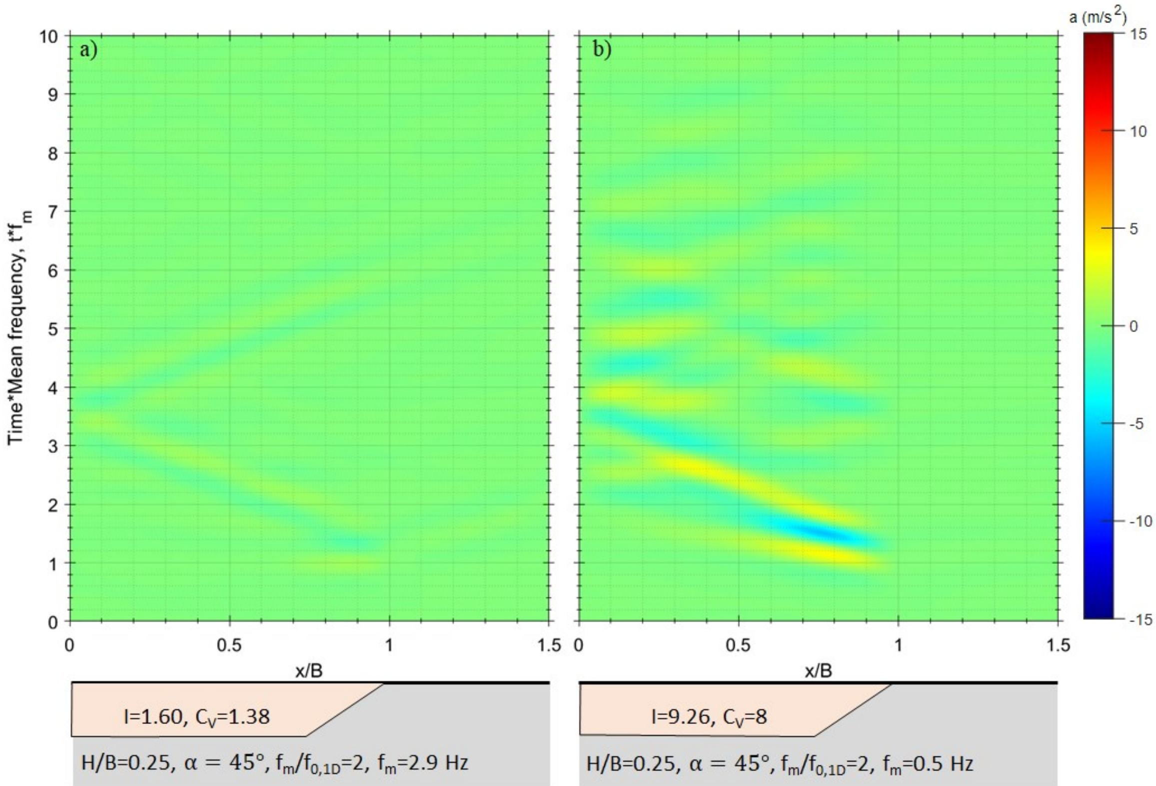

Figure III.4.16 – Vertical acceleration at surface for I: a) 1.60; b) 9.26

Figure III.4.17 shows the horizontal time histories of acceleration obtained at the centre of the valley carrying out 1D and 2D analyses, considering the two different impedance ratio values. In the case of I=1.60 the response at the centre of the valley is not affected by geometrical effect: the time histories computed at surface by 1D and 2D analyses are identical despite the high value of H/B equal to 0.25. This depicts that the seismic response of the alluvial valleys is ruled by a combination of the shape and impedance ratio rather than by the values assumed by the single parameter (see Figure II.2.2).

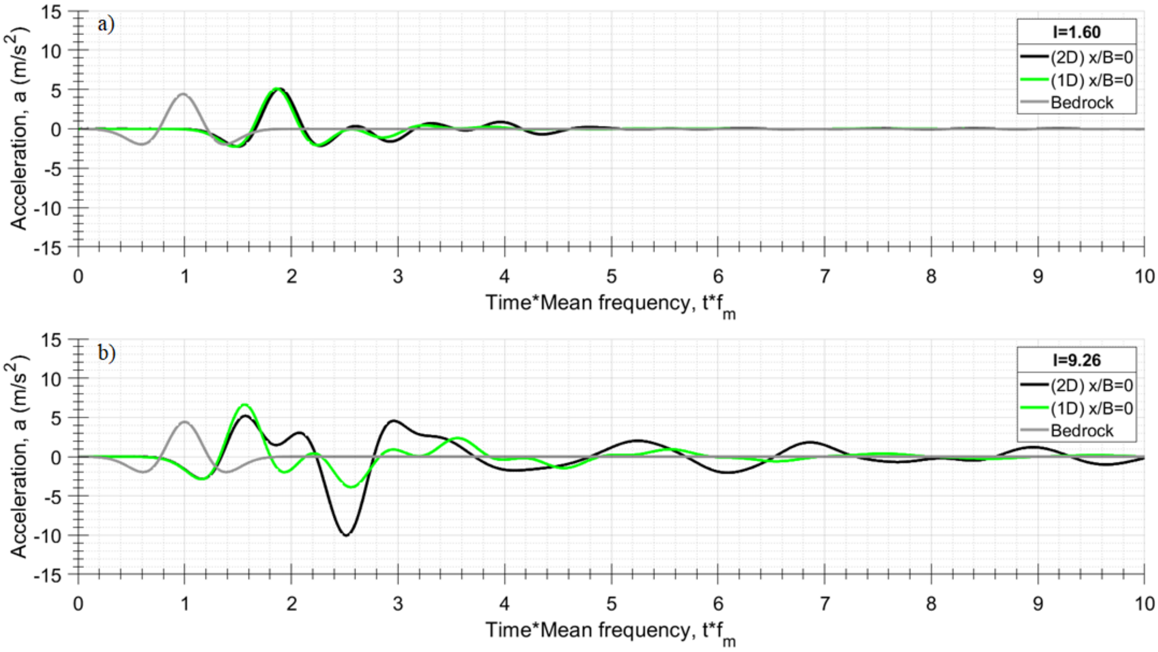

Figure III.4.17 – Comparison between horizontal accelerograms obtained at the centre of the valley (x/B=0) with 2D (black line), 1D (green line) and the reference input motion (grey line) for I: a) 1.60; b) 9.26

The low value of the impedance contrast results in flat amplification function along the valley, as shown in Figure III.4.18a,b, highlighting that in this case the ground response of the valley with a high value of shape ratio is not affected by the 2D effects because of the low impedance ratio.

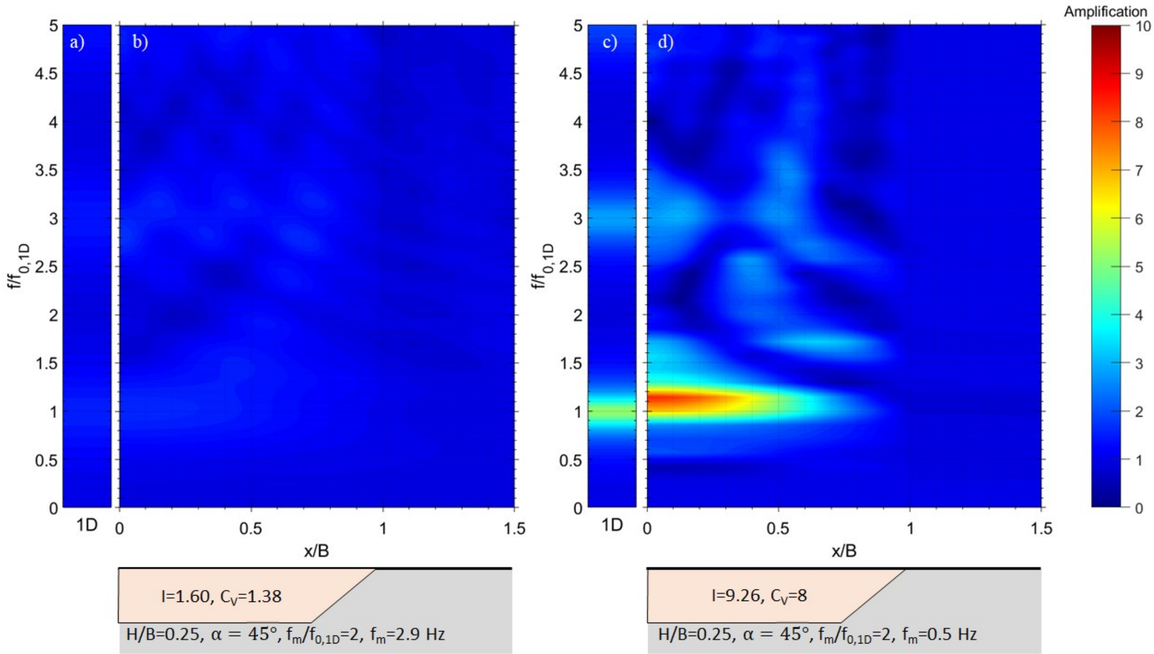

Figure III.4.18 – Ratio between Fourier spectra at the surface and bedrock for a,c) 1D analysis and b,d) 2D analysis.

As an example, in Figure III.4.19 the comparison between the amplification functions obtained at the centre of the valley are plotted. For I=1.60 the 1D function is coincident with the 2D one, both are almost flat and the maximum amplification values are compatible with those computed adopting the Eq. III.4.3.

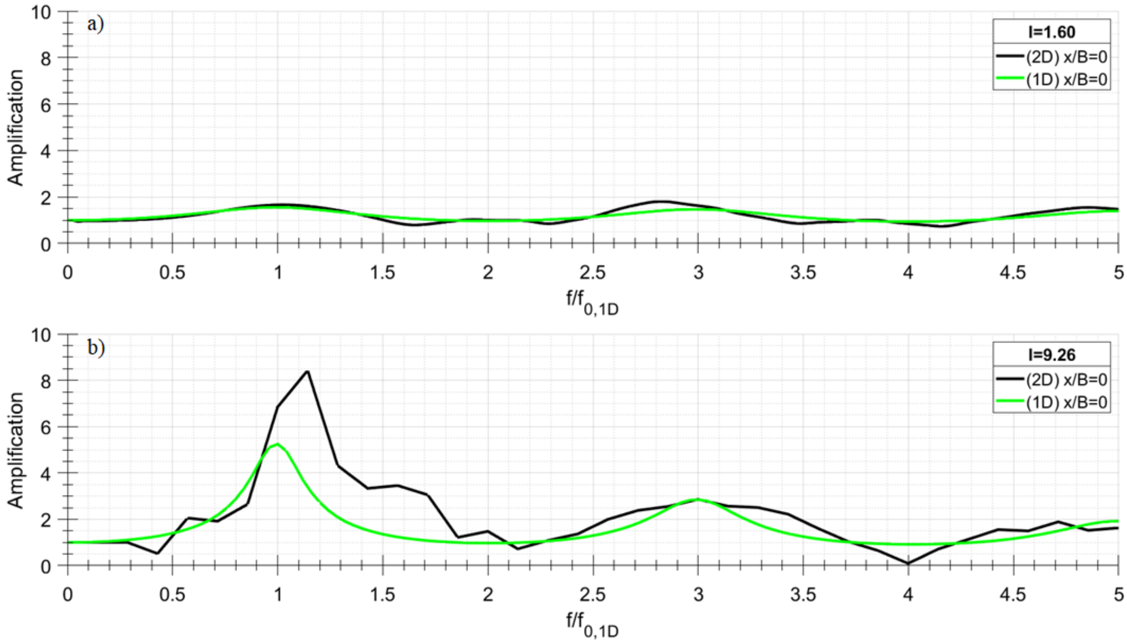

Figure III.4.19 – Comparison between the amplification functions obtained at centre of the valley with 2D (black lines), 1D (green line) analysis for I: a)1.60; b) 9.26.

These trends are confirmed by the 2D spectral accelerations (Figure III.4.20c) that are comparable to that of the 1D column (Figure III.4.20b), both are poorly affected by the propagation. Indeed, they have the same spectral ordinates which are slightly higher than those of the reference input motion, except for a narrow area at the valley edge where there is a slight amplification for periods equal to 0.4-0.6 $T_{0,1D}$.

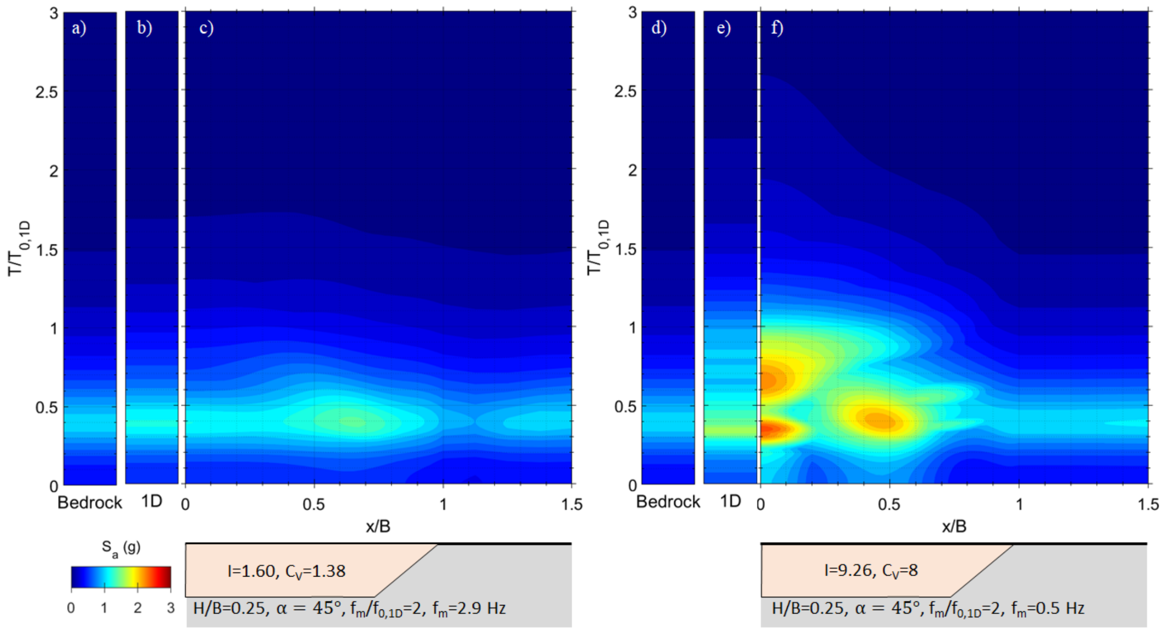

Figure III.4.20 – Acceleration response spectra for: a,d) input motion; b,e) 1D analysis; c,f) 2D analysis

Consequently, the $AG_{2D/1D}$, (Figure III.4.21a) is almost equal to 1 throughout the entire valley and thus no relevant 2D effects can be detected in the case of low impedance ratio, whereas they are relevant for the more deformable basin as already observed in the previous paragraph (§III.4.1).

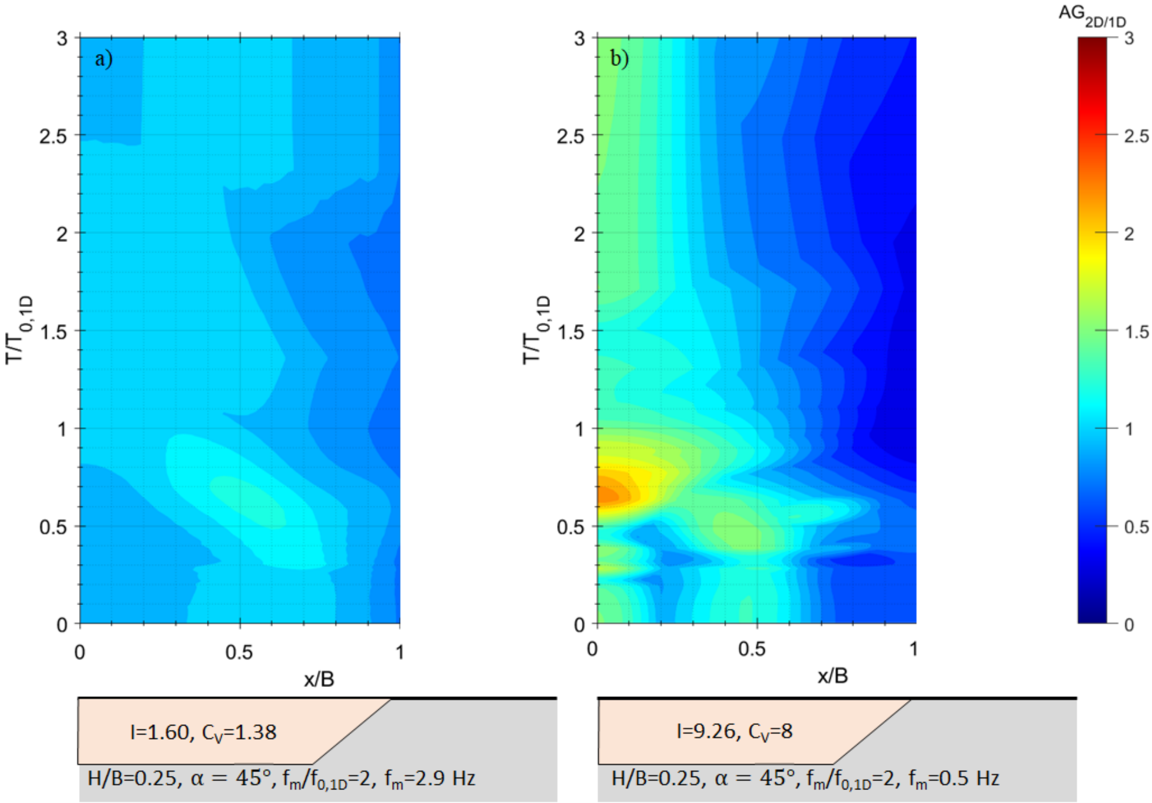

Figure III.4.21 – $AG_{2D/1D}$ obtained for I equal to a) 1.6; b) 9.26

III.4.3 Slope of the edge

To evaluate the effect of the edge slope five different angle values (Table III.1.1) are considered in the analyses, varying between 90° and 15°. Here, to better highlight this effect, the results corresponding to the analyses carried out considering two valleys with the same mechanical properties and shape ratio, but with an edge slope respectively equal to 90° and 45°, are compared. The 2D time history of horizontal accelerations computed for both slope angles (Figure III.4.22c,d) at the centre of the valleys are very similar and characterised by a PGA higher than that computed in the 1D analysis (Figure III.4.22b), hence the response at the centre of the valley is not significantly affected by the edge slope, but only by the H/B, I and $f_m/f_{0,1D}$. This become clearer looking to the plot of Figure III.4.24, where the comparison between the accelerograms obtained on the surface for the two angles is shown (red line for 90° and black line for 45°). The figure shows that the 2D acceleration in the two cases is very similar and significantly different from the 1D one. A different behaviour can be observed at the edge where the abscissa of the maximum acceleration moves from the edge to the centre as the slope angle decreases. As a matter of fact, the vertical acceleration time history reported in Figure III.4.23, for the two considered slope angles, show that the direction of transmitted waves, and then the location of maximum interaction between the direct and the Rayleigh waves, depends on the slope angle, α.

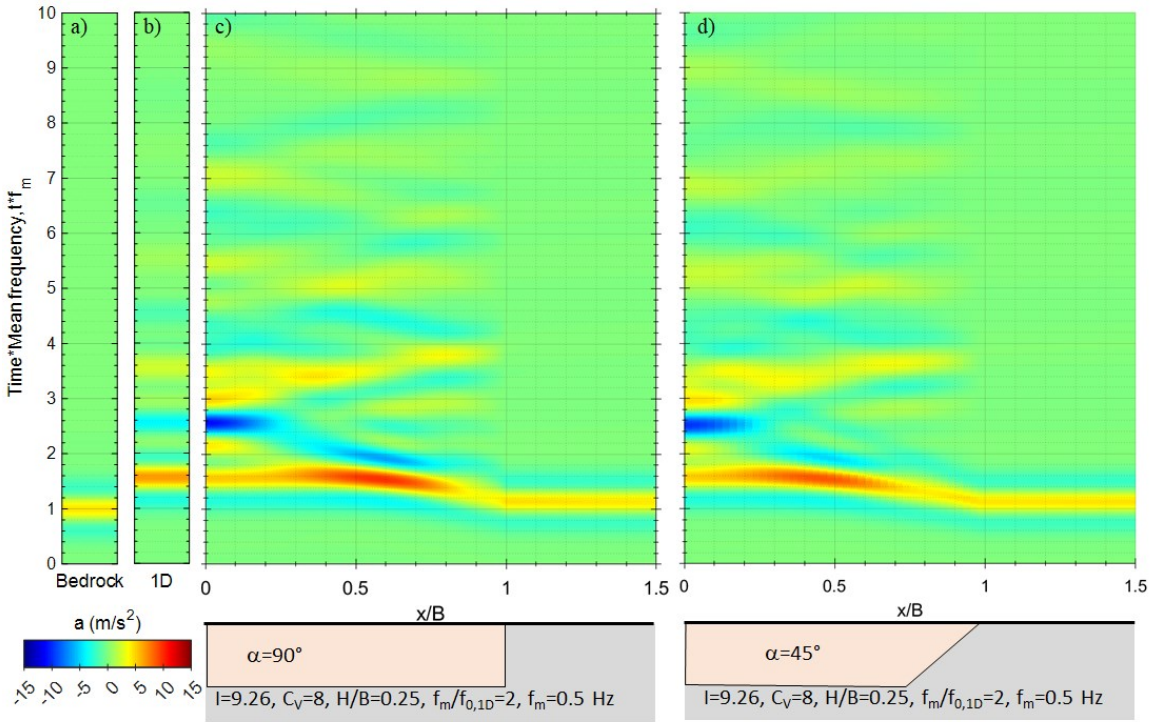

Figure III.4.22 – Horizontal accelerograms for α=90° and 45°

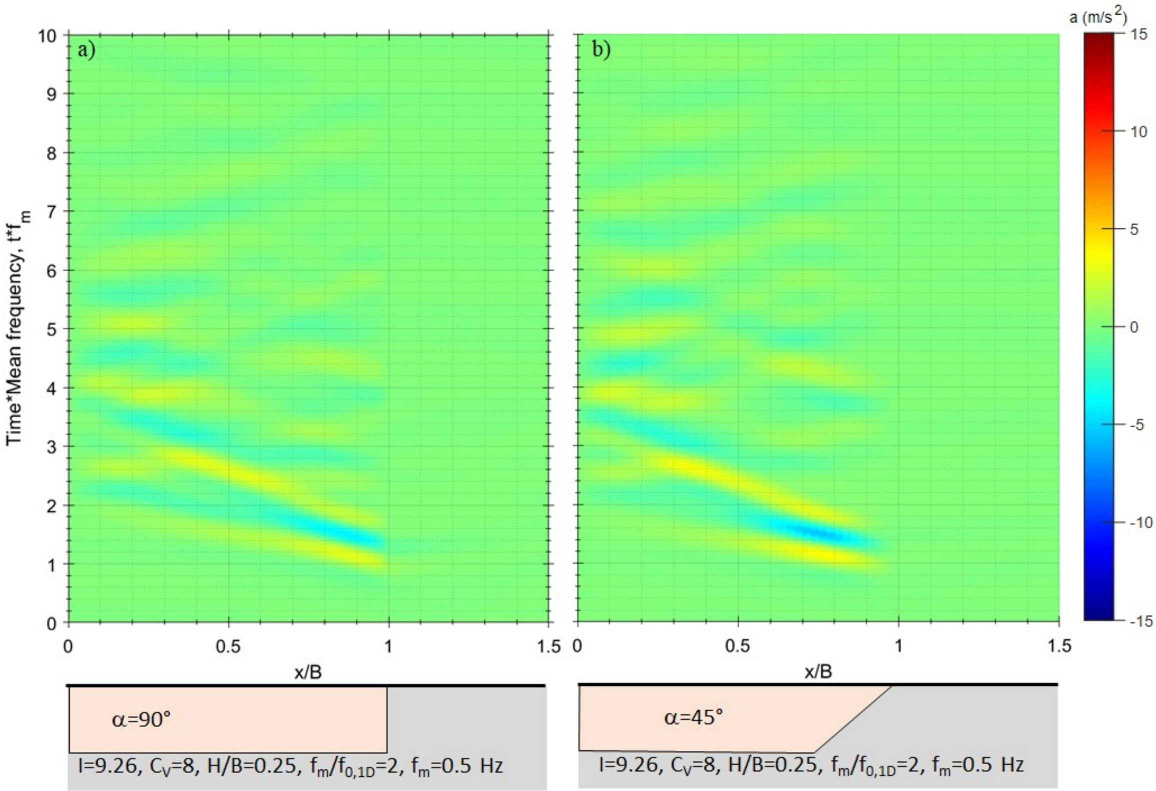

Figure III.4.23 – Vertical accelerograms for α=90° and 45°

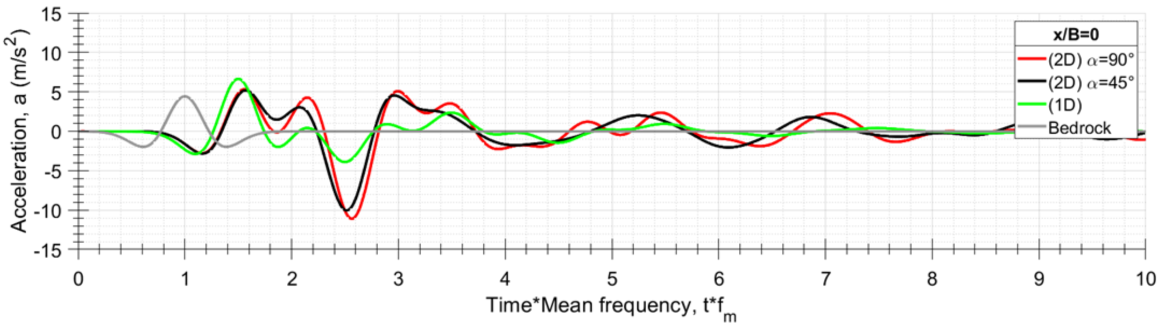

Figure III.4.24 – Comparison between the horizontal accelerograms at centre of the valley for α=90° and 45°.

Along the two analysed valleys the first 2D resonance frequency is not significantly influenced by the slope, on contrary on how happens to the higher modes, as clearly shown in Figure III.4.25, where the amplification functions are plotted.

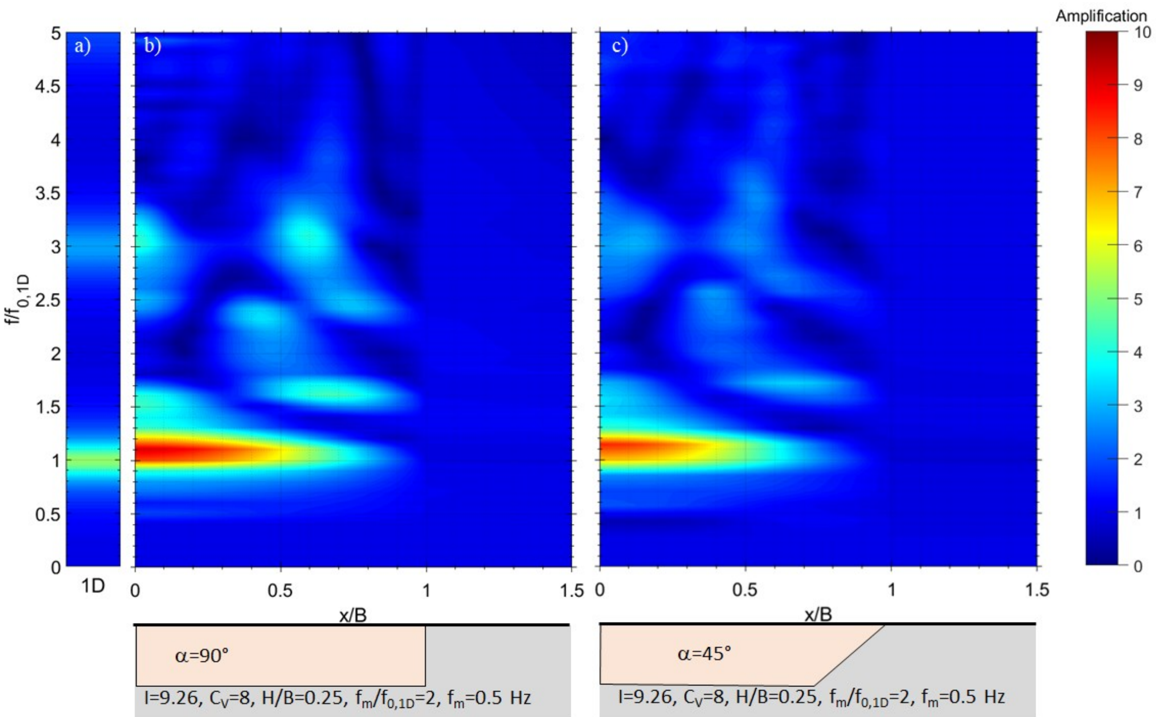

Figure III.4.25 – Ratio between Fourier spectra at the surface and bedrock for a) 1D analysis and b,c) 2D analysis

This is further confirmed by the plot of Figure III.4.26, showing the comparison between the amplification function obtained at the centre of the valley for α equal to 90° (red line) and 45° (black line). Both $f_{0,2D}$ and maximum amplitude are not significantly affected by α, $f_{0,2D}$ ranges between 1.1-1.2 $f_{0,1D}$ while the amplification is about 8.5-9. On the other hand, the second mode of vibration affects a greater range of frequencies and amplitudes in the case of α=90°.

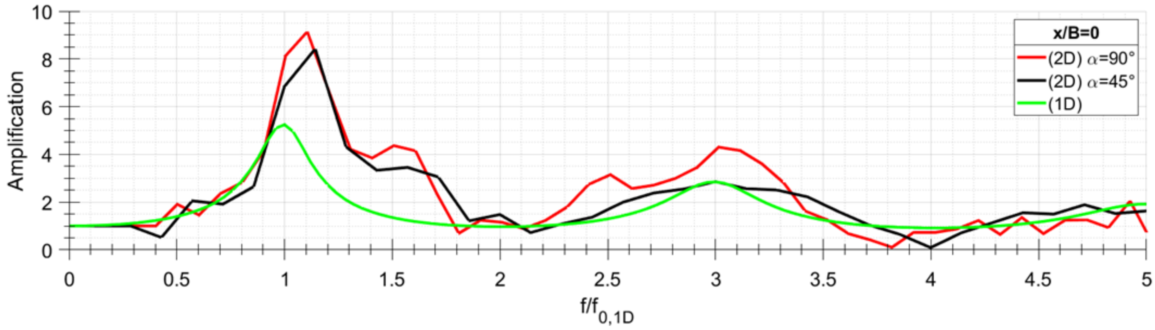

Figure III.4.26 – Comparison between the amplification functions obtained at centre of the valley for α=90° and 45°.

The trends shown by the accelerograms are confirmed by both the surface response spectra (Figure III.4.27) and the $AG_{2D/1D}$ (Figure III.4.28). Indeed, the spectral ordinates at the centre of the valley are slightly affected by the slope angle, while at the edges the abscissa of the peak of the spectral acceleration and its value strongly depend on the angle of inclination at the edges, and the distribution of $AG_{2D/1D}$ as well.

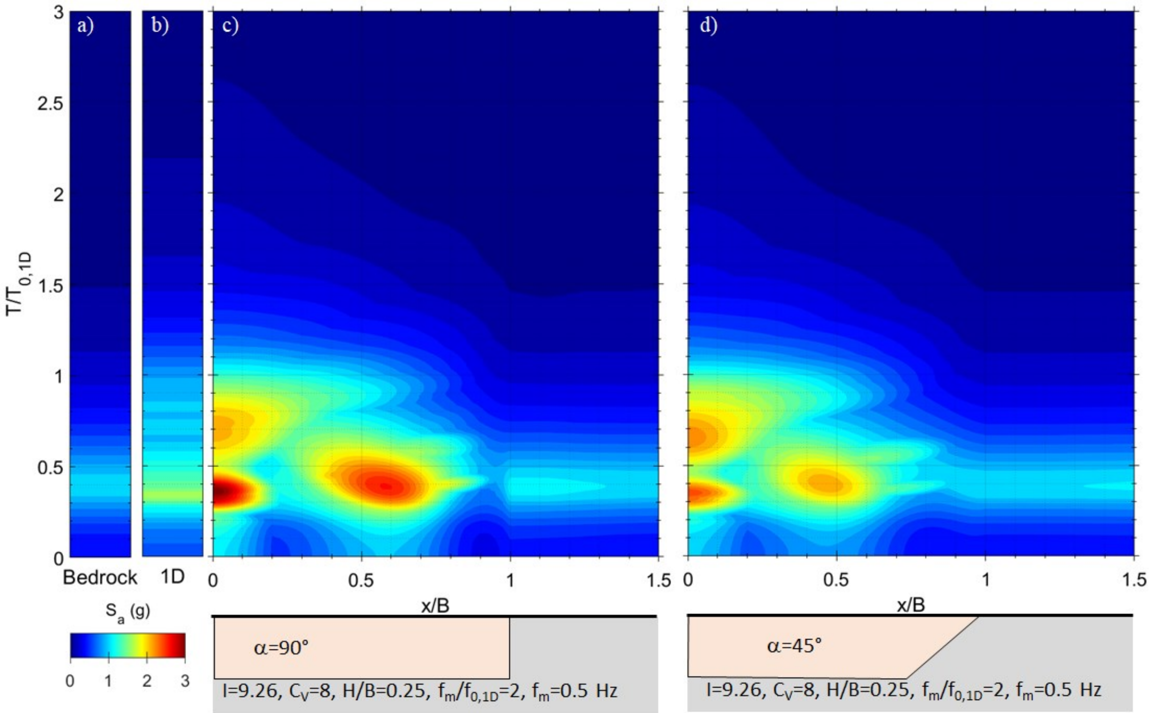

Figure III.4.27 – Acceleration response spectra for: a) input motion; b) 1D analysis; c,d) 2D analysis

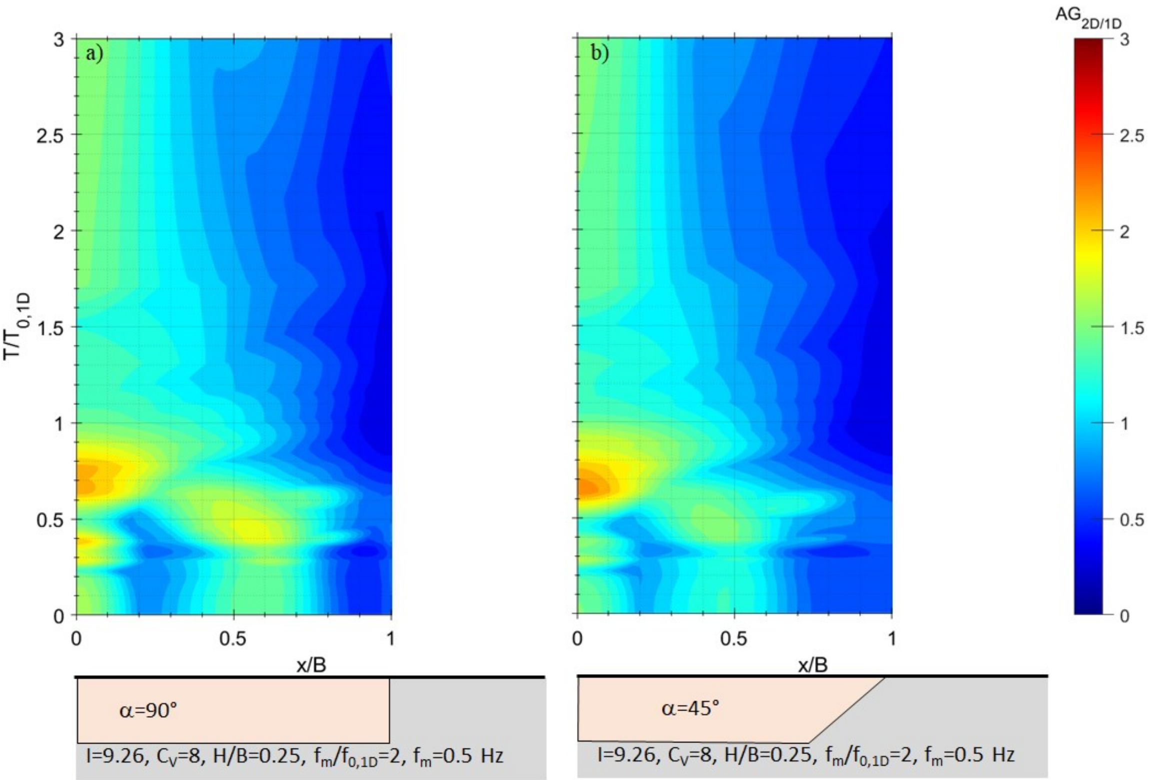

Figure III.4.28 – $AG_{2D/1D}$ for α: a) 90°; b) 45°

III.4.4 Frequency content

The frequency content of the reference input motion strongly affects the seismic response of the valleys. In the following, 3 different cases are examined, with f_m significantly lower, close to and higher than $f_{0,1D}$, respectively.

In the case of $f_m << f_{0,1D}$ (e.g. $f_m/f_{0,1D}<0.2$), $\lambda >> H$ (e.g. $\lambda/H > 10 - 20$), whatever H/B, I, α are, the ground motion is not influenced at all by the presence of the deformable soil filling the valley and the accelerations obtained with both 1D and 2D analyses are equal to the input one. As an example, Figure III.4.29 shows AG_{2D} and $AG_{2D/1D}$ obtained for H/B=0.25, I=9.26, α=45° and $f_m/f_{0,1D}=0.2$, both amplification factors are equal to 1.0 along the whole valley and for all periods.

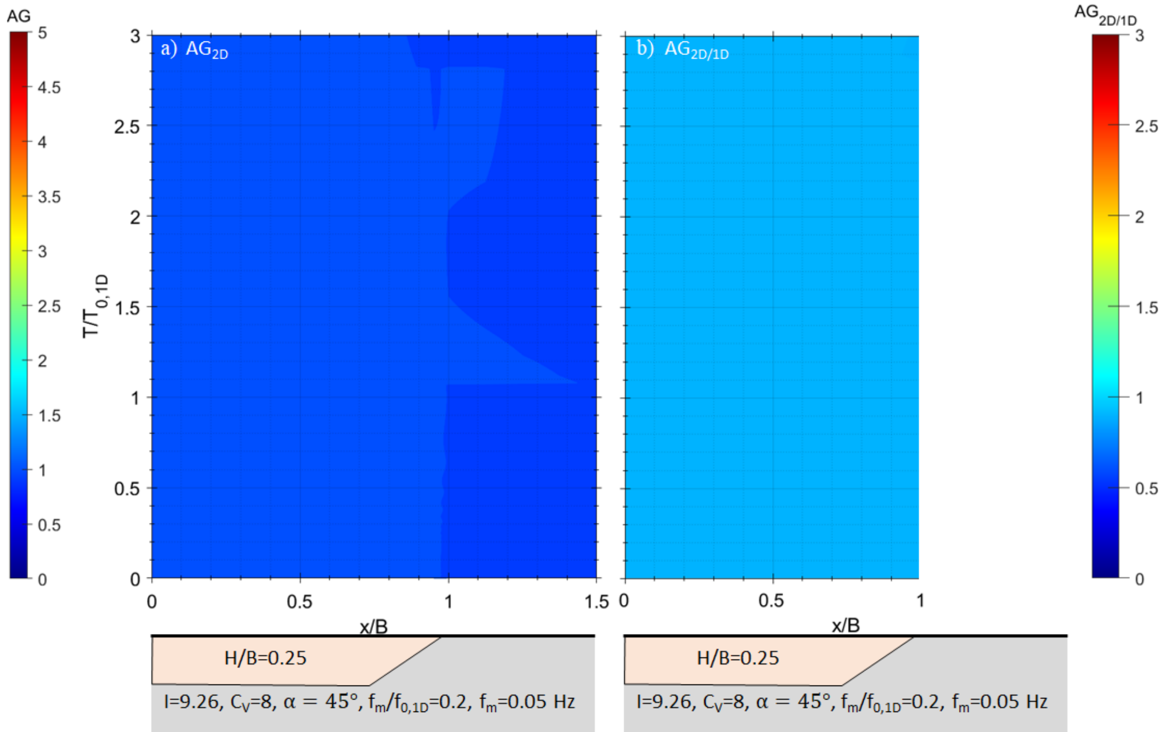

Figure III.4.29 – a) AG_{2D}, b) $AG_{2D/1D}$ for H/B=0.25, I=9.26, $f_m/f_{0,1D}=0.2$, and α=45°

As the frequency increases up to $f_m/f_{0,1D}=0.7\text{-}1$, depending on I and H/B, the 2D amplification is very comparable to the 1D one. Figure III.4.30 shows $AG_{2D/1D}$

calculated for I=9.26 and H/B=0.05 (a,c,e,g) and 0.25 (b,d,f,h) as the frequency varies.

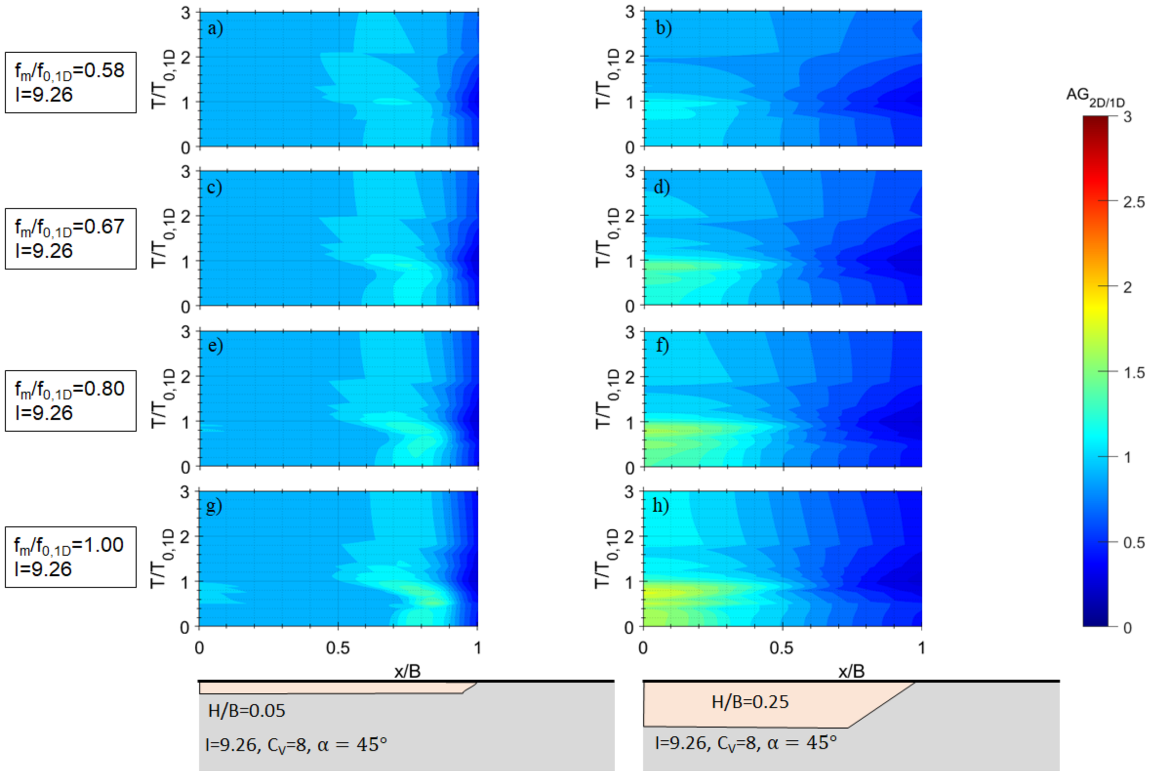

Figure III.4.30 – $AG_{2D/1D}$ obtained for I=9.26, H/B=0.05 and $f_m/f_{0,1D}$: a) 0.58; c) 0.67; e) 0.80; g) 1.00. $AG_{2D/1D}$ for I=9.26, H/B=0.25 and $f_m/f_{0,1D}$: b) 0.58; d) 0.67; f)0.80; h) 1.00.

For $f_m/f_{0,1D}$=0.58 (Figure III.4.30a,b) for both valleys the 2D amplification is at most equal to the 1D one. As the frequency increases, for the shallowest valley (H/B=0.05) $AG_{2D/1D}$ is at most equal to 1.1 for $f_m=f_{0,1D}$, while for H/B=0.25 such amplification already occurs for $f_m/f_{0,1D}$=0.67 (Figure III.4.30d), and for f_m close to $f_{0,1D}$, $AG_{2D/1D}$ is at most equal to 1.6-1.7. However, if the impedance contrast decreases, e.g. I=3.43 (Figure III.4.31), even for H/B=0.25 $AG_{2D/1D}$ is at most 1.1-1.2 for $f_m=f_{0,1D}$. This is due to the fact that for H/B=0.25 and high impedance values the shape factor is close to the critical one, defined by Bard & Bouchon (1985), which divides the valleys into shallow and deep. Therefore, in this case, it is possible that 2D phenomena occur even if the input frequencies are lower than $f_{0,1D}$.

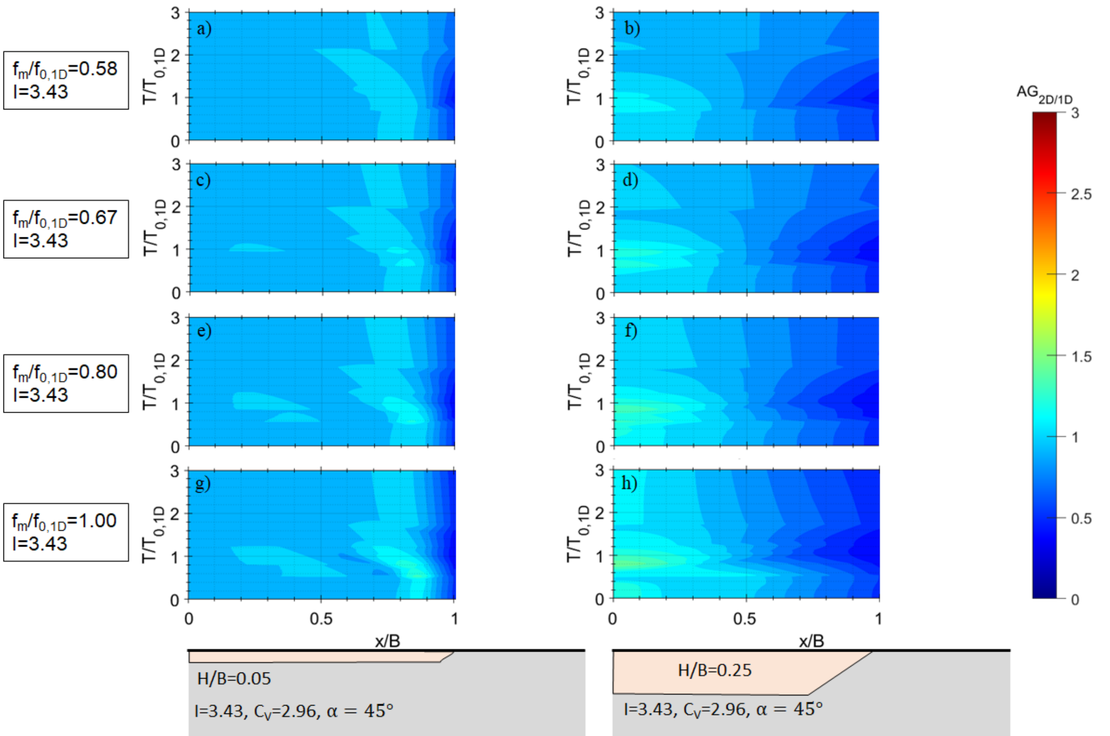

Figure III.4.31 – $AG_{2D/1D}$ obtained for I=3.43, H/B=0.05 and $f_m/f_{0,1D}$: a) 0.58; c) 0.67; e) 0.80; g) 1.00. $AG_{2D/1D}$ for I=3.43, H/B=0.25 and $f_m/f_{0,1D}$: b) 0.58; d) 0.67; f)0.80; h) 1.00.

Finally, if $f_m > f_{0,1D}$, 2D effects predominate over 1D ones and $AG_{2D/1D}$ is significantly greater than 1 and the value of maximum amplification increases with f_m.

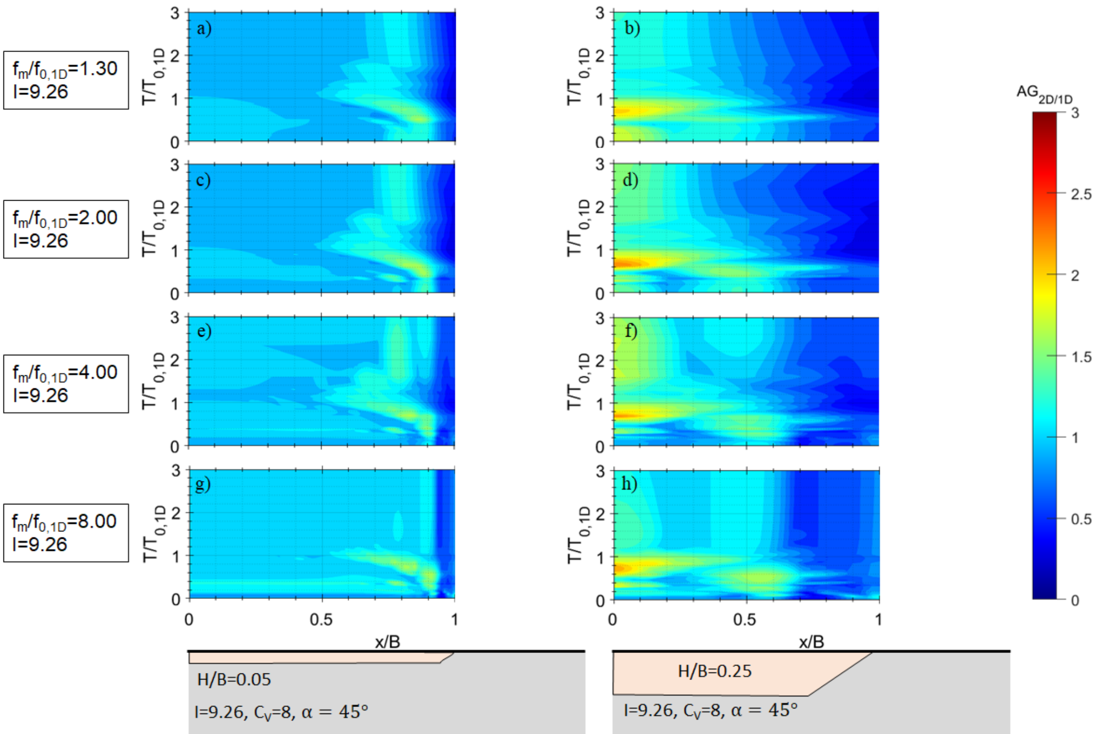

Figure III.4.32 – $AG_{2D/1D}$ obtained for I=9.26, H/B=0.05 and $f_m/f_{0,1D}$: a) 1.30; c) 2.00; e) 4.00; g) 8.00. $AG_{2D/1D}$ for I=9.26, H/B=0.25 and $f_m/f_{0,1D}$: b) 1.30; d) 2.00; f) 4.00; h) 8.00.

III.4.5 Wedge-shaped valleys

The wedge shape significantly influences the propagation mechanisms of the seismic waves within the basin, and therefore differentiates its seismic response from that of trapezoidal valleys. Indeed, for the latter, most part of the basin has a constant thickness equal to that at the centre of the valley, and only a narrow area at the edge has a variable thickness. This explains the common assumption of comparing the ground motion of the valley with that obtained from a 1D analysis, carried out on a vertical profile corresponding to the centre of the valley. Instead, in the case of a wedge, the thickness is always variable, and it is also difficult to identify a 1D reference column. The slope angle is a function of the shape ratio as it is simply the tangent of H/B. For very shallow valleys, α is very small (i.e. for H/B=0.05 α is 2.86°) and the basin can be considered as a series of 1D columns of different thicknesses, increasing towards the centre. Indeed, α is such that the base of the single column can be considered quasi-horizontal, and therefore there is no significant change in the angle of the waves transmitted from the bedrock, which propagate in a quasi-vertical direction within the valley. Therefore, the seismic response of the basin can be regarded as equivalent to that of a set of vertical columns having different thickness. Note that, since the waves are transmitted in a quasi-vertical direction, the Rayleigh waves are not so significant, even if their generation anyway influence the seismic motion especially at the centre of the valley. As H/B increases, α increases (i.e. for H/B=0.25, α=14.04°) and this causes a change in the valley response. Indeed, the inclination of the edges is such that the transmitted waves can no longer be considered quasi-vertical, but they converge towards the centre of the valley.

Figure III.4.33 shows the horizontal accelerograms obtained at the surface for all 5 values of H/B and $f_m/f_{0,1D}$=0.5. Whatever the value of H/B the ground motion at the valley centre is comparable to that obtained for 1D column while elsewhere the amplitude of the motion is lower. The reason is that only close to the centre of the valley the thickness is comparable to that of the 1D column, while in other areas it is smaller. Since for $f_m/f_{0,1D}$=0.5 the mean wavelength is equal to 8H, and for x/B>0.5 the thickness of the valley is less than half of H, λ_m is 16 times greater than the thickness of those portions of the valley, thus the waves do not interact with them. Instead, at the centre of the valley the ground motion is comparable to that of the 1D column since the Rayleigh waves generated in this case are negligible.

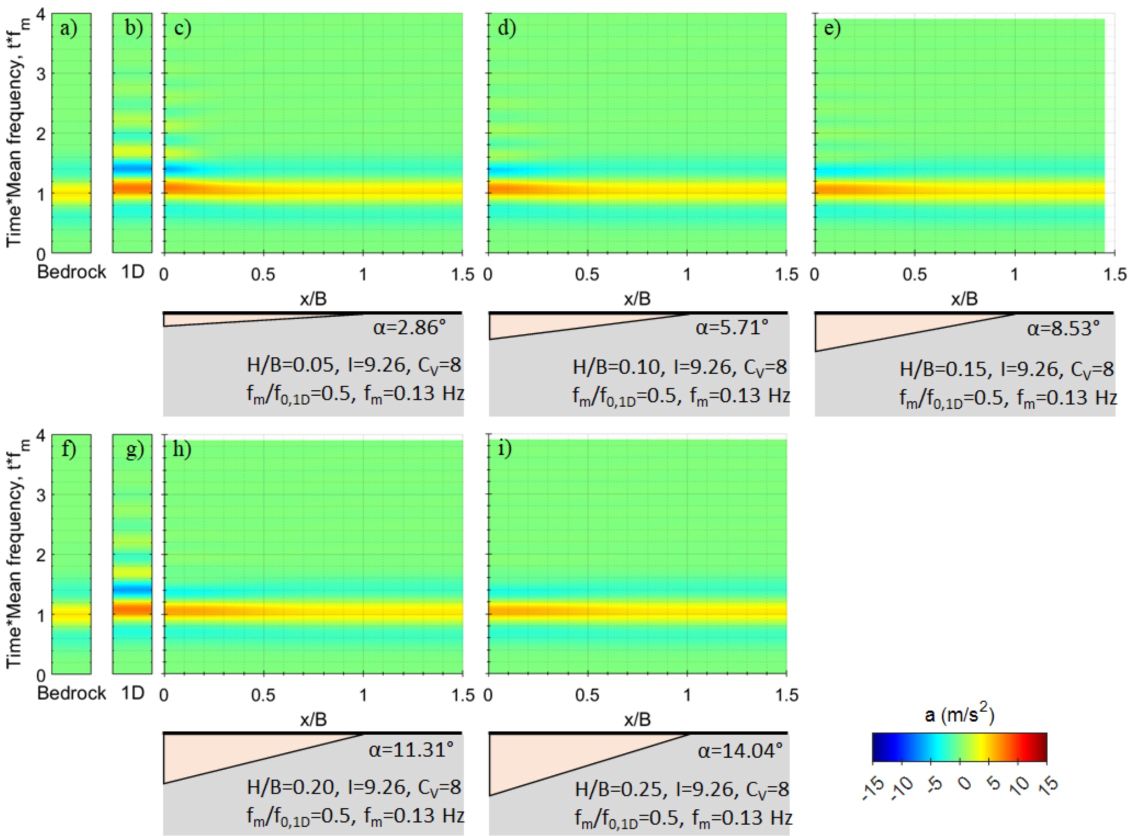

Figure III.4.33 – Horizontal accelerograms: a,f) input motion ($f_m/f_{0,1D}$=0.5), b,g) at the surface of the 1D profile at the centre of the valley; at surface of the valley with H/B: c) 0.05; d) 0.10; e) 0.15; h) 0.20; i) 0.25.

Increasing the frequency of the input motion up to $f_m=f_{0,1D}$ (Figure III.4.34) the effect of thickness variability along the valley is clearly visible. Indeed, the seismic waves first arrive at the surface at the edges and then at the centre of the valley. Moreover, in the central part of the valley area the acceleration is clearly amplified, especially in the last part of the time history because of the arrival of the Rayleigh waves.

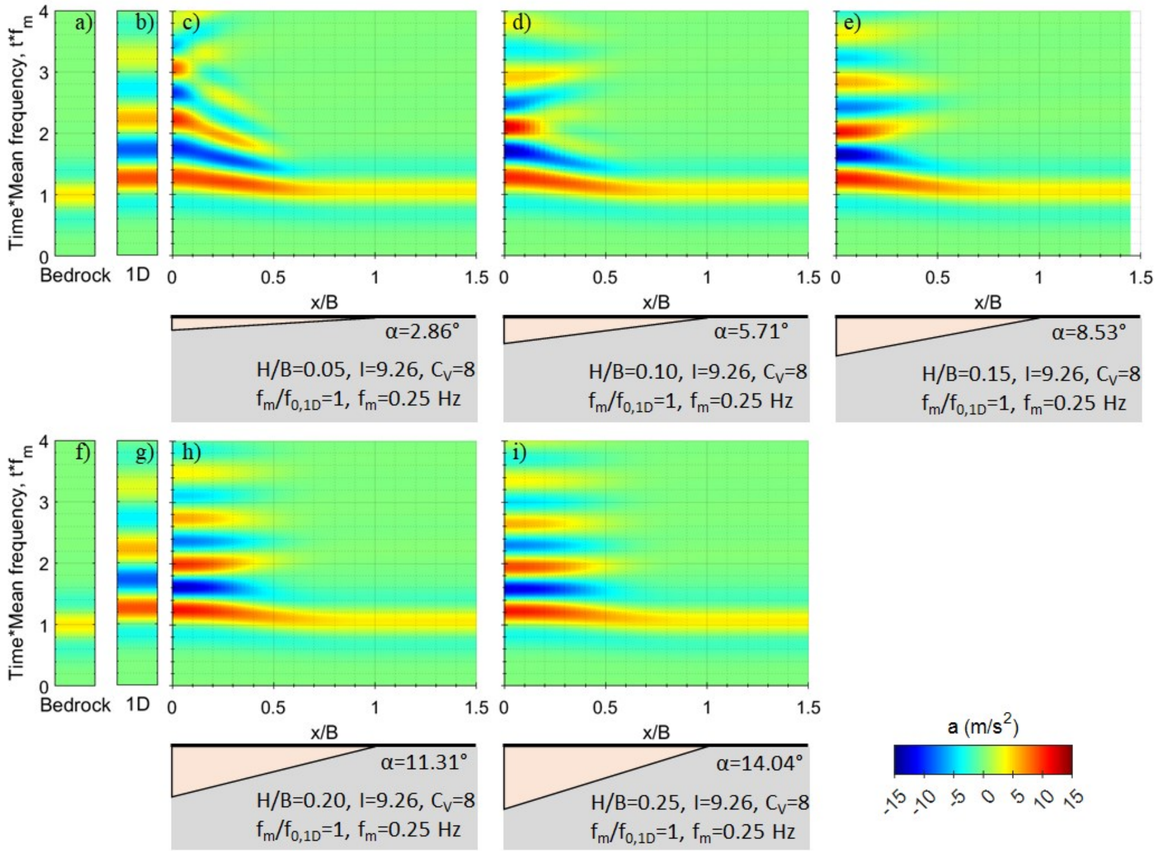

Figure III.4.34 – Horizontal accelerograms: a,f) input motion ($f_m/f_{0,1D}=1$), b,g) at the surface of the 1D profile at the centre of the valley; at surface of the valley with H/B: c) 0.05; d) 0.10; e) 0.15; h) 0.20; i) 0.25.

Figure III.4.35 shows the accelerograms obtained at the surface for $f_m/f_{0,1D}=2$. In this case the λ_m is equal to 2H, hence for x/B=0.5 it is equal to 4H and leads to the resonance of the areas close to that vertical. For H/B=0.05 (Figure III.4.35c) this phenomenon is very clear, indeed the maximum accelerations are not located in the centre of the valley, where the motion is almost 1D (Figure III.4.35b), but close to x/B=0.5. As H/B increases, this effect is less evident because the Rayleigh waves influence the response significantly. Indeed, in this case the λ_m is sufficiently close to the thickness of the basin and therefore the generation of surface waves affects the whole valley. This is also confirmed by the vertical accelerations (Figure III.4.36) which are negligible for H/B=0.05 (Figure III.4.36a) while they are significant for H/B=0.25 (Figure III.4.36e).

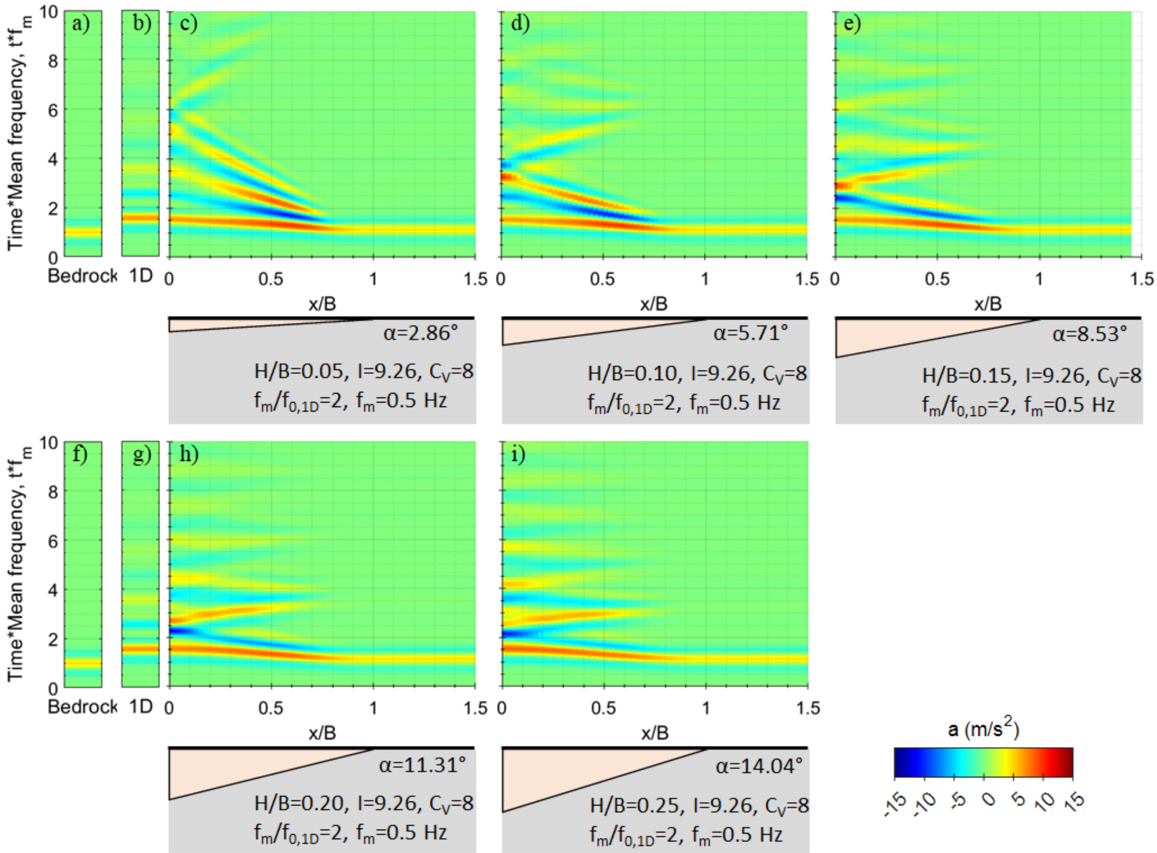

Figure III.4.35 – Horizontal accelerograms: a,f) input motion ($f_m/f_{0,1D}$=2), b,g) at the surface of the 1D profile at the centre of the valley; at surface of the valley with H/B: c) 0.05; d) 0.10; e) 0.15; h) 0.20; i) 0.25.

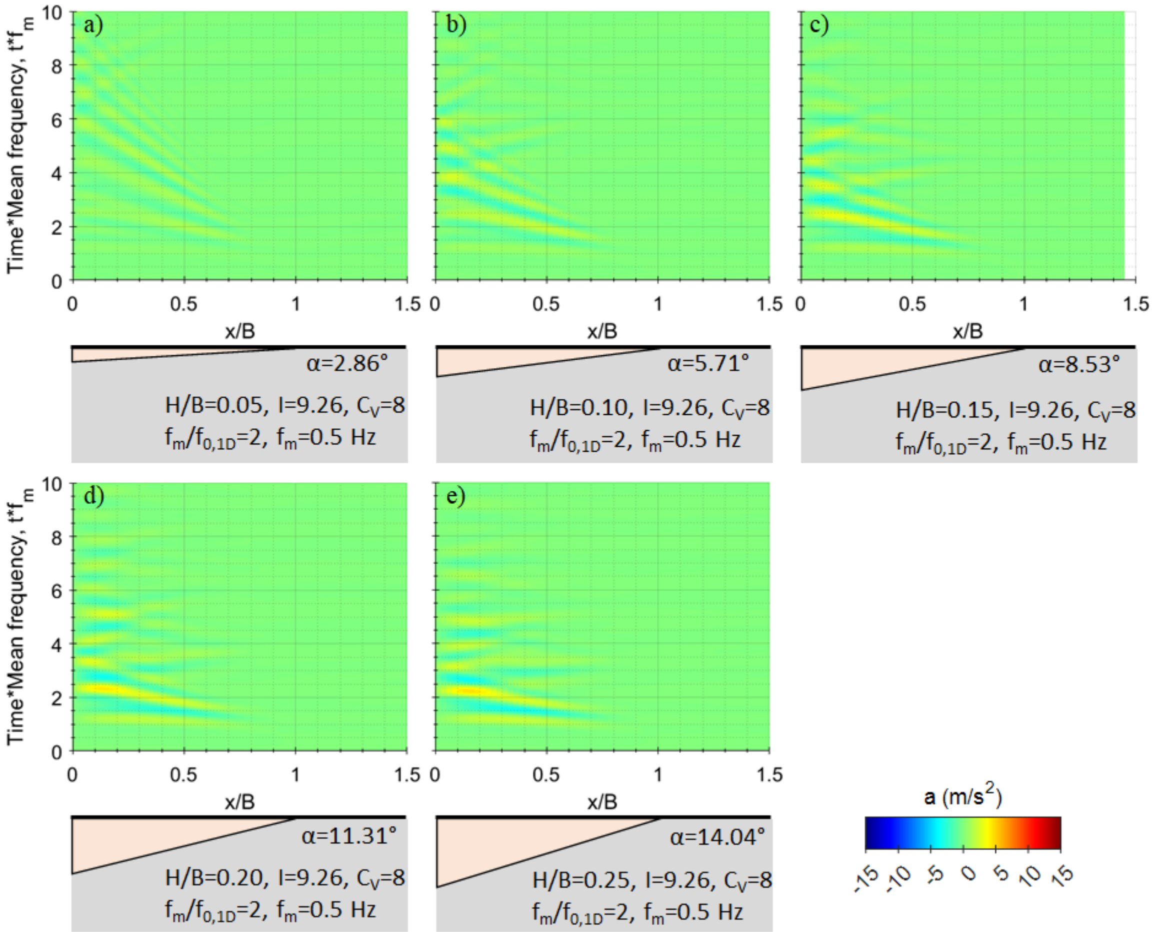

Figure III.4.36 – Vertical accelerograms at surface of the valley with H/B: a) 0.05; b) 0.10; c) 0.15; d) 0.20; e) 0.25.

The aggravation factor computed in the case of wedge-shaped valleys reflects the observed trends of the ground motion at the surface. Indeed, for $f_m/f_{0,1D}$=0.5 (Figure III.4.37), $AG_{2D/1D}$ is less than 1 for the whole valley regardless of the shape ratio. On the other hand, if $f_m=f_{0,1D}$ (Figure III.4.38), it is less than 1 at the valley edge for all shape ratios, while for x/B<0.5 it is 1-1.5 depending on the period and H/B. In particular, for H/B=0.05 (Figure III.4.38a) the maximum amplification is at the centre of the valley for periods close to $T_{0,1D}$, while as H/B increases, both the valley area and the range of amplified periods increase. Furthermore, the maximum amplifications occur for $T/T_{0,1D}$ ranging between 0.6-0.8.

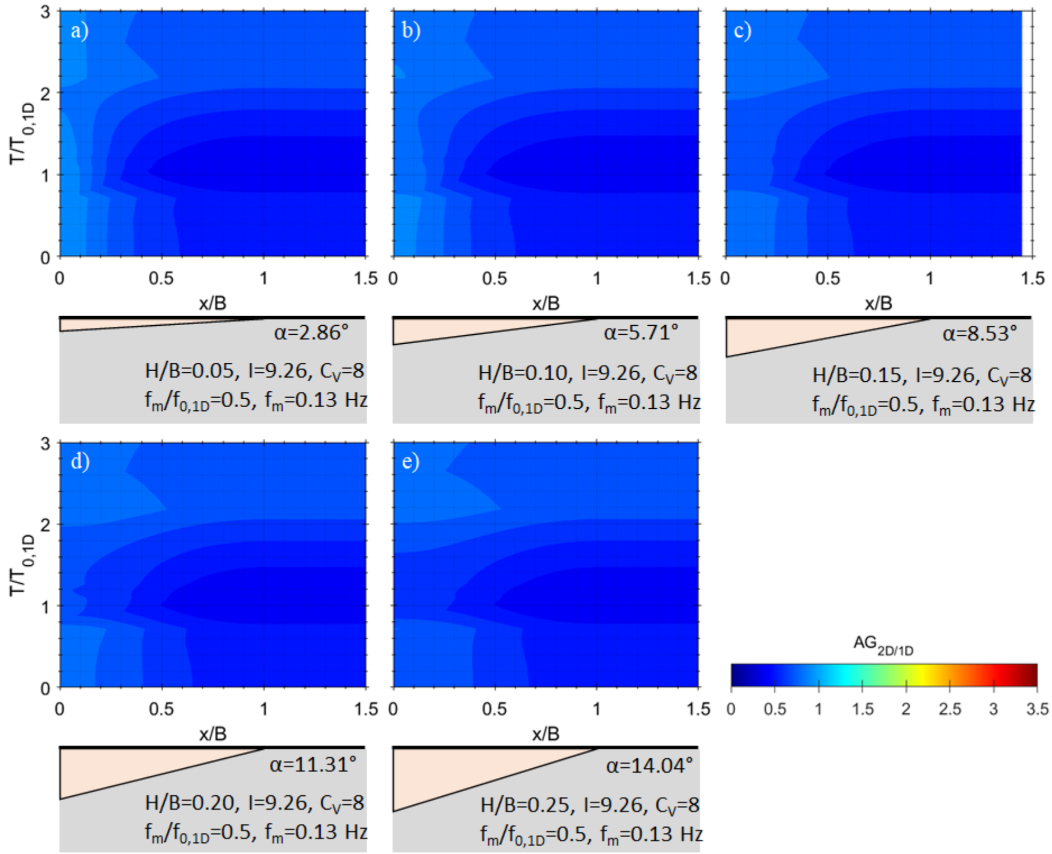

Figure III.4.37 – $AG_{2D/1D}$ for $f_m/f_{0,1D}$=0.5 and H/B, a) 0.05; b) 0.10; c) 0.15; d) 0.20; e) 0.25.

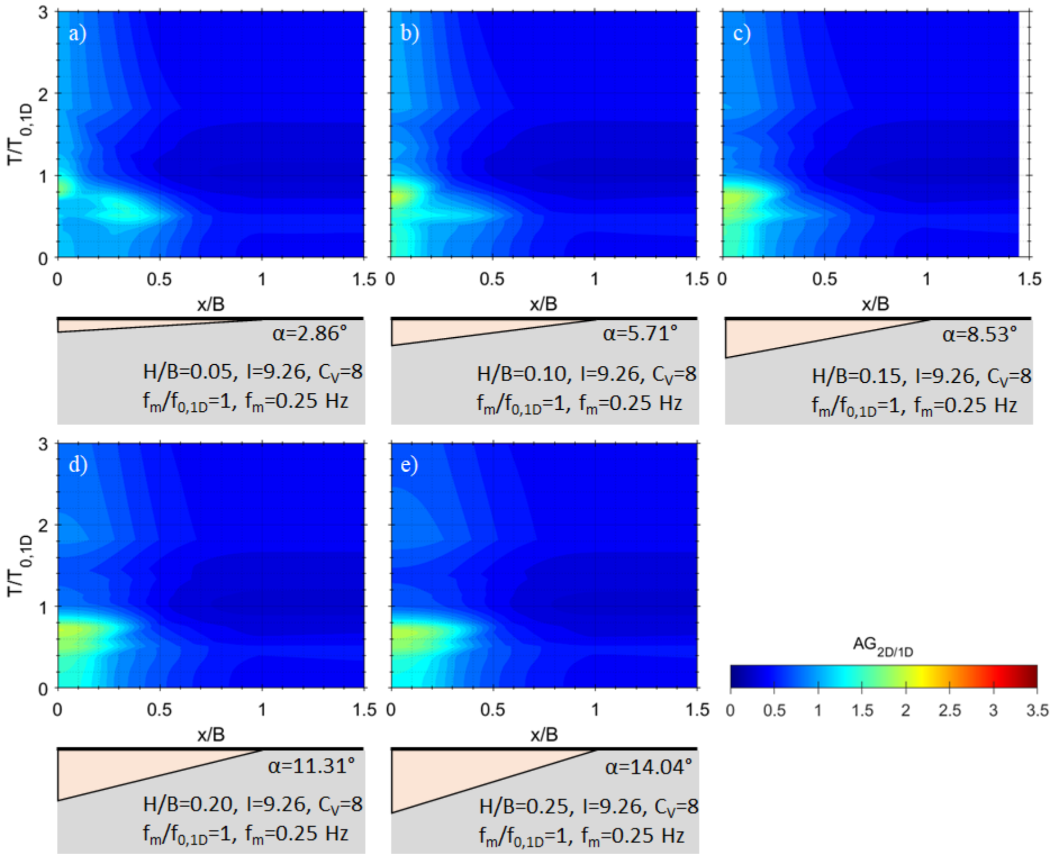

Figure III.4.38 – $AG_{2D/1D}$ for $f_m/f_{0,1D}$=1 and H/B, a) 0.05; b) 0.10; c) 0.15; d) 0.20; e) 0.25.

Finally, for $f_m/f_{0,1D}$=2 (Figure III.4.39) the maximum value of aggravation factor along the very shallow valley (Figure III.4.39a) occurs at x/B and $T/T_{0,1D}$ close to 0.5, i.e. in correspondence with the resonance periods of 1D columns having thicknesses close to 0.5H. As H/B increases, the focusing of the waves towards the centre of the valley causes a strong amplification of the 2D motion with respect to the 1D one at the centre of the valley, while the resonance effect decreases in the rest of the basin.

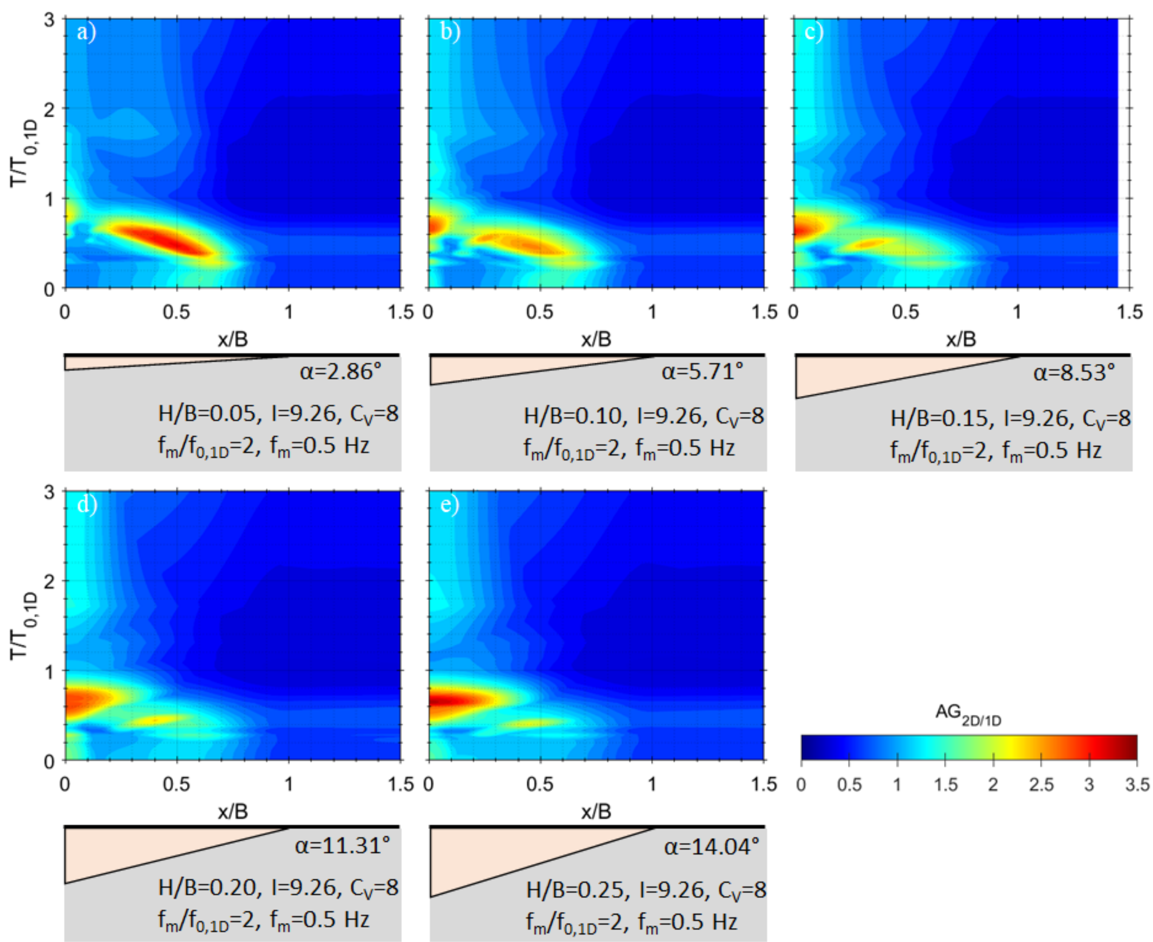

Figure III.4.39 – $AG_{2D/1D}$ for $f_m/f_{0,1D}$=2 and H/B, a) 0.05; b) 0.10; c) 0.15; d) 0.20; e) 0.25.

III.4.6 Resonance frequency

The first resonance frequency computed at the centre of the valley carrying out a 2D numerical analysis, $f_{0,2D}$, can be sensibly higher than that evaluated by 1D analysis, depending on the shape ratio of the valley. Figure III.4.40 reports the results obtained in this study in terms of ratio $f_{0,2D}/f_{0,1D}$ as a function of H/B, distinguished by different valley shapes.

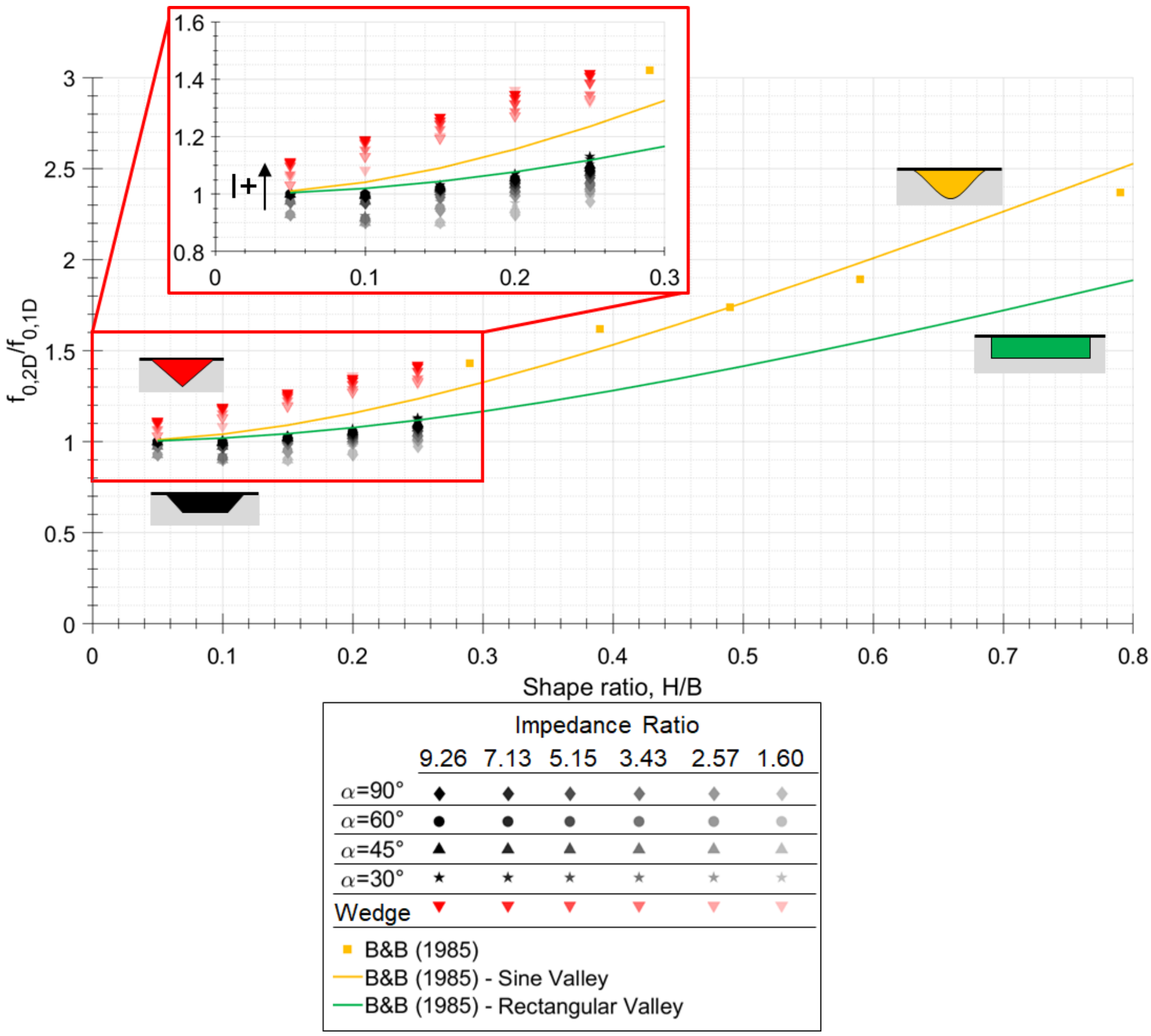

Figure III.4.40 – Variation of the 2D resonance frequency with H/B for different values of α, I.

$f_{0,2D}$ computed in this study in the case of wedge-shaped valleys (red triangle) are comparable to those obtained by Bard & Bouchon (1985) for sinusoidal valleys (dark yellow square and line), and higher than those calculated for trapezoidal basins (black point) that are in good agreement with those obtained by Bard & Bouchon (1985) for rectangular valleys (green line). Furthermore, the slope of the edges and the impedance ratio do not significantly influence $f_{0,2D}$; typically for a fixed edge slope $f_{0,2D}$ increases with I, while it is almost constant as the slope angle varies keeping the impedance ratio constant.

III.5 Evaluation of Valley Amplification Factor

The results show that the 2D effects are not negligible for most of the analysed cases, thus a geometrical Valley Amplification Factor, VAF, is defined with the aim of identifying a simple relationship describing the aggravation along the valley, as a function of its geometry and the mechanical properties.

At each point of the mesh on surface and for each period, the average of $AG_{2D/1D}$ obtained from the analyses, carried out adopting m=12 input motions, are calculated. Thus, obtaining an amplification factor independent of the input frequency, defined as:

$$\overline{AG_{2D/1D}\left(T,\frac{x}{B}\right)}=\frac{1}{m}\sum_{i=1}^{m}AG_{2D/1D}\left(T,\frac{x}{B}\right) \qquad \text{III.5.1}$$

This factor is further averaged within a period range between 0s and $T_{0,1D}$ and a synthetic VAF is then defined as follows:

$$VAF\left(\frac{x}{B}\right)=\frac{1}{T_{0,1D}}\int_{0}^{T_{0,1D}}\overline{AG_{2D/1D}\left(T,\frac{x}{B}\right)}\cdot dT \qquad \text{III.5.2}$$

The integral is calculated up to $T_{0,1D}$ because, as shown in the previous section (§III.4), in this interval of periods the ground response seems to be more sensible to 2D effects. The VAF so defined varies along the valley and depending on its shape ratio, edges slope, and impedance ratio. In the following, only VAF values greater than or equal to 1 are considered, thus neglecting any attenuation effects that could be generated near to the edges.

Figure III.5.1a,b,c shows the influence of the H/B, α and I on VAF, respectively. In the central area of the valley the VAF increases with H/B (Figure III.5.1a) and I

(Figure III.5.1c), it is independent of α (Figure III.5.1b) except for the wedge-shaped valley. The value of maximum amplification at the edge is independent of H/B and increases with α and I, while its position is strongly influenced by all the factor, it moves toward the centre as H/B, and I increase and α decreases.

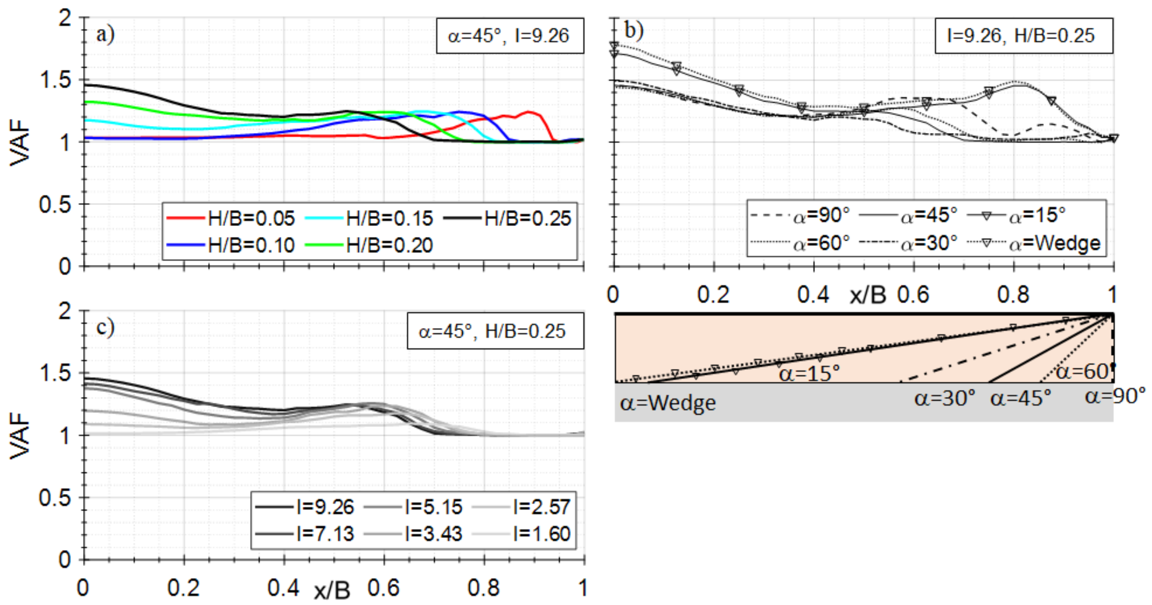

Figure III.5.1 – VAF obtained for variable a) H/B; b) α; c) I.

The results of the parametric study, synthesised in terms of VAF, highlight some peculiar trend of the aggravation factor along the trapezoidal valley, allowing to classify them based on the value of the shape ratio. Two type can be distinguished: basins whose H/B<0.1 can be considered as very shallow, since they are characterised by a slight aggravation factor along the central sector (i.e. VAF lower than 1.05-1.10, depending on I) gradually increasing approaching the edges; valleys with H/B>0.1, instead, are characterised by a VAF along the valley presenting two distinct peaks, one corresponding to the centre of the valley and a second one near the edges.

Table III.5.1 summarises the influence of the different factors examined on the 2D amplification along the valley for the trapezoidal shape.

Table III.5.1 – Summary of the influence of the parameter on VAF

Parameter	Amplification		Relative position of edge peak
	Centre	Edge	
H/B (↑+)	(↑+)	(=)	(→←)
α (↑+)	(=)	(↑+)	(↔)
I (↑+)	(↑+)	(↑+)	(→←)

Key:
(↑+)=increase; (=)=no influence; (→←)=moves from edge to centre; (↔)=moves from centre to edge

The results, in terms of VAF, are studied in the following paragraphs trying to identify an analytical relationship, that describe the aggravation factor as a function of H/B, I and α. The peculiar path characterising the wave propagation within the wedge-shaped basins makes the VAF significantly different from those computed for the trapezoidal shallow valleys (see Figure III.5.1b). For this reason, in the following the case of the trapezoidal basin (§III.5.1) is analysed separately from that of wedge ones (§III.5.3). Furthermore, the analyses results obtained of trapezoidal valleys characterised by α = 15 ° have been not considered because for H/B = 0.2 and 0.25 this angle is very close to that of the wedge.

III.5.1 Trapezoidal basin

The variation of VAF along the valley is approximated as the sum of two Gaussian-like functions (Figure III.5.2), the first one describing the aggravation factor at the valley centre (cyan line) and the second expressing its trend along the edges (red line).

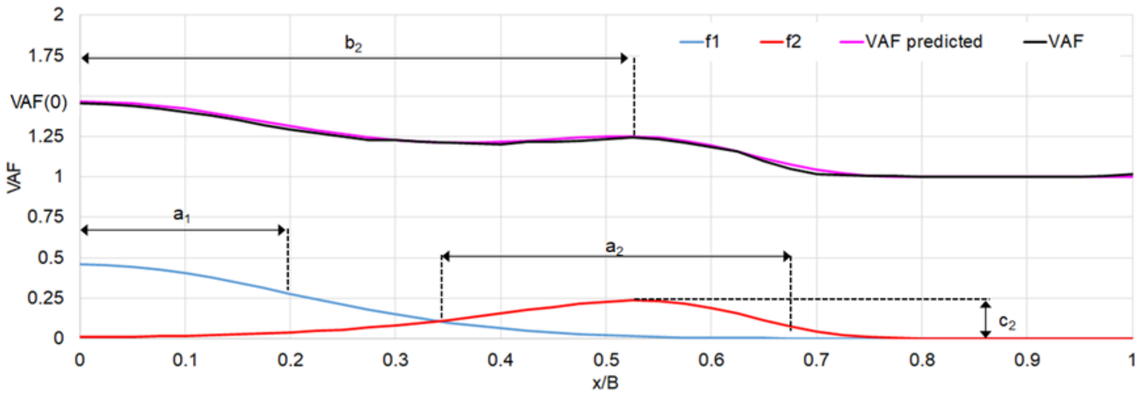

Figure III.5.2 – VAF model proposed in this study.

The proposed analytical VAF function is then defined as:

$$\mathrm{VAF} = 1 + \left(\mathrm{VAF}(0) - 1\right) \cdot f_1\left(\frac{x}{B}, \frac{H}{B}, I\right) + f_2\left(\frac{x}{B}, \frac{H}{B}, I, \alpha\right) \qquad \text{III.5.3}$$

where VAF(0) is the amplification computed at the middle of the valley, f_1 and f_2 the functions describing the VAF distributions along the central sector and at the edge, respectively. They can be expressed as:

$$\mathrm{VAF}(0) = 1 + c_0 \cdot \left(1 - \exp\left(-\frac{(I-1)^2}{2 \cdot a_0^2}\right)\right) \qquad \text{III.5.4}$$

$$f_1\left(\frac{x}{B}, \frac{H}{B}, I\right) = \exp\left(-\frac{\left(\frac{x}{B}\right)^2}{2 \cdot a_1^2}\right) \qquad \text{III.5.5}$$

$$f_2\left(\frac{x}{B},\frac{H}{B},I,\alpha\right)=c_2\cdot\exp\left(\frac{\frac{x}{B}-b_2}{a_2}-\exp\left(\frac{\frac{x}{B}-b_2}{a_2}\right)\right) \qquad \text{III.5.6}$$

where c_0, a_0, a_1, a_2, b_2 and c_2 are coefficients defining the Gaussian-like functions. In a preliminary stage they are chosen with engineering judgement to fit the results of the numerical analysis. In the sequel, their dependency on the geometrical and mechanical properties of the valley is analytically expressed. Details about the calibration of the coefficients, that analytically describe the VAF along the valley, are reported in Appendix A.

The five charts in Figure III.5.3 show the dependency of the above-described coefficients on I, H/B and α; in the charts both the data points and the fitting functions are reported with symbols and curves of the same colours.

The aggravation factor at the valley centre, VAF(0), is represented in Figure III.5.3a as an exponential function of I, increasing with H/B and independent of α. For a fixed geometry, VAF(0) increases with I up to a limit value of impedance ratio, that increases with H/B, beyond which VAF(0) remains constant.

a_1 (Figure III.5.3b) describes the extension of the 2D aggravation sector around the centre of the valley; its value decreases with H/B and I.

a_2 (Figure III.5.3c) is proportional to the extension of the 2D aggravation zone at the valley edge and depends on H/B and I. It increases with the impedance ratio for H/B<0.15 and decreases in the other cases.

b_2 (Figure III.5.3d), which describes the location of the amplification peak at the edge with reference to the centre of the valley, depends on H/B, I and α. The lateral peak of the VAF moves from the edge towards the middle of the valley as the impedance ratio increases for a given shape ratio, and as H/B increases for a given I.

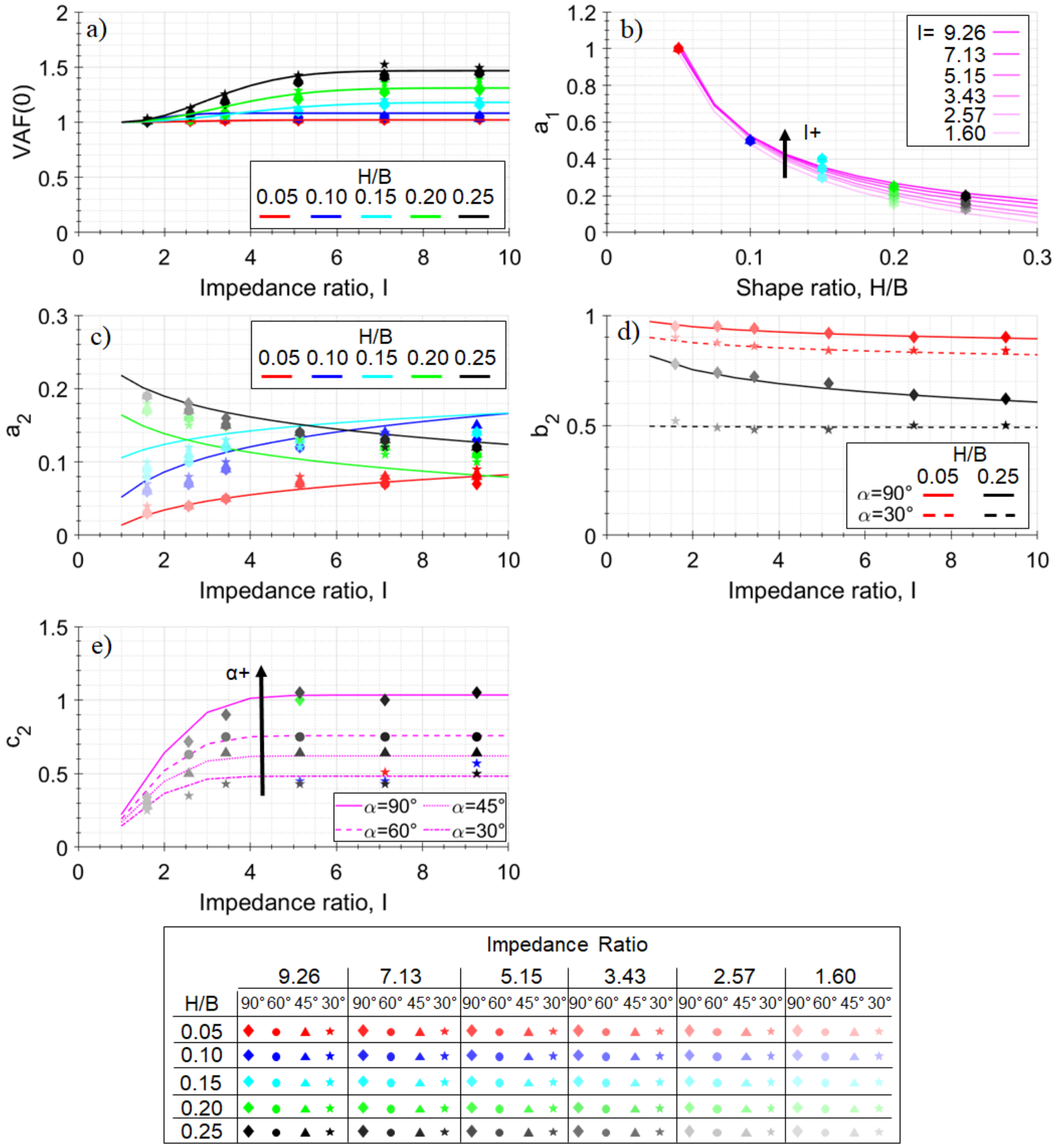

Figure III.5.3 – Data and fitting functions for: a) VAF(0); b) a_1; c) a_2; d) b_2; e) c_2.

c_2 (Figure III.5.3e) is proportional to the maximum value of VAF at the edge and it is a function of I and α. As for VAF(0), there is a limit value of I beyond which this peak value remains constant, but, in this case, the maximum value of VAF at the edge depends on the edge slope, α, while it is independent of H/B.

Summarising the above observations, the aggravation at the centre of the valley (expressed by VAF(0) and a_1) is not influenced by the slope angle, whereas the maximum amplification at the edge (c_2) depends on I and α, while its position and extension (b_2 and a_2) along the valley vary with both geometrical and mechanical parameters.

The charts in Figure III.5.4 compare the values of VAF obtained with numerical analysis (solid lines) with those predicted by the analytical functions (dashed lines): it can be noted that the latter generally overestimate the amplification because the coefficients are calibrated with a slightly over-conservative approach. This is more clearly and extensively shown by the scatter plots in Figure III.5.5, reporting the whole amount of the numerical data relevant to each surface node of the FDM meshes plotted versus the corresponding analytical predictions.

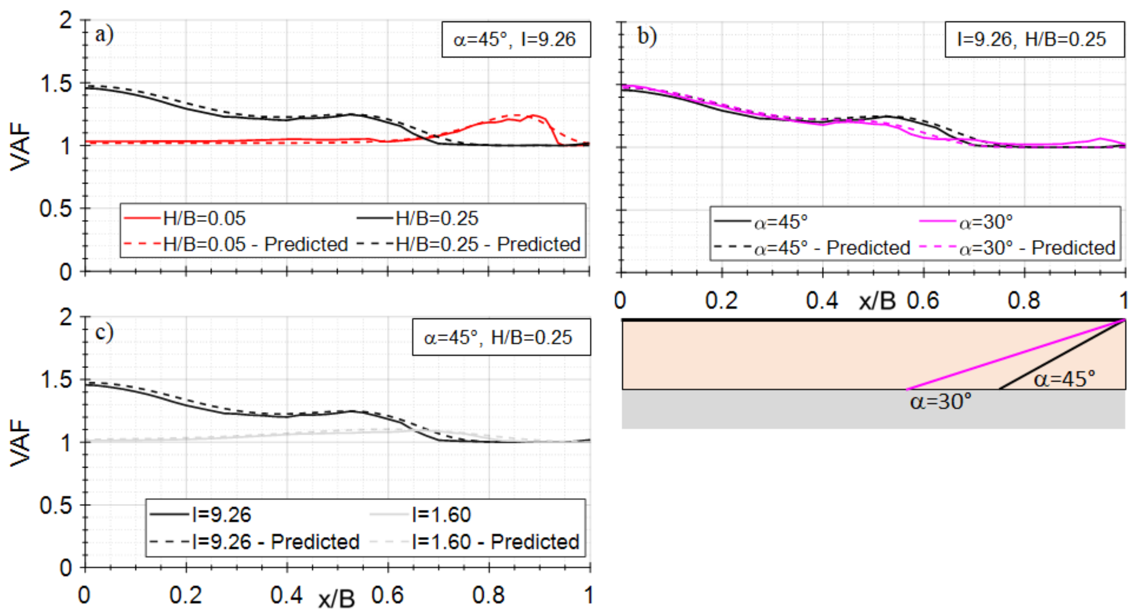

Figure III.5.4 – Comparison between numerical and predicted VAF for: a) H/B=0.05 and H/B=0.25; b) α=45° and α=30°; c) I=9.26 and I=1.60.

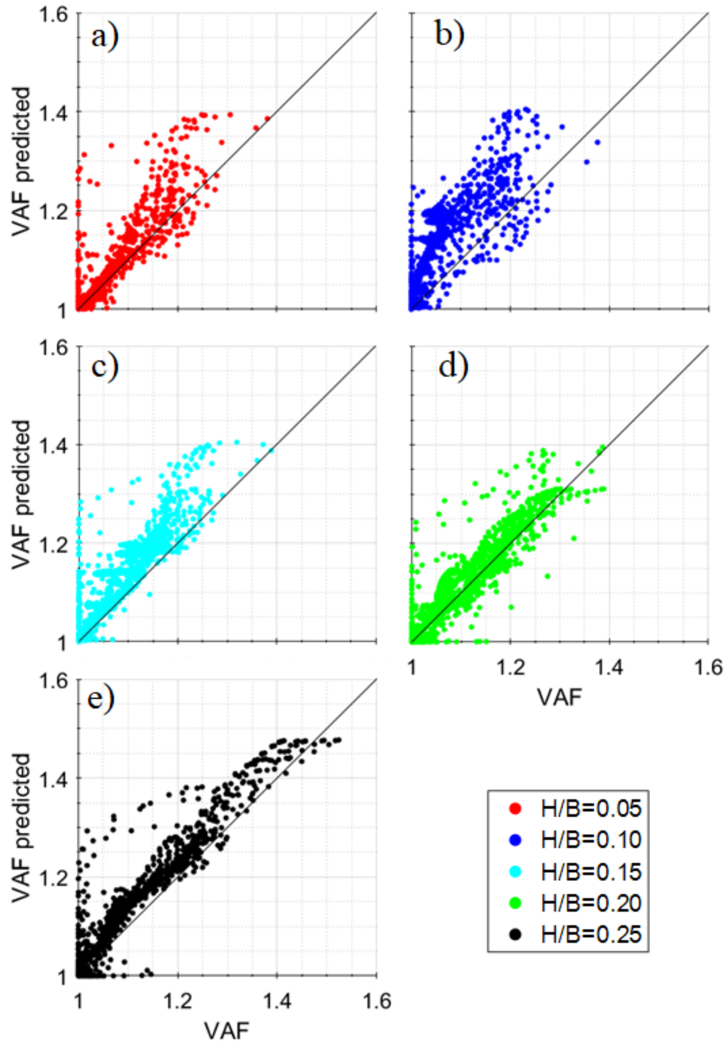

Figure III.5.5 – Comparison between VAF obtained with numerical analysis and that predicted with the proposed equation for all H/B.

III.5.2 Neural network

The results obtained from the numerical analysis are also used to calibrate a neural network through the Matlab Deep Learning toolbox (The MathWorks Inc., 2021) which, given as input the 4 key parameters (H/B, α, I, x/B), returns the corresponding VAF value. The neural network performs the following steps (explained in detail in The MathWorks Inc., 2021):

1. Generation of the input parameter matrix [X]:

$$[X]=\begin{bmatrix} \left(\frac{H}{B}\right)_1 & \left(\frac{H}{B}\right)_i & \left(\frac{H}{B}\right)_n \\ I_1 & I_i & I_n \\ \alpha_1 & \alpha_i & \alpha_n \\ \left(\frac{x}{B}\right)_1 & \left(\frac{x}{B}\right)_i & \left(\frac{x}{B}\right)_n \end{bmatrix}=[4\times n] \qquad \text{III.5.7}$$

   with $(H/B)_i$, I_i, α_i and $(x/B)_i$ the value of shape ratio, slope of the edge, impedance ratio and position of the generic surface point and n is the total number of them;

2. Normalisation of input data through the following steps:

$$[X_{P1}]=[X]-[X_{offset}]=[4\times n] \qquad \text{III.5.8}$$

$$[X_{P2}]=[X_{P1}]\times[X_{gain}]=[4\times n] \qquad \text{III.5.9}$$

$$[X_{P3}]=[X_{P2}]-[I]=[4\times n] \qquad \text{III.5.10}$$

   with $[X_{offset}]$ the matrix with the minimum values of the parameters, $[X_{gain}]$ the gain matrix that is calculated during the calibration of the neural network and [I] the identity matrix;

3. Creation of the matrices of the neurons:

$$[m]=\begin{bmatrix} b_{1,1} & b_{1,i} & b_{1,n} \\ b_{j,1} & b_{j,i} & b_{j,n} \\ b_{q,1} & b_{q,i} & b_{q,n} \end{bmatrix}+\begin{bmatrix} c_{1,1} & c_{1,2} & c_{1,3} & c_{1,4} \\ c_{j,1} & c_{j,2} & c_{j,3} & c_{j,4} \\ c_{q,1} & c_{q,2} & c_{q,3} & c_{q,4} \end{bmatrix}\times[X_{P3}]=[B]+[C]\times[X_{P3}]=[q\times n] \qquad \text{III.5.11}$$

with q the number of the neuron of the network, [B] and [C] matrix of coefficient calculated during the calibration phase;

4. Definition of the interpolation function:

$$a_1=\frac{2}{1+\exp\left(-2\times[m]\right)}-1=[q\times n] \qquad \text{III.5.12}$$

5. Computation of VAF corresponding to the input parameters:

$$[a_2]=[d_{1,1} \quad d_{1,i} \quad d_{1,n}]+[g_{1,1} \quad g_{1,j} \quad g_{1,q}]\times[a_1]=[D]+[G]\times[a_1]=[1\times n] \qquad \text{III.5.13}$$

$$[Y_{P1}]=[a_2]-[Y_{min}]=[1\times n] \qquad \text{III.5.14}$$

$$[Y_{P2}]=\frac{[Y_{P1}]}{[Y_{gain}]}=[1\times n] \qquad \text{III.5.15}$$

$$[VAF]=[VAF_1 \quad VAF_i \quad VAF_n]=[Y_{P2}]-[Y_{offset}]=[1\times n] \qquad \text{III.5.16}$$

with [D], [G], [Y_{min}], [Y_{gain}] and [Y_{offset}] calculated in the calibration phase.

First, the total dataset is split into three groups, the first used to calibrate the neural network, the second and third used to validate the results obtained. The partitioning must be such that there are sufficient representative samples of the different key parameters in the 3 groups. For example, using in the calibration dataset the results obtained for only one or two shape ratios, i.e. impedance ratios or slope of the edges, may lead to issues because the results may not be used to extrapolate the behaviour for all other parameter values. In the present study it is chosen to divide the dataset so that 60% is assigned to the calibration set, and the remaining 40% divided equally between the other 2 groups. Then, after choosing the number of neurons of the network, coefficients are calibrated to minimize the difference between the VAFs obtained from the analyses and those calculated by the neural network with the input data of the calibration set. Indeed, at this stage both the matrix [X] of the input parameters and the matrix [VAF] of the result are known. After calibrating the coefficients, the input parameters of the other 2 data sets are used and the predicted VAF is compared with the one obtained numerically.

Figure III.5.6, Figure III.5.7 and Figure III.5.8 show the comparisons between the VAFs obtained from the numerical analyses, those predicted by Eq. III.5.3 and the neural network using 4, 10, 50 and 100 neurons for several valleys.

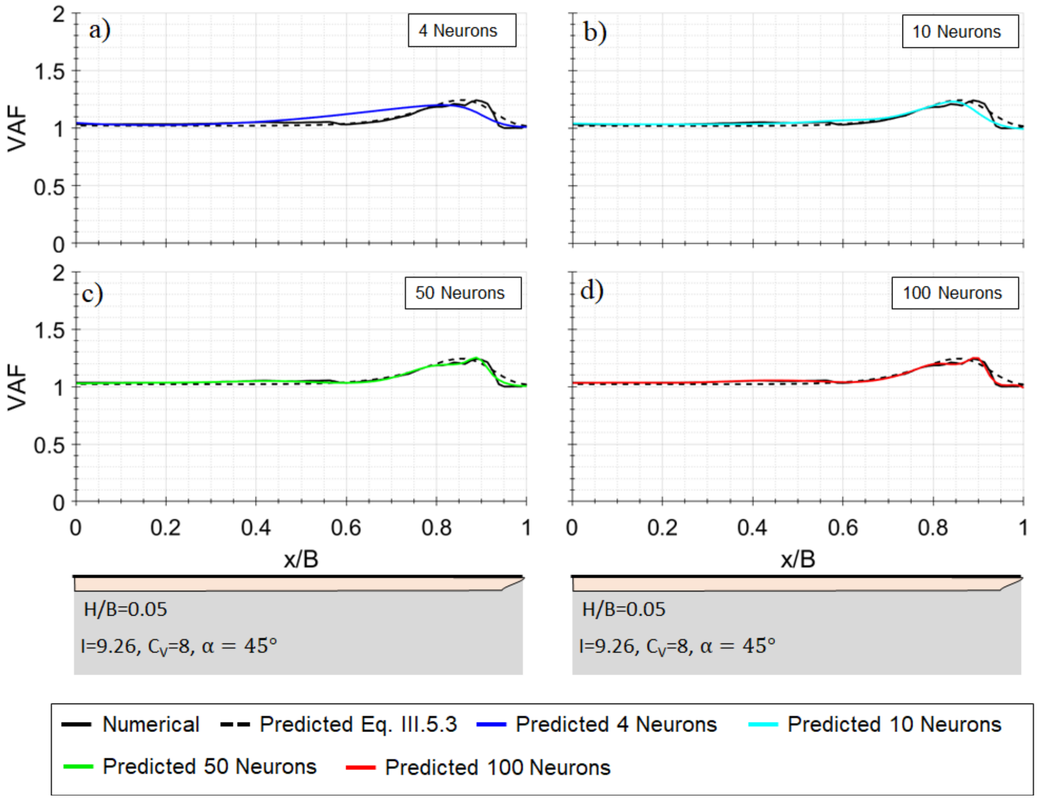

Figure III.5.6 – Comparison between VAF obtained with the numerical analysis and predicted by Eq. III.5.3 and neural network with a) 4 neurons; b) 10 neurons; c) 50 neurons; d) 100 neurons, for H/B=0.05, I=9.26 and α=45°.

By using only 4 neurons the prediction is very approximate, while even with 10 neurons there is good agreement between the numerical data and the predicted one. The accuracy increases even more when considering cases with 50 and 100 neurons.

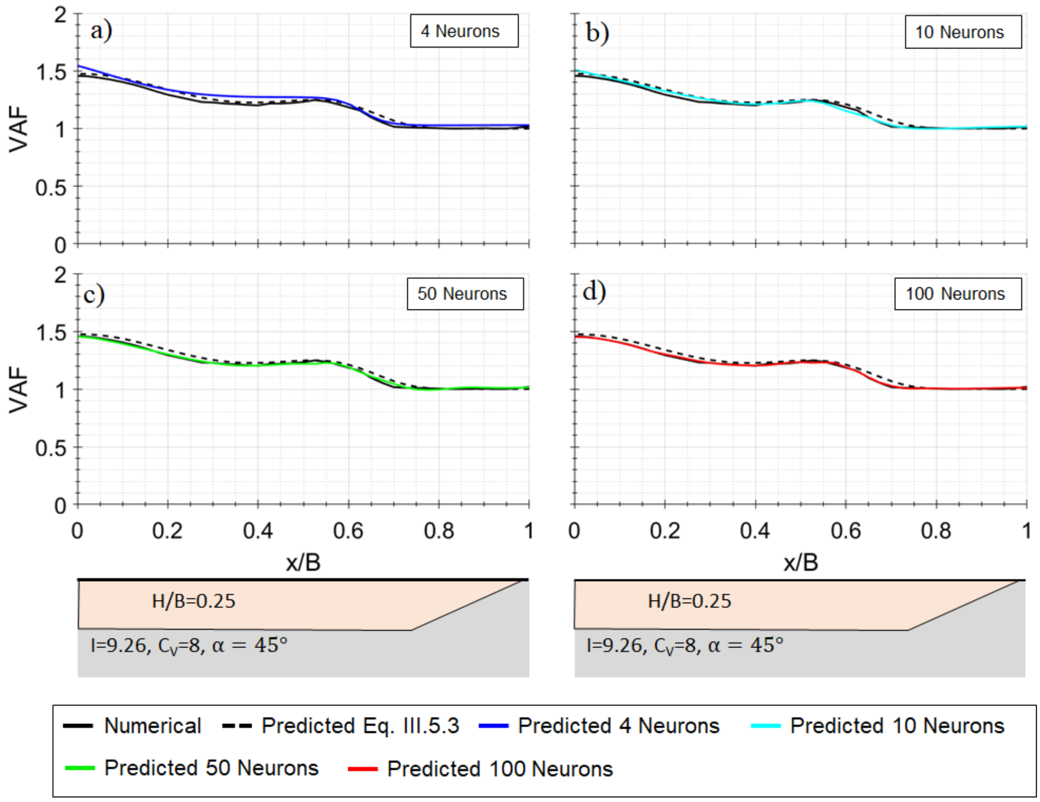

Figure III.5.7 – Comparison between VAF obtained with the numerical analysis and predicted by Eq. III.5.3 and neural network with a) 4 neurons; b) 10 neurons; c) 50 neurons; d) 100 neurons, for H/B=0.25, I=9.26 and α=45°.

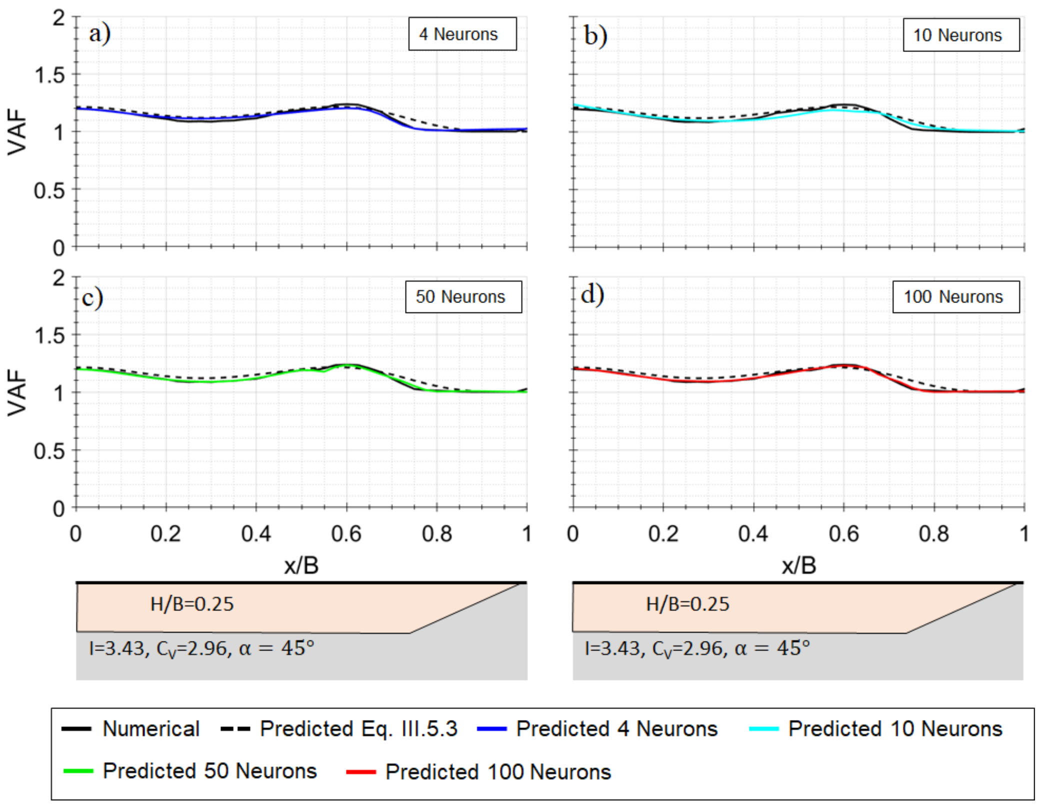

Figure III.5.8 – Comparison between VAF obtained with the numerical analysis and predicted by Eq. III.5.3 and neural network with a) 4 neurons; b) 10 neurons; c) 50 neurons; d) 100 neurons, for H/B=0.25, I=2.96 and α=45°.

These trends are most clearly visible in the comparisons between all the VAFs obtained numerically and those predicted with the different models, shown in Figure III.5.9. In the case of the model of Eq. III.5.3, as previously noted, there is an overestimation of the amplification since in the calibration phase the VAF is chosen to be overestimated. In the case of the neural networks the data are equally dispersed in both overestimating and underestimating the VAF, and this dispersion decreases as the number of neurons increases. This is since the calibration procedure of the neural network is designed to minimize the mean square deviation.

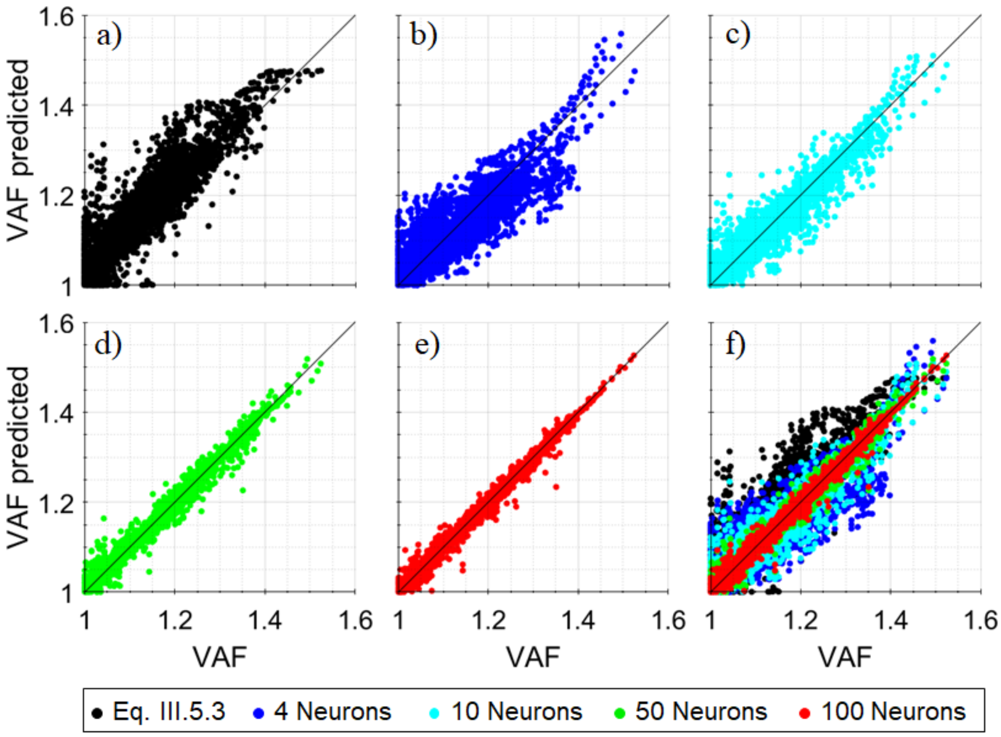

Figure III.5.9 – Comparison between VAF obtained with numerical analysis and that predicted with the proposed equation and neural network.

It should be noted that the calibration process of the neural networks does not follow any physical principle of the problem under investigation, unlike the results obtained for the model previously reported (Eq. III.5.3). As a matter of fact, the various coefficients used by the neural networks are obtained from pure statistical computations and do not consider the results and evidence that emerged from the study of accelerograms, amplification functions and response spectra. On the other hand, the shape of the functions f_1, f_2 as well as the calibration of the coefficients a_0, c_0, a_1, a_2, b_2 and c_2 is carried out considering all the physical phenomena that resulted from the study, with the aim of highlighting the most important factors which influence the seismic response of the alluvial valleys. For example, the equation of VAF(0) (Eq. III.5.4) is chosen to be independent of the angle of inclination of the edges because the study of accelerograms and response spectra has shown that the influence of alpha is negligible compared to that of the shape and impedance ratio.

Furthermore, to use neural networks, it is necessary to have a computer and suitable software, while the functions previously proposed can be more easily calculated. Indeed, the use of neural networks requires the calculation of matrices with a maximum size of [q x n], with q being the number of neurons and n the number of surface points whose VAF is to be calculated. For the present case q must be at least equal to 10 and therefore calculating the various matrix operations can be very laborious, without the use of a computer. Lastly, the equation of the VAF previously find (Eq. III.5.3) is used, in the next section (§III.6), to obtain charts that can be easily implemented in the technical codes and used for a quick evaluation of the amplification due to alluvial valleys.

III.5.3 Wedge basin

The results obtained by the parametric analyses show that the VAF trend computed along a wedge-shaped valley is significantly different from that evaluated for the trapezoidal shaped basin. The ground motion of the wedge-shaped valleys is strongly affected by the geometry (as described in §III.4.5), so that a question arises about the opportunity of comparing the 2D results with the 1D response computed at the centre of the valley. As a matter of fact, the wedge basin has a variable thickness always lower than H, except for the centre of the valley. For small values of H/B (small values of α) the basin can be approximated to a series of 1D columns of variable thickness that, especially at the edges, have a dynamic response that is very different from that of the valley centre. On the other hand, for H/B > 0.1, α is such that it focuses the seismic waves towards the centre of the valley and Rayleigh waves significantly influence the motion at surface.

Notwithstanding these observations, it has been chosen to quantify the 2D effects by adopting the same valley aggravation factor defined in the case of trapezoidal valley, since the 1D response of the vertical at the valley centre is the only reference datum that can be obtained easily with sufficient accuracy.

The VAF computed in the case of wedge-shaped valley are plotted in Figure III.5.10a as a function of H/B: the different mechanism affecting the motion at surface can be clearly detected. As a matter of fact, for H/B<0.1, the VAF is maximum at the edges because in these portions of the valley resonance condition are attained if $f_m > f_{0.1D}$ (see Figure III.4.39) and the amplifications are greater than in the middle of the valley. It is worth to highlight that VAF is calculated as the average of $AG_{2D/1D}>1$ for each input, and since for $f_m < f_{0,1D}$ (see Figure III.4.37) it is less than 1 around the edges, the VAF of these zones is calculated by averaging only the results obtained for $f_m > f_{0,1D}$. The amplification at the centre of the valley is mainly related to the generation of Rayleigh waves which increasingly affect the response at the valley centre as H/B increases.

Figure III.5.10b,c reports the VAF as a function of the impedance ratio for H/B equal to 0.25 and 0.05, respectively. In both cases the VAF decreases with the impedance ratio, in accordance with the results presented previously (§III.4.5).

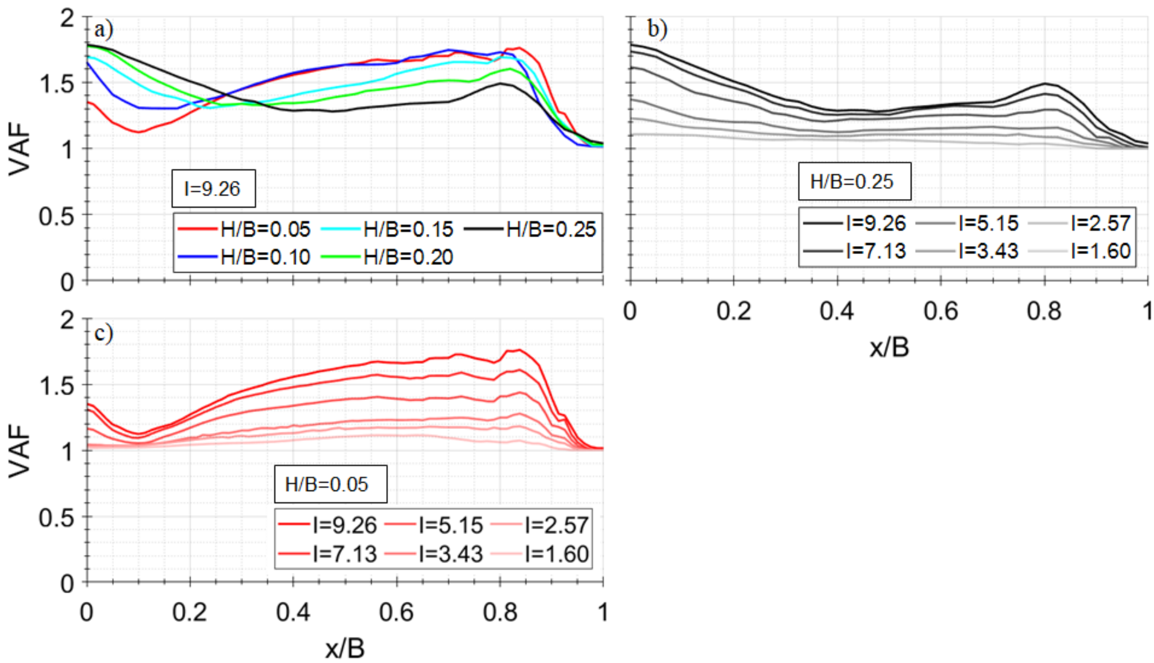

Figure III.5.10 – VAF obtained for the wedge basin for variable a) H/B with I=9.26 and for variable I for H/B equal to b) 0.25 and c) 0.05

The VAF computed from the analyses has been interpreted introducing an analytical relationship, as already done for the trapezoidal shaped valley. The same equation proposed for the trapezoidal basin case has been adopted (Eq. III.5.3), except for f_1 which is set equal to:

$$f_1\left(\frac{x}{B},\frac{H}{B},I\right)=c_1\cdot\exp\left(-\frac{\left(\frac{x}{B}\right)^2}{2\cdot a_1^2}\right) \quad \text{III.5.17}$$

The equation describing the variation of VAF(0) with I and H/B is the same as in the trapezoid case (Eq. III.5.4), and Figure III.5.11 shows the comparison between the data obtained (triangles), the corresponding fitted functions (dashed lines) and those obtained in the trapezoidal case (continuous lines). The amplification at the valley centre is greater for the wedge than for the trapezoid valleys, for all shape ratios.

Details about the calibration of the different coefficients are reported in the Appendix B.

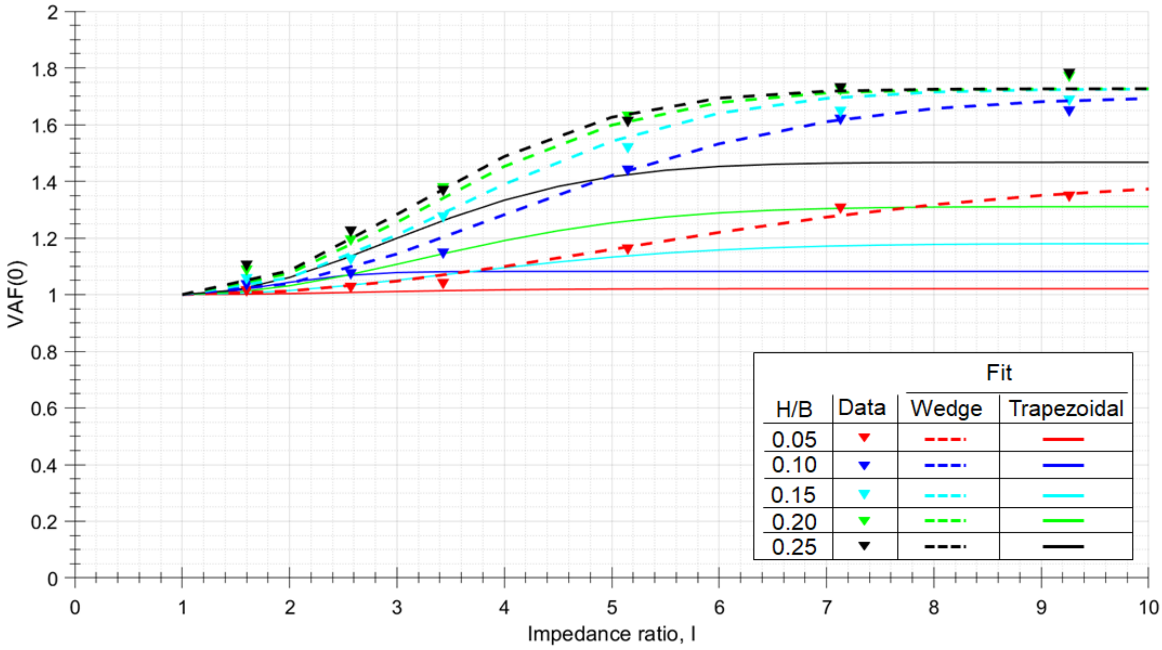

Figure III.5.11 – Comparison between the VAF(0) calculated for the wedge (triangle), and the fitted functions for the wedge (dashed lines) and the trapezoidal (continuous lines) basins.

Figure III.5.12 shows a comparison between the VAF profiles obtained from the analysis and those predicted by the previous equations. The proposed model slightly overestimates the amplification, however this is purposely intended in the calibration phase as well as in the case of trapezoidal basins.

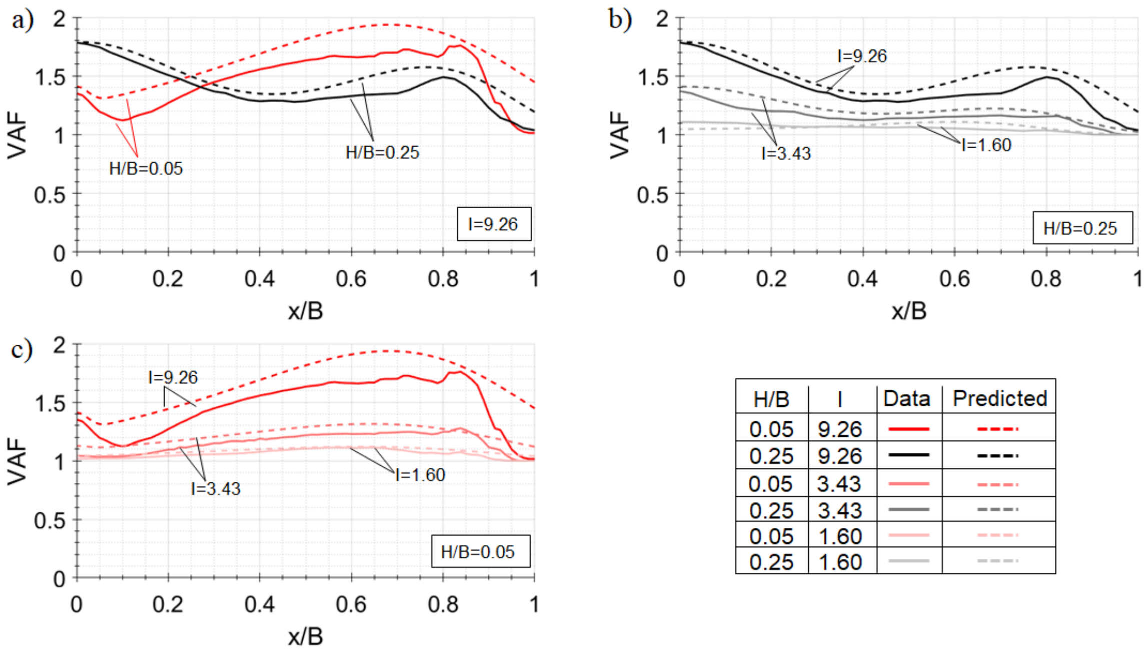

Figure III.5.12 – Comparison between numerical and predicted VAF for: a) I=9.26; b) H/B=0.25; c) H/B=0.05

III.6 Charts

The results obtained in the previous section are used to define a simplified methodology to estimate the seismic response of trapezoidal valleys. The VAF profiles along the valley have been further simplified defining a piecewise linear trend, identified by five relevant points (Figure III.6.1). The first is the VAF(0) computed at the centre of the valley, x/B=0, (Point 0 in Figure III.6.1), the second (Point 1 in Figure III.6.1) identifies the lowest value of VAF between the peaks computed at the centre and near the edge of the valley, the third and the fourth (Point 2,3 in Figure III.6.1) are used to describe the maximum value of the VAF at the side of the valley and the last one (Point 4, x/B=1) is set equal to 1, therefore neglecting any attenuation at the border of the valley.

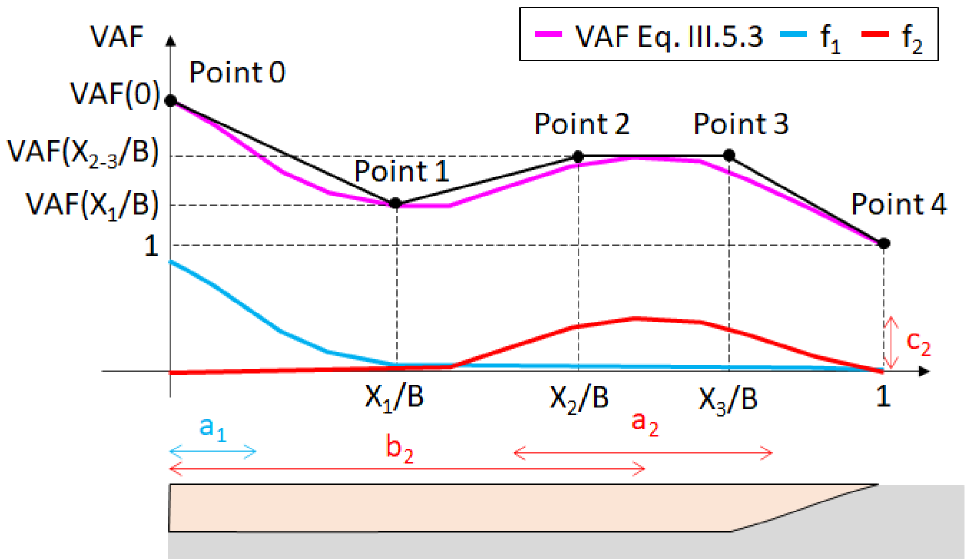

Figure III.6.1 – VAF profiles obtained from Eq. III.5.3 (magenta line) and its simplified piecewise linear trend (black line) with the identification of 5 relevant points, and , function f_1 (cyan line) and f_2 (red line)

The VAF and x/B of the different points are calculated using the equations defined for VAF(0) (Eq. III.5.4), a_1 (Eq. A.7), a_2 (Eq. A.11), b_2 (Eq. A.14) and c_2 (Eq. A.21), and Table III.6.1 shows their analytical expressions. They are designed to be exclusively dependent on the shape and impedance ratio, so they can be represented in charts similar to that of Bard & Bouchon (1985), which distinguish the behaviour of deep and shallow valleys based on the combination between their shape and impedance ratio. Note that since a_2, b_2 and c_2 also depend on the edge slope, the definition of each point of the piecewise linear trend is based on α that maximises the amounts and extension of amplification. In this way, following an overconservative approach, the values of VAF predicted through these charts will overestimate all possible values resulting from specific 2D seismic response analyses.

Specifically at the centre of the valley the amplification is given by VAF(0), that is expressed as a function of I and H/B (Figure III.5.3a): a very shallow valley (H/B<0.1) results in negligible 2D effects at its centre, whatever I. The normalised abscissa x_1/B is representative of the width of the amplification zone at the centre of the valley. It is equal to b_2 coefficient of Eq. A.14 minus a quantity that is a function of a_2 (see Eq. A.11) and increases as H/B decreases, i.e. moves towards the edges. Since a_2 (Figure III.5.3c) and b_2 (Figure III.5.3d) are function of α, as explained in Appendix A, it has been calculated for a given slope edge equal to 30°. This is due to the fact that for such angle the lateral amplification zone is closer to the valley centre than for larger alphas (Figure III.5.3d). x_2/B and x_3/B are calculated respectively as b_2 minus and plus 0.25 times a_2, which is a measure of the standard deviation of the Gaussian type function used to describe f_2. For x_2/B, α=30° is chosen for the same reasons as for x_1/B, while for x_3/B α is set equal to 90° because for this angle the zone of lateral amplification is closer to the edges (Figure III.5.3d). VAF($x_{2\text{-}3}/B$) is computed considering that for $x/B=b_2$, the effect of f_1 is negligible, so the VAF of Eq. III.5.3 is approximately equal to $1 + c_2 \cdot \exp(-1)$. For the sake of safety, a minimum contribution of f_1 has been considered and therefore 1.05 has been used instead of 1. Since c_2 also varies with the angle of inclination of the edges, α=90° has been used because, for this value, the maximum c_2 is obtained (Figure III.5.3e).

Table III.6.1 – Coordinates of the point of the simplified piecewise linear trend of VAF

Point	x/B	VAF
0	0	VAF(0)
1	$\frac{x_1}{B} = b_2 - \left(2 - 4 \cdot \frac{H}{B}\right) \cdot a_2$	$VAF\left(\frac{x_1}{B}\right)$
2	$\frac{x_2}{B} = b_2 - 0.25 \cdot a_2$	$1.05 + c_2 \cdot \exp(-1)$
3	$\frac{x_3}{B} = b_2 + 0.25 \cdot a_2$	
4	1	1

Figure III.6.2 shows the charts which can altogether permit to approximate through a piecewise linear trend the irregular variability of VAF along a trapezoidal valley characterised by a given H/B and I.

The chart in Figure III.6.2a shows the contour plot of the amplification at the valley centre, VAF(0), expressed as function of H/B and I. The red line represents the isoline corresponding to VAF(0)=1.05 that can be assumed as a threshold line below which the seismic response at the centre of the valley can be reasonably predicted with a one-dimensional analysis. The equation of the threshold curve is the following:

$$\left(\frac{H}{B}\right)_{VAF(0)=1.05} = \frac{0.214}{\sqrt{I-1}} \qquad \text{III.6.1}$$

The threshold curve is described by an equation comparable to that given by Bard and Bouchon (1985), which separates shallow from deep valleys. This curve, instead, allows to subdivide the shallow basins in two further classes:

- the first one is constituted by '<u>very shallow valleys</u>' (red and white zones of the charts in Figure III.6.2), characterized by negligible 2D effects along most part of the basin, and by a concentration of amplification in the area close to the edges;
- the second class, represented by the area of the chart above the threshold curve, is constituted by '<u>moderately shallow valleys</u>' (light blue zone of the charts of Figure III.6.2) with VAF significantly greater than 1 both at the edges and at the centre of the valley.

More in details, the behaviour of 'very shallow valleys' can be further classified based on the value of H/B. For $H/B<0.1$ (red zone in Figure III.6.2), VAF(0) is almost unitary (being lower than 1.05), VAF(x_1/B) is lower than 1.1, and the abscissa x_1/B is poorly affected by the impedance ratio, decreasing with the shape ratio to about 0.5 for H/B approaching 0.1. Therefore, these basins are characterised by a VAF lower than 1.1 for a large area, extending from the centre of the valley up to x_1/B. This means that in these zones, for this class of valleys, a ground response computed referring to the results of 1D seismic analysis, carried out along the profile corresponding to the centre of the valley, leads to underestimate the mean spectral amplification by about 10%. However, it should be noted that for these basins the 2D effects are not negligible at the edge. As a matter of fact, the amplification in the lateral zone, represented by VAF(x_{2-3}/B), is independent of H/B and varies with I, resulting at least equal to 1.2. The abscissa of the maximum amplification at the edges ranges between x/B=0.7-0.9 depending on the values of x_2/B and x_3/B. For H/B > 0.1 (white zone in Figure III.6.2), the overall behaviour of the valley is mainly ruled by the effects of geometric and material damping that significantly reduce the energy of Rayleigh waves propagating towards the centre of the valley, thus poorly influencing the motion therein. On the other hand, amplification at the valley edge cannot be neglected, being VAF($x_{2\text{-}3}$/B) at least equal to 1.2.

The 'moderately shallow valleys' (light blue area), instead, are characterized by a VAF(0) significantly higher than unity (Figure III.6.2a), and increasing with H/B and I. The abscissa x_1/B (Figure III.6.2b) is poorly variable around 0.4, while the value of VAF(x_1/B) ranges between 1.1 and 1.2 (Figure III.6.2c) and is typically lower than VAF(0). The amplification peak at the valley edge (Figure III.6.2e) has a significant value too, i.e. between 1.3 and 1.5 for realistic impedance ratio values. It covers a wide area between x_2/B=0.4-0.6 and x_3/B=0.7-0.8.

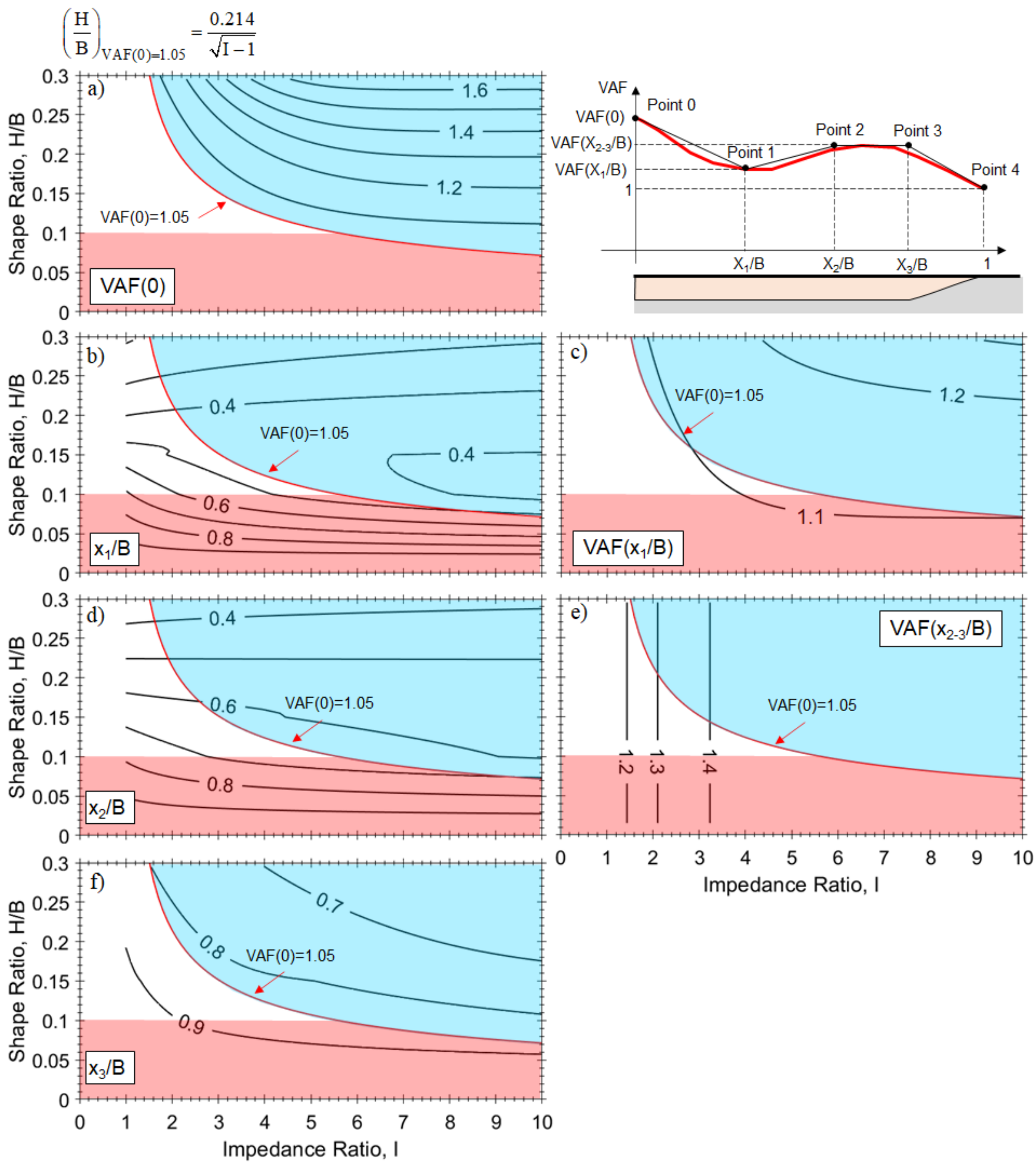

Figure III.6.2 – Chart of: a) VAF(0); b) x_1/B; c) VAF(x_1/B); d) x_2/B; e) VAF($x_{2\text{-}3}/B$); f) x_3/B as function of H/B and I.

In conclusion, the charts highlight that 'shallow valleys' can be further distinguished into two classes based on the value of the shape ratio (Figure III.6.3). If H/B<0.1, they can be considered as 'very shallow' basins, characterised by slight 2D amplification between the centre of the valley and x_1/B, thereafter gradually increasing approaching the edges. In other words, the evaluation of site response by

1D numerical analyses can lead to an underestimation by a maximum of 10% of the spectral ordinates around the centre of the valley, while it can be completely misleading close to the edge. If H/B>0.1, instead, the 2D effects are not negligible everywhere in the valley, and thus they must be taken into account, being possible to conservatively predict them with the proposed charts or equations if not by 2D numerical analyses

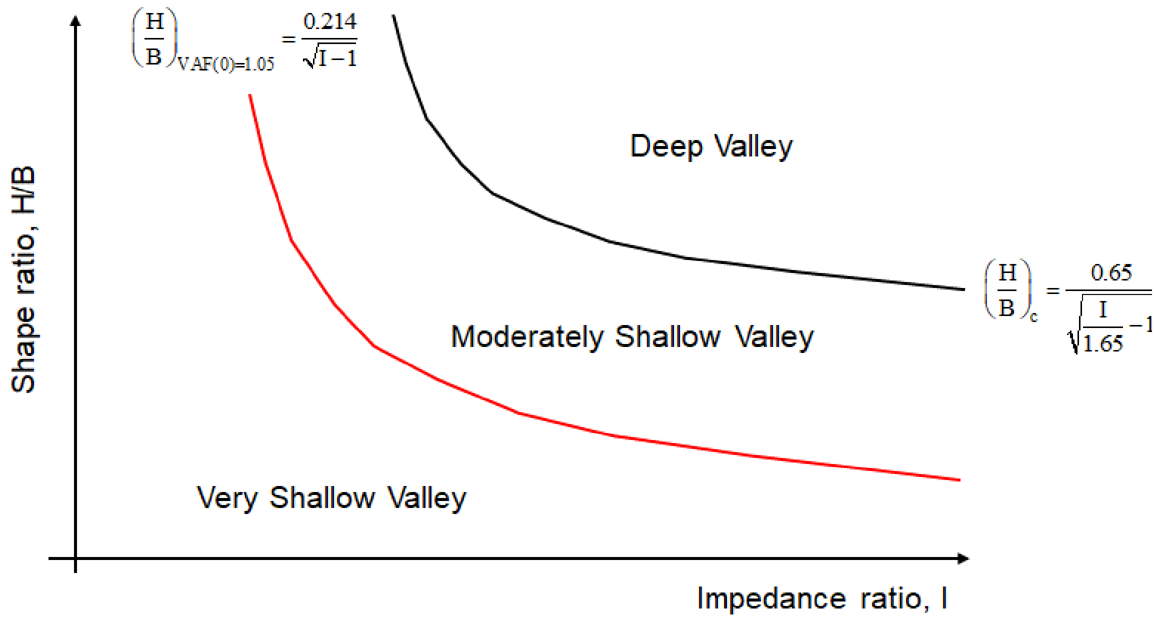

Valley	Central zone	Edge zone
Very Shallow	VAF<1.05 $\longrightarrow$ $AG_{2D} \approx AG_{1D}$	VAF>>1 $\longrightarrow$ $AG_{2D} > AG_{1D}$
Moderately Shallow	VAF>>1 $\longrightarrow$ $AG_{2D} > AG_{1D}$	VAF>>1 $\longrightarrow$ $AG_{2D} > AG_{1D}$

Figure III.6.3 – Scheme of the proposed new classification of shallow valley

III.7 Discussion

In the above sections, a Valley Amplification Factor has been defined as an index of how much, on average, the 2D spectrum is greater than the 1D one for T between 0s and $T_{0,1D}$. Two different methodologies have been provided to calculate the VAF, i.e. Eq. III.5.3 and charts. It has been observed that, along the valley, the VAF has two different peaks, one in the centre and one near the edges. In the first case it is mainly a function of I and H/B and increases with them. In the second case, the area of maximum amplification also depends on the angle of inclination of the edges. At the centre the VAF is between 1 and 1.6 while at the edges it varies between 1 and 1.45 and these values are similar to those found in the literature (see §II.7).

As a matter of fact, if the mean values of the valley amplification factors are considered, Vessia et al. (2011) found that for shallow valleys with H/B<0.2 the amplification at the centre of the valley is equal to 1.35 while at the valley edge it is equal to 1.5. It should be noted that Vessia et al. (2011) defines a single value without taking into account the variability with the shape and impedance ratio. Therefore, it is reasonable that there is a difference between the VAF calculated in this study and those provided by Vessia et al. (2011).

On the other hand, the values provided by the studies, that calculate the maximum of the ratio between 2D and 1D spectra (Chávez-García & Faccioli, 2000; Riga et al., 2016; Zhu, Thambiratnam, et al., 2018), range between 1 and 3 and are obviously higher than those predicted in this study.

IV. INFLUENCE OF SOIL INHOMOGENEITY AND NON-LINEARITY

The alluvial deposits are usually characterised by a non-linear increase of stiffness with depth (d'Onofrio & Silvestri, 2001), which affects the seismic response at surface. The inhomogeneity of Vs profile leads to an increase of the amplification respect to that observed in the homogeneous case, both at the edges and at the centre of the valley (Bard & Gariel, 1986). In addition, at the lateral borders the interface between the bedrock and the deformable deposit is characterised by an impedance ratio decreasing with depth, which influences the ray paths of both refracted and surface seismic waves. This in turn affects the abscissa of the maximum amplification related to the constructive interference between the different waves moving it towards the edge of the valley (Bard & Gariel, 1986)

Soil non-linearity also modifies the seismic response of the basin inducing a change in the amplitude, frequencies content and duration of the ground motion respect to those computed assuming a homogeneous visco-elastic soil model. The overall effect on ground response depends on both the non-linear properties of the soils, i.e. the shear modulus and damping variation curves with strain, and the characteristics of the reference seismic motion. Indeed, as the energy content and the duration of the latter increase, the shear strain generally grows, since both the amplitude and the number of loading cycles increase (Gelagoti et al., 2010, 2012; Iyisan & Khanbabazadeh, 2013; Riga et al., 2018).

Soil non-linearity in various ways affects the response at ground surface since it causes an inhomogeneity of the V_S profile, even in a homogeneous valley, and therefore a variation of the impedance ratio within the valley and an increase of soil dissipative properties at increasing shear strains.

Both described mechanisms differently affect the seismic response along the valley since direct, indirect and surface waves variously combine each other at the edge and at the centre of the valley. As a matter of fact, at the valley edges the phenomenon of trapping seismic waves occurs, since the increase of damping causes a rapid decrease of the amplitude of the Rayleigh waves, that remains relevant only at the valley borders. At the centre of the valley the interaction among the different wave fields is hardly affected by Rayleigh waves, and usually results in a reduction of the ground motion if compared to the visco-elastic case (Gelagoti et al., 2010, 2012; Iyisan & Khanbabazadeh, 2013; Riga et al., 2018).

In this chapter the influence of inhomogeneity and non-linearity have been analysed carrying out an additional set of numerical analyses on a single geometrical model. Inhomogeneity and the non-linearity of soil have been modelled in the analyses (§IV.1), then the effect inhomogeneity (§IV.2) and non-linearity (IV.3) on the ground response at ground surface have been examined. Finally, the influence of both factors on VAF has been investigated (§IV.4), providing a procedure to modify the visco-elastic VAF to account for the soil nonlinearity and heterogeneity.

IV.1 Geotechnical model including inhomogeneity and non-linearity

A unique geometrical model has been adopted in the following set of analyses. A basin with a shape ratio of 0.25 and an edge slope angle of 45° has been chosen, since these geometric parameters gave rise to the maximum amplification both at the edges and the centre of the valley in the visco-elastic analyses shown in the previous chapter. Since the selected model is also used subsequently to evaluate the effect of soil nonlinearity, it is chosen to reduce its size to ease the computational effort and save time. A reduced valley thickness, H, of 30 m has been assumed keeping the shape ratio equal to 0.25, all the domain dimensions has been consequently adjusted to guarantee the optimization of the numerical model as described in §III.3. Furthermore, it has been verified that the already computed visco-elastic response does not change if the geometrical model of reduced size is adopted. To this aim, several preliminary analyses have been carried out on the model of reduced size, modelling the deformable soil as a homogeneous visco-elastic material, and adopting a reference input motion that ensure a value of frequency ratio, $f_m/f_{0,1D}$, equal to that adopted in the previous set of numerical analyses. The results obtained adopting the reduced geometrical model are then compared to those obtained in the previous set of analyses in terms of $AG_{2D/1D}$ and VAF. As an example the contours of $AG_{2D/1D}$, computed for both thicknesses and for $f_m/f_{0,1D}$ respectively equal to 1 (a,b) and 2 (c,d), are plotted in Figure IV.1.1 and show that the model response is independent on the individual values of H, B, x and f_m, if the dimensionless variables H/B, $f_m/f_{0.1D}$ and x/B are the same. Thus confirming the validity of the dimensionless variables adopted in the parametric analysis.

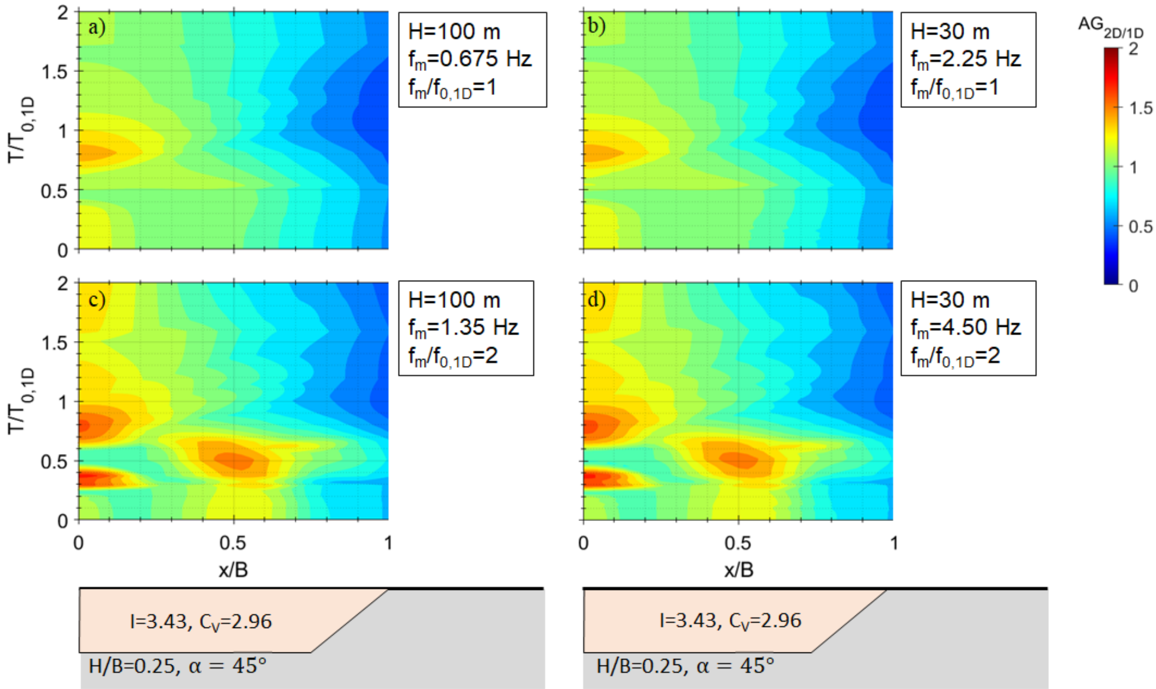

Figure IV.1.1 – $AG_{2D/1D}$ obtained for: a) H=100m, $f_m/f_{0,1D}$=1; b) H=30m, $f_m/f_{0,1D}$=1; c) H=100m, $f_m/f_{0,1D}$=2; d) H=30m, $f_m/f_{0,1D}$=2

The influence of inhomogeneity has been analyses modelling the soil deposit with an equivalent velocity of 270 m/s laying on a bedrock with a Vs equal to 800 m/s. The equivalent velocity $V_{s,eq}$,is defined as:

$$V_{S,eq} = \frac{H}{\sum_{i=1}^{n} \frac{h_i}{V_{S,i}}} \qquad \text{IV.1.1}$$

with H the total thickness of the soil deposit at the centre of the valley, h_i and $V_{S,i}$ the height and shear wave velocity of the i-th layer and n the number of the layers. A power law, with an exponent lower than one, has been assumed to describe the stiffness variation with depth:

$$\frac{G_0}{p_r} = S \cdot \left(\frac{p'}{p_a} \right)^n \qquad \text{IV.1.2}$$

Where, p' is the actual confinement stress, p_r is the reference confinement stress, p_a is the atmospheric pressure. The stiffness index, S, and the stiffness coefficient, n, has been defined based on the relationship proposed by d'Onofrio & Silvestri (2001):

$$S = 217 + 805.84 \cdot \exp\left(\frac{PI}{18.94}\right) \qquad \text{IV.1.3}$$

$$n = 0.68 - 0.162 \cdot \exp\left(-\frac{PI}{23}\right) \qquad \text{IV.1.4}$$

as a function of the plasticity index, PI, of the soil.

The plasticity index adopted in the following analyses has been selected to be representative of a typical alluvial soil characterised by a $V_{S,eq}$ equal to 270 m/s. Since the modelled soil deposit fall into the class C of the Italian technical code (NTC 2018), typically associated with loose to medium dense sands and low to medium consistent clays, a PI equal to 15% has been assigned. Nevertheless, Eq. IV.1.2 provides a non-realistic zero stiffness at ground surface, to overcome this drawback a linear variation of G_0 has been defined between 0 m and 10 m, so as to be tangent to the curve of Eq. IV.1.2 at the depth of 10 m. A further stiffness profile (Max EM) has been assumed in the analyses, not related to a defined PI value, with the aim of maximising the effect of inhomogeneity. Also in this latter case the G_0 profile has been constructed to ensure that $V_{S,eq}$ is equal to 270 m/s. The related Vs(z) profile is described by the following equation:

$$V_S(z) = 91 + 19.2 \cdot z^{0.813} \qquad \text{IV.1.5}$$

with z the considered depth in meters, while V_s is given in m/s.

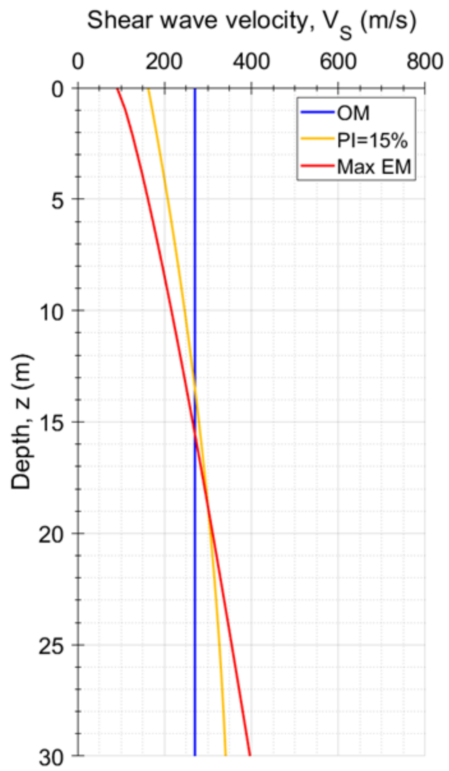

Figure IV.1.2 – Profile of inhomogeneity of V_S with depth

The shear modulus, $G(\gamma)/G_0$, and damping, $D(\gamma)$, variation curves with shear strain are selected from the literature to be representative of materials corresponding to class C, as defined by the Italian technical code (NTC 2018). Since this class includes loose to medium dense sands and low to medium consistent clays, two different curves are used, the Seed & Idriss (1970), S&I, average for sands and the Vucetic & Dobry (1991), V&D, for clays with PI=15%. Figure IV.1.3a,b shows the comparison between the literature curves and those implemented in FLAC for S&I and V&D respectively. Note that for both, the shear modulus decay curves used in FLAC are almost overlapped to the literature curves, while the damping at medium to high strains is significantly overestimated. This is explained by the fact that FLAC predicts the stiffness decay by using a 3-parameter sigmoid model, which is calibrated based on the experimental $G(\gamma)/G_0$ curve, and then it computes the hysteretic damping with the use of the Masing criteria, which leads to an overestimation of the dissipative behaviour at medium to high deformations (Phillips & Hashash, 2009). Figure IV.1.3c shows a comparison of the S&I and V&D curves implemented in FLAC, with the latter exhibiting a higher damping value at high strains.

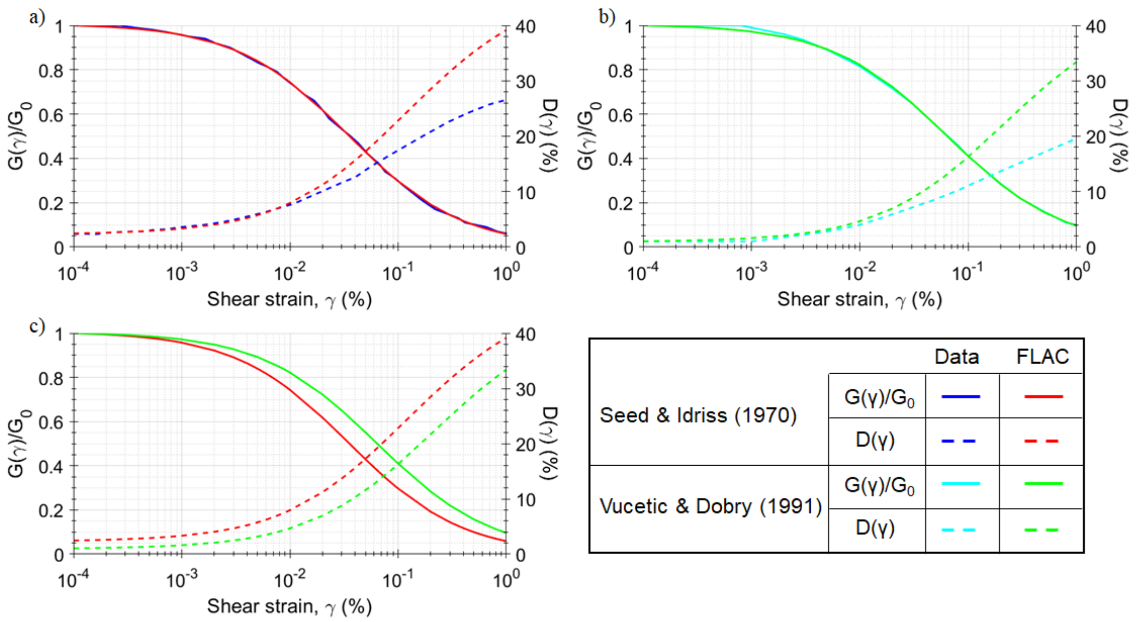

Figure IV.1.3 – Comparison between the shear modulus ($G(\gamma)/G_0$), on left vertical axis, and damping ($D(\gamma)$), on right vertical axis, variation curves with strain retrieved from literature and those computed by FLAC for: a) Seed & Idriss (1970); b) Vucetic & Dobry (1991). c) Comparison between the non-linear curves used by FLAC for Seed & Idriss (1970) and Vucetic & Dobry (1991)

The same Ricker wavelets of Chapter III are used as the reference seismic motion, but the mean frequency is modified to obtain the same $f_m/f_{0,1D}$. Indeed, by varying the thickness of the valley and keeping the same V_S, $f_{0,1D}$ is increased and consequently the mean frequencies of the input motion as well.

Lastly, it should be noted that STRATA and FLAC use different ways to model nonlinearity, the former carrying out equivalent linear analyses and the latter non-linear ones. Therefore, in the following (and in Chapter V) also the 1D analyses are carried out using FLAC, in order to have a non-linear behaviour consistent with the 2D ones.

IV.2 Effects of inhomogeneity

Before analysing the results, it is necessary to explain how the one-dimensional resonance period has been defined in the following analyses. As a matter of fact, the inhomogeneity of the V_S profile leads to a change in the frequency response of the one-dimensional column, with resonance frequencies and amplifications generally increasing respect to the visco-elastic case (Gazetas, 1982; Rovithis et al., 2011). Figure IV.2.1a shows the comparison among the 1D amplification functions, obtained for the 3 analysed profiles shown in Figure IV.1.2, computed as the ratio between the amplitudes of the Fourier spectra obtained at the surface and at the bedrock. The frequencies in the abscissae are divided by $f_{0,1D}$ which, in agreement with the results shown above (§III), is defined as:

$$f_{0,1D} = \frac{V_{S,eq}}{4 \cdot H} \qquad \text{IV.2.1}$$

with $V_{S,eq}$=270m/s (i.e. the velocity of the homogeneous layer), and H=30m.

The amplification function of the homogeneous case (blue line in Figure IV.2.1) is consistent with the results obtained for a deformable visco-elastic layer on a deformable half-space, with the first 3 resonance frequencies equal to 1, 3 and 5 times $f_{0,1D}$ with decreasing amplitudes (Kramer, 1996). On the other hand, the amplification functions computed along the two inhomogeneous profiles (orange and red lines in Figure IV.2.1) are characterised by a first resonance frequency higher and equal to about 1.1 $f_{0,1D}$, for both PI=15% and Max EM profiles, the amplitudes increase with the degree of inhomogeneity, and the frequencies of the higher modes are closer to each other, in agreement with what is known in the literature (e.g. Gazetas, 1982;

Rovithis et al., 2011). Furthermore, the 2D amplification functions calculated at the centre of the valley in the 3 cases (Figure IV.2.1b) also show the same differences between the homogeneous and the inhomogeneous cases. Since the first resonance frequency of the inhomogeneous profiles is about 10% higher than that of the homogeneous case, in the following the inhomogeneity effect on resonance frequency is neglected and $f_{0,1D}$ is calculated with Eq. IV.2.1, in accordance with what has been done in Chapter III. This assumption is further justified by the aim of providing a relatively simple tool to take into account the 2D valley effect.

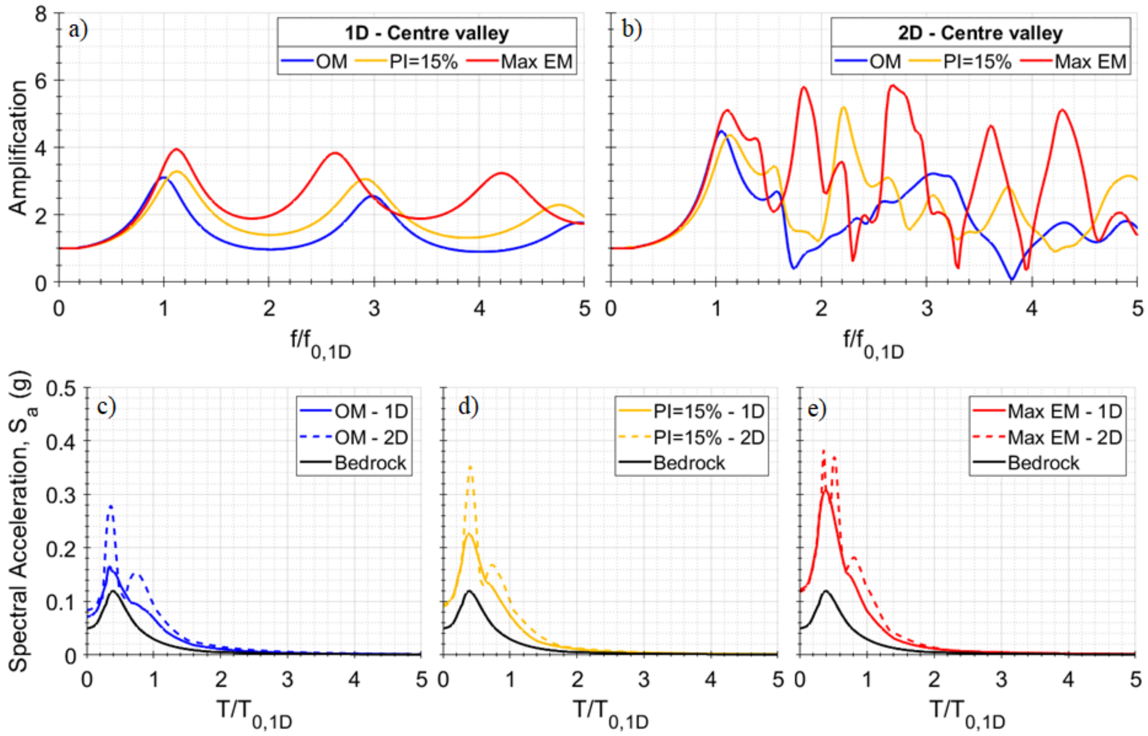

Figure IV.2.1 – Comparison between the a)1D and b) 2D amplification function, c,d,e) 1D, 2D and input response spectra calculated for OM, PI=15%, Max EM.

Moreover, it is worth highlighting that the results of the analyses have been again synthesised in terms of VAF that has been computed considering the ratio between 2D and 1D response spectra (Figure IV.2.1c,d,e), extended to a range of periods not exceeding $T_{0,1D}$ (the inverse of $f_{0,1D}$ calculated with Eq. IV.2.1), where 2D effects are most relevant (see Figure IV.2.1c,d,e).

Figure IV.2.2 shows the contours of AG_{2D} and AG_{1D} calculated on the three analysed models OM, PI=15% and Max EM, for $f_m/f_{0,1D}$ equal to 1 and 2. 1D and 2D amplification increases with the degree of inhomogeneity of the soil deposit, whatever the input adopted.

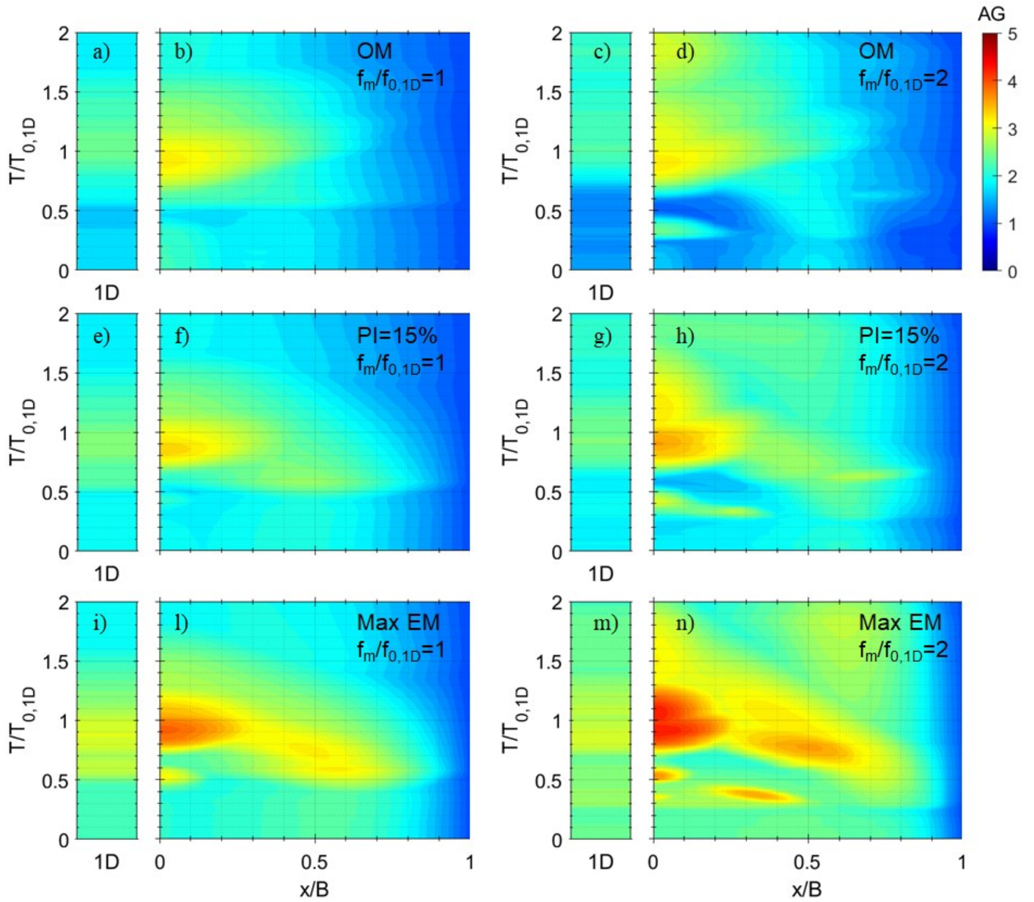

Figure IV.2.2 – AG_{2D} and AG_{1D} calculated for OM, PI=15%, Max EM and $f_m/f_{0,1D}$ equal to 1 and 2.

There is a relevant increase of both AG_{1D} and AG_{2D} at the centre of the valley for period close to the resonance one. Furthermore, at the valley edge there is a significant increase in amplification, due to the different mechanisms of seismic wave focalization, which are generated due to the variation of the impedance ratio in correspondence with the inclined interface between the bedrock and the soil (Bard & Gariel, 1986).

The effect of inhomogeneity on the ground response is no more evident if the results are expressed in terms of ratio $AG_{2D/1D}$ since it affects in a similar way both 1D and 2D response. As a matter of fact, the highest values of $AG_{2D/1D}$ (Figure IV.2.3) are obtained for the homogeneous model both at the centre valley and at the edge for both inputs. AG_{1D} increases slightly more than AG_{2D} and, therefore, the ratio AG_{2D} / AG_{1D} decreases as the inhomogeneity of the V_S profile increases.

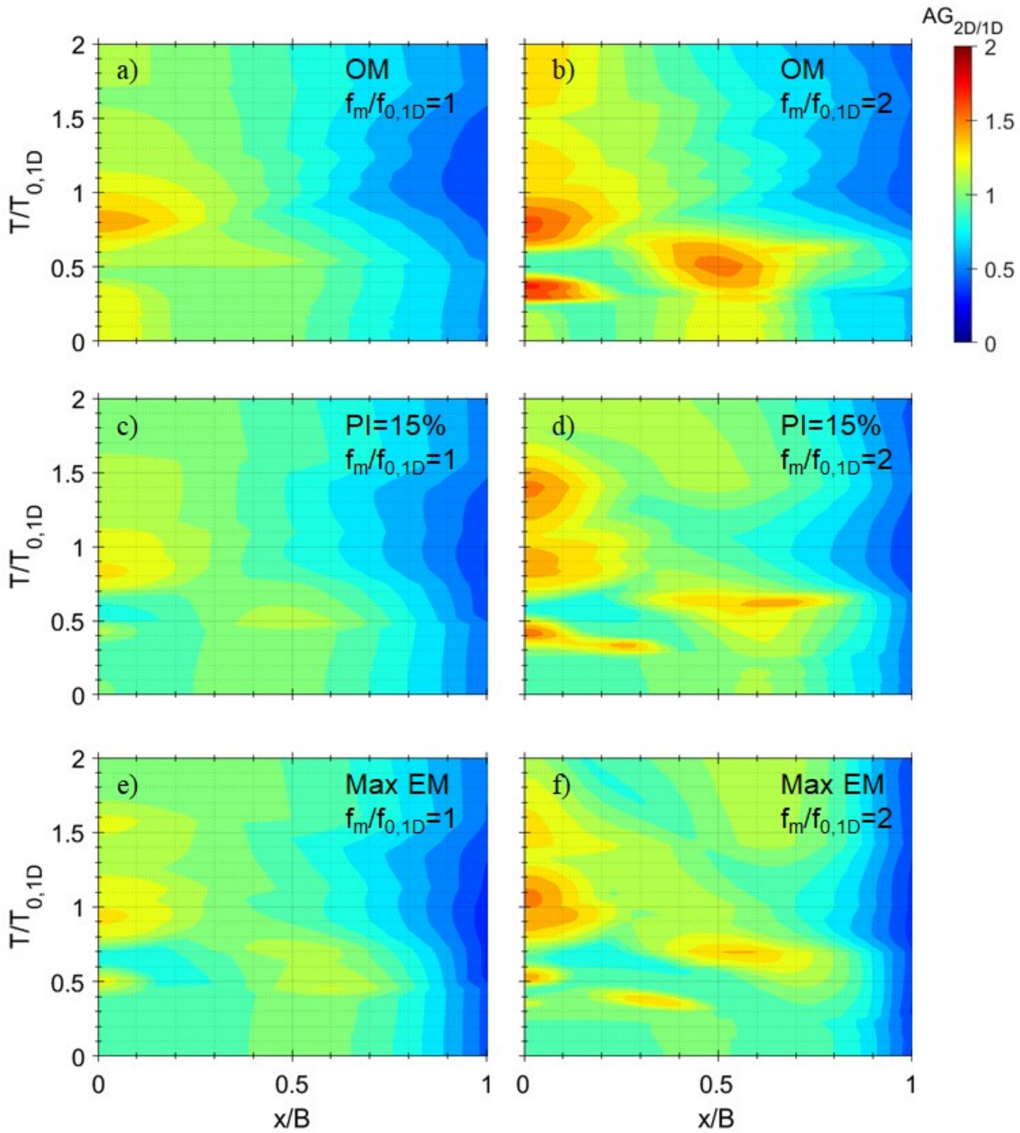

Figure IV.2.3 – $AG_{2D/1D}$ calculated for OM, PI=15%, Max EM and $f_m/f_{0,1D}$ equal to 1 and 2.

The effect of inhomogeneity on geometric amplification can be easily understood by studying the VAF variation profiles along the valley for the different models, and comparing them with the one analytically computed adopting the Eq. III.5.3 (Figure IV.2.4a). The VAF calculated considering the inhomogeneity (orange and red line) are almost coincident and lower than that computed on the homogeneous model and by the analytical procedure proposed. To better highlight this effect Figure IV.2.4b shows the same results expressed in terms of ratio between the VAF obtained in the inhomogeneous cases and that computed by Eq. III.5.3: independently of the inhomogeneity degree, the ratio slightly varies along the valley between 0.9 at the centre and 1 at the edges with a linear trend.

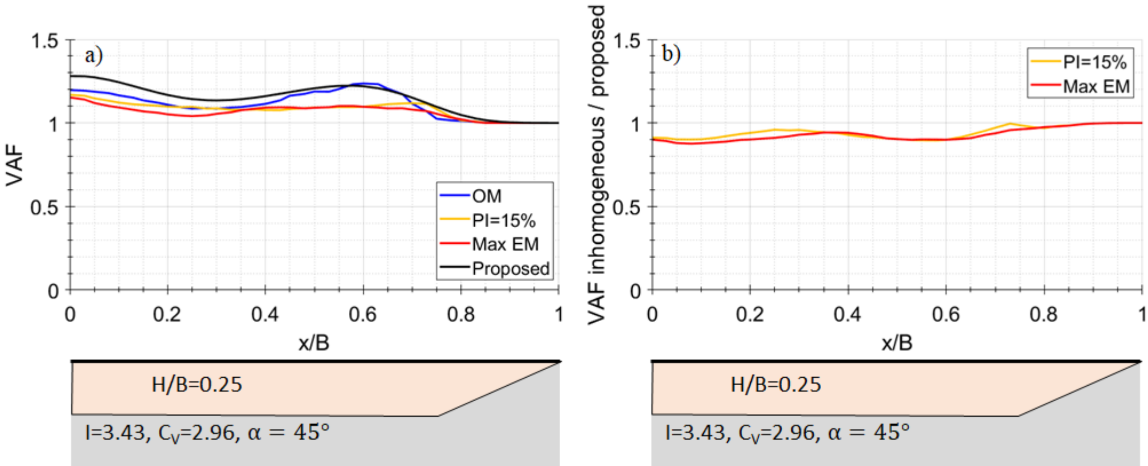

Figure IV.2.4 – Comparison between: a) VAF obtained with the OM, PI=15%, Max EM and that of the proposed equation. b) Profile of the variation of the ratio between VAF calculated considering the inhomogeneity and that of the proposed equation.

Ultimately, the results obtained showed that the VAF is slightly affected by inhomogeneity independently on its degree. As a matter of fact, two valleys characterised by very different Vs profiles with the same $V_{S,eq}$, have the same VAF, that is lower than that computed on the same valley and assuming a linear visco-elastic model. Practically, neglecting the inhomogeneity of the mechanical properties with depth and adopting the simplified VAF proposed in Eq. III.5.3 leads to a conservative evaluation of 2D effects overestimating the amplification by at most about 10%.

IV.3 Effects of non-linearity

In the following, the results obtained by considering the non-linear behaviour of the soil are reported. The model adopted has the same geometrical parameters used in the previous set of analyses (H/B=0.25 and α= 45°, §IV.2), while the soil deposit has been considered as homogeneous and characterised by a V_S equal to 270 m/s.

Ricker wavelets with f_m equal to those used in the inhomogeneous case have been used as reference seismic motion. The PGA outcrop, PGA_o, has been varied from 0.05g to 0.45g to investigate the behaviour from small to large shear strains.

A clarification should be done about the 1D fundamental period, $T_{0,1D}$, used to express the results in terms of VAF. As a matter of fact, non-linearity affects the resonance frequency reducing it as the PGA_o increases. Figure IV.3.1a,b shows the amplification functions obtained at the valley centre, both in 1D and 2D conditions, computed assuming the soil as a visco-elastic or non-linear material and adopting increasing values of PGA_o. In the figures the frequencies are normalised respect to the 1D resonance frequency, $f_{0,1D}$, calculated with Eq. IV.2.1 using a V_S equal to the initial one of 270m/s. It should be noted that both the first resonance frequency and the amplification decrease as the PGA_o increases. In detail, the resonance frequency decreases by at least 20%, for a PGA_o of 0.45g, which is a value significantly greater than those usually considered in typical Italian engineering design applications. While for a more realistic value (PGA_o<0.30g) the decrease of the resonance frequency is negligible not exceeding 10%. Furthermore in Figure IV.3.1c,d,e,f the related response spectra are shown, plotted using as abscissa the ratio $T/T_{0,1D}$, being $T_{0,1D}$ the inverse of $f_{0,1D}$. As the PGA outcrop increases, the motion amplitude decreases and the 2D predominant period increases, remaining lower than $T_{0,1D}$. Since nonlinearity hardly affects $f_{0,1D}$ in the following it is computed with Eq. IV.2.1 assuming a V_S of 270 m/s and $T_{0,1D}$ is obtained as the inverse of $f_{0,1D}$. This assumption clearly simplifies the procedure to calculate the VAF. Indeed, it is not currently possible to easily estimate the reduction of the resonance frequency without carrying out a seismic response analysis, because it depends on the intensity, frequency content and duration of the reference seismic motion, and on the $G(\gamma)/G_0$ and $D(\gamma)$ curves used. Instead, an estimation of the initial V_S should be the starting point of any seismic geotechnical engineering design problem and, therefore, the calculation of $f_{0,1D}$ with Eq. IV.2.1 should always be possible.

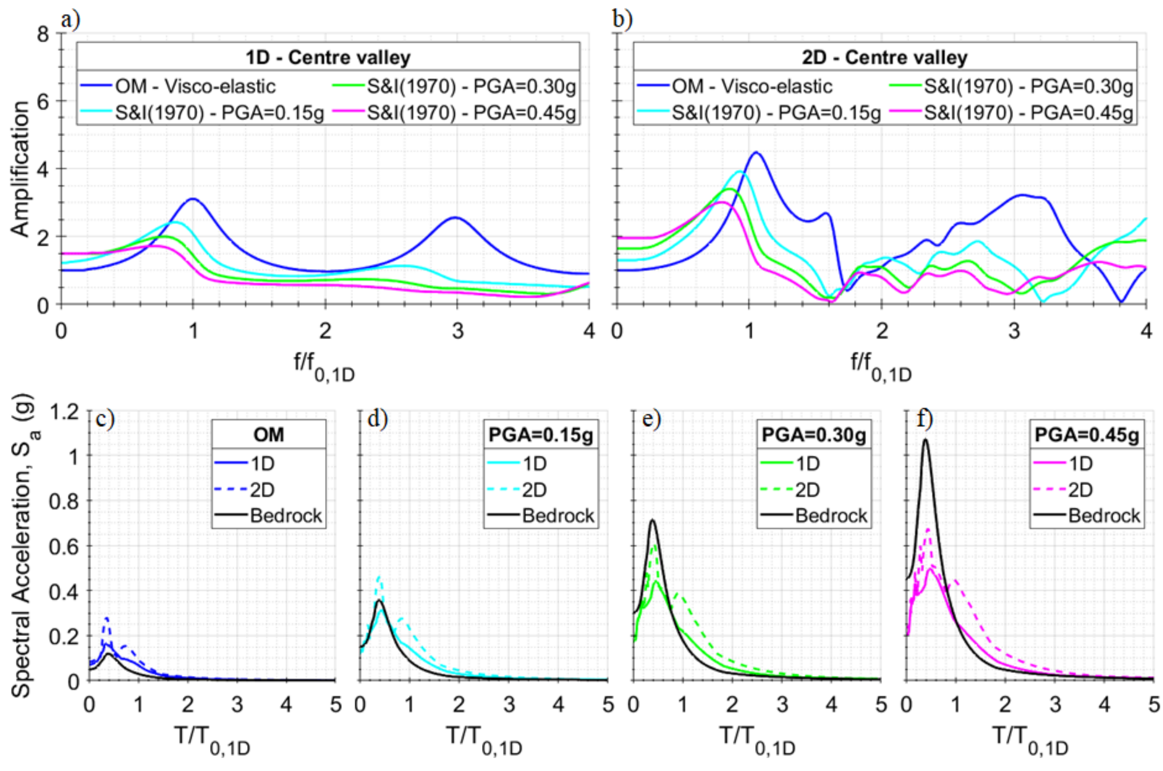

Figure IV.3.1 – Comparison between the a)1D and b) 2D amplification function, c,d,e) 1D, 2D and input response spectra calculated, at centre of the valley, for the model homogenous with visco-elastic (OM) and non-linear analysis for several value of the PGA outcrop.

Figure IV.3.2 shows the results of 1D and 2D analyses carried out using input of increasing PGA_o. The results are expressed in terms of contour of normalised maximum accelerations and mobilised G(γ)/G_0 within the analysed domain, both modelling the soil as a visco-elastic material or introducing soil nonlinearity by adopting the S&I curves. Note that the dimensions of the model are scaled in the abscissa with respect to the half-width of the valley, x/B, and in the ordinate with respect to the thickness of the valley, y/H.

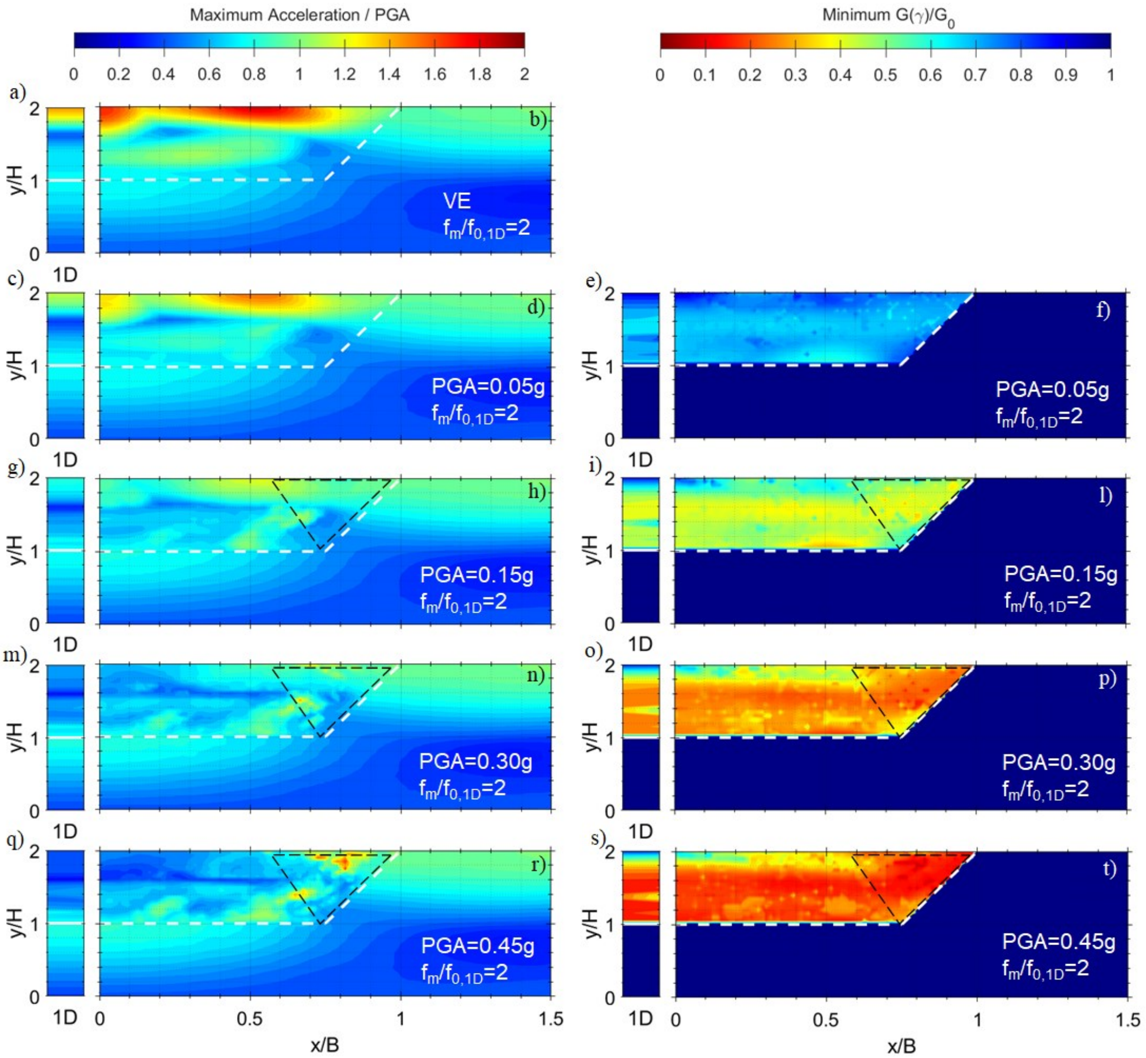

Figure IV.3.2 – 1D and 2D contour of the ratio between maximum acceleration and the PGA outcrop for visco-elastic (a,b) and non-linear analysis, considering Seed & Idriss (1970) curves and PGA outcrop of: c,d) 0.05g; g,h) 0.15g; m,n) 0.30g; q,r) 0.45g. 1D and 2D contour of the ratio between the minimum G(γ) and G_0 for PGA outcrop of: e,f) 0.05g; i,l) 0.15g; o,p) 0.30g; s,t) 0.45g.

In the visco-elastic case (Figure IV.3.2a,b) the maximum accelerations take place at the surface in the central part of the valley and near the edges. Furthermore, the 2D effects lead to an increase of the acceleration at about half of the thickness of the whole valley, that does not characterise the 1D response. Soil nonlinearity (Figure IV.3.2c-t) involves a non-uniform reduction of the maximum amplification within the whole valley, becoming more significant as PGA_o increases, due to the increase of the mobilised damping ratio, in both the 1D and 2D cases. The mobilised shear modulus varies depending on the value of PGA_o adopted. For low values of PGA_o (Figure IV.3.2e,f) it assumes an almost uniform distribution within the valley similar to that mobilised in 1D case, characterised by a shear modulus decreasing from the surface to the bedrock interface. As the PGA_o increases, the amplification at the edge becomes significant due to the combination between the inhomogeneity of the impedance ratio, along the inclined interface, and the Rayleigh wave trapping. This combination results in a high concentration of shear strains at the valley edge along the inclined interface. This effect is clearly distinguishable in Figure IV.3.2l,p,t where a black dashed line limits a triangular zones characterised by a significant decay of the shear modulus, which does not take place at the valley centre. It should be noted that the maximum amplifications of the PGA_o are also concentrated in this zone (Figure IV.3.2d,h,n,r). In the middle of the valley, on the other hand, the decay of the shear modulus is close to that observed in 1D analyses.

Figure IV.3.3 shows the contours of the response spectra calculated on the surface in both the 1D and 2D conditions, adopting two different input motions characterised by $f_m/f_{0,1D}$ equal to 1 and 2, and adopting a visco-elastic model or considering the non-linearity modelled through the S&I curves.

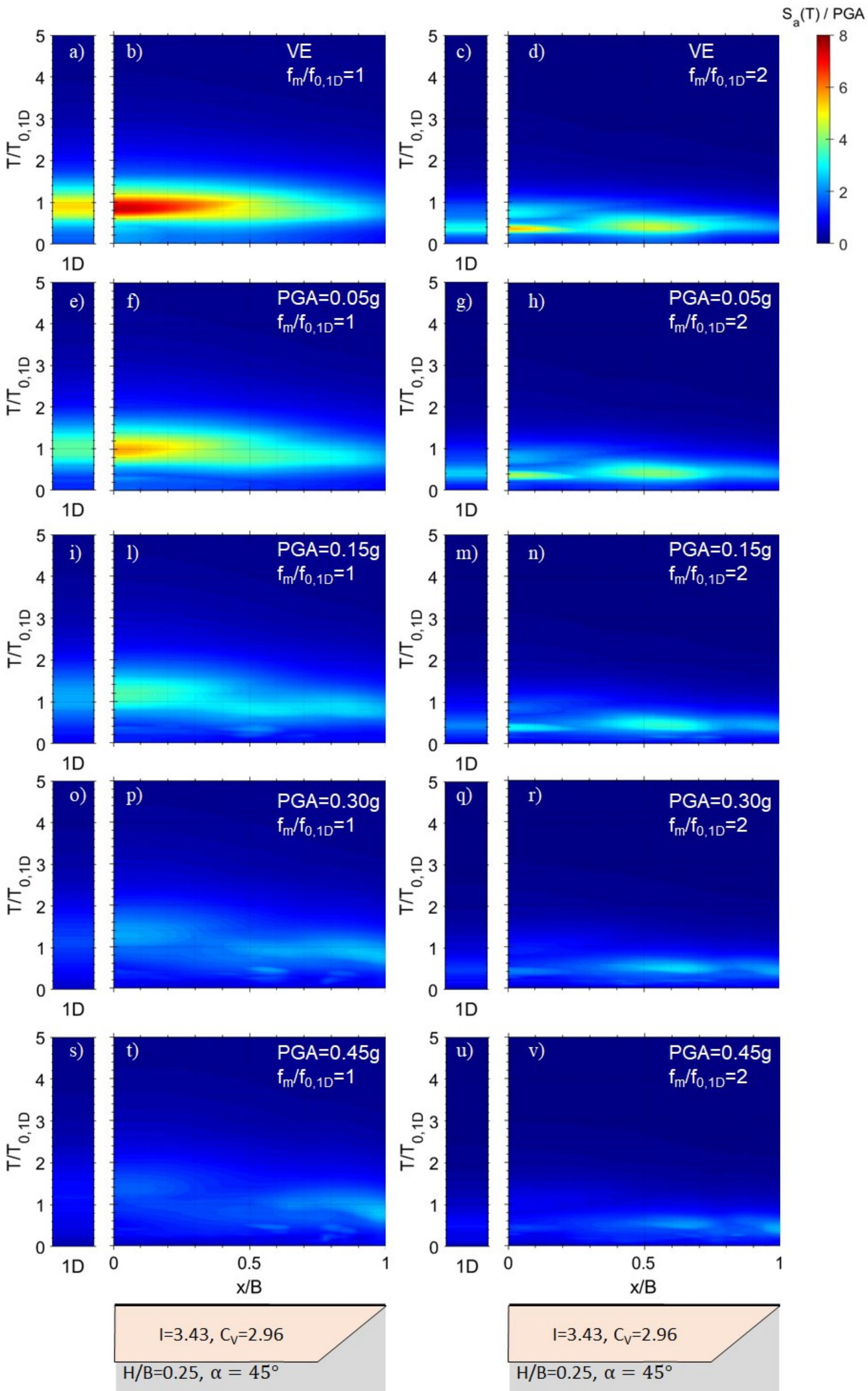

Figure IV.3.3 – 1D and 2D contour of the ratio between $S_a(T)$ and the PGA outcrop for visco-elastic (a-d) and non-linear analysis, considering Seed & Idriss (1970) curves and PGA outcrop of: e-h) 0.05g; i-n) 0.15g; o,r) 0.30g; s-v) 0.45g.

The highest spectral ordinates take place in the case of the visco-elastic analyses. When nonlinearity is taken into account, as the PGA_o increases, a decrease of the amplification can be detected from the centre to x/B equal to about 0.7-0.8 due to the increase of the damping, and an increase of the predominant period can also be observed due to the decay of the shear modulus. Such effects occur both in 1D and 2D analyses. On the other hand, at the valley edge, for x/B between 0.7-0.8 and 1, the ratio between $S_a(T)$ and PGA_o remains constant and equal to about 2.5-3, independently of the value of PGA_o. Indeed, in these areas, as previously observed (black triangles in Figure IV.3.2), the increase in deformability, due to the decay of the shear modulus, is such that the effect of the increase in damping is less significant than in the rest of the valley.

The above results are confirmed by the trend of AG_{2D} and AG_{1D} reported in Figure IV.3.4. Again, the maximum values of the amplification factor occur in the visco-elastic case and a decrease of them can be observed as the PGA_o increases. More in detail, in the area close to the valley centre ($x/B<0.2$) AG_{2D} and AG_{1D} are very similar and close to unity for $PGA_o< 0.15g$, thus $AG_{2D/1D}$ is almost constant, and close to the visco-elastic one, while for higher values of PGA_o $AG_{2D/1D}$ increases with its. For the rest of the valley ($x/B > 0.2$), it results that $AG_{2D/1D}$ increases with PGA_o moving from the centre towards the edges, while both AG_{2D} and AG_{1D} decrease.

The trends presented above for the curves of Seed & Idriss (1970) are confirmed by those obtained for Vucetic & Dobry (1991) and are therefore not shown here.

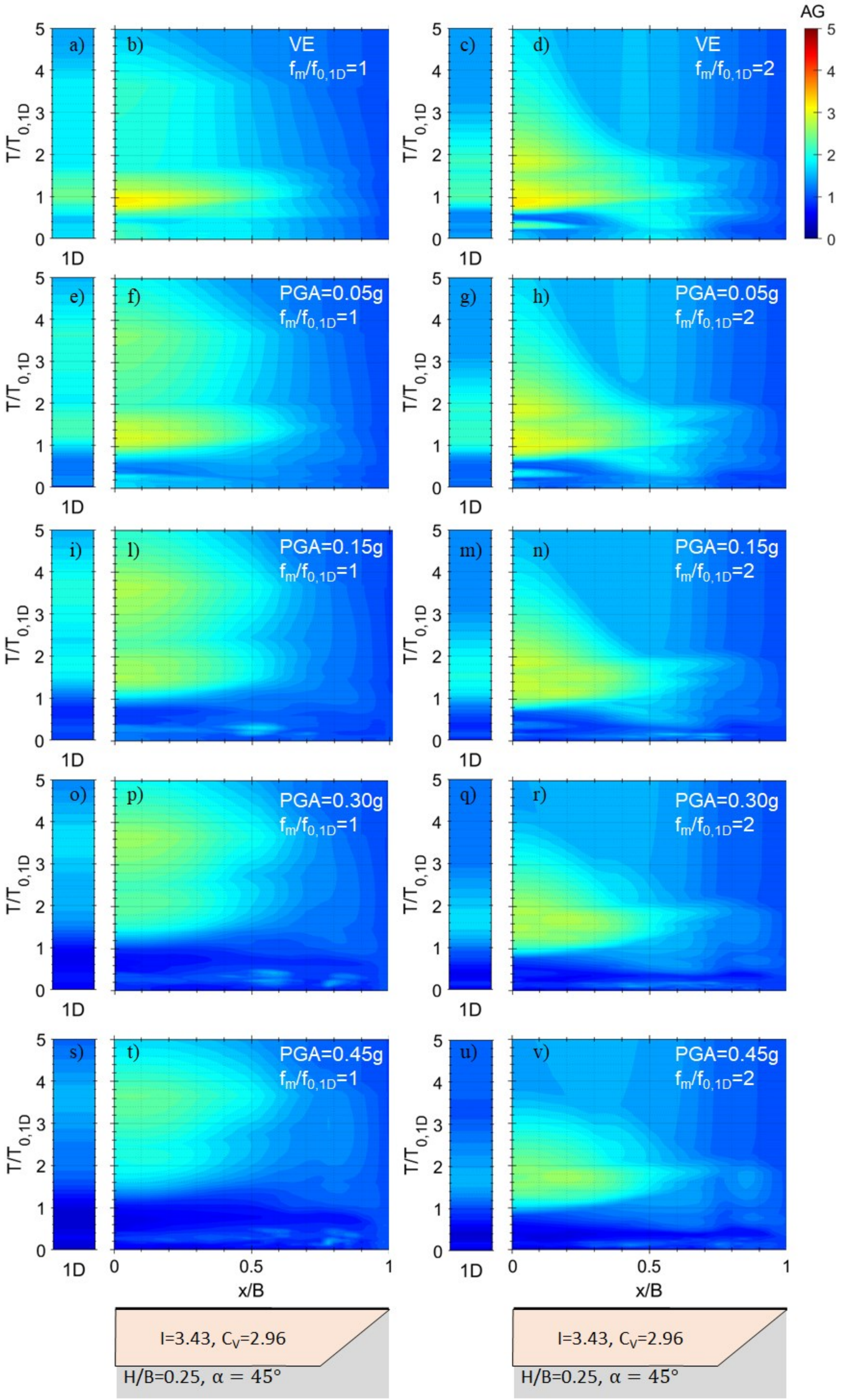

Figure IV.3.4 – 1D and 2D contour of AG for visco-elastic (a-d) and non-linear analysis, considering Seed & Idriss (1970) curves and PGA outcrop of: e-h) 0.05g; i-n) 0.15g; o,r) 0.30g; s-v) 0.45g.

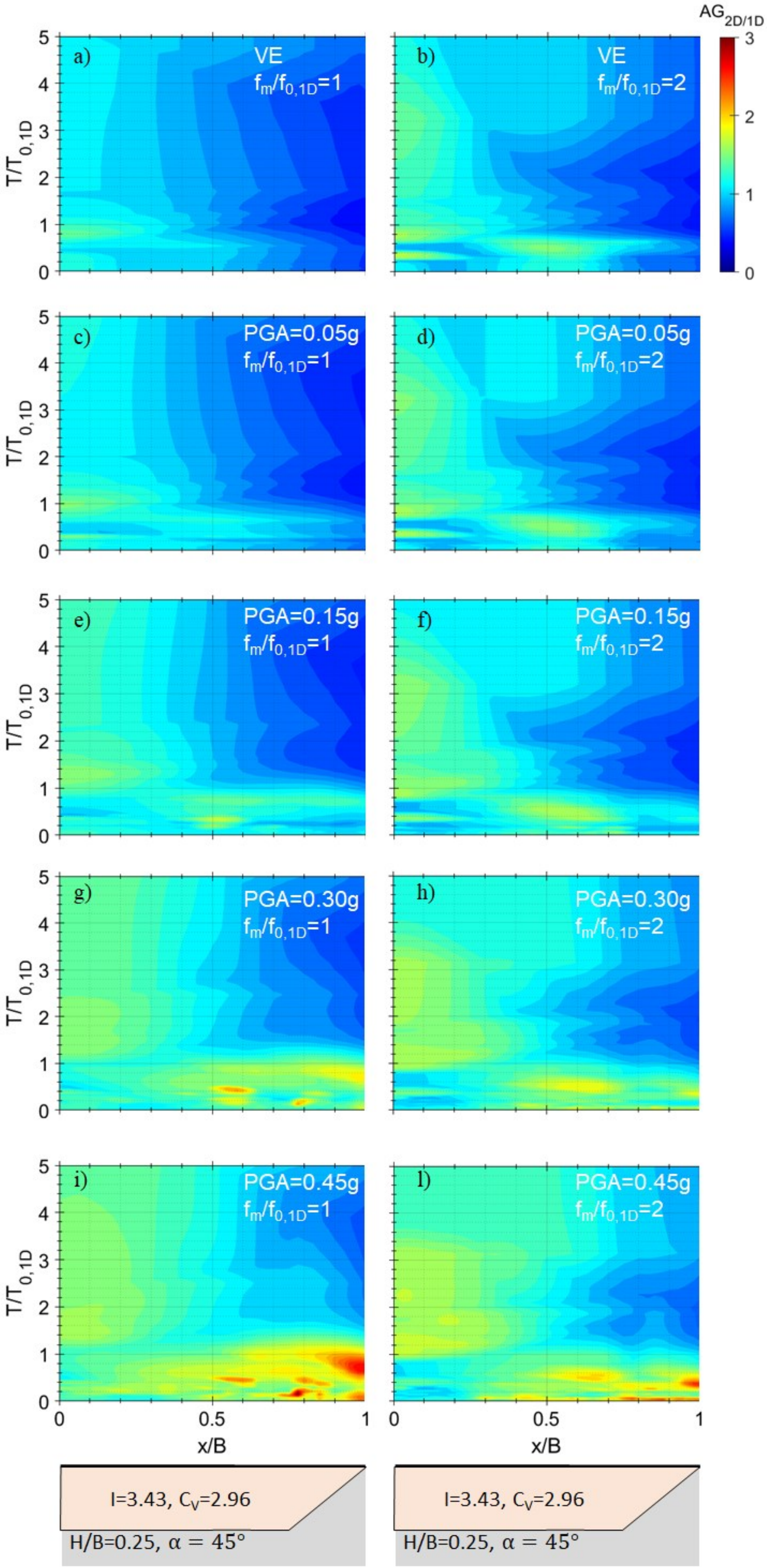

Figure IV.3.5 – 1D and 2D contour of $AG_{2D/1D}$ for visco-elastic (a-d) and non-linear analysis, considering Seed & Idriss (1970) curves and PGA outcrop of: e-h) 0.05g; i-n) 0.15g; o,r) 0.30g; s-v) 0.45g.

The analyses results have been finally synthesised in terms of VAF as shown in Figure IV.3.6a,b where the VAF, calculated using both S&I and V&D curves and applying input motions with increasing PGA_o, are compared to those computed adopting a homogeneous visco-elastic model (OM) and to those obtained by applying the proposed simplified procedure.

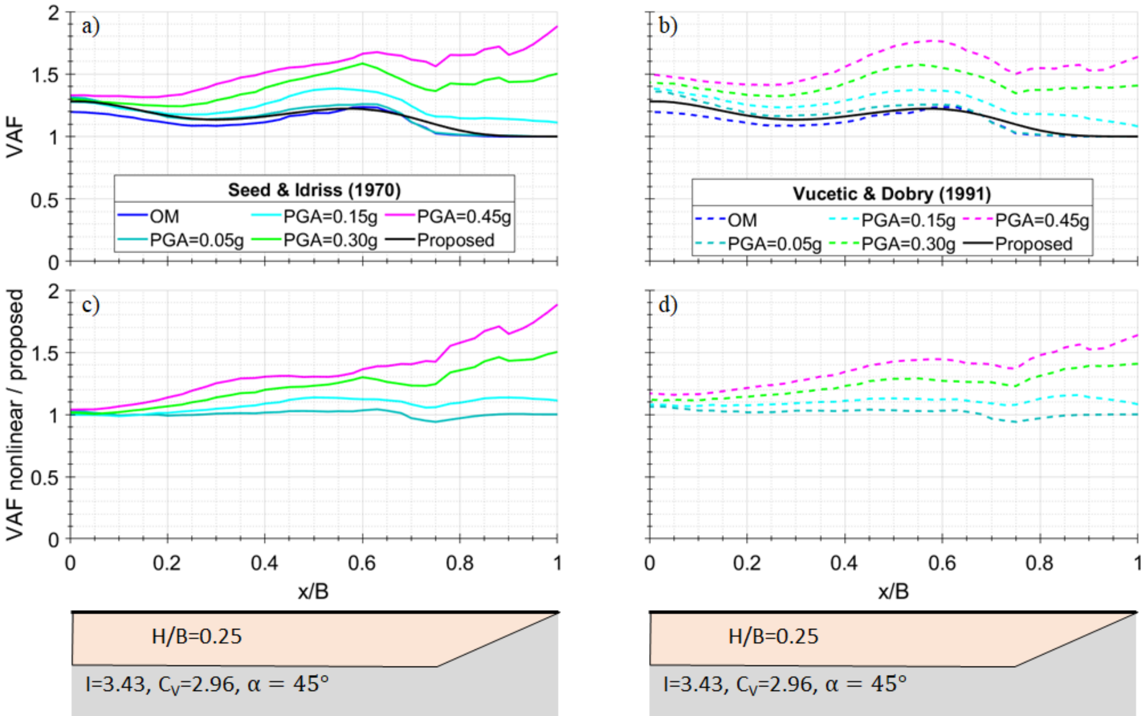

Figure IV.3.6 – Comparison between the proposed VAF and those calculated for visco-elastic (OM) and non-linear analysis for several value of the PGA outcrop with: a) Seed & Idriss (1970); b) Vucetic & Dobry (1991) curves. Comparison between the ratio between the non-linear VAF, calculated for several value of PGA outcrop, and the proposed one for: c) Seed & Idriss (1970); b) Vucetic & Dobry (1991) curves.

For PGA_o<0.15g the effects of nonlinearity are negligible as confirmed by the trends of VAFs, very close to the visco-elastic ones, and, consequently, to that obtained by the proposed procedure. On the contrary, PGA_o>0.15g, the effects of non-linearity become increasingly significant as the PGA_o increases. It is worth noting that the observed VAF trend seems to be independent on the way the nonlinearity has been modelled, since the VAF obtained adopting two different set of curves expressing the nonlinearity of soil behaviour are very close to each other. This is better highlighted in Figure IV.3.6c,d where the results are shown in terms of ratio between the non-linear VAF, obtained adopting both S&I and V&D curves, and the visco-elastic one as predicted by the proposed procedure. The ratio is always greater than unity and has an almost linear increasing trend going from the centre to the lateral border of the valley. The results obtained seems to evidence that nonlinearity starts to significantly affect the ground response at surface for PGA_o higher than 0.15g. Furthermore, non-linear effects are mainly taken into account in the 1D response, therefore nonlinear VAFs could be considered independent of the non-linear soil properties. In this way, the nonlinearity could be considered by modifying the visco-elastic VAFs with a unique relation independent of the $G(\gamma)/G_0$ and $D(\gamma)$ curves. It is worth to note that this latter is far to be a general conclusion, since it is based on the results obtained adopting limited variety of non-linear curves, even if it should be also highlighted that the curves used represent the behaviour of a strongly non-linear soil and it is expected that, for more linear soil, this effect on VAF become increasingly less significant.

IV.4 VAF accounting for non-linearity and heterogeneity

In the following, the combined effect of inhomogeneity and nonlinearity on the seismic response of the valleys is investigated. To this aim, further set of analyses has been carried out considering the same geometrical model adopted in the previous analyses, modelling the non-linear soil behaviour by using the $G(\gamma)/G_0$ and $D(\gamma)$ curves by S&I, since the previous results have shown that VAF is poorly dependent on the curves adopted to model the nonlinearity, and adopting two V_S profiles to model the soil inhomogeneity (PI=15% and Max EM).

Figure IV.4.1 shows the 1D and 2D contours of the ratio a_{max}/PGA_o and of the mobilised of $G(\gamma)/G_0$ obtained within the analysed domain, both considering a visco-elastic and the non-linear soil model, and assuming the moderate inhomogeneous Vs profile (PI=15%); the non-linear analyses have been carried out using Ricker wavelet with increasing values of the PGA_o. In the visco-elastic case the inhomogeneity of the V_S causes an increase of the maximum acceleration respect to that computed in the homogeneous case, as extensively discussed in §IV.2 (see also Figure IV.3.2a,b for comparison). Inhomogeneity causes an amplification of maximum ground acceleration, respect to the response of the homogenous case, also when the non-linearity is taken into account in the case of low to moderate input motions, $PGA_o \leq 0.15g$ (Figure IV.3.2c,d,g,h for the homogeneous case and Figure IV.4.1c,d,g,h for the inhomogeneous one). The inhomogeneity also influences the decay of the shear modulus (Figure IV.4.1e,f,i,l,o,p,s,t) which is greater than in the homogeneous case (Figure IV.3.2e,f,i,l,o,p,s,t), while in both cases it is possible to observe a triangular zone, close to the lateral border, where the maximum deformations take place, inducing the maximum decay of the shear modulus and the maximum accelerations at the surface. At the centre of the valley, as the PGA$_o$ increases, the behaviour of the valley is close to that obtained in the 1D case. This is due to the trapping of Rayleigh waves in the area close to the edges, that keep the waves from reaching the centre of the valley.

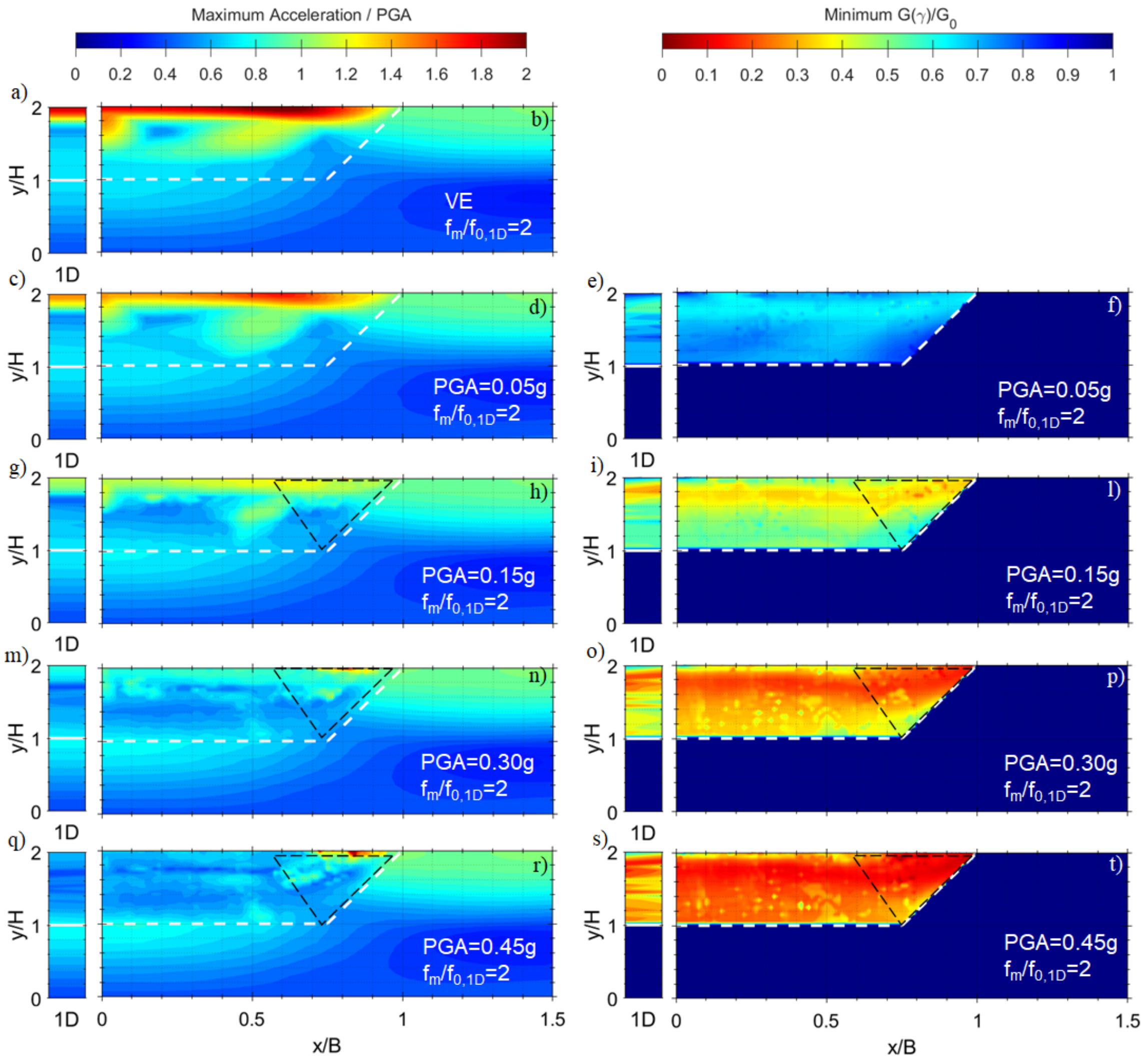

Figure IV.4.1 – 1D and 2D contour of the ratio between maximum acceleration and the PGA outcrop for visco-elastic (a,b) and non-linear analysis, considering Seed & Idriss (1970) curves, model inhomogeneous with PI=15% and PGA outcrop of: c,d) 0.05g; g,h) 0.15g; m,n) 0.30g; q,r) 0.45g. 1D and 2D contour of the ratio between the minimum G(γ) and G_0 for PGA outcrop of: e,f) 0.05g; i,l) 0.15g; o,p) 0.30g; s,t) 0.45g.

Figure IV.4.2a,b shows the VAFs obtained for both inhomogeneous models and for different values of PGA$_o$ compared with that obtained in the visco-elastic case and that calculated adopting Eq. III.5.3.

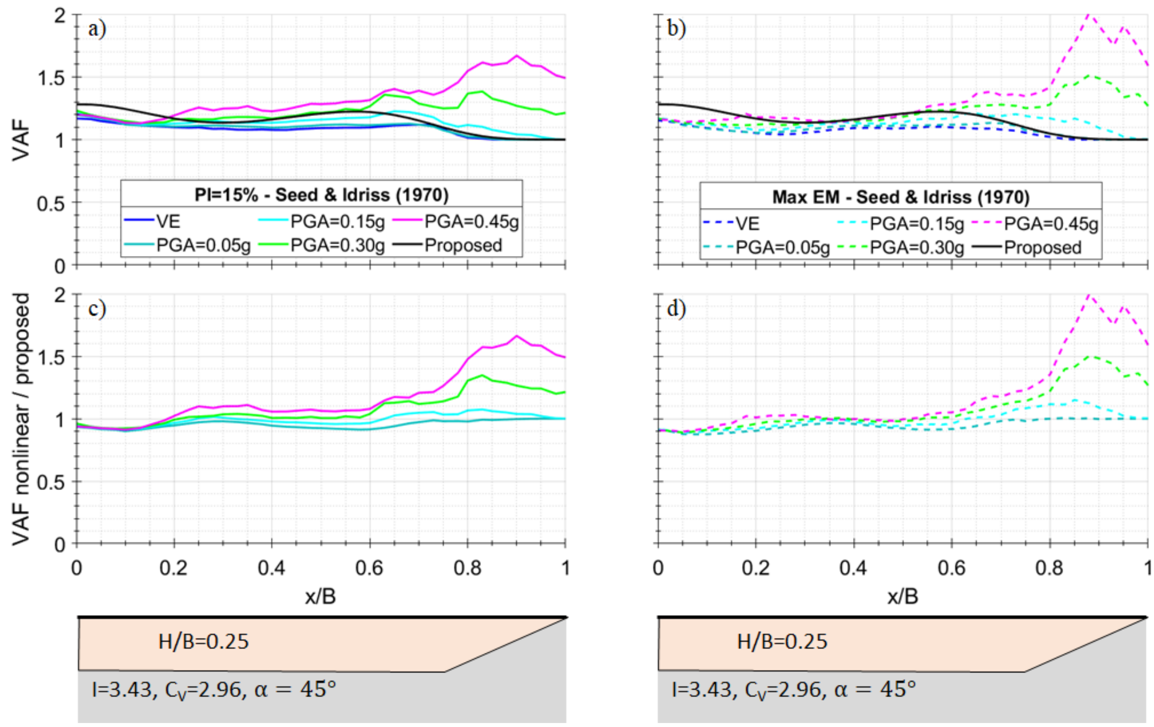

Figure IV.4.2 – Comparison between VAF obtained with the model: a) inhomogeneous with PI=15%; b) maximizing inhomogeneity (Max EM). Profile of the variation of the ratio between VAF calculated considering the inhomogeneity and nonlinearity and that of the proposed equation, for the model: c) inhomogeneous with PI=15%; d) maximizing inhomogeneity (Max EM) for several value of PGA outcrop and Seed & Idriss (1970) curves.

The combined effect of non-linearity and inhomogeneity causes a reduction of VAF both at the valley edge and at the centre, if compared to that computed on the homogeneous non-linear model (Figure IV.3.6). This reduction is due to the inhomogeneity which, as observed for the visco-elastic case (Figure IV.2.4), causes a decrease of the VAF since the 1D response at surface results amplified more than the 2D response. Therefore, it results that for most of the valley, except the lateral zone close to the edges, the VAF obtained considering nonlinearity and inhomogeneity is lower or close to that proposed by Eq. III.5.3 for $PGA_o \leq 0.3g$. Moreover, considering a $PGA_o \leq 0.15g$ it is shown that the proposed model is conservative for the whole valley. Figure IV.4.2c,d shows the ratios between the VAF calculated taking into account the inhomogeneity, nonlinearity and the proposed one.

They are for most of the valley close to unity while increase at the edges for $PGA_o \geq 0.3g$, consistently with the trends observed for the VAF.

Based on the above results a relationship is here proposed to modify the relationship proposed to compute the VAF for homogeneous visco-elastic soil deposits, and take into account for the inhomogeneity and the non-linearity of soil deposits. It is a function of PGA_o and x/B, taking into account their influence on VAF. It is reported in the following:

$$f\left(\frac{x}{B}, PGA_o\right) = \frac{VAF_{nl}}{VAF} \qquad \text{IV.4.1}$$

where VAF_{nl} is calculated considering nonlinearity and inhomogeneity and VAF is computed by Eq. III.5.3. In this way, the $f\left(\frac{x}{B}, PGA_o\right)$, expresses how the VAF computed assuming a homogeneous visco elastic model is, on average, modified when the non-linear effects are considered. $f\left(\frac{x}{B}, PGA_o\right)$ is simply the ratio of the VAFs shown in Figure IV.2.4c,d (inhomogeneous, non-linear soil model) and Figure IV.3.6c,d (homogeneous, non-linear soil model) and can therefore be approximated by a linear equation:

$$f\left(\frac{x}{B}, PGA_o\right) = a + b \cdot \frac{x}{B} \qquad \text{IV.4.2}$$

Where *a* and *b* are parameters depending on PGA_o. Figure IV.4.3 shows the values obtained for *a* and *b* for the various models analysed, homogeneous considering S&I and V&D (full and empty blue dots), inhomogeneous considering S&I for PI=15% and Max EM (red and orange dots).

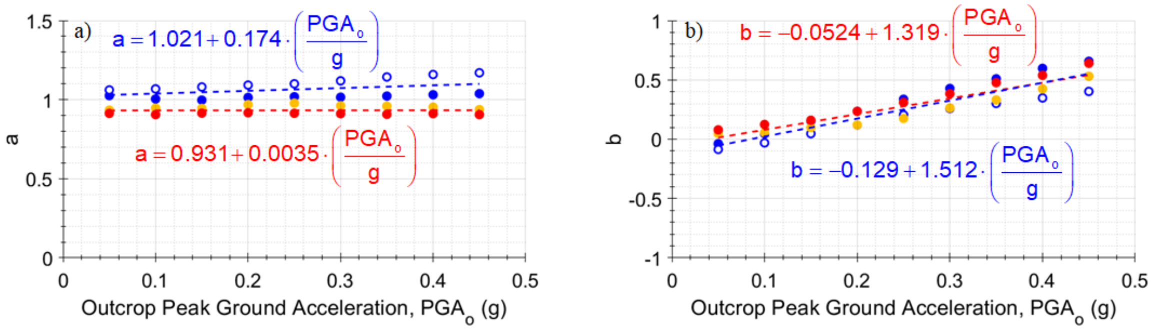

Profile of V_S	$G(\gamma)/G_0$ and $D(\gamma)$	Data	Fit
Homogeneous	S&I (1970)	●	– –
	V&D (1991)	○	
PI=15%	S&I (1970)	●	– –
Max EM		●	

Figure IV.4.3 – Variation of a and b with PGA_o

a is the value of the $f\left(\frac{x}{B}, PGA_o\right)$ at the valley centre, in the inhomogeneous case it is equal to about 0.9 and is independent of the PGA_o, also the trends are similar for the two cases analysed. *a* is constant with PGA_o and it is slightly lower than 1 because, as previously observed, the combination of the effects due to nonlinearity and inhomogeneity leads to the trapping of Rayleigh waves at the edges, hence at the valley centre the surface motion is less affected by geometric effects. Thus, the VAF is lower because the 2D amplification is closer to the 1D amplification, compared to the visco-elastic case. On the other hand, in the homogeneous case, it depends slightly on the type of decay curve used, it is equal to about 1 for low values of the PGA_o and grows linearly up to 1.1-1.2. This is because for low values of the input acceleration the non-linear effects are not very significant, and therefore the behaviour is similar to the visco-elastic case. Therefore, *a* can be expressed by as a linear function of PGA_o, distinguishing the homogeneous nonlinear case (dashed blue line in Figure IV.4.3a) from the inhomogeneous nonlinear case (red dashed line in Figure IV.4.3a). For the homogeneous model that the following relationship is obtained:

$$a = 1.021 + 0.174 \cdot \left(\frac{PGA_o}{g} \right) \qquad \text{IV.4.3}$$

while for inhomogeneous one:

$$a = 0.931 + 0.0035 \cdot \left(\frac{PGA_o}{g} \right) \qquad \text{IV.4.4}$$

The parameter *b* (Figure IV.4.3b) is the slope of $f\left(\frac{x}{B}, PGA_o\right)$ and it is independent of the model used, homogeneous or inhomogeneous, and of the decay curves of shear modulus adopted, therefore it is close to 0 for low values of PGA_o and increases with it. In other words, for low accelerations the non-linearity is not significant and VAF_{nl} is close to the visco-elastic VAF for the whole valley. As the PGA_o increases at the valley edge, a higher VAF_{nl} is observed, compared to the visco-elastic case where the VAF = 1.0. In the homogeneous case *b* is:

$$b = -0.129 + 1.512 \cdot \left(\frac{PGA_o}{g} \right) \qquad \text{IV.4.5}$$

while for inhomogeneous one:

$$b = -0.0524 + 1.319 \cdot \left(\frac{PGA_o}{g} \right) \qquad \text{IV.4.6}$$

Finally, in Figure IV.4.4, Figure IV.4.5 the comparisons between the VAFs obtained for the various models and decay curves and the one predicted by multiplying the $f\left(\frac{x}{B}, PGA_o\right)$ to the visco-elastic VAF obtained from Eq. III.5.3 are reported. In the homogeneous case (Figure IV.4.4) the comparison is very satisfactory since the VAFs obtained from the analysis are very close to those calculated using the $f\left(\frac{x}{B}, PGA_o\right)$ for both $G(\gamma)/G_0$ and $D(\gamma)$ curves.

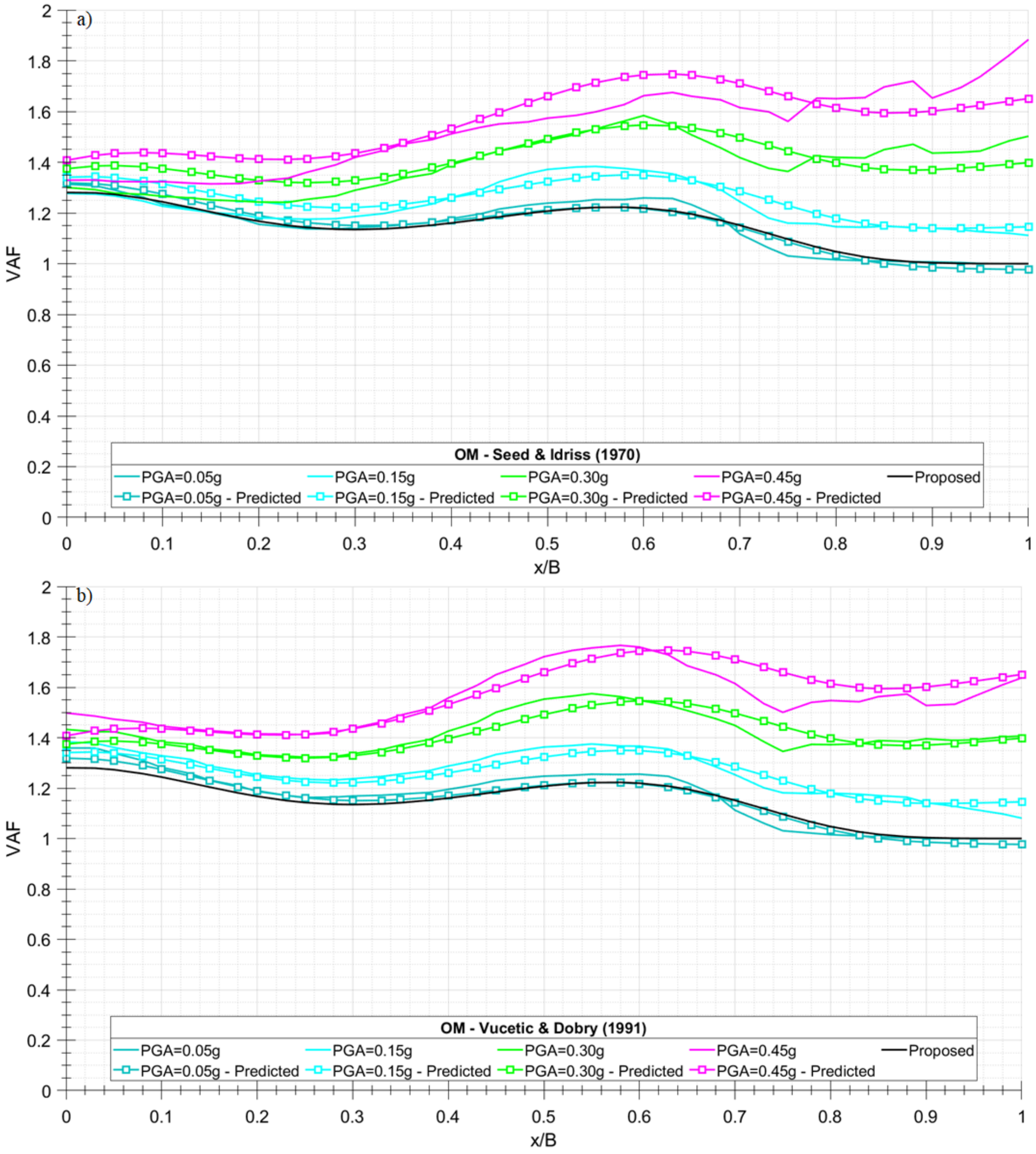

Figure IV.4.4 – Comparison between the VAF obtained with numerical analysis and those predicted with the use of f(PGA) for a homogeneous model and: a) Seed & Idriss (1970); b) Vucetic & Dobry (1991) curves

The proposed procedure slightly overestimates the VAF in the area close to the valley centre when the nonlinearity is modelled adopting the S&I curves and the input PGA_o is higher than 0.30g. This is due to the way the parameter *a* (dashed line in Figure

IV.4.3a) is obtained. As a matter of fact, it is defined considering the VAF computed adopting two different set of curves to model nonlinearity, therefore for high values of PGA_o, it overestimates the amplification for S&I (full blue points in Figure IV.4.3a) and underestimates it for V&I (empty blue points in Figure IV.4.3a).

In the case where nonlinearity and inhomogeneity are considered (Figure IV.4.5) the predicted VAF is close to that obtained numerically, for PI=15% and $PGA_o \leq 0.30g$ and for Max EM for $PGA_o \leq 0.15g$, while for higher acceleration values it overestimates the amplification in the central area and underestimates it at the edges. This discrepancy between the VAF computed by the predictive simplified procedure and the one computed by 2D numerical analyses is due to the linear relationship chosen to express $f\left(\frac{x}{B}, PGA_o\right)$, which for high values of PGA_o catches the trend properly for $x/B \leq 0.8$ while for the area close to the edges it does not. To improve the prediction, a Gaussian interpolating function could be used to better approximate the bell shape that $f\left(\frac{x}{B}, PGA_o\right)$ shows at the edges (Figure IV.4.2c,d). However, this has not been done because the aim of the present chapter is only to overview what are the effects of nonlinearity and inhomogeneity, and how they can be considered in a simplified way using the results obtained in Chapter III for visco-elastic homogeneous valleys. In the future, the results obtained could be extended by using a larger number of $G(\gamma)/G_0$ and $D(\gamma)$ curves, inhomogeneity profiles, impedance ratios and geometries.

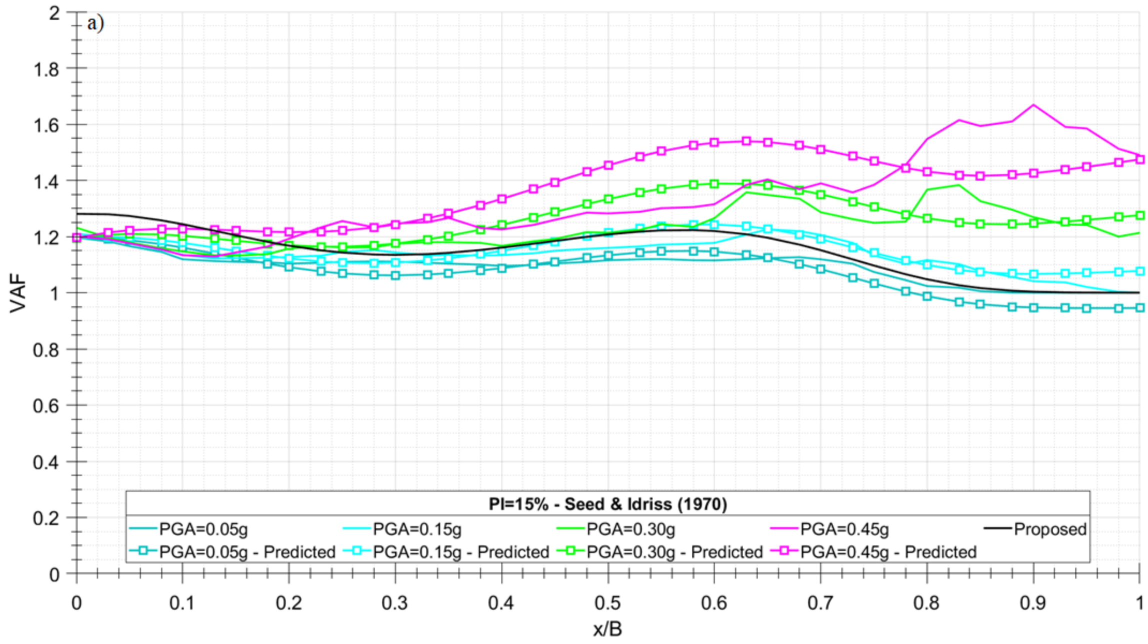

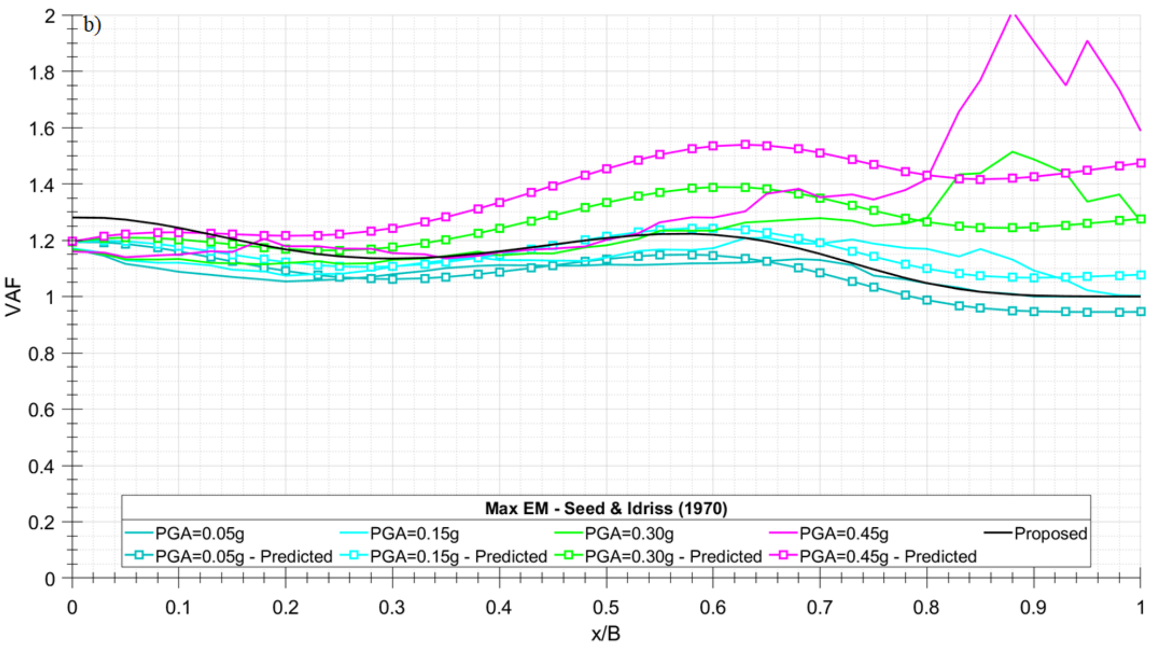

Figure IV.4.5 – Comparison between the VAF obtained with numerical analysis and those predicted with the use of f(PGA) using the model: a) inhomogeneous with PI=15%; b) maximizing inhomogeneity (Max EM) and Seed & Idriss (1970) curves.

V. APPLICATION TO CASE STUDIES

In this Chapter, simplified evaluations of the valley amplification factor, VAF, will be applied to study the seismic response of some real valleys of Central Italy. Firstly, the simplified procedure proposed in this study will be described; thereafter, the case study of Visso will be considered as a validation test site, being there possible to compare the results obtained from numerical analysis with the seismic motion recorded at the centre of the valley. Finally, the three small villages of Montefranco, Pretare and Piedilama, severely hit by the Central Italy earthquake in 2016 will be considered as verification case studies for comparing the results of the simplified procedure against those of two-dimensional seismic response analyses.

V.1 The proposed procedure

When evaluating site effects for the seismic assessment of ordinary civil structures, national technical standards of practice (e.g., NTC 2018) typically specify to modify shape and amplitude of reference response spectra defined for a rock outcrop through stratigraphic and topographic amplification coefficients. Stratigraphic coefficients are expressed as a more or less decreasing function of the outcrop peak ground acceleration, PGA_o, depending on the subsoil class, while topographic coefficients depend on the slope inclination and on the position along it. When the stratigraphic or geometric conditions do not allow the use of simplified coefficients, the codes usually prescribe to carry out a specific seismic response analysis.

The VAF defined in this study is a synthetic measure of the average amplification of the 2D spectral ordinates with respect to those pertaining to a 1D soil column representative of the valley centre. Thus, it can be adopted to account for valley effects following two alternative procedures, reported in Table V.1.1 and Figure V.1.1. Namely, the 1D response can be either predicted with specific site response analyses, SRA, or by applying the simplified approach suggested by the technical standards.

In other words, the 2D elastic response spectrum at surface, $S_{a,s}(T)$, can be calculated at any point along the valley profile by multiplying the VAF, as obtained using the equations or charts proposed in this study, by the spectrum representative of the 1D response at valley centre. This latter can be either computed through specific seismic response analyses (Approach 1 or Standard) or estimated using the stratigraphic coefficients suggested by the code (Approach 2 or Simplified).

Both proposed procedures rely on two fundamental hypotheses, which might appear over-simplified but were analysed and discussed in detail.

Table V.1.1 – Proposed procedure

Standard Approach:	Simplified Approach
1. 1D seismic response analysis for a soil column with properties and geometry similar to that of the valley centre, to calculate the 1D response spectrum at the surface, $S_{a,1D}(T)$; 2. Calculation of VAF with the equations or the charts provided in this study. In the latter case only the shape ratio of the valley and the impedance ratio are required to be estimated, while in the former case also the slope of the valley edges; 3. Definition of the surface elastic response spectrum, $S_{a,s}(T)$, as obtained by considering both stratigraphic and valley effects	1. Definition of the reference PGA_o and response spectrum, $S_{a,r}(T)$, from the national hazard map, as expected at a flat rock outcrop (subsoil class A, V_S>800m/s), for a given return period. 2. Measurement of the equivalent shear wave velocity of the site, $V_{S,H}$, for the definition of the subsoil class in accordance with the national building code. 3. Calculation of the nonlinear stratigraphic amplification factor, S_S, as a function of PGA_o defined for each subsoil class. 4. Computation of the 1D response spectrum, $S_{a,1D}$, as the product of S_S by $S_{a,r}(T)$. 5. Calculation of VAF through the equations or the charts. In the latter case, only the shape ratio of the valley and the impedance ratio need to be estimated, while in the former case also the slope of the valley edges should be known. 6. Definition of the surface elastic response spectrum, $S_{a,s}(T)$, as obtained by considering both stratigraphic and valley effects.

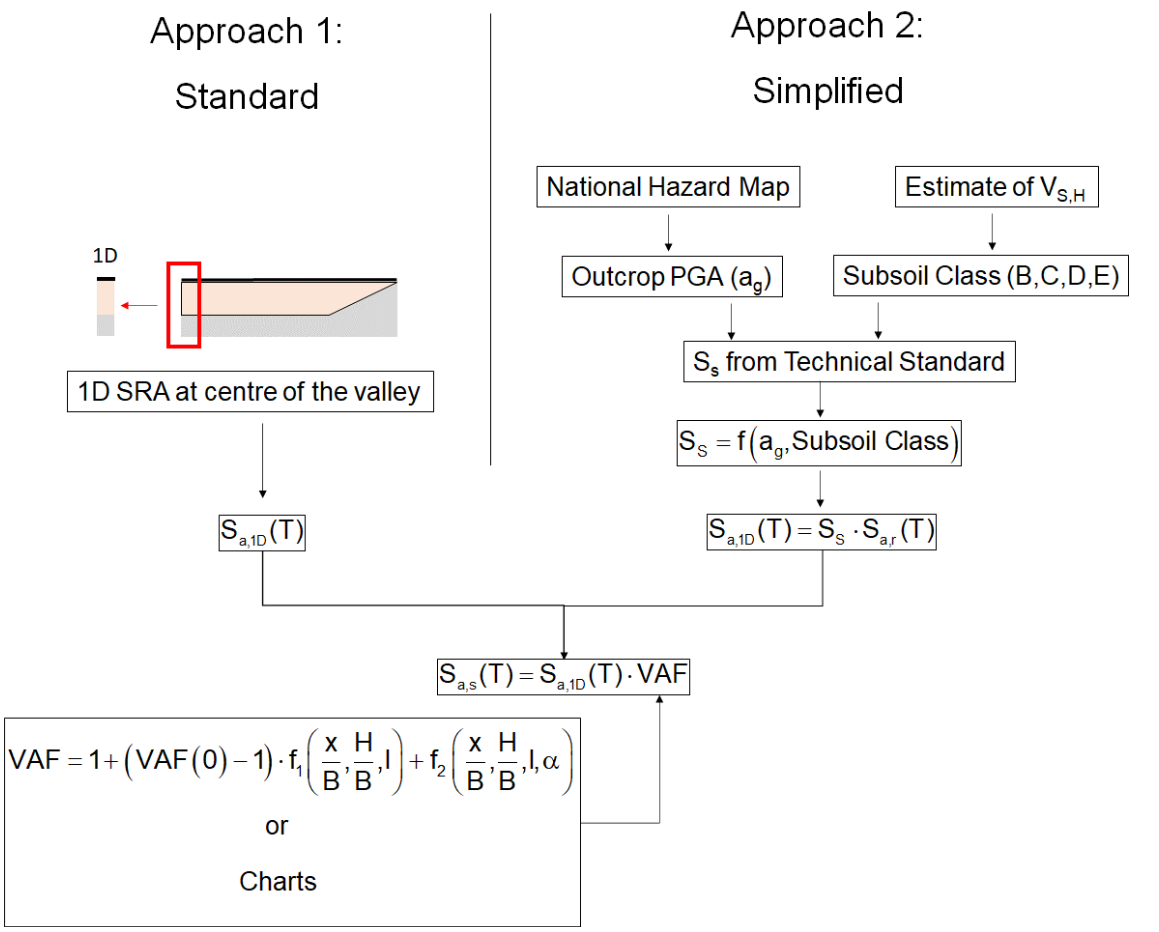

Figure V.1.1 – Flow chart of the proposed procedure.

Firstly, the proposed VAF was computed by assuming a homogeneous visco-elastic soil with V_S constant with depth. This assumption can appear as over-simplified in the case of layered soil deposits subjected to strong-motion earthquakes, hence the VAF should be in principle modified to take into account inhomogeneity and non-linearity, as discussed the results obtained in Chapter IV evidenced that both factors mainly influence the 1D response in such a way that the coupling between stratigraphic and geometric effects plays a secondary role. Therefore, in both approaches above suggested, it is considered reasonable to use the VAF by assuming that the main effects of non-linearity and inhomogeneity are already considered in the 1D analysis.

Furthermore, the VAF was defined as the mean amplification of the 2D spectral ordinates with respect to the 1D condition, averaging its dependence on frequency, hence on the structural period. Indeed, as analysed in Chapter III, the amplification of the spectral ordinates due to geometric effects varies with the period, especially close to the 2D resonance frequency.

In the formulation of the equations and charts defining VAF, the influence of the frequency content of the reference seismic motion was not taken into account, although the ratio between dominant wavelengths and the dimension of the basin is expected to affect 2D amplification. Indeed, this approach is consistent with that proposed by the national technical code to account for stratigraphic and topographic effects. As above recalled, following the code specifications the reference elastic response spectrum can be modified by means of:

- the stratigraphic amplification factor, S_S, that uniformly increases the spectral ordinates accounting for non-linear soil behaviour, while the coefficient C_c enlarges the spectral shape extending the range of periods characterised by the maximum spectral acceleration proportionally to soil deformability;
- the topographic amplification coefficient, S_T, which uniformly increases the spectral ordinates in proportion to the slope angle (i.e. the shape factor characterising the topographic irregularity), thus assuming that the geometric effects are independent of frequency. This hypothesis was also adopted in the approach proposed herein, being the valley amplification factor independent of frequency and increasing the spectral ordinates in an uniform way.

V.2 Validation on the test site of Visso

Visso (MC) is a small Italian village located in the southern part of the Umbria-Marche Apennines. The settlement is placed almost completely on an alluvial valley created from the confluence of the Nera and the Ussita rivers. The topographical features of the valley are shown by the plan and the perspective views in Figure V.2.1a,b,c. The geolithological map reported in Figure V.2.2a shows that the alluvial soils mainly consist of gravels, covered and locally interbedded by fine-grained lenses, covering a limestone bedrock (Lemmi et al., 2017). The buried geometry of the valley is reported in the sections AA' and BB' (Figure V.2.2b,c), which show that the valley assumes a roughly trapezoidal shape along NW-SE direction, while it is almost wedge-shaped along SW-NE.

Visso is located in a highly seismically hazardous area, that underwent numerous destructive events over the centuries. As a matter of fact, the town has been significantly affected by the seismic sequence that, since 2016, has occurred in Central Italy, with several earthquakes of moment magnitude, M_w, between 5 and 6.5. Figure V.2.3 shows the map elaborated by the Italian National Institute of Geophysics and Volcanology (INGV) with the localization of all the events with magnitude higher than 2.5 from 1985 to 18/10/2021. It should be noted that the seismic activity has not been interrupted and it is still ongoing at the time of writing this dissertation. Given the high number of strong earthquakes, the subsoil of Visso has been extensively investigated over the years. In 2017, a Grade 3 seismic microzonation study (Lemmi et al., 2017) has been carried out, which collected and made accessible all the data available from the geological, geophysical and geotechnical surveys carried out (https://sisma2016data.it/microzonazione/).

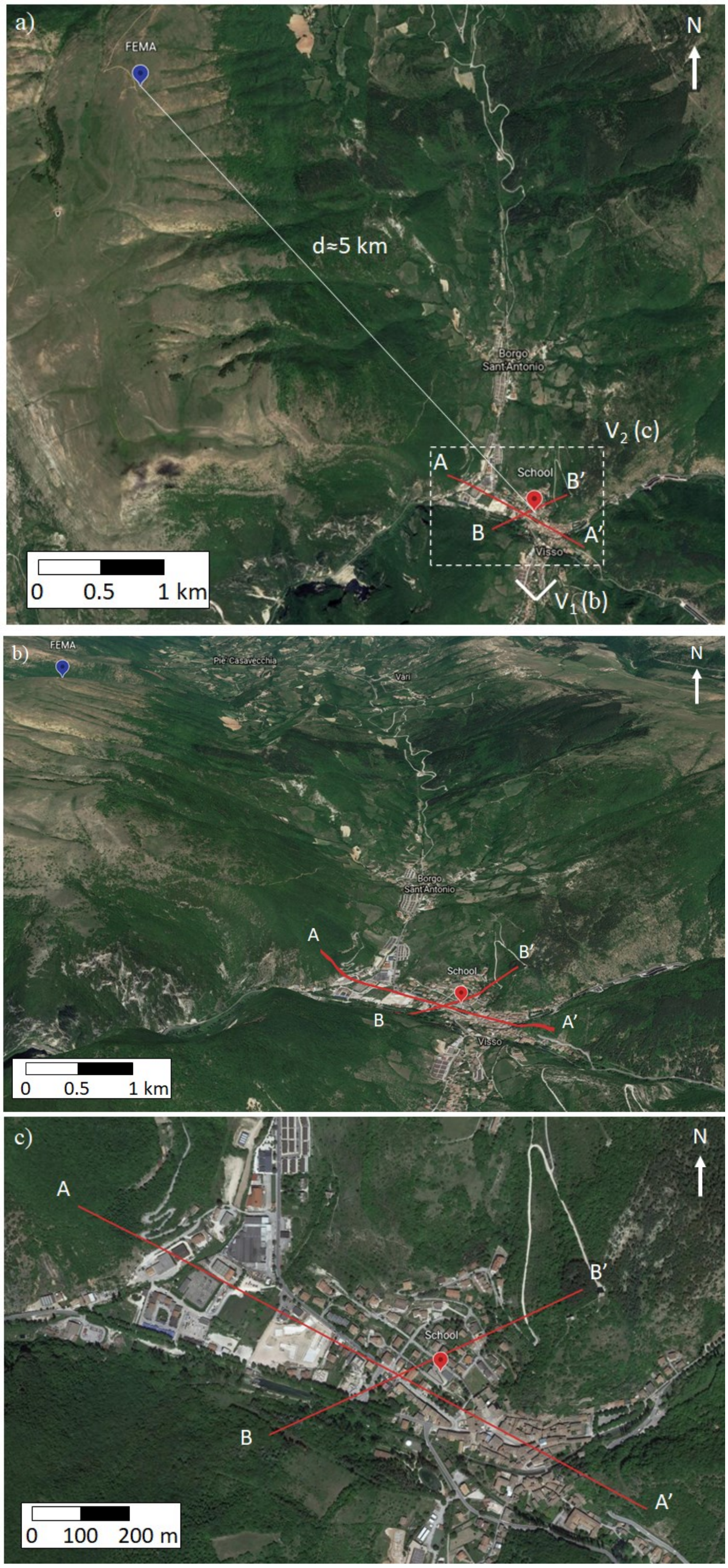

Figure V.2.1 – a) Plan view of Visso; b) V_1; c) V_2 (modified from Google Earth, https://earth.google.com/)

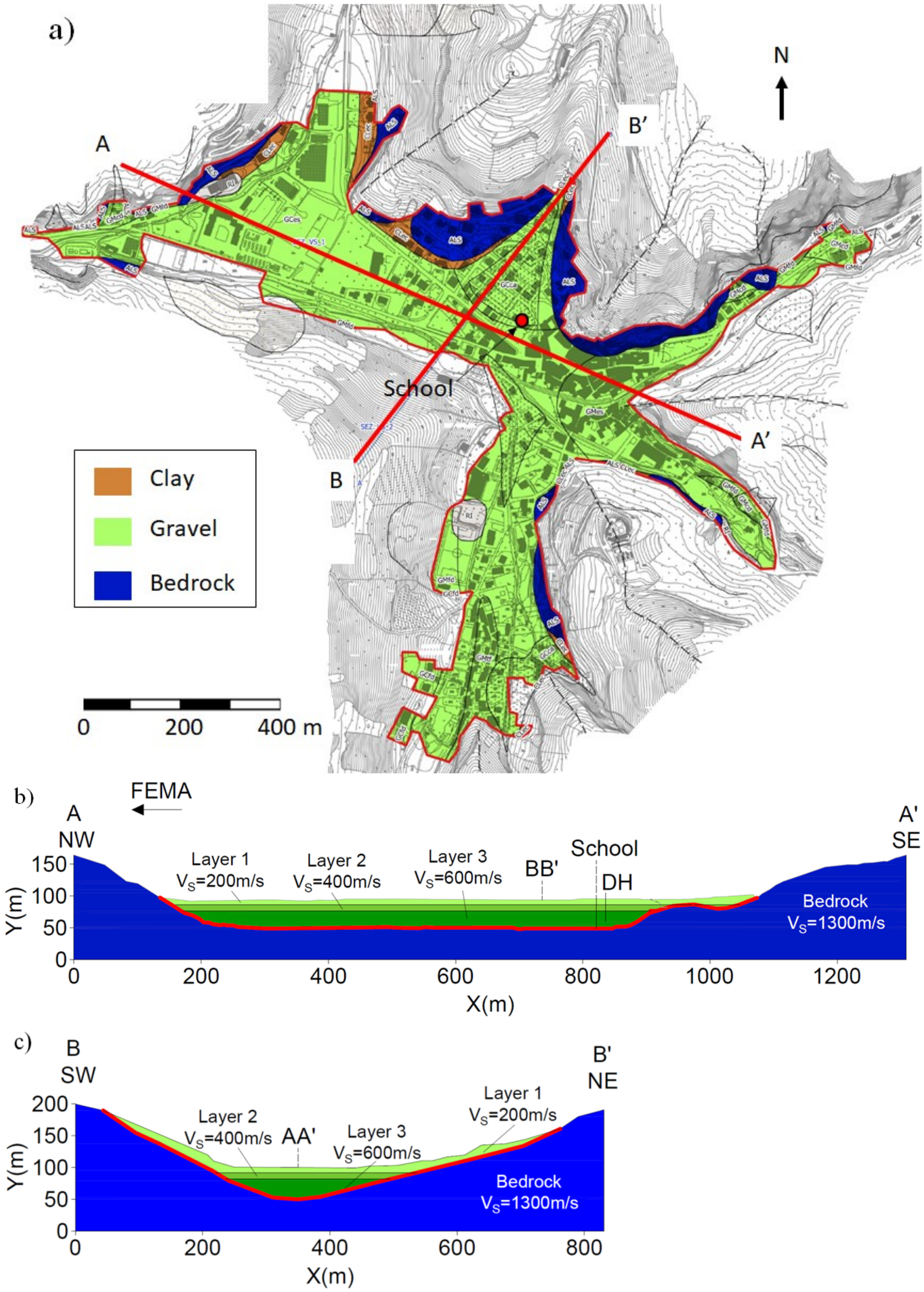

Figure V.2.2 – a) Geolithological map; b) section AA' and c) section BB' of Visso valley (modified from Lemmi et al., 2017*).*

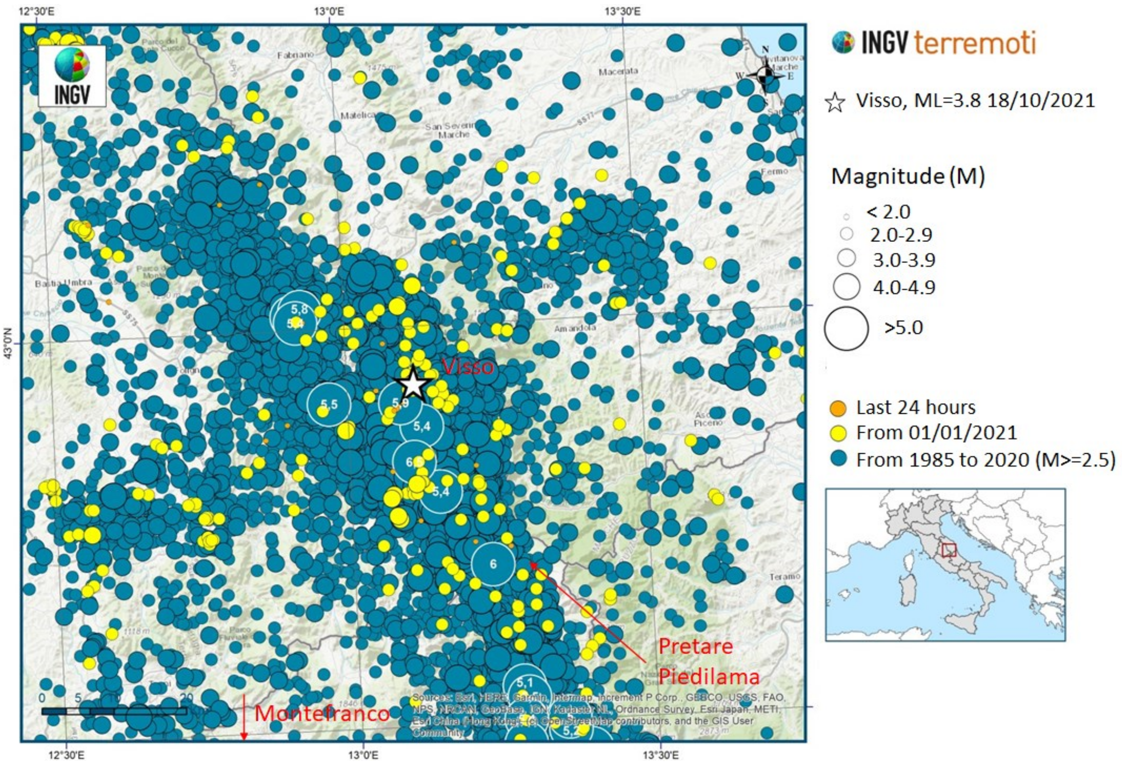

Figure V.2.3 – Seismicity since 1985 of the studied area (modified from Istituto Nazionale di Geofisica e Vulcanologia, https://ingvterremoti.com/2021/10/18/evento-sismico-mw-3-7-in-provincia-di-macerata-18-ottobre-2021, last access 27/12/2021).

Moreover, the *Osservatorio Sismico delle Strutture*, OSS, of the Italian Civil Protection Department placed several accelerometers (Dolce et al., 2017), both on the structure and at the foundations of the Pietro Capuzi school, located close to the valley centre, near to the intersection between sections BB' and AA'. The accelerometer stations recorded different events and allowed to compare the observed school damage with that simulated with numerical analyses accounting for soil-structure interaction (Brunelli et al., 2019, 2021). In the present study, the records will be used to validate the subsoil model obtained by processing all the available data and for the seismic response analyses of the two sections.

The black dots and line in Figure V.2.4 show the profile of the V_S measured with the DH test carried out close to the school, while the red line represents that used for the numerical analysis. The cover deposits can be divided into three layers with V_S increasing with depth. A shallow fine-grained layer with a thickness of 8m and V_S=200m/s overlies a 10m thick coarse-grained layer with V_S=400m/s, covering a 22m succession of coarse and fine soils with a mean V_S=600m/s, which lies on a bedrock characterised by V_S=1300m/s. The bedrock velocity and depth were not measured by the DH test, but were inferred on the basis of surface geophysical tests reported in the microzonation study. The layered soil profile has been extended horizontally to the whole valley, as shown by the sections in Figure V.2.2b,c, where the green colour intensity increases with V_S and the interface between the bedrock and the alluvial soils is highlighted with a red line.

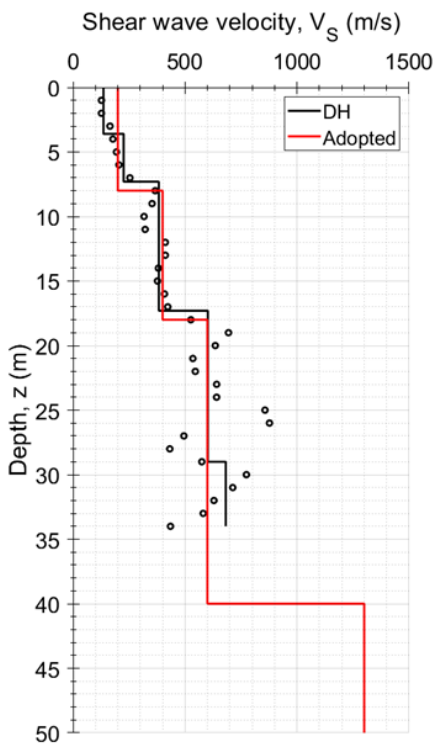

Figure V.2.4 – Profile of V_S measured with DH test (black line and dots) and adopted in the numerical analysis (red line).

The non-linear and dissipative soil behaviour has been modelled following Brunelli et al. (2021). The G(γ)/G_0 and D(γ) curves have been assigned to the first fine-grained layer (Figure V.2.5a) through the relations developed by Ciancimino et al. (2019) for Central Italy soils, by considering a PI=17%. For the following layers (Figure V.2.5b,c), the relationships suggested by Liao et al. (2013) for gravelly soils have been used, by considering a confining pressure of 52kPa and 207kPa, respectively, in order to reproduce the dependence of the nonlinear behaviour on the stress state.

Figure V.2.5a,b,c shows the above mentioned literature curves describing the decay of the normalised modulus and the increase of the damping ratio with the shear strain (in black) compared with the sigmoidal functions implemented in FLAC (in green). As already noted in Chapter IV, the combined use of sigmoidal functions and Masing criteria adopted in FLAC tends to overestimate the damping at high strains, while the shear modulus decay is satisfactorily approximated. A comparison among the 3 couples of curves is shown in Figure V.2.5d: it can be noted that the hysteretic soil model assigned to the shallowest fine soil cover presents a more extended linear behaviour with respect to the underlying gravels; on the other hand, for the deeper coarse-grained layers, the increasing confining pressure causes an increase in the linear threshold with depth.

Table V.2.1 summarises the geotechnical model used in the analyses for the Visso valleys.

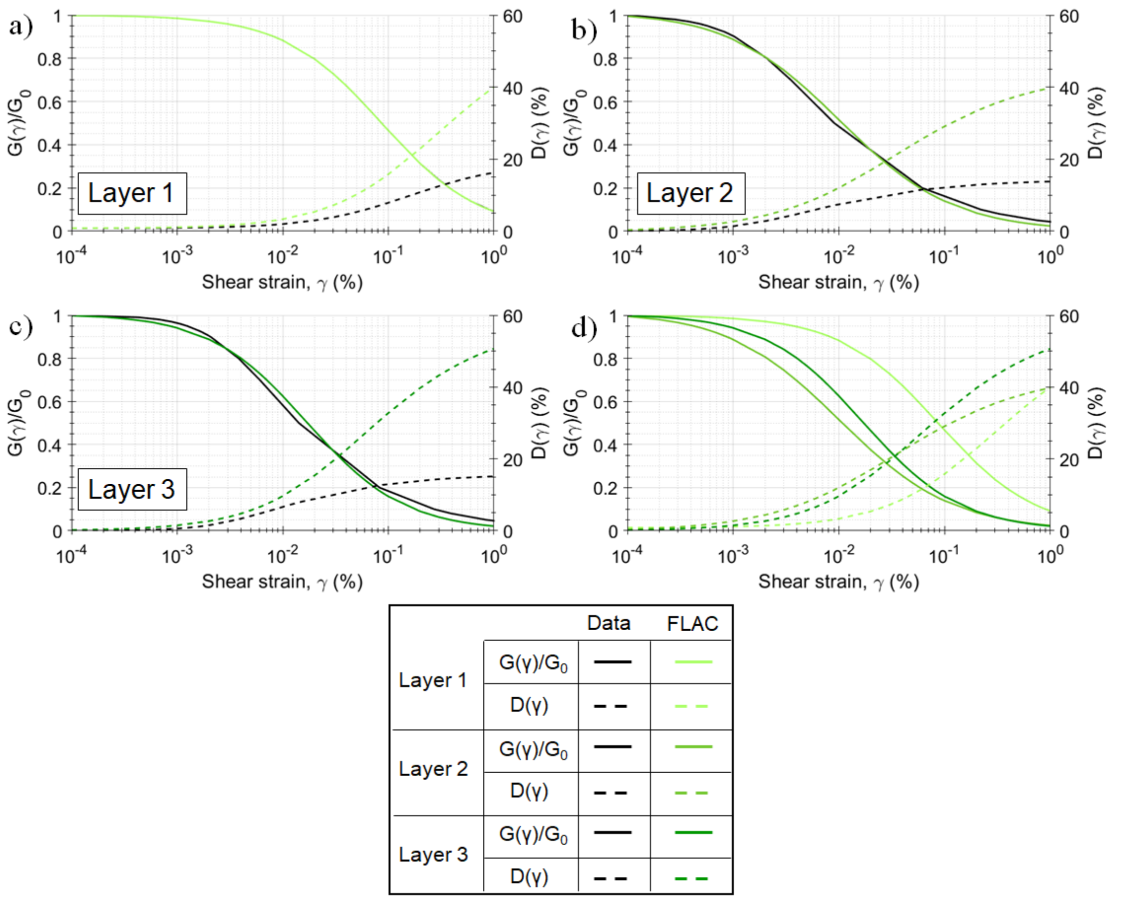

Figure V.2.5 – G(γ)/G₀ and D(γ) curves used in the numerical analysis (modified from Brunelli et al., 2021*).*

Table V.2.1 – Geometrical and mechanical properties of Visso soils

	Thickness h_i (m)	Unit weight γ (kN/m^3)	Shear wave velocity V_S (m/s)	Poisson ratio ν	Initial damping D_0 (%)	$G(\gamma)/G_0$ and $D(\gamma)$ curves
Layer 1	8	20	200	0.4	0.8	Brunelli et al. (2021)
Layer 2	10	21	400	0.3	1.4	
Layer 3	22	21	600	0.3	1.4	
Bedrock	-	22	1300	0.3	0.5	Visco-elastic

During the seismic sequence in 2016-2017 an accelerometric station (FEMA) installed by INGV (D'Amico et al., 2020) was located about 5 km from the city centre, on a rock outcrop. One more station had been installed by OSS at the foundation level of the school building. Figure V.2.1a shows the location of both the FEMA and the school stations. Both recorded several events at the same time and, therefore, they have been used to validate the subsoil model adopted in the numerical analyses. The M_W 6.0 event occurred on 24/08/2016 has first been considered, with an epicentre located at Accumoli, at a distance of about 30 km from Visso. The NS and EW recordings obtained at FEMA have been projected along the directions of sections AA' and BB' and adopted as input motions in the analyses.

One-dimensional seismic response analyses have been first carried out along the soil column below the school, accounting for the non-linear and dissipative soil behaviour. Figure V.2.6 shows the comparisons between the accelerograms, Fourier spectra and response spectra calculated at surface (blue lines) and those recorded by the FEMA station (black lines) and at the school foundation level (red lines).

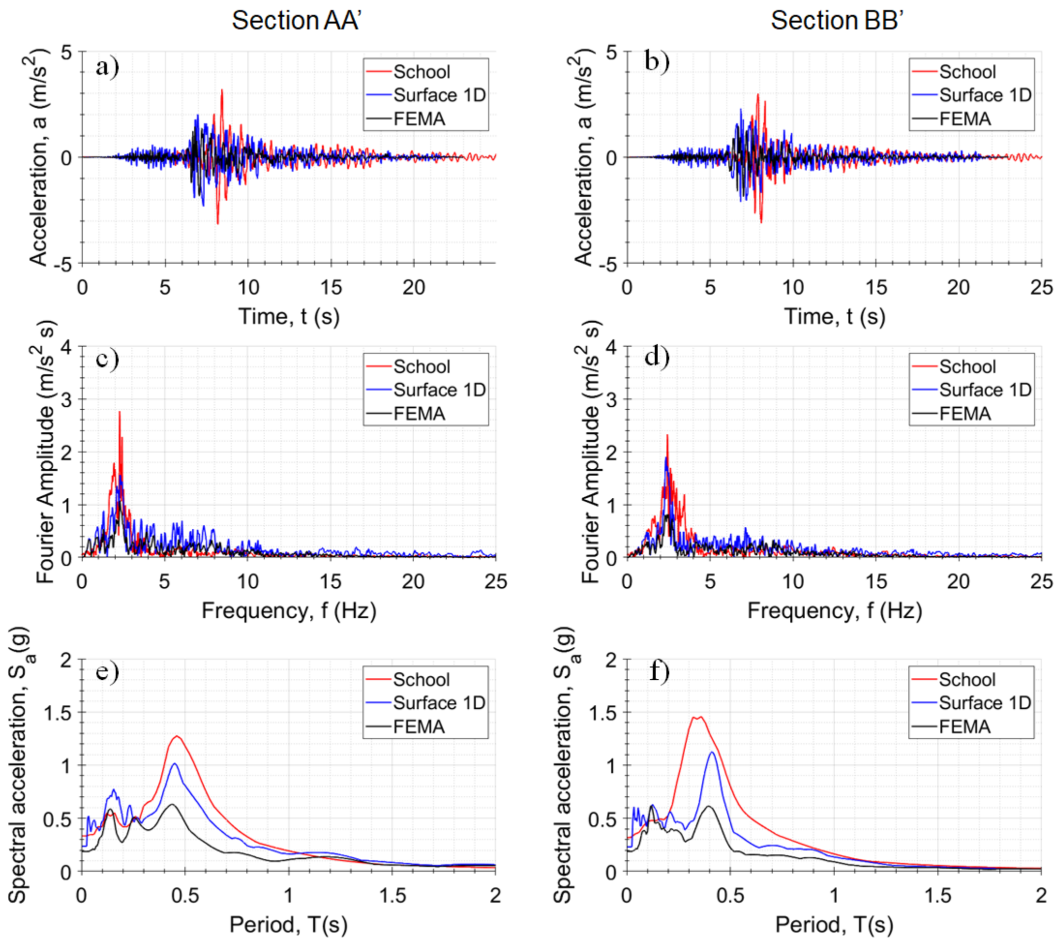

Figure V.2.6 – Comparison between the: a,b) accelerograms, c,d) Fourier; e,f) response spectra calculated with 1D analysis and recorded at FEMA and School stations.

The time history of the acceleration (Figure V.2.6a.b), as computed considering only the 1D propagation, does not adequately reproduce the accelerogram recorded at the school, for both directions. On the other hand, both the response and Fourier spectra show a frequency content quite close to that of the motion recorded at surface, even if its overall amplitude is underestimated by the 1D analysis.

Therefore, 2D seismic response analyses have been carried out for the sections AA' and BB' in Figure V.2.2b,c, by applying the signals recorded at FEMA station projected along the respective directions. Figure V.2.7 shows the comparison between the accelerograms, Fourier spectra and response spectra calculated with the analyses at the school and those recorded by the school and FEMA stations.

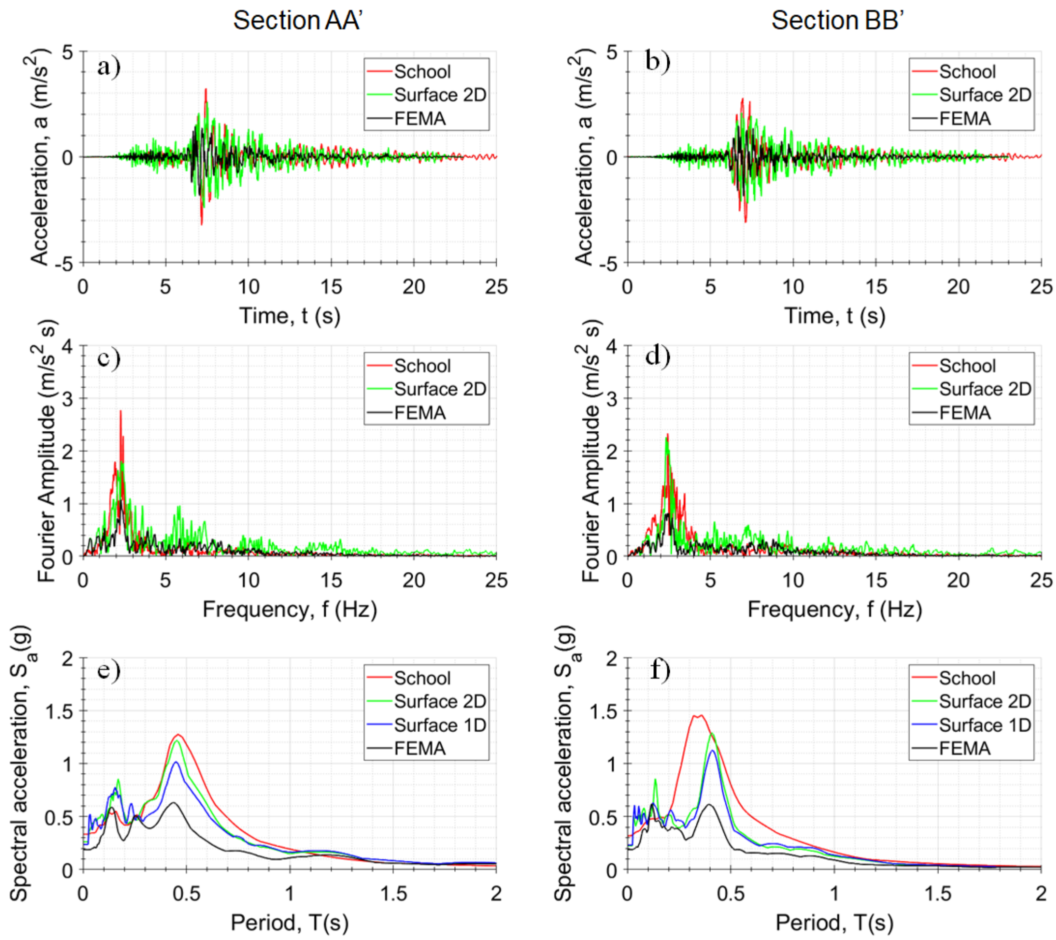

Figure V.2.7 – Comparison between the: a,b) accelerograms, c,d) Fourier; e,f) response spectra calculated with 2D analysis and recorded at FEMA and School stations.

As far as the accelerograms are considered, there is a fairly good agreement between the simulated motions and those recorded at the school, for both directions. However, the records show slightly higher PGA, while the frequency content is similar (Figure V.2.7c,d). The 2D response spectra (Figure V.2.7e,f) show peaks for slightly shorter periods and with little higher amplitudes with respect to the 1D analyses. For section AA', it can be observed that the 2D spectrum is practically coincident with that recorded at the school station, while for section BB' it is found that the simulation underestimates the ground motion. This could be explained reminding that the hysteretic model implemented in FLAC overestimates the damping at high strain levels; furthermore, the BB' section does not cross the school, thus the geometry of the valley under the school could be significantly different. As a matter of fact, looking to the geolithological map in Figure V.2.2a, it can be observed that the valley section BB' is larger than that crossing the school. Since the thickness of the valley is almost constant, a smaller width leads to a higher shape ratio, hence to a greater amplification of the ground motion.

As a result, taking into account the results obtained for section AA' and the observations made for section BB', the model proposed is considered to be enough accurate.

The charts proposed in this study (Figure V.2.8a-f) were also used to estimate the amplification along the two valley sections, shown in Figure V.2.8g,h along with the approximated trapezoidal geometries considered to evaluate the VAF. A homogeneous visco-elastic model has been assumed for the alluvial soil, with $V_{S,eq}$=470m/s and γ=20kN/m^3, while for the bedrock V_S=1300m/s and γ=22kN/m^3

have been used; therefore the impedance ratio is about 3. The valley section AA' has a width of about 410m, while BB' is about 180m wide; the thickness is 40m for both sections, and therefore the shape ratio H/B is equal to 0.1 and 0.22, respectively.

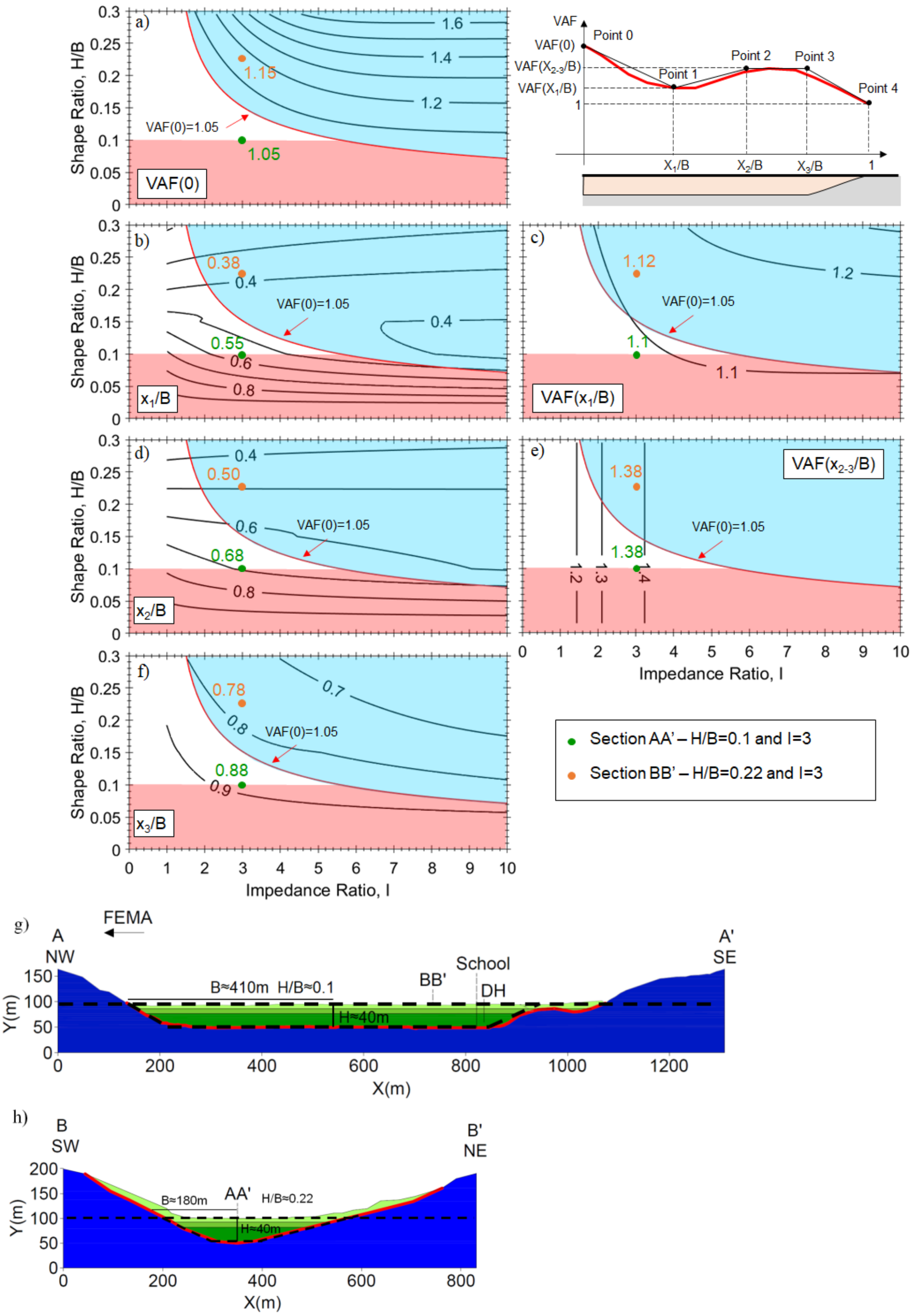

Figure V.2.8 – a-f) Proposed charts to estimate VAF; g,h) schematic valley considered to calculate the VAF (dashed black lines).

It follows that section AA' (green dots in the charts in Figure V.2.8a-f) falls at the edge of the zone of the 'very shallow' valleys, while BB' section (orange dots in Figure V.2.8a-f) is entirely within the zone of the 'moderately shallow' valleys. Thus, for the former it is expected that in the centre of the valley the behaviour is predominantly 1D, with 2D amplification concentrated in the area close to the edges, while for the latter the VAF is significant both at the centre and at the edges of the valley.

V.2.1 Prediction of the seismic response under code-conforming input motions

The set of reference seismic motions used for predictive seismic response analyses is composed of 7 accelerograms chosen using Rexel v3.5 (Iervolino et al., 2010), in a way that their mean spectrum is compatible with that provided by the Italian building code (NTC 2018) for subsoil class A and horizontal ground surface. Table V.2.2 shows the main properties of the selected signals, while Figure V.2.9a shows the comparison between the response spectra of the seven individual accelerograms, their mean spectrum and that specified by NTC 2018 for class A. In Figure V.2.9b, the same spectra are shown but with the periods scaled with respect to $T_{0,1D}$ (equal to 0.34s) computed as the inverse of $f_{0,1D}$ defined by Eq. IV.2.1 considering $V_{S,eq}$=470m/s and H=40m. Note how the higher spectral ordinates are mostly located for periods below $T_{0,1D}$, so that significant 2D effects are expected.

Table V.2.2 – Main features of the 7 accelerograms used for Visso

Earthquake	Date	M_w	Epicentral Distance (km)	Station	Site class	Component
Cazulas	24/06/1984	4.9	24	Presa de Beznar	A	N-S
Bingol	01/05/2003	6.3	14	Bingol	A	E-W
Lazio Abruzzo	07/05/1984	5.9	22	Ponte Corvo	A	N-S
Campano Lucano	23/11/1980	6.9	25	Auletta	A	N-S
Lazio Abruzzo	07/05/1984	5.9	22	Ponte Corvo	A	E-W
Friuli	06/05/1976	6.5	23	Tolmezzo	A	N-S
Campano Lucano	23/11/1980	6.9	25	Auletta	A	E-W
	Mean	6.2	22			

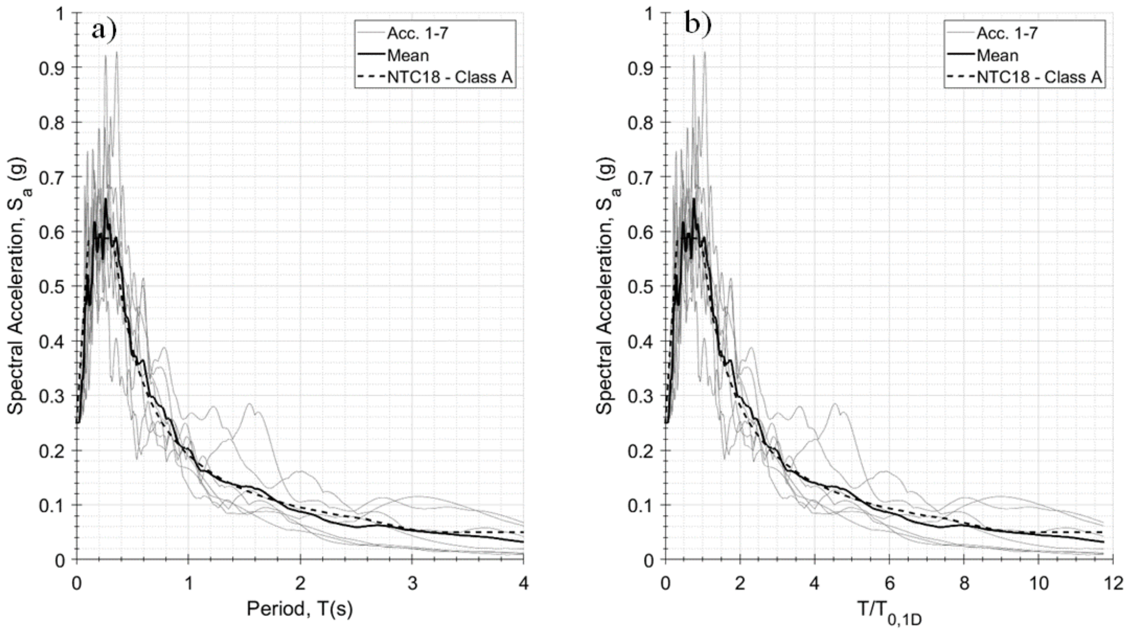

Figure V.2.9 – Comparison between the response spectra of the 7 individual accelerograms considered, the mean spectrum and that specified by NTC 2018.

Both visco-elastic and non-linear analyses have been carried out to compare the VAFs obtained with the two different models. At first, the results obtained for section AA' and then those of BB' are examined in terms of response spectra and VAF.

Figure V.2.10a,d shows the response spectra obtained at the centre of the valley of section AA', considering both the visco-elastic and non-linear behaviour of the soils, compared with the average spectrum of the 7 input motions and the NTC 2018 spectra for subsoil classes A and B. Furthermore, in Figure V.2.10b,e the same comparisons are reported considering, instead, the results obtained from 1D analyses for the soil column at the valley centre. Finally, in Figure V.2.10c,f the 1D and 2D mean spectra are compared to the average spectrum at bedrock and that adopted by the national building code, NTC 2018. In general, in the visco elastic case, the ground motion is strongly amplified considering both 1D and 2D analyses, while in the non-linear case the mean surface spectra are very close to those specified by NTC 2018 for class B. In addition, both in the visco-elastic and in the non-linear analysis, the 1D and 2D spectra are very close each other, confirming what estimated through the charts: the valley of section AA' belongs to the zone of very shallow valleys and therefore the 2D motion at the surface of the valley centre is similar to that computed by 1D analysis.

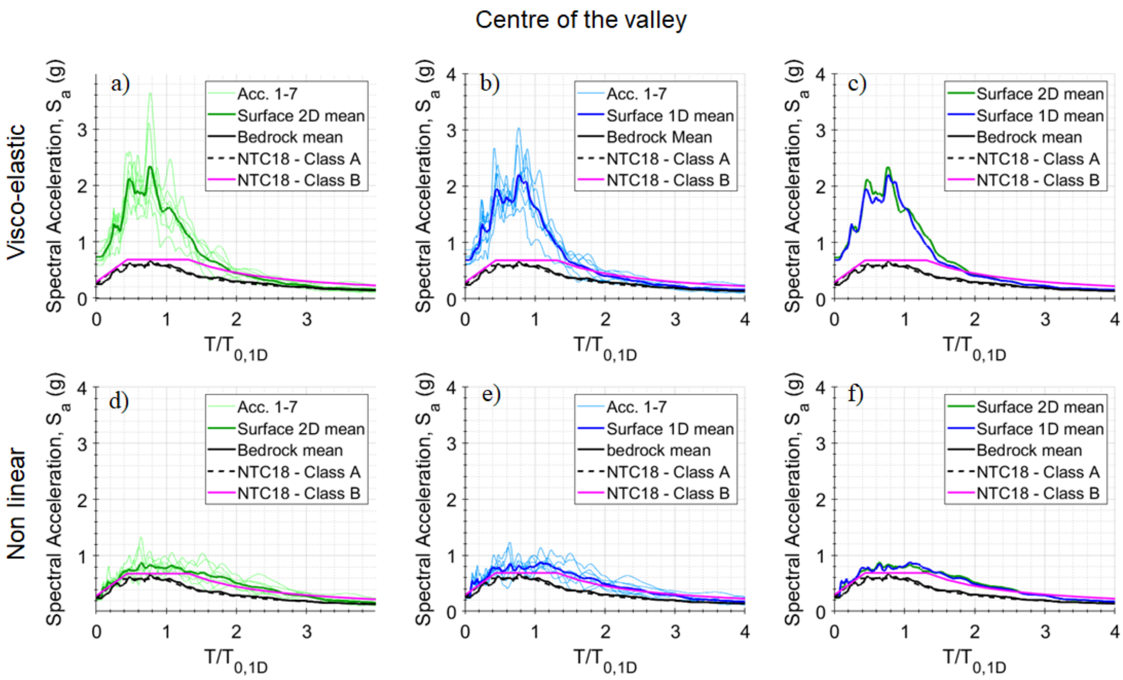

Figure V.2.10 – 1D and 2D response spectra calculated at the centre of the valley of section AA’

Figure V.2.11 shows the same comparisons of Figure V.2.10 but for the vertical in correspondence of the school. Figure V.2.8g shows that the building is located close to the valley edge, indeed the 2D mean spectrum is higher than the 1D one, both in the visco-elastic and in the non-linear analyses; furthermore, the maximum differences occur for periods shorter than $T_{0,1D}$.

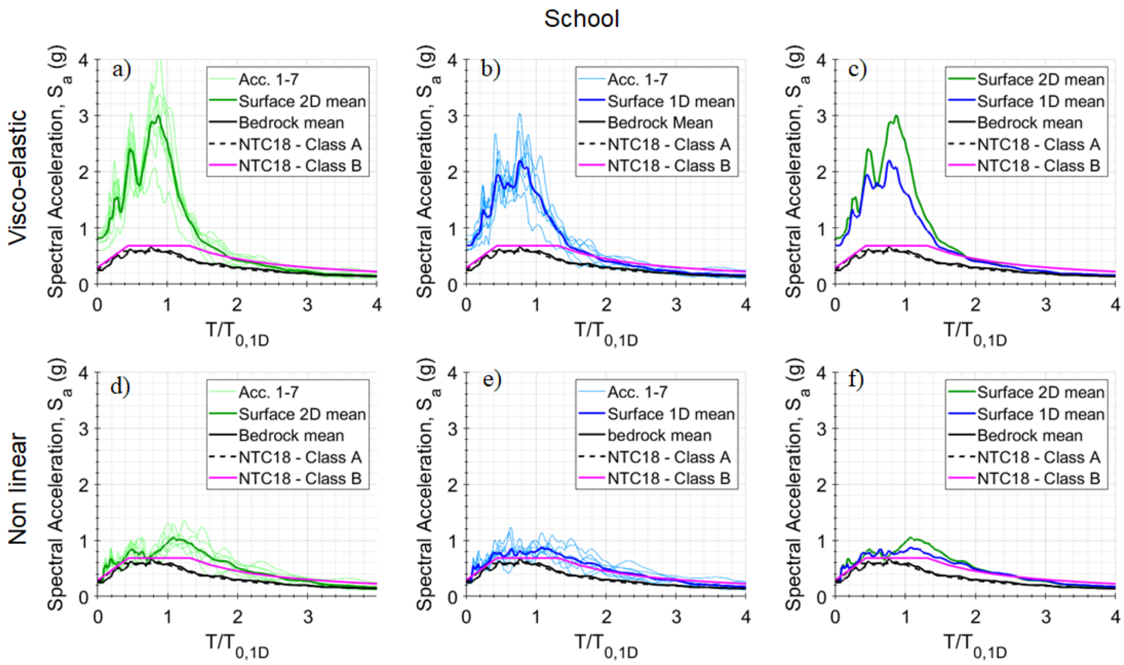

Figure V.2.11 – 1D and 2D response spectra calculated at the school for the section AA'

Figure V.2.12 shows the same comparisons, but for a site closer to the edges, with x/B=0.8. Even in this case, the 2D mean spectral accelerations are higher than those computed by 1D analysis.

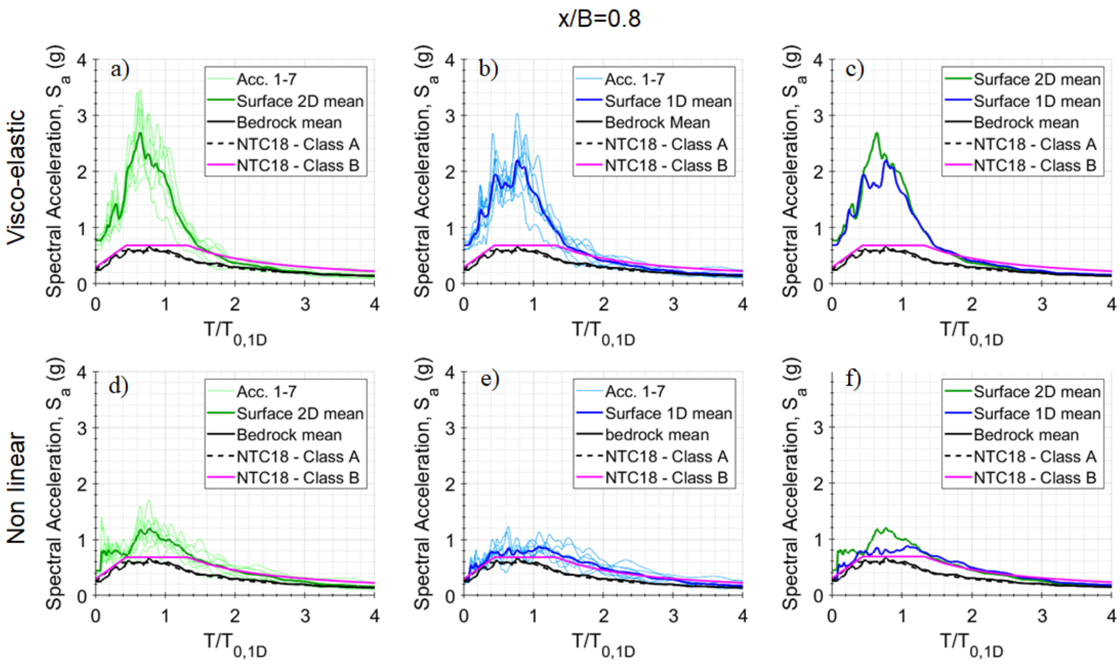

Figure V.2.12 – 1D and 2D response spectra calculated at x/B=0.8 for the section AA'

The analysed numerical results confirm what predicted by the proposed charts, namely: given the geometry and the impedance ratio of the AA' section, the ground motion response at surface is characterised by a significant influence of 2D effects at the valley borders, while it is definitely 1D at the centre.

To verify the effectiveness of the proposed simplified procedure, the VAF based on the numerical results have been compared to the values analytically computed by applying the procedures outlined in §V.1. Figure V.2.13a shows the comparison between the VAF calculated by the visco-elastic analyses for the 7 individual input motions and the mean profile, while Figure V.2.13b shows the comparison among the mean, maximum and minimum values (black continuous and dashed lines), that calculated with Eq. III.5.3 (red line) and the value obtained using the charts (green line).

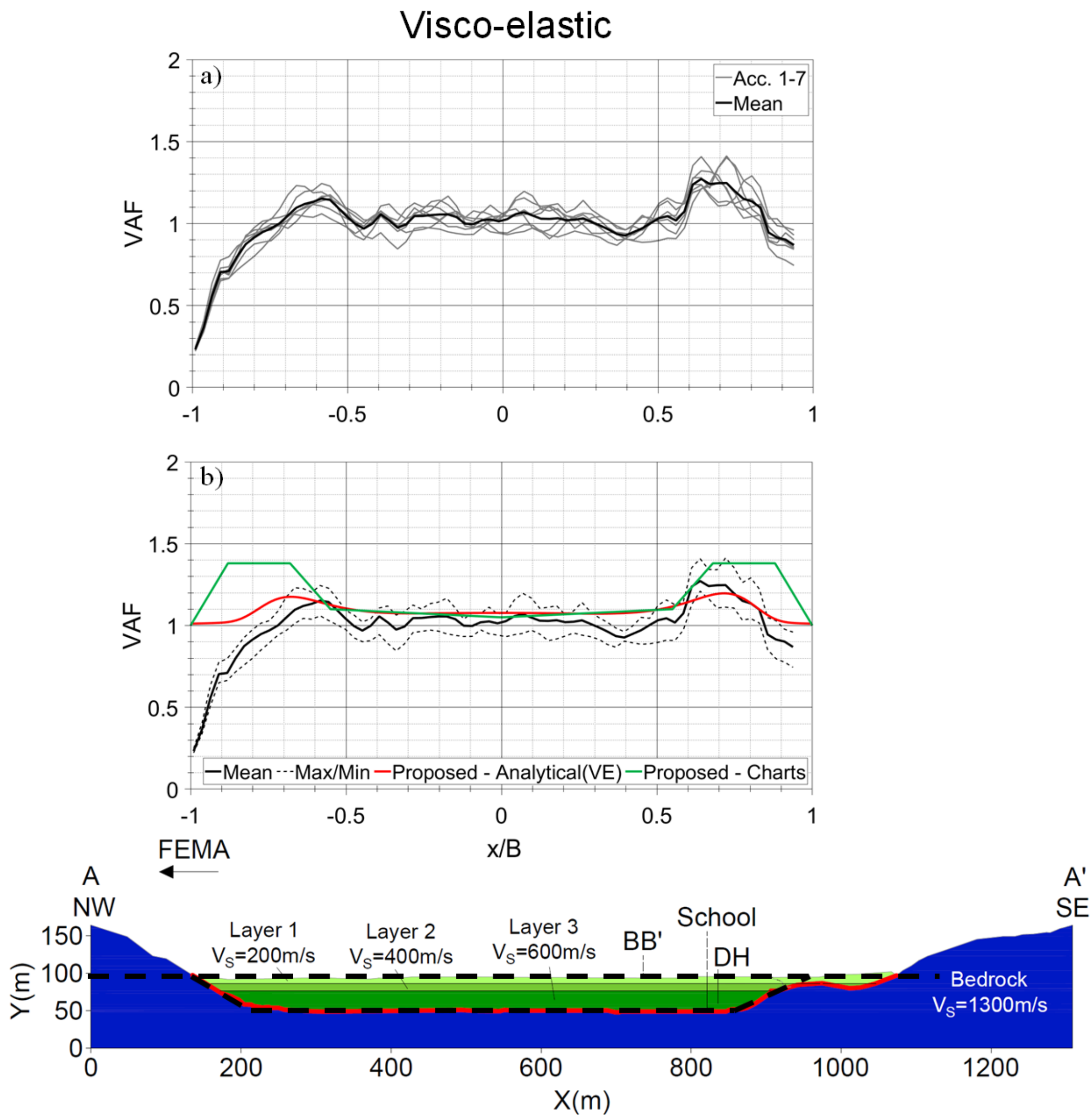

Figure V.2.13 – Comparison between the VAF calculated for the 7 input motions and those proposed in this study, for visco-elastic analysis and section AA'.

The VAF predicted with Eq. III.5.3 is mostly close to the mean VAF numerically calculated, while that estimated using the charts is comparable to the maximum numerical VAF. This is because the charts for simplicity do not account for the angle of inclination of the edges, and therefore provide the upper bound values of VAF. At the valley centre, the VAF is practically unitary while at the edges it becomes quite considerable, in agreement with the general behaviour predictable for a 'very shallow' valley. Furthermore, it should be observed that at the left edge, located between x/B equal to -1 and -0.5, the maximum value of the numerical VAF is slightly shifted to the right and it is slightly lower than that predicted by the proposed relationship. This is caused by the inclined outcropping bedrock, which causes a reduction of the ground motion at the toe of the slope and a shift of the amplification peak towards the valley (Bouckovalas & Papadimitriou, 2005; Papadimitriou, 2019).

Figure V.2.14a shows the VAF calculated with non-linear analysis: at the centre of the valley the VAF decreases, while at the edge of the valley it increases with respect to the visco-elastic case. Figure V.2.14b shows the comparisons among the average VAF computed by non-linear analyses, its values calculated applying Eq. III.5.3 and the charts (red and green lines), and that computed with Eq. IV.4.1 to take into account the non-linear effects. The VAF predicted by Eq. III.5.3 underestimates the numerical amplification, while the prediction improves if non-linearity is taken into account by Eq. IV.4.1. Since the VAF computed by charts overestimates the visco-elastic response, it better predicts the nonlinear VAF.

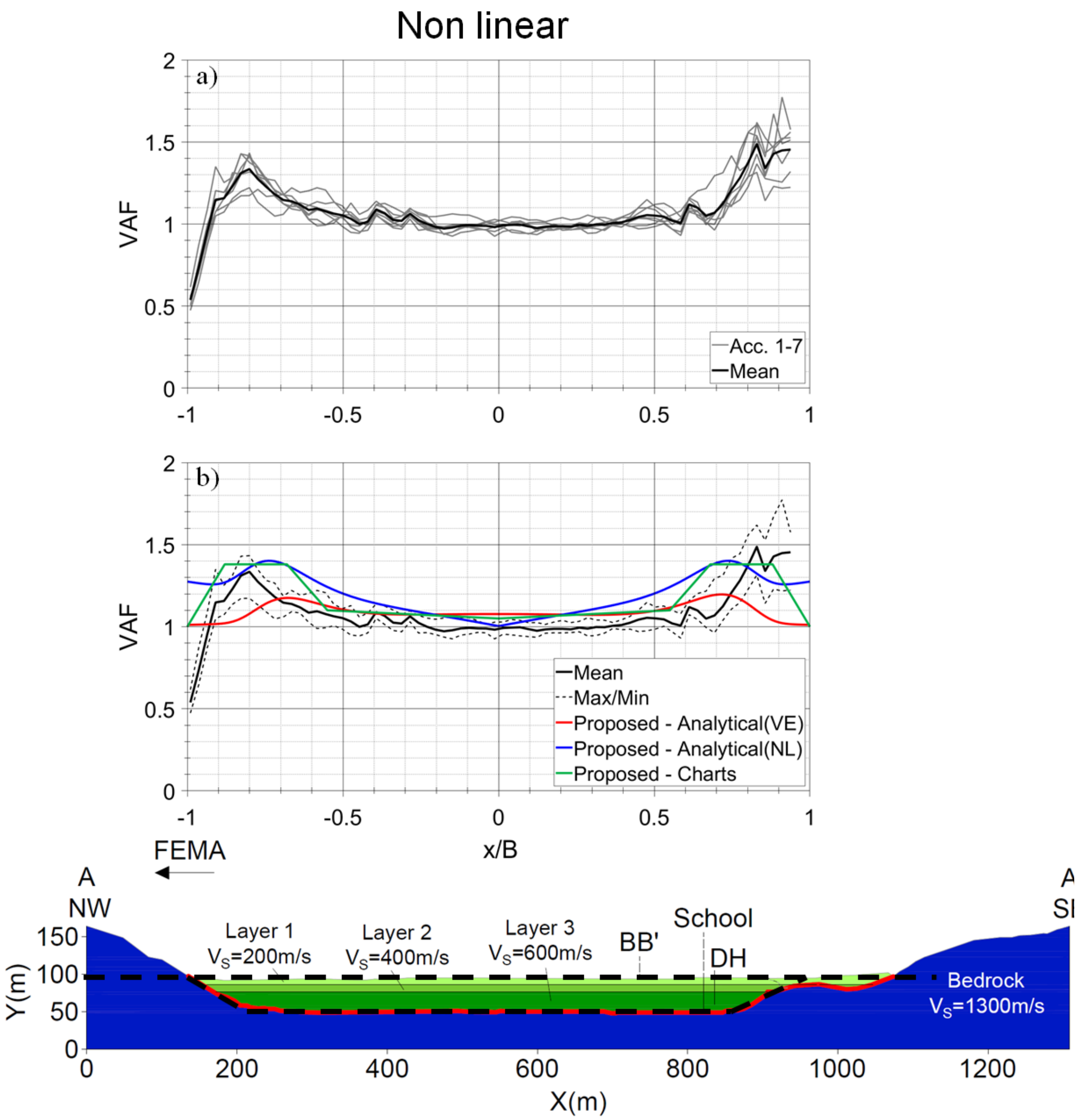

Figure V.2.14 – Comparison between the VAF calculated through non-linear analysis of section AA' for the 7 input motions and those proposed in this study.

Figure V.2.15 compares the response spectra obtained at the valley centre with 2D (green lines) and 1D analyses (blue lines) with those resulting by multiplying the VAF by either the spectrum specified by NTC 2018 for class B (red lines in Figure V.2.15a,c) or the mean spectrum predicted by 1D analyses (red lines in Figure V.2.15b,d). These comparisons have been carried out also at the school position (Figure V.2.16) and at the abscissa x/B=0.8 (Figure V.2.17). Note that the VAF in these cases is calculated with Eq. III.5.3.

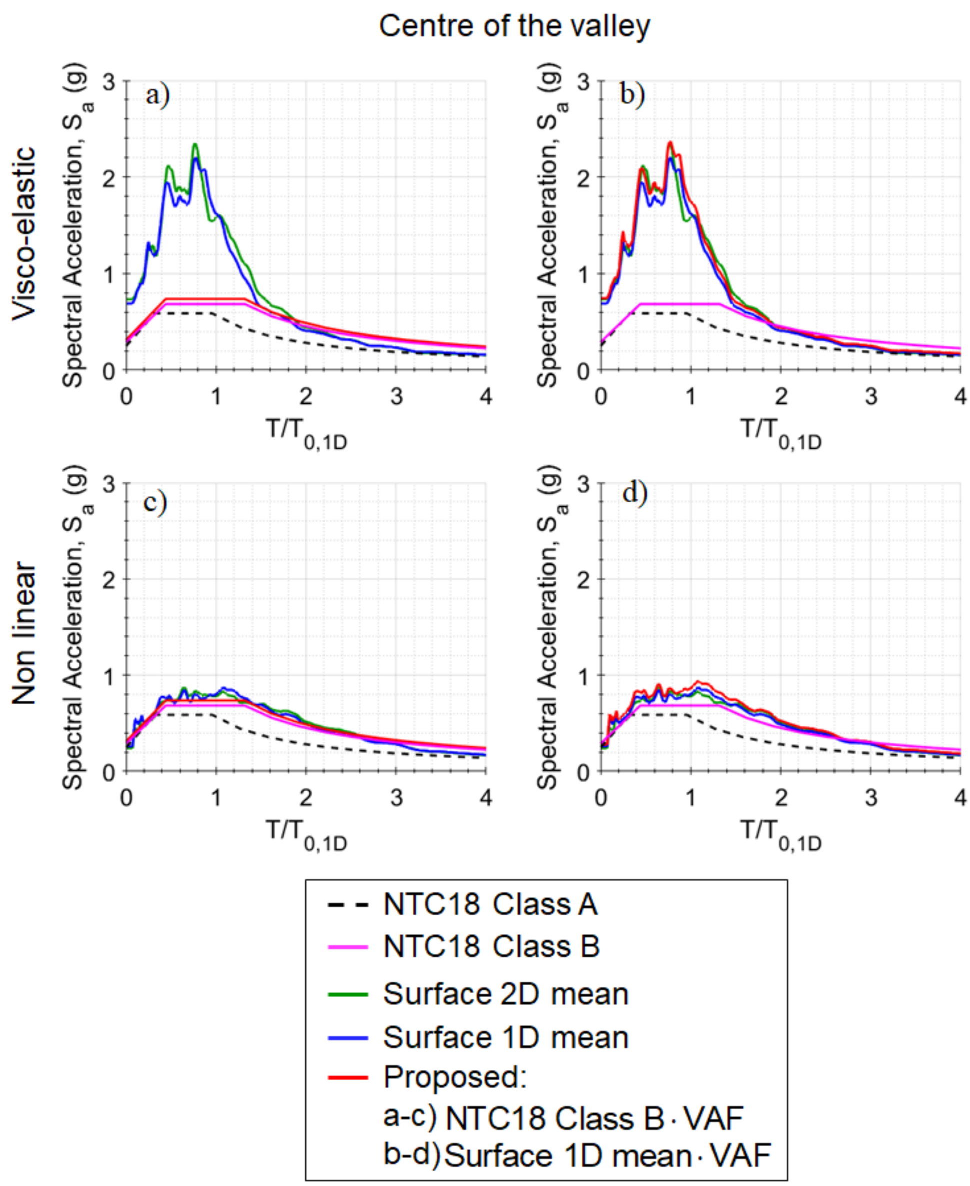

Figure V.2.15 – Comparison between the spectra obtained from 1D, 2D analysis and those calculated with the two proposed approach with VAF of Eq. III.5.3, for the centre valley of section AA'.

At the valley centre, 1D and 2D spectra result about comparable, therefore the proposed VAF slightly improves the already good matching. The code spectrum, opportunely amplified by VAF does not comply with the response computed adopting the visco elastic hypothesis.

In the non-linear case, instead, the corrected code spectrum is practically superimposed to that obtained from 1D and 2D analyses.

Same observations can be made with reference to the response predicted at the school site by applying the VAF to the code spectrum. Concerning the standard approach (1D mean spectrum amplified by VAF), the visco-elastic model provides a slight overestimation, while the results of nonlinear 1D analysis practically coincide with those obtained from the 2D model.

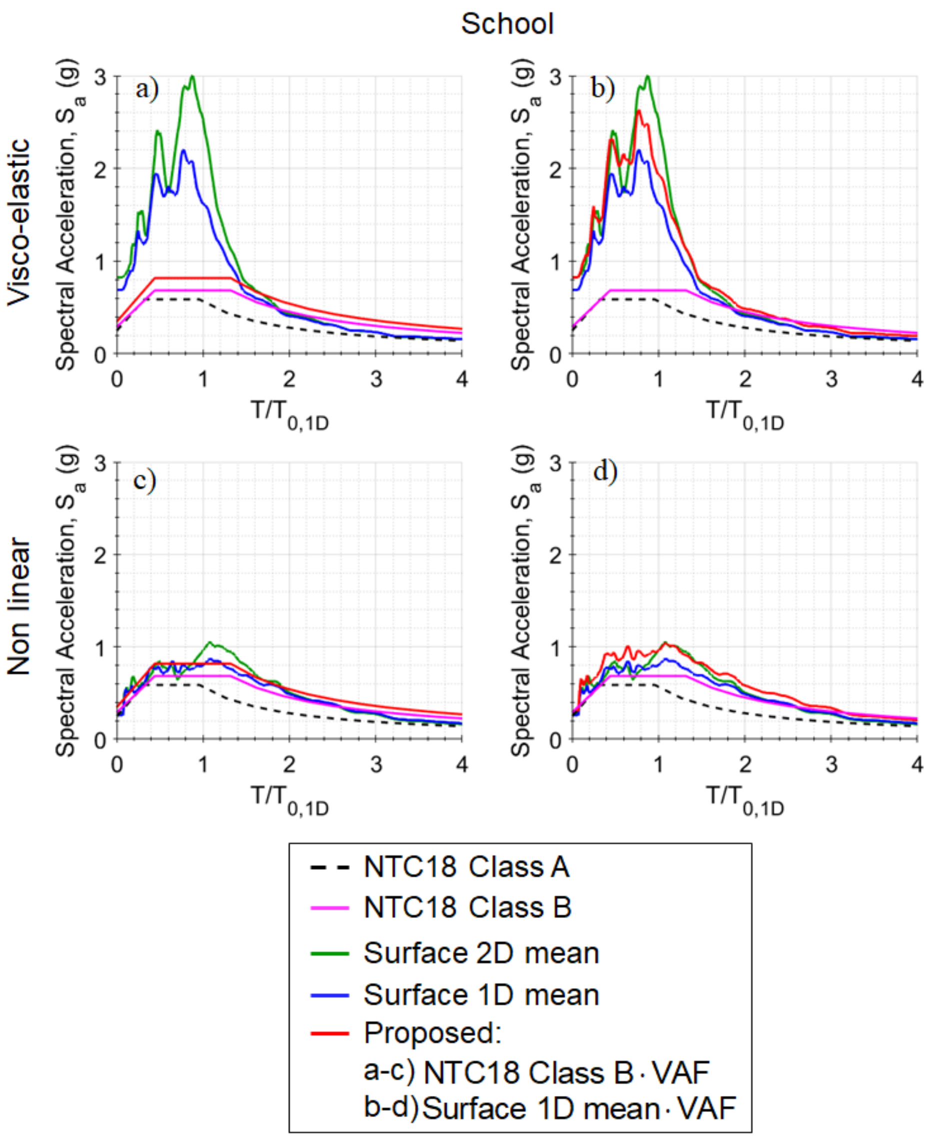

Figure V.2.16 – Comparison between the spectra at the school site along section AA' as obtained from 1D or 2D analyses and those calculated with the two proposed approaches with VAF from Eq. III.5.3.

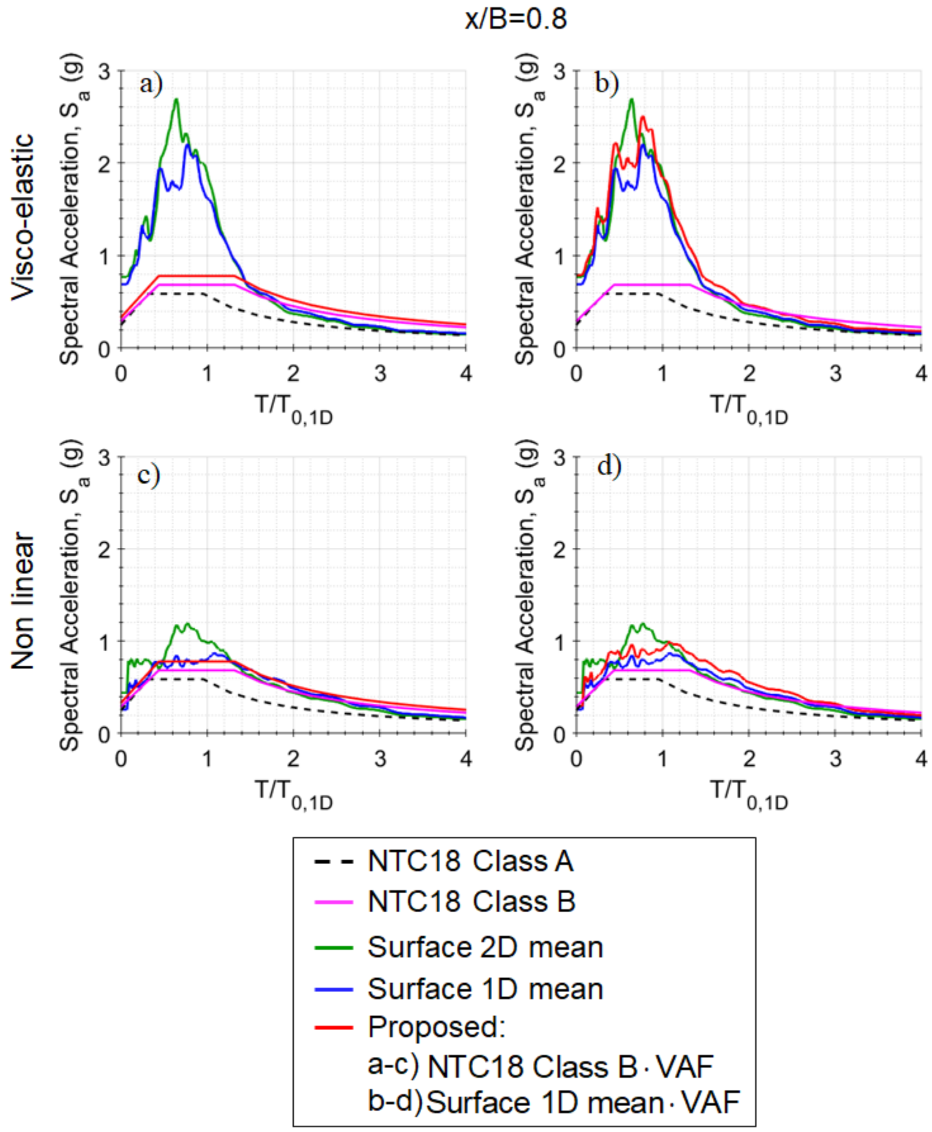

Figure V.2.17 – Comparison between the spectra at x/B=0.8 along section AA' as obtained from 1D or 2D analyses and those calculated with the two proposed approaches with VAF from Eq. III.5.3.

Finally, for x/B=0.8 (Figure V.2.17) both approaches underestimate the numerical 2D amplification, the simplified (VAF applied to code spectrum) more significantly both through visco-elastic and non-linear soil models, while the standard (VAF applied to the 1D response spectra) presents less differences.

Figure V.2.18, Figure V.2.19 and Figure V.2.20 show the comparisons between the mean spectra computed with the 1D and 2D analyses and those obtained for the two approaches for the centre of the valley, the school and x/B=0.8, but in this case the

VAF is estimated using the proposed charts. At the centre of the valley (Figure V.2.18) the same trends are observed as in the case with the VAF calculated with Eq. III.5.3, because at that point the VAF value is the same.

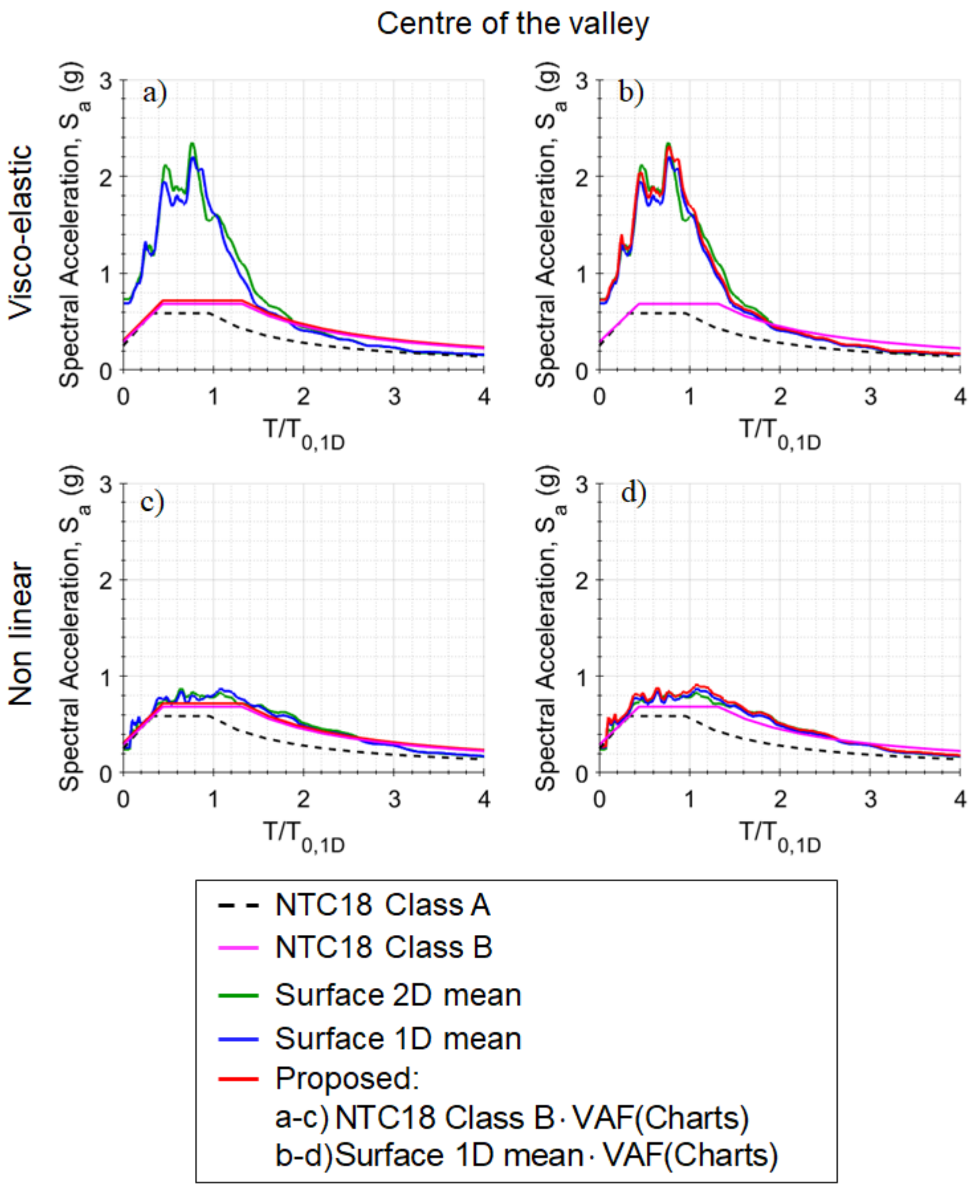

Figure V.2.18 – Comparison between the spectra obtained from 1D, 2D analysis and those calculated with the two proposed approach with VAF of charts, for the centre valley of section AA'.

At the school (Figure V.2.19) and at x/B=0.8 (Figure V.2.20) the VAF applied to the non-linear code spectrum improves the prediction. On the other hand, the prediction obtained by multiplying the mean 1D spectrum by the VAF estimated with the charts, overestimates the mean 2D numerical spectrum.

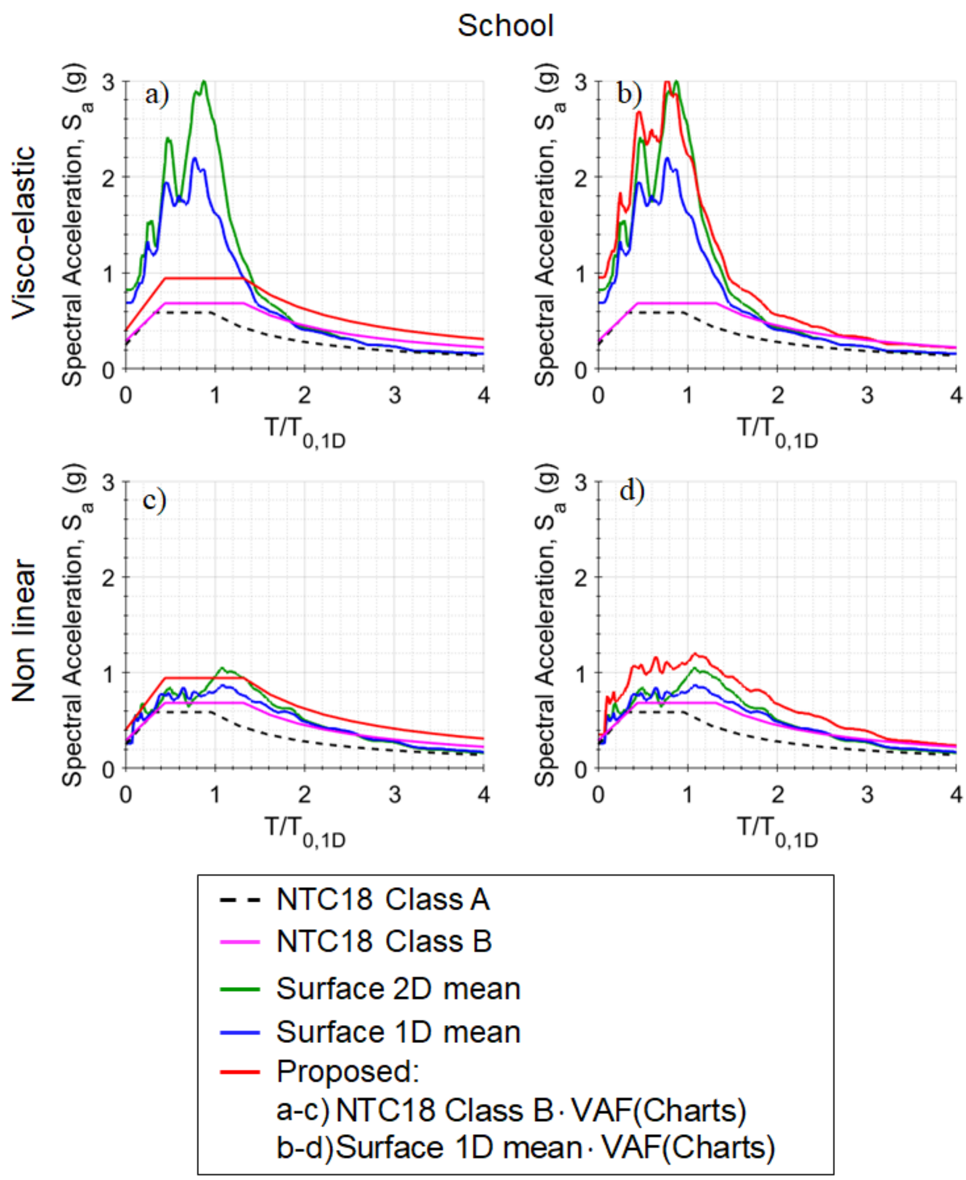

Figure V.2.19 – Comparison between the spectra at the school site along section AA' as obtained from 1D or 2D analyses and those calculated with the two proposed approaches with VAF from charts.

In conclusion, it should be noted that estimating VAF with charts provides over-conservative predictions. It is recalled that they do not account for the edge slope angle, unlike the VAF calculated with Eq. III.5.3, and therefore their predictions are not significantly affected by the real shape of the valley edge. The latter significantly influences the ground motion in the lateral zone especially when the outcropping bedrock does not have a horizontal ground surface.

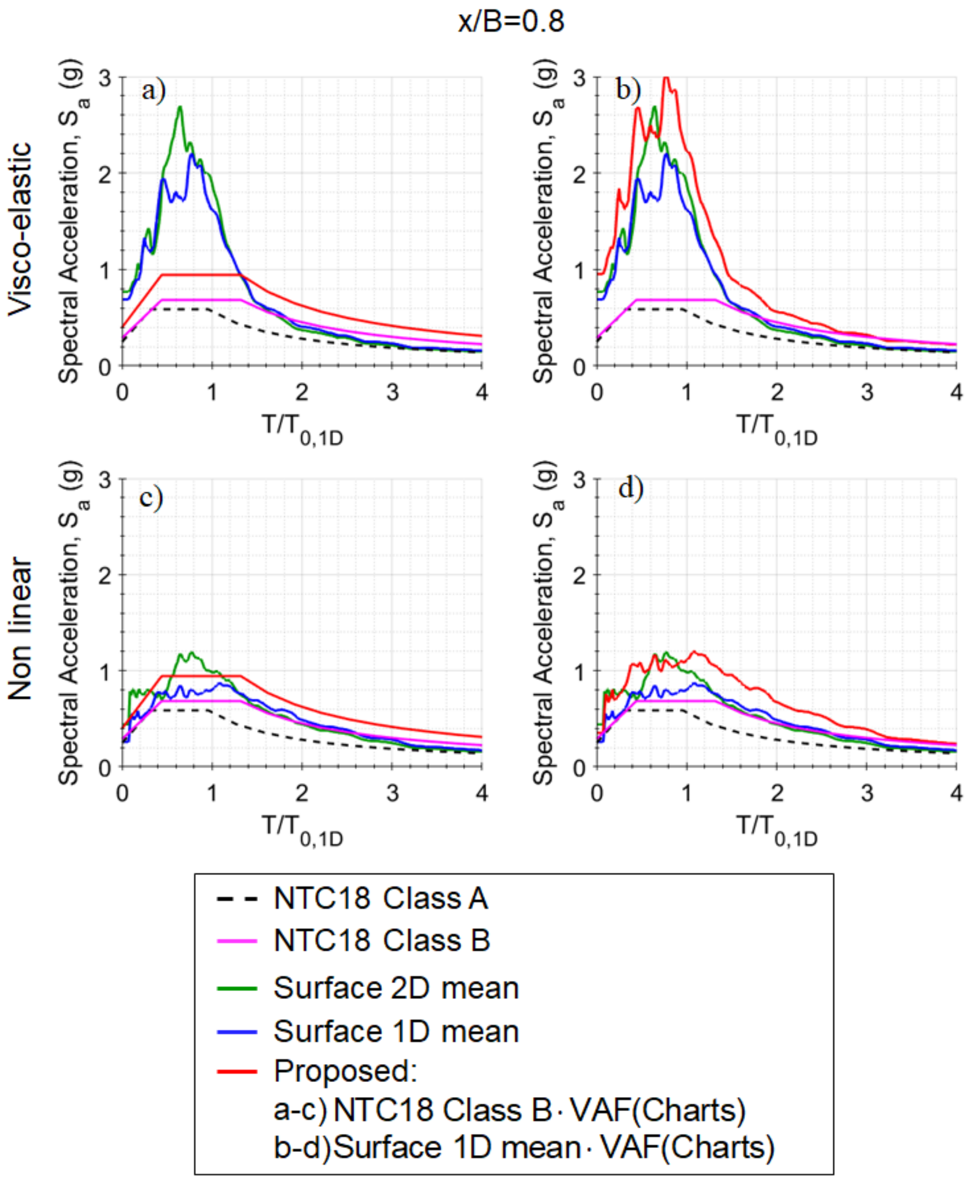

Figure V.2.20 – Comparison between the spectra at x/B=0.8 along section AA' as obtained from 1D or 2D analyses and those calculated with the two proposed approaches with VAF from charts.

The results obtained for section BB' of Visso are discussed in the following. Figure V.2.21a shows, for the visco-elastic case, the VAF calculated for the seven accelerograms and their mean value, while Figure V.2.21b shows the comparison between the mean VAF and those calculated with Eq. III.5.3 and the charts.

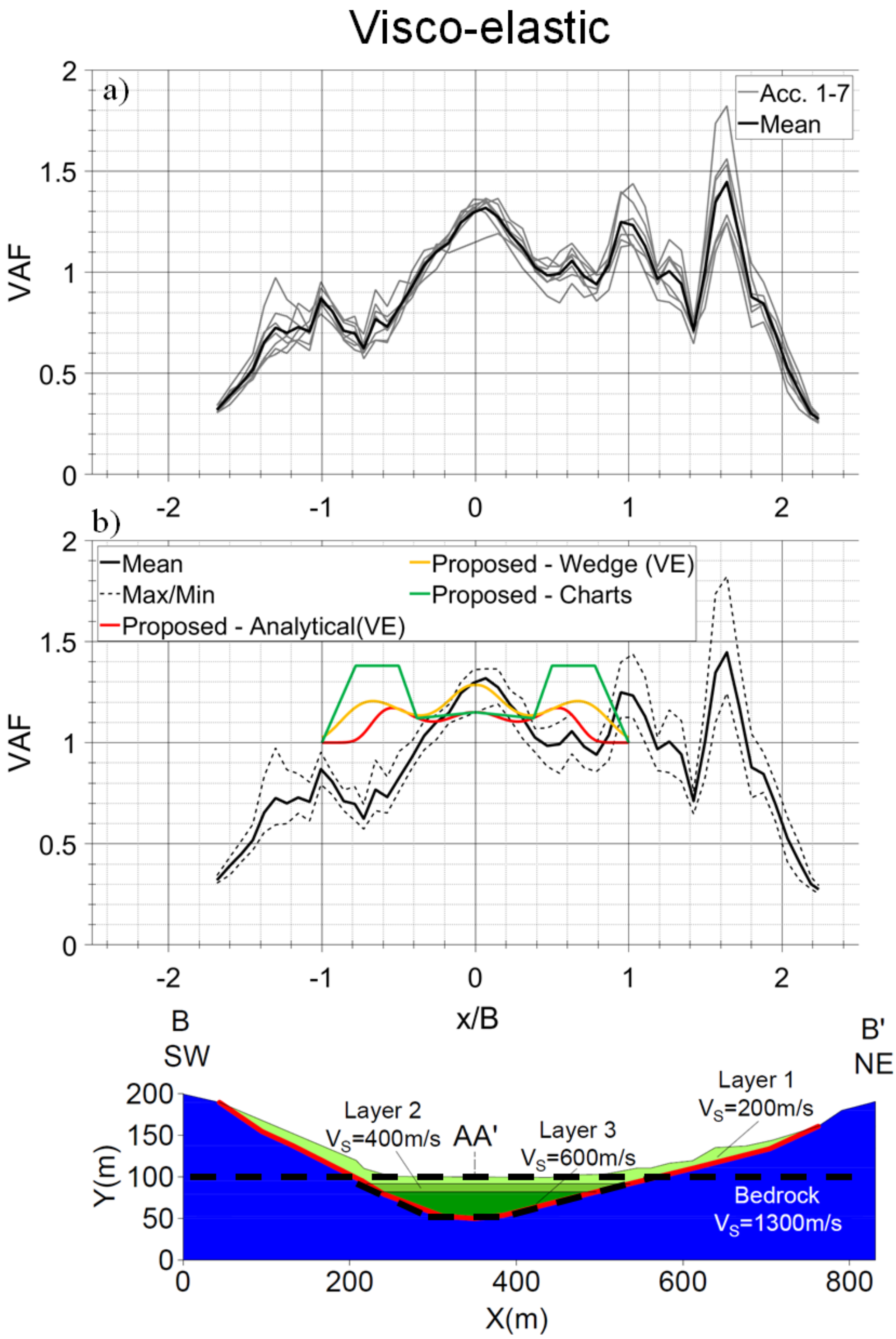

Figure V.2.21 – Comparison between the VAF calculated by visco-elastic analysis along section BB' for the 7 input motions and those proposed in this study.

In this case, the geometry of the valley strongly influences the VAF, because the inclination of the edges is close to the threshold that distinguishes trapezoidal from wedge-shaped valleys. Furthermore, the combination of the inclined outcrop bedrock with a thin layer of deformable material significantly modifies the dynamic response of the valley. As a matter of fact, both lateral peaks are flattened by the attenuation effects due to the outcropping bedrock topography, whereas the wedge-like shape focuses the seismic waves towards the centre of the valley increasing the amplification. This is evidenced by the VAF calculated with the equations provided in §III.5.3 for the wedge (ochre line in Figure V.2.21b). Indeed, in the centre of the valley the VAF obtained through these equations approximates well that resulting from the analyses, while at the edges the topographic attenuation effects causes a strong decrease of the amplification. The results obtained show that the seismic motion of the valleys is strongly dependent on the real geometry of the basin and of the outcropping bedrock.

Figure V.2.22 shows the same comparisons as Figure V.2.21 but considering the non-linear analysis. In this case, the latter mitigates the strong geometric effects previously examined and indeed the trend of the VAF calculated with Eq. III.5.3 (red line) is very close to the average one calculated both at the valley centre and at the edges.

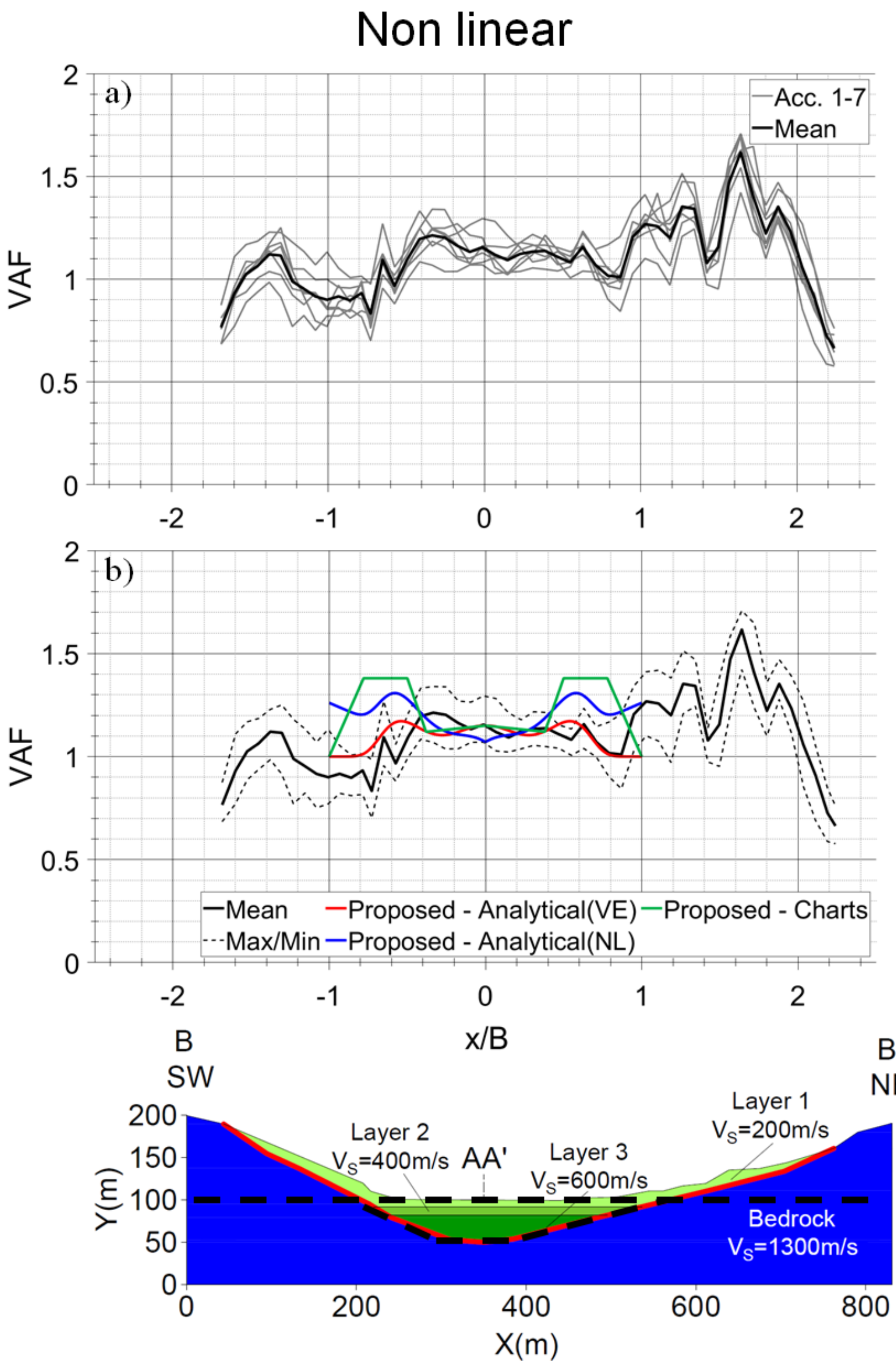

Figure V.2.22 – Comparison between the VAF calculated by non-linear analysis along section BB' for the 7 input motions and those proposed in this study.

The two simplified approaches proposed for estimating the spectrum have been used for the centre of the valley (Figure V.2.23) and for x/B=0.6 (Figure V.2.24); the latter point has been chosen because it is the location of the maximum VAF. It should be noted that the VAF is calculated using Eq. III.5.3, obtained for the trapezoidal valleys and not for the wedge, because the non-linear results have highlighted that the dissipative effects lead the trapezoidal VAF to approximate well the numerical one.

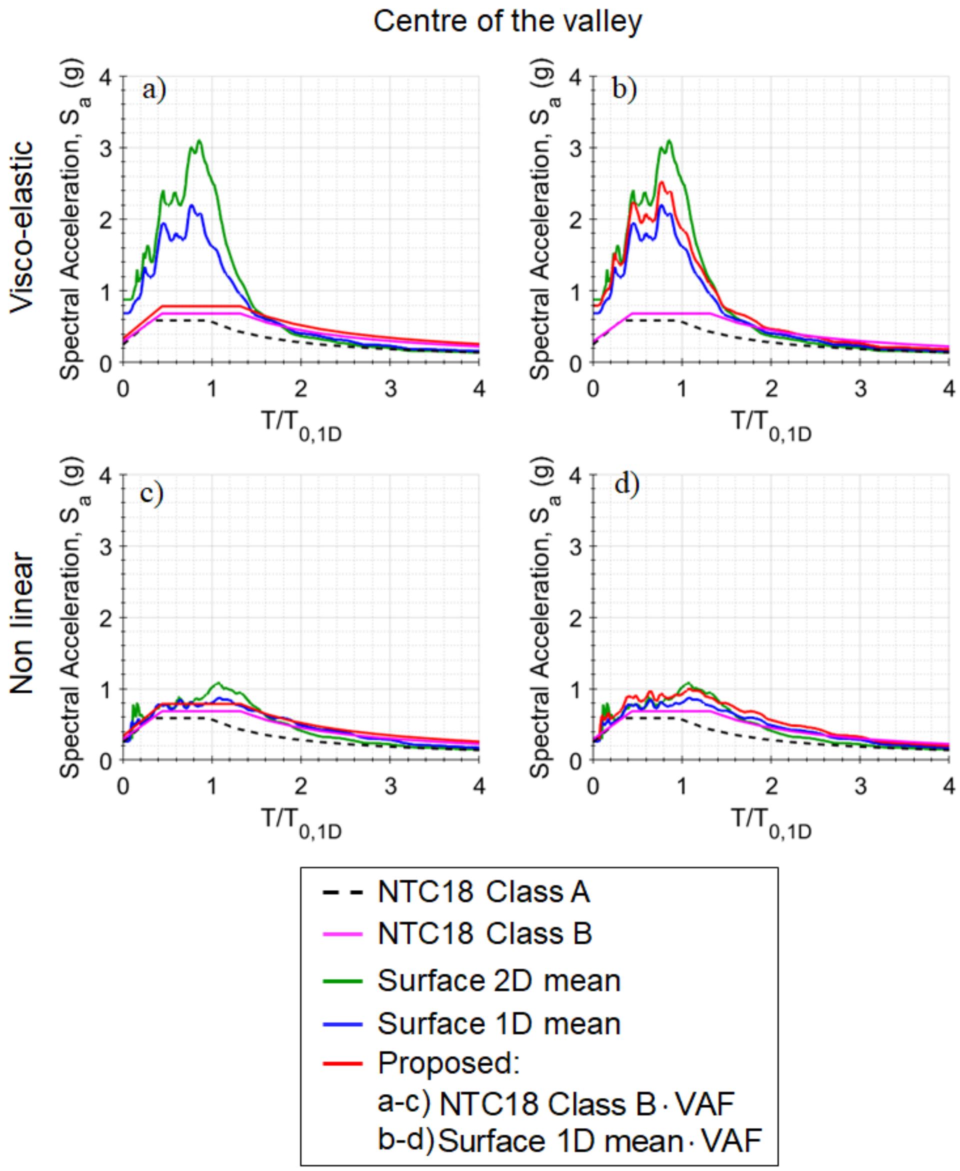

Figure V.2.23 – Comparison between the spectra obtained from 1D, 2D analysis and those calculated with the two proposed approaches with VAF of Eq. III.5.3, for the centre valley of section BB'.

Figure V.2.23 shows the results obtained for the centre of the valley of section BB' for the two approaches: in the simplified case the same trends as for the centre of the valley of section AA' are found, with the visco-elastic spectrum being significantly underestimated (Figure V.2.23a), while the non-linear one is slightly underestimated (Figure V.2.23c) due to the VAF trend shown above (Figure V.2.21). As a matter of fact, considering the standard approach, in the visco-elastic case (Figure V.2.23b) the calculated mean VAF is greater than the proposed one, while considering the non-linear behaviour (Figure V.2.23d), the difference between the two is small.

Figure V.2.24 shows the same comparisons for x/B=0.6.

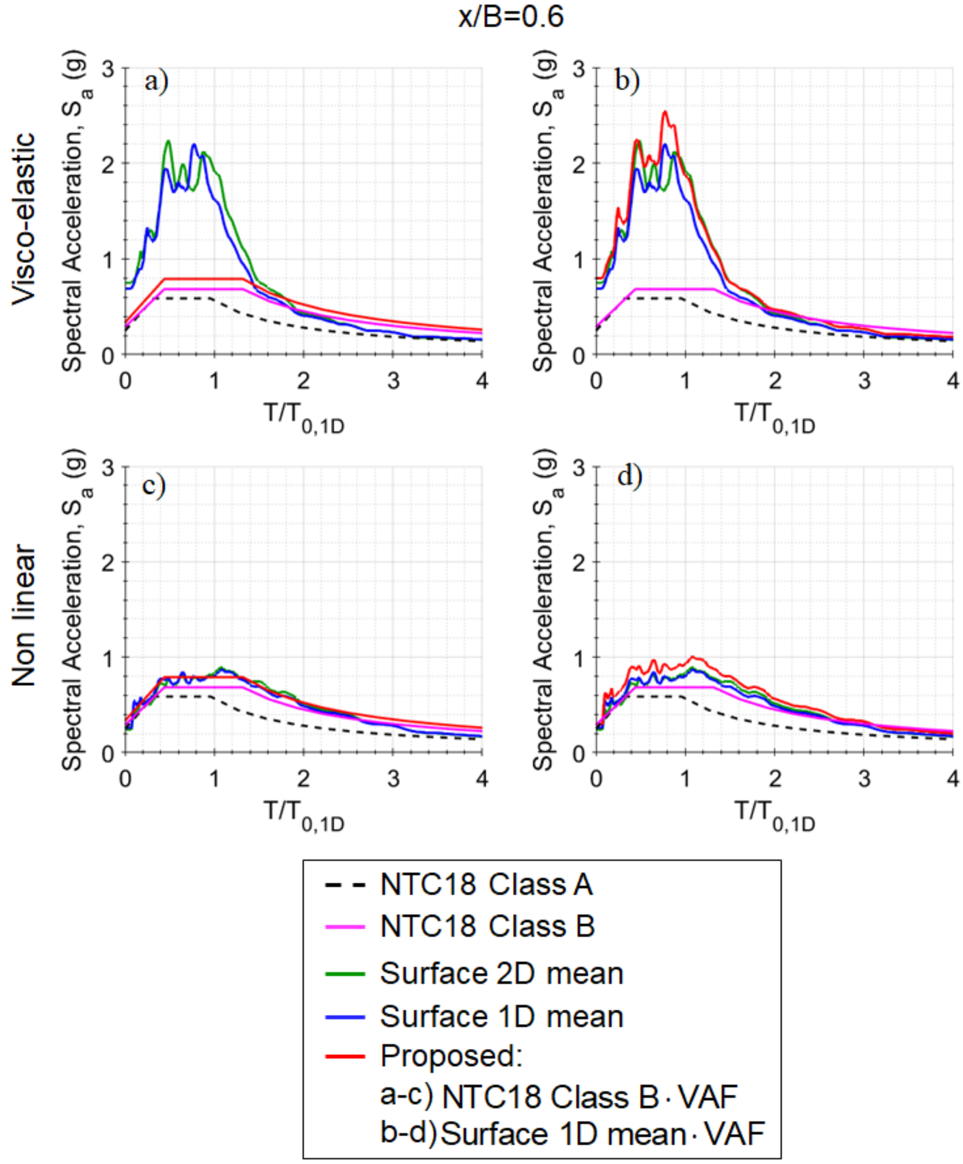

Figure V.2.24 – Comparison between the spectra at x/B=0.6 along section BB' as obtained from 1D or 2D analyses and those calculated with the two proposed approaches with VAF from Eq. III.5.3.

In this case, the simplified approach approximates satisfactorily the mean spectrum obtained with nonlinear analysis (Figure V.2.24c) while, as usual, significantly overestimates the predictions of the visco-elastic model (Figure V.2.24a). The standard approach slightly overestimates the ground motion predicted by both visco-elastic (Figure V.2.24b) and nonlinear analyses (Figure V.2.24d).

Finally, Figure V.2.25 and Figure V.2.26 show the same comparisons considering the VAF estimated with the charts for both sites of interest. For both verticals the same trends as in the previous case (Figure V.2.23 and Figure V.2.24) are found, the simplified approach significantly underestimates the visco-elastic response (Figure V.2.25a, Figure V.2.26a) while the nonlinear one is only slightly underestimated at the centre of the valley (Figure V.2.25c) and slightly overestimated for x/B=0.6 (Figure V.2.26c). The standard approach always overestimates the surface motion except in the visco-elastic case at the centre of the valley (Figure V.2.25b).

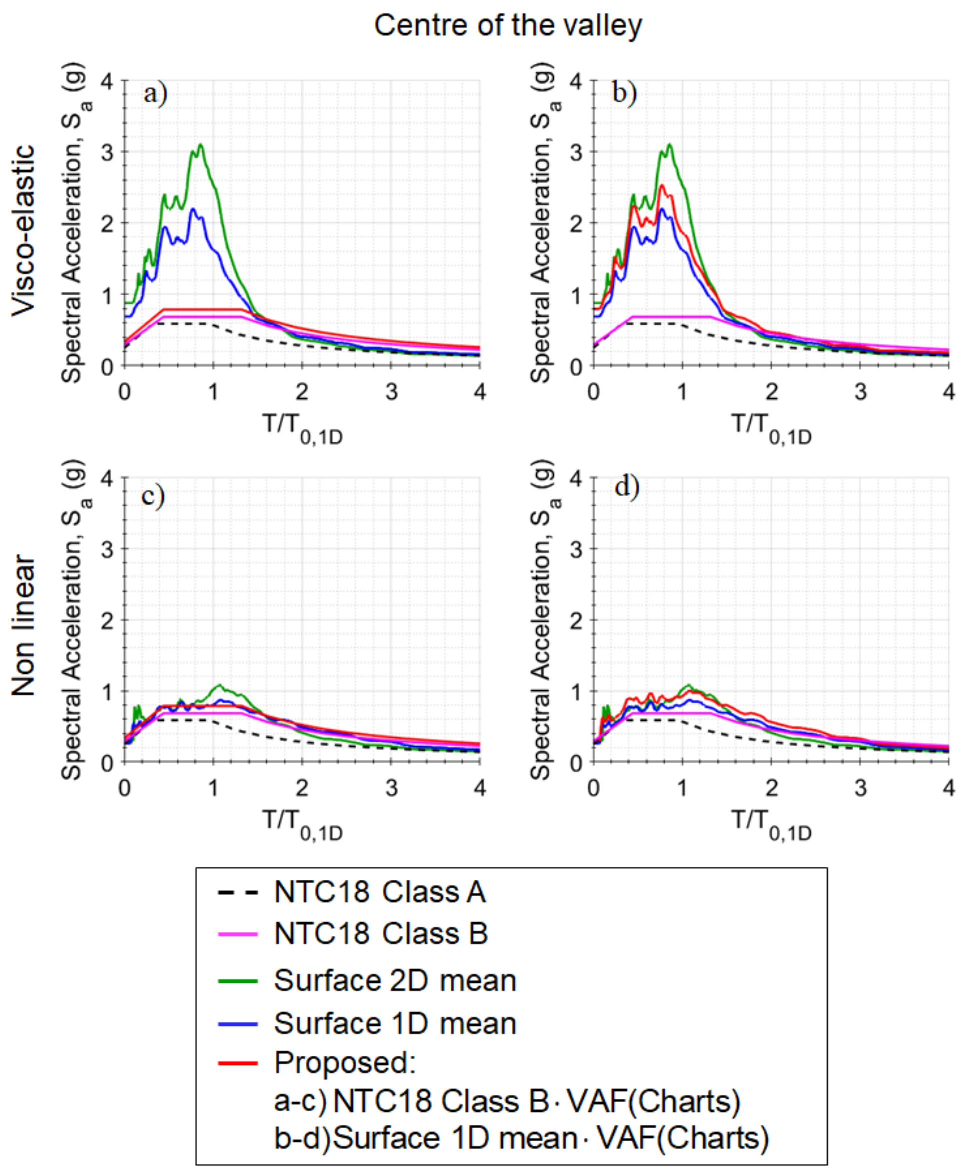

Figure V.2.25 – Comparison between the spectra obtained from 1D, 2D analysis and those calculated with the two proposed approaches with VAF of charts, for the centre valley of section BB'.

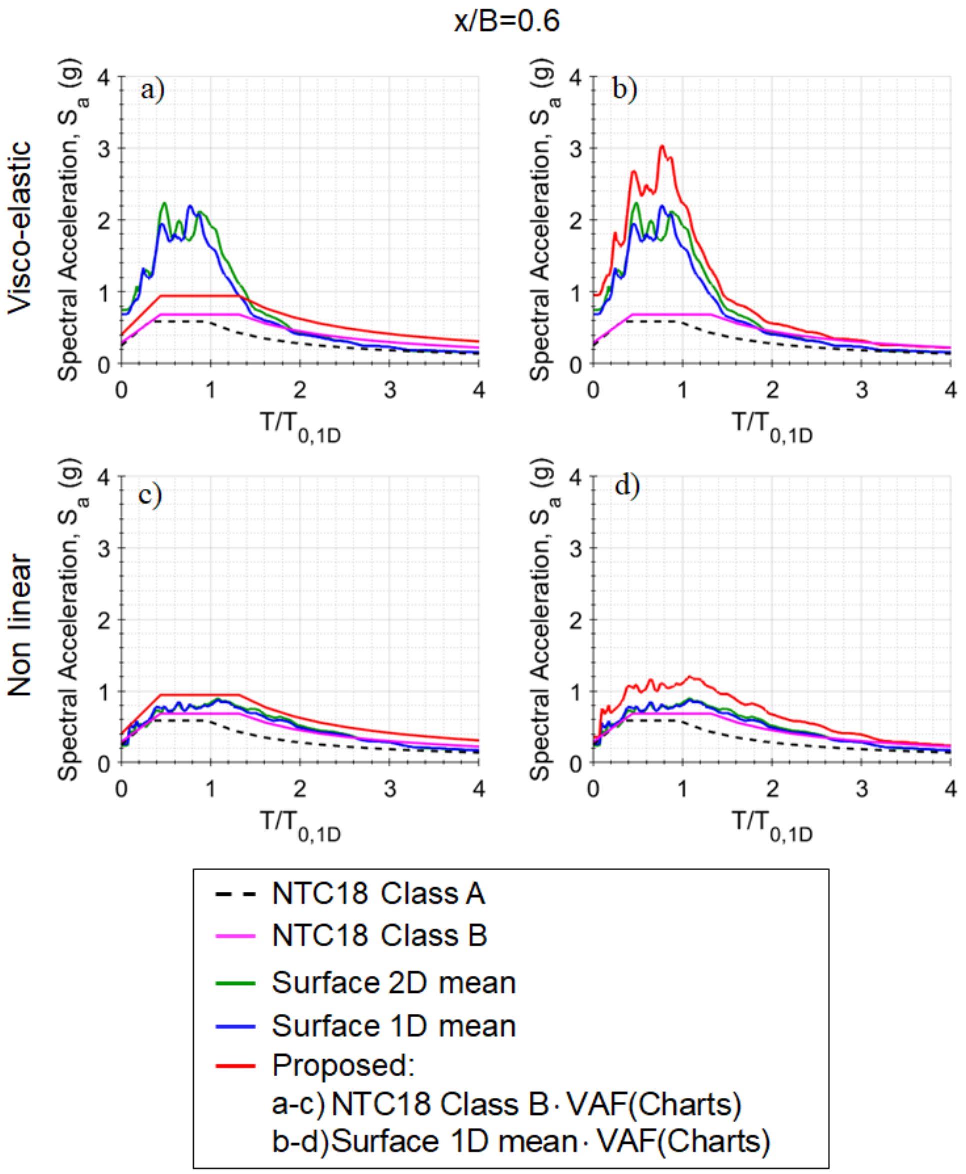

Figure V.2.26 – Comparison between the spectra at x/B=0.6 along section BB' as obtained from 1D or 2D analyses and those calculated with the two proposed approaches with VAF from charts..

V.3 Verification case studies

In the following, the seismic response of three alluvial valleys of Central Italy is analysed, in particular those where the municipalities of Montefranco, Pretare and Piedilama are located. As opposed to the case of Visso, in these valleys no seismic records were available which could be useful to validate the geotechnical model. The latter was therefore characterised by processing the data available from previous studies for all three towns. Hence, the results obtained from 2D numerical analyses, carried out in accordance with the best practice and the guidelines of the Italian technical standards, will be compared with those obtained from the two simplified proposed approaches.

V.3.1 Montefranco

Montefranco is a small town in central Italy located on an alluvial valley originated by the Nera river. It is one of the numerous villages damaged by the Central Italy seismic sequence started in 2016 (Figure V.2.3). After the earthquake, the small town was involved in the seismic microzonation studies carried out to manage the reconstruction process of the 138 municipalities severely hit by the seismic sequence. Figure V.3.1 shows the geolithological map of Montefranco and the investigated section taken from that study (Faralli et al., 2018). The valley has a maximum thickness of about 100m, a width of about 850m and it is mainly filled by fine-grained soil. During the microzonation studies, a 30m deep Down Hole (DH) test and measurements of the spectral ratio between the horizontal and vertical components of microtremors (HVSR) were carried out close to the centre of the valley; several

HVSR were also collected at numerous points along the examined section. Table V.3.1 shows the main subsoil properties adopted in this study; Figure V.3.2a shows the comparison between the V_S profile measured by the DH (black line) and that resulting from the inversion of the HVSR measurements carried out along the valley (blue line), which allowed to reconstruct the deep geometry of the basin and to obtain the average V_S value adopted in the seismic response analyses (red line). Since the V_S does not vary significantly along the profile (except for the first few metres) and ranges between 200 and 350m/s, an equivalent shear wave velocity value equal to 260m/s, calculated using Eq. IV.1.1, has been adopted in the analyses for the whole valley. A velocity of 850m/s has been assigned to the bedrock, in agreement with the seismic microzonation studies (Faralli et al., 2018). The curves expressing the shear modulus decay, $G(\gamma)/G_0$, and the increase of damping with the shear strain, $D(\gamma)$, were introduced in the seismic response analyses as sigmoidal functions best-fitting the results of dynamic tests on an undisturbed soil sample taken along the DH profile, reported in the same microzonation studies (Figure V.3.2b).

Table V.3.1 – Geometrical and mechanical properties of Montefranco

	Thickness h_i (m)	Unit weight γ (kN/m^3)	Shear wave velocity V_S (m/s)	Poisson ratio ν	Initial Damping D_0 (%)	$G(\gamma)$/G0 and $D(\gamma)$ curves
Soil	110	18	260	0.3	2.0	Faralli et al. (2018)
Bedrock	-	23	850	0.25	0.5	Visco-elastic

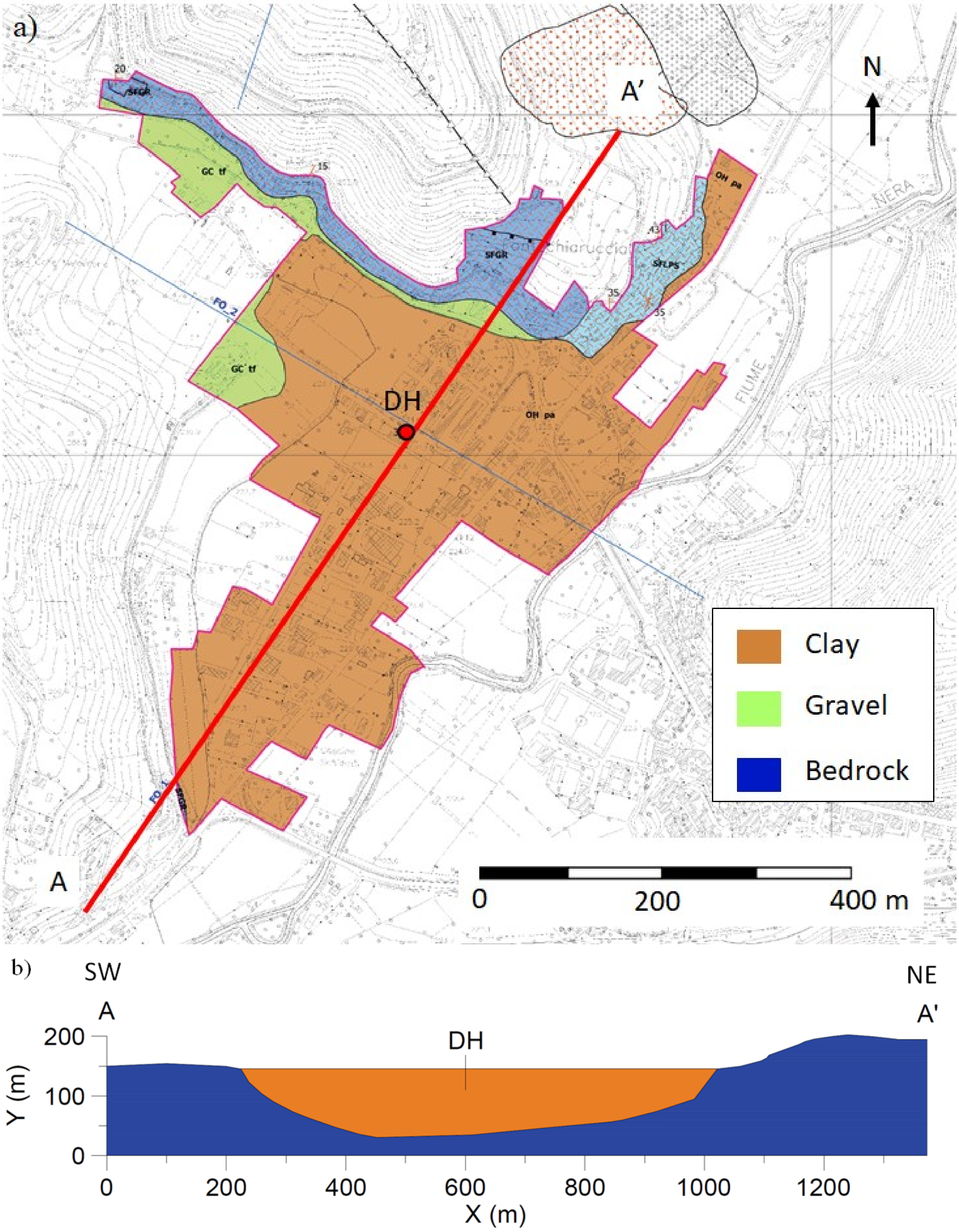

Figure V.3.1 – a) Geolithological map and b) section AA' of Montefranco (modified from Faralli et al., 2018)

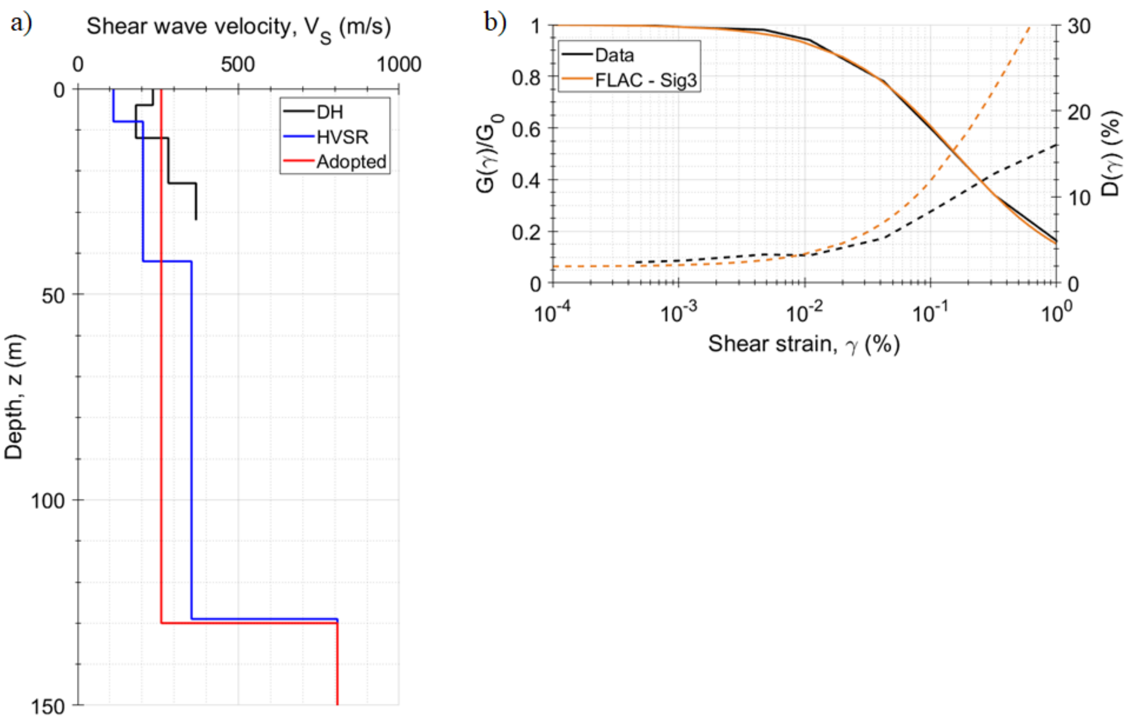

Figure V.3.2 – a) Profiles of V_S at Montefranco as measured by a DH test, back-calculated from HVSR records and adopted in the analysis; b) $G(\gamma)/G_0$ and $D(\gamma)$ curves as measured in laboratory tests and implemented in the seismic response analyses by FLAC.

Before carrying out the numerical analysis of the site seismic response, the charts developed in this study are used to estimate the valley amplification effects. Figure V.3.3a-f shows these charts with the point representative of the basin geometry as approximated with a trapezoidal homogeneous valley (Figure V.3.3g). The half-width is about 425m while the thickness is about 110m, hence the shape ratio is about 0.26. By assuming a homogeneous alluvial soil with V_S=260m/s and γ=18kN/m^3 and a bedrock with V_S=850m/s and γ=23kN/m^3, the impedance ratio results equal to 4.2. Therefore, the valley is classified as ‘moderately shallow’ and 2D amplification is expected to be significant both at the centre of the valley and at the edges.

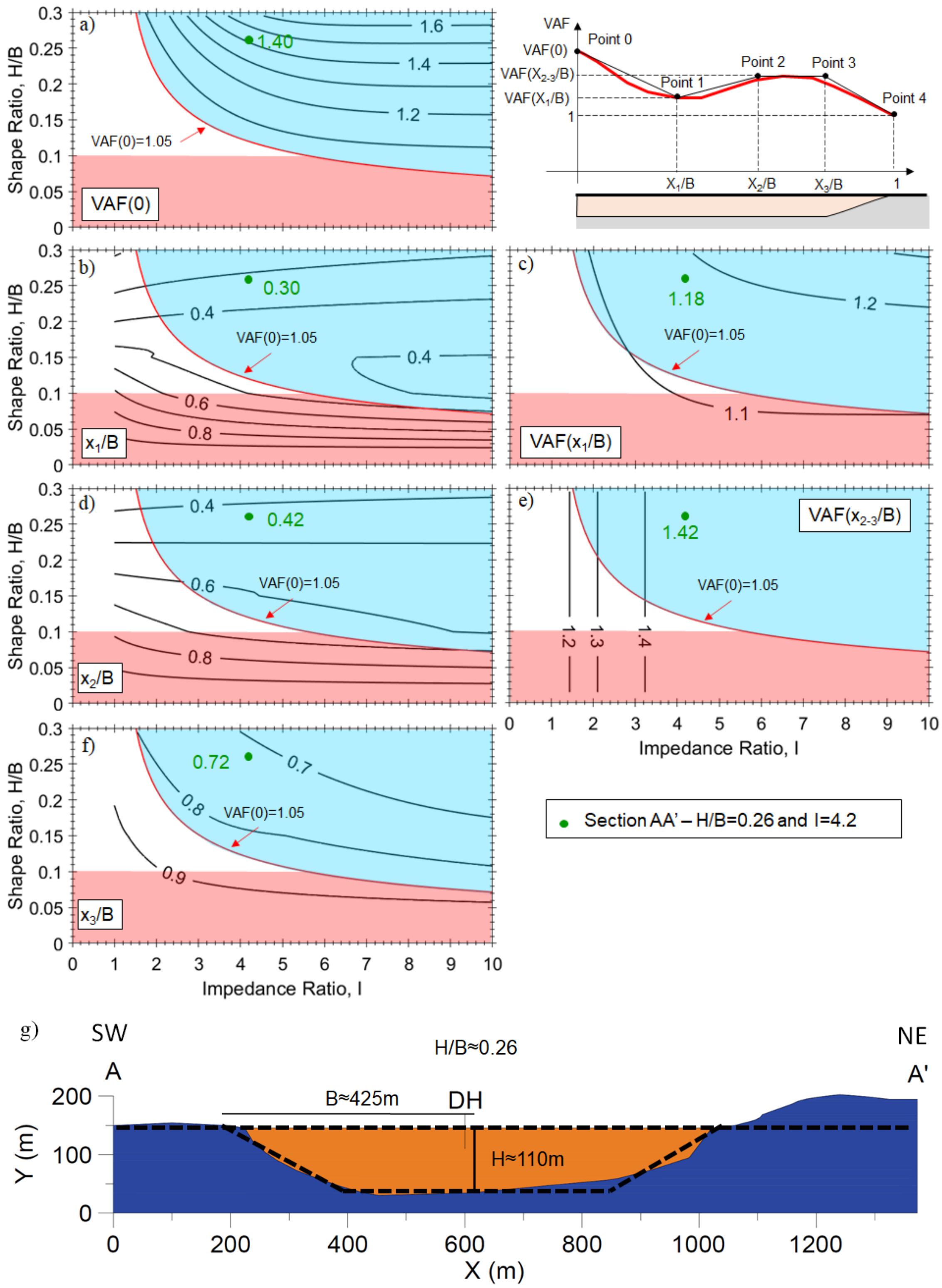

Figure V.3.3 – a-f) Proposed charts to estimate VAF; g) Schematic valley considered to calculate the VAF (black dashed lines).

The reference seismic motion used in the seismic response analyses is composed by 7 accelerograms chosen using Rexel v3.5 (Iervolino et al., 2010), in such a way that the mean spectrum results compatible with that specified by the Italian technical standards (NTC18) for subsoil class A and horizontal ground surface. Table V.3.2 shows the main properties of the selected signals while the Figure V.3.4a shows the comparison among the response spectra of the seven selected accelerograms, the mean and the one defined by NTC 2018 for class A. In Figure V.3.4b, the same spectra are shown but with the periods scaled with respect to $T_{0,1D}$ (equal to 1.69s), computed as the inverse of $f_{0,1D}$ defined by Eq. IV.2.1 considering $V_{S,eq}$ of 260 m/s and H of 110 m. Since the thickness of the valley is very large and the soil is very deformable, it can be noted that the resonance period is much higher than the predominant period of the signals used as reference seismic motion.

Table V.3.2 – Main features of the 7 accelerograms selected for Montefranco

Earthquake	Date	M_w	Epicentral Distance (km)	Station	Site class	Component
Bingol	01/05/2003	6.3	14	Bingol	A	E-W
Reykjanes Peninsula	19/03/1990	4.7	16	Reykjavik	A	N-S
Izmit (aftershock)	13/09/1999	5.8	15	Izmit	A	N-S
Lazio Abruzzo (aftershock)	11/05/1984	5.5	14	Pescasseroli	A	N-S
South Iceland (aftershock)	21/06/2000	6.4	6	Selfoss	A	N-S
South Iceland (aftershock)	21/06/2000	6.4	15	Hella	A	E-W
South Iceland	17/06/2000	6.5	5	Selfoss	A	E-W
	Mean	5.9	12			

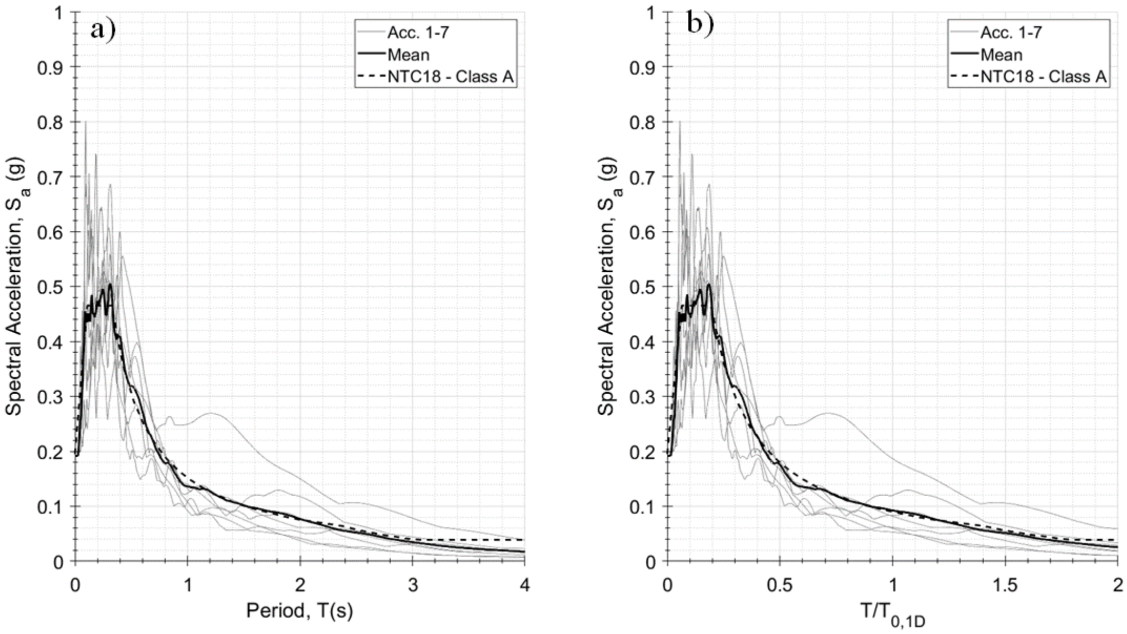

Figure V.3.4 – Comparison between the response spectra of the 7 and mean accelerogram considered, and those obtained with NTC 2018.

Figure V.3.5 shows the comparison between the VAF calculated for each one of the 7 accelerograms through visco-elastic analyses, the mean value and those estimated with Eq. III.5.3 and with the charts. The VAF proposed by the analytical relationship (red curve) is comparable to the maximum VAF computed by numerical analyses at the centre of the valley, while in most of the other zones (except for those along the sloping bedrock) it ranges between the maximum and the mean VAF. On the other hand, the charts lead to a proper estimate of the VAF at the centre of the valley (green line), while overestimating it considerably at the edges. This happen because the charts were designed to be independent of the angle of inclination of the edges, and therefore conservatively defined on the basis of the upper bound of the maximum analytical VAF values.

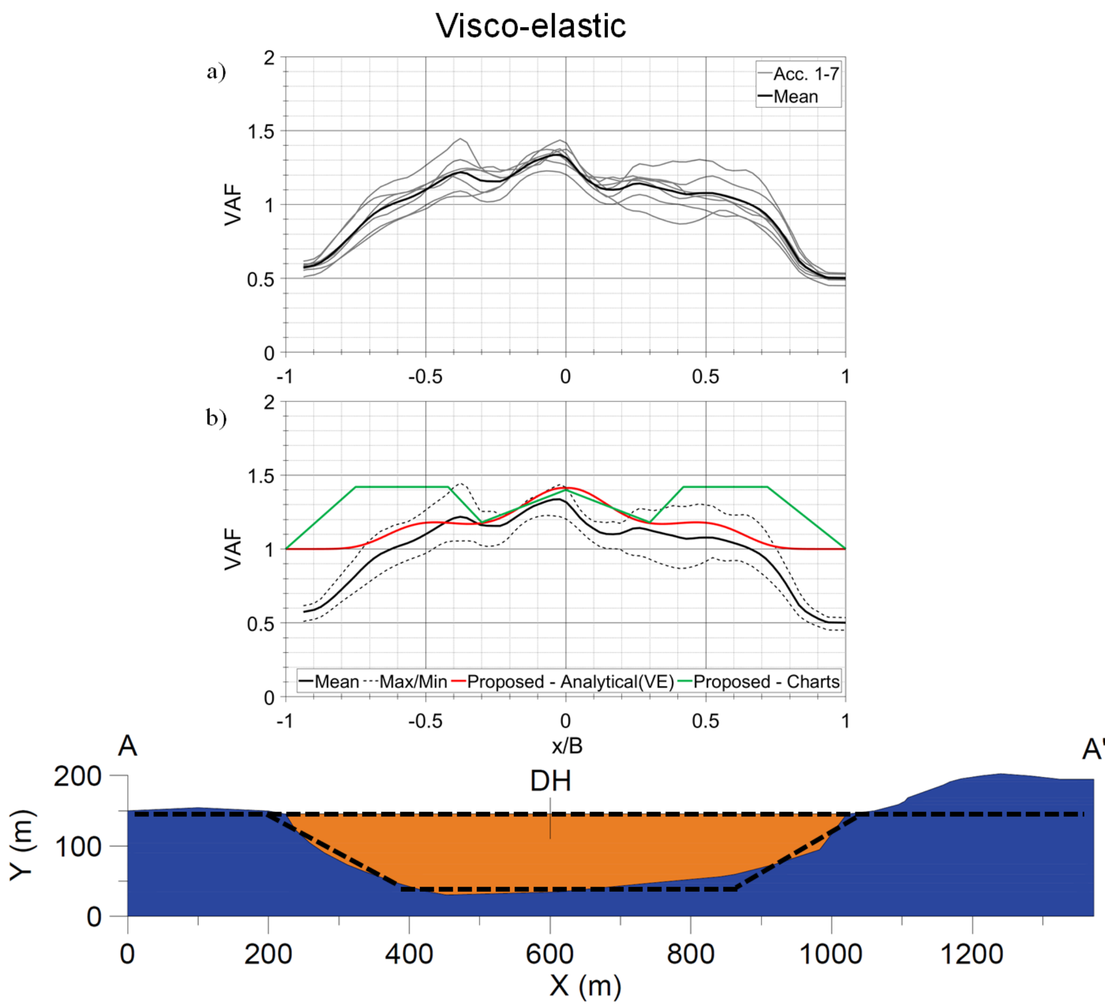

Figure V.3.5 – Comparison between the VAF calculated for the 7 input motions and those proposed in this study, for visco-elastic analysis and section AA'.

In the non-linear case (Figure V.3.6) at the centre of the valley the VAF calculated from the analysis is slightly lower than the visco-elastic one while in the lateral zone the behaviour is the opposite, confirming the results obtained in Chapter IV. Indeed, if the analytical VAF modified with Eq. IV.4.1, to take into account the non-linearity, is considered, the prediction improves both at the centre of the valley and at the edge. It should be noted that the latter relationship is obtained by considering $G(\gamma)/G_0$ and $D(\gamma)$ curves different from those used for Montefranco, moreover it also takes into account the inhomogeneity of the V_S while in the present case the soil has a constant velocity. In addition, it should be noted that in this case the VAF is overestimated in the area closest to the bedrock, where the analysis shows a VAF of less than 1.

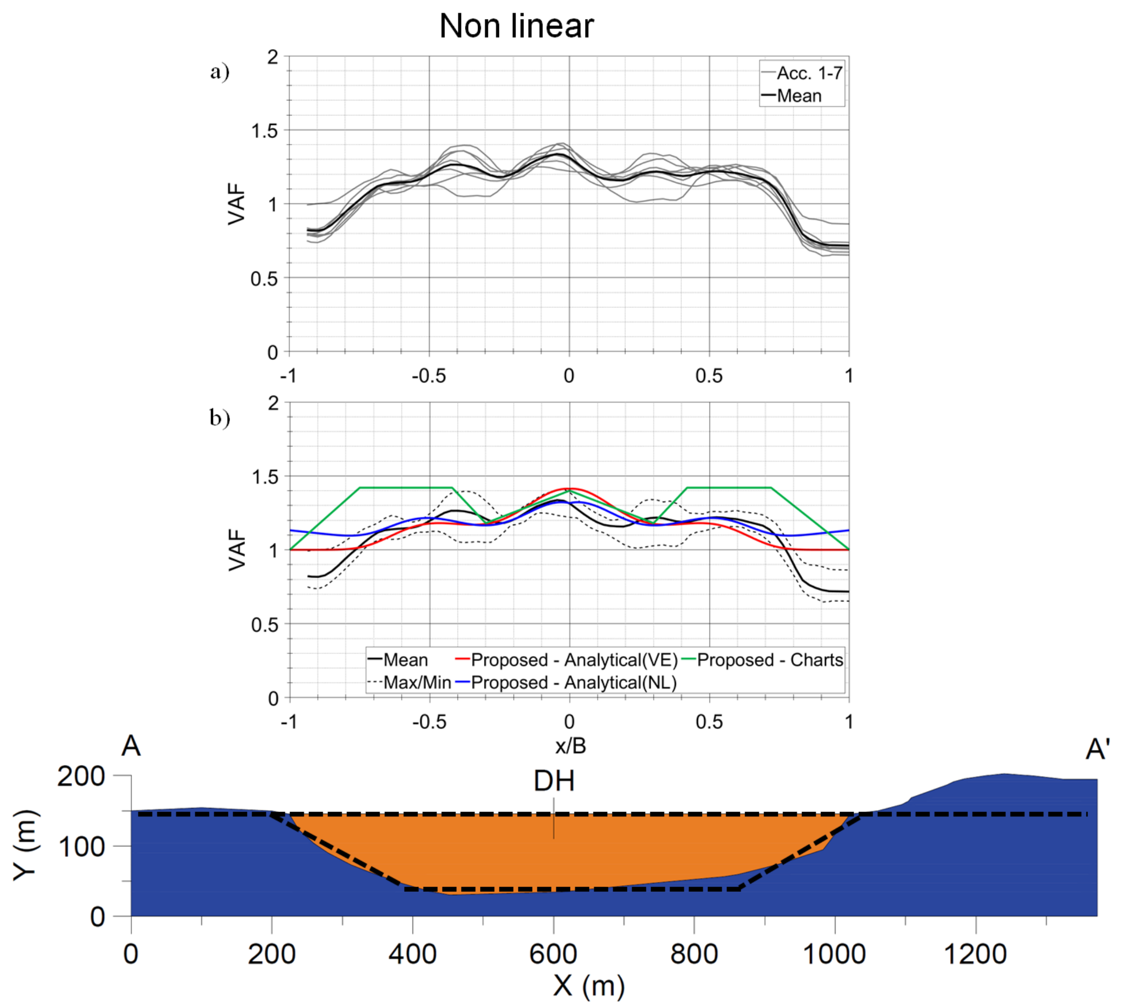

Figure V.3.6 – Comparison between the VAF calculated for the 7 input motions and those proposed in this study, for non-linear analysis and section AA'

Figure V.3.7a,b,c,d show the comparisons among the mean response spectra obtained at the valley centre with either 1D (blue line) or 2D (green line) visco-elastic (a, b) and non-linear (c, d) analyses, and those obtained applying the proposed procedure to the spectra specified by NTC 2018 and those computed at the centre of the valley by 1D analysis. In details, Figure V.3.7a,c report the spectrum obtained by multiplying that suggested by NTC 2018 for class C soil by the VAF calculated with Eq. III.5.3 (simplified approach), while in Figure V.3.7b,d the mean 1D spectrum computed along the profile at the centre of the valley is multiplied by the same VAF (standard approach).

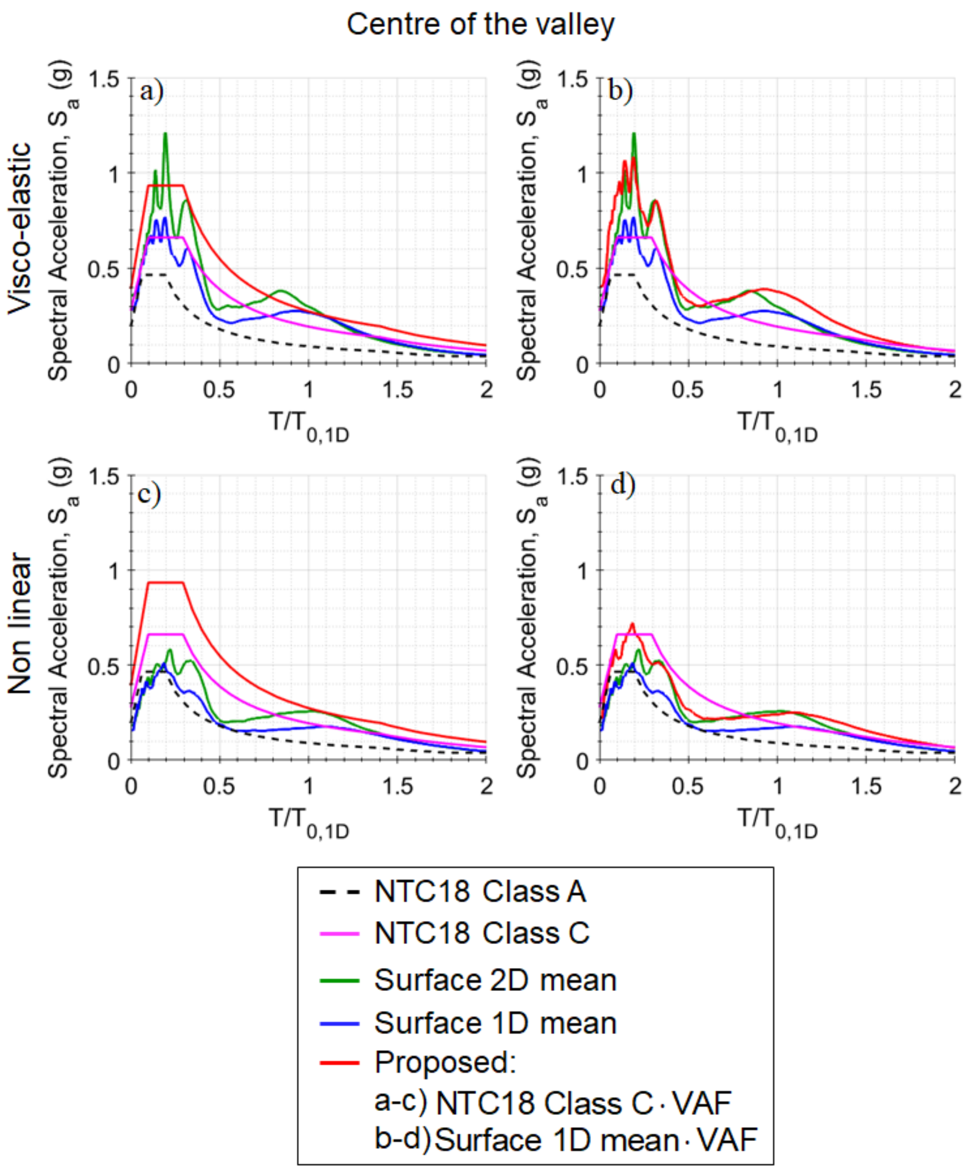

Figure V.3.7 – Spectra obtained from visco-elastic (a, b) or non-linear (c, d) analyses versus those calculated with the simplified (a, c) or standard (b, d) approaches with VAF resulting from Eq. III.5.3, at the centre of Montefranco valley

For the visco-elastic case, the proposed model catches well the trend of the 2D spectrum both using approach, standard and simplified. In this case, the spectrum of NTC 2018 for class C approximates moderately good the trend of the 1D spectrum, except for periods close to the 1D resonance period. In the non-linear case the simplified approach (red line in Figure V.3.7c) overestimates the numerical response because the NTC spectrum does not accurately consider the non-linearity. On the other hand, in the case of the standard approach (Figure V.3.7d) the non-linearity is effectively accounted in the 1D site response (blue line) leading to a better match between the numerical and the proposed spectra.

The findings obtained for the valley centre are confirmed by examining the spectra obtained for x/B=0.5 (Figure V.3.8), corresponding to the position of the peak VAF value along the valley edge. As a matter of fact, in the hypothesis of visco-elastic soil behaviour the proposed procedure fairly predicts the 2D response whatever the approach followed (Figure V.3.8a,b), while the simplified (Figure V.3.8c) and standard (Figure V.3.8d) approaches respectively overestimates and slightly underestimates the response spectra predicted through 2D non-linear analyses.

Figure V.3.9 demonstrates that 2D motion at the centre of the Montefranco valley is well captured also using the proposed charts. On the other hand, at x/B=0.5 (Figure V.3.10), both approaches significantly overestimate the 2D response predicted by visco-elastic analyses (Figure V.3.10a,b), while by following standard approach the charts lead to a better prediction of the non-linear response (Figure V.3.10d).

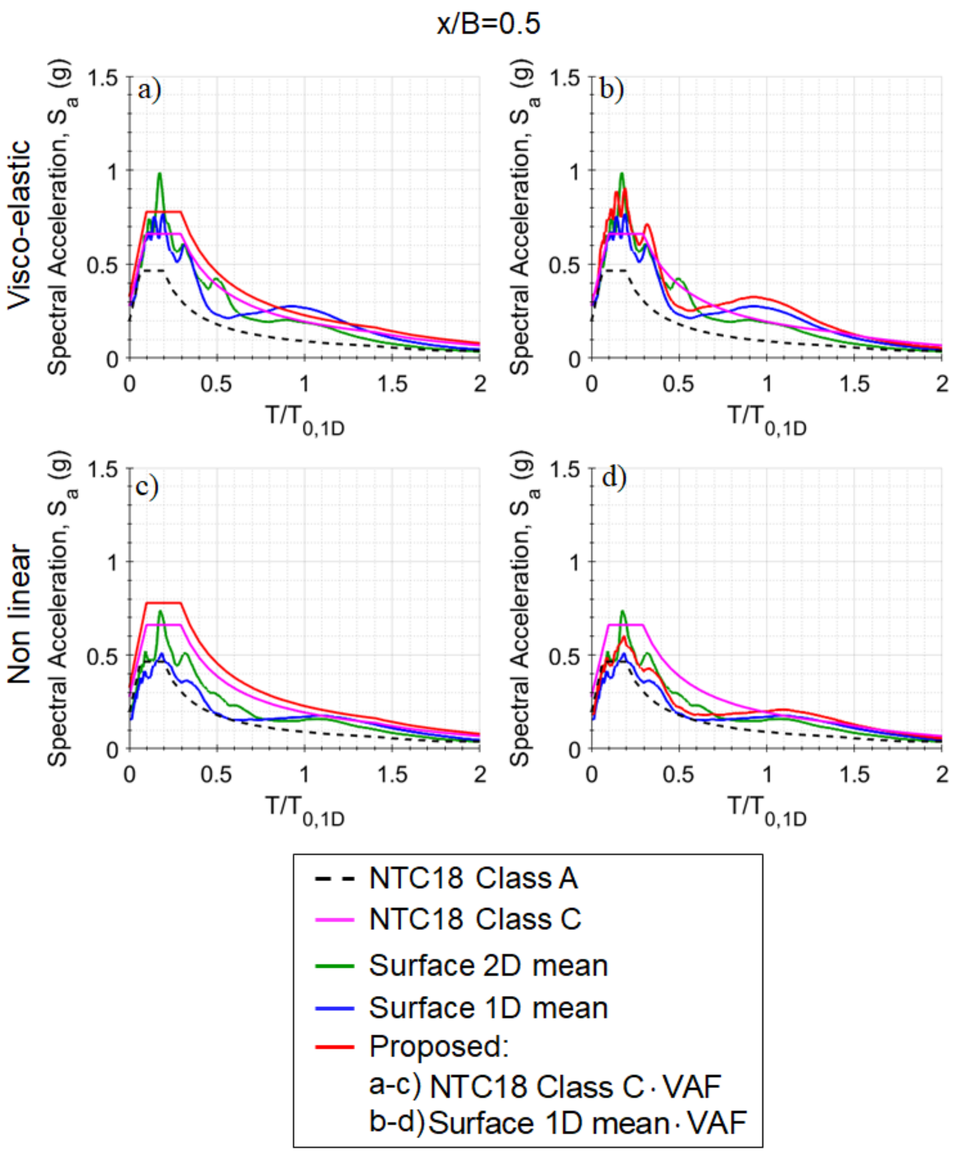

Figure V.3.8 – Spectra obtained from visco-elastic (a, b) or non-linear (c, d) analyses versus those calculated with the simplified (a, c) or standard (b, d) approaches with VAF resulting from Eq. III.5.3, at the position x/B = 0.5 along Montefranco valley

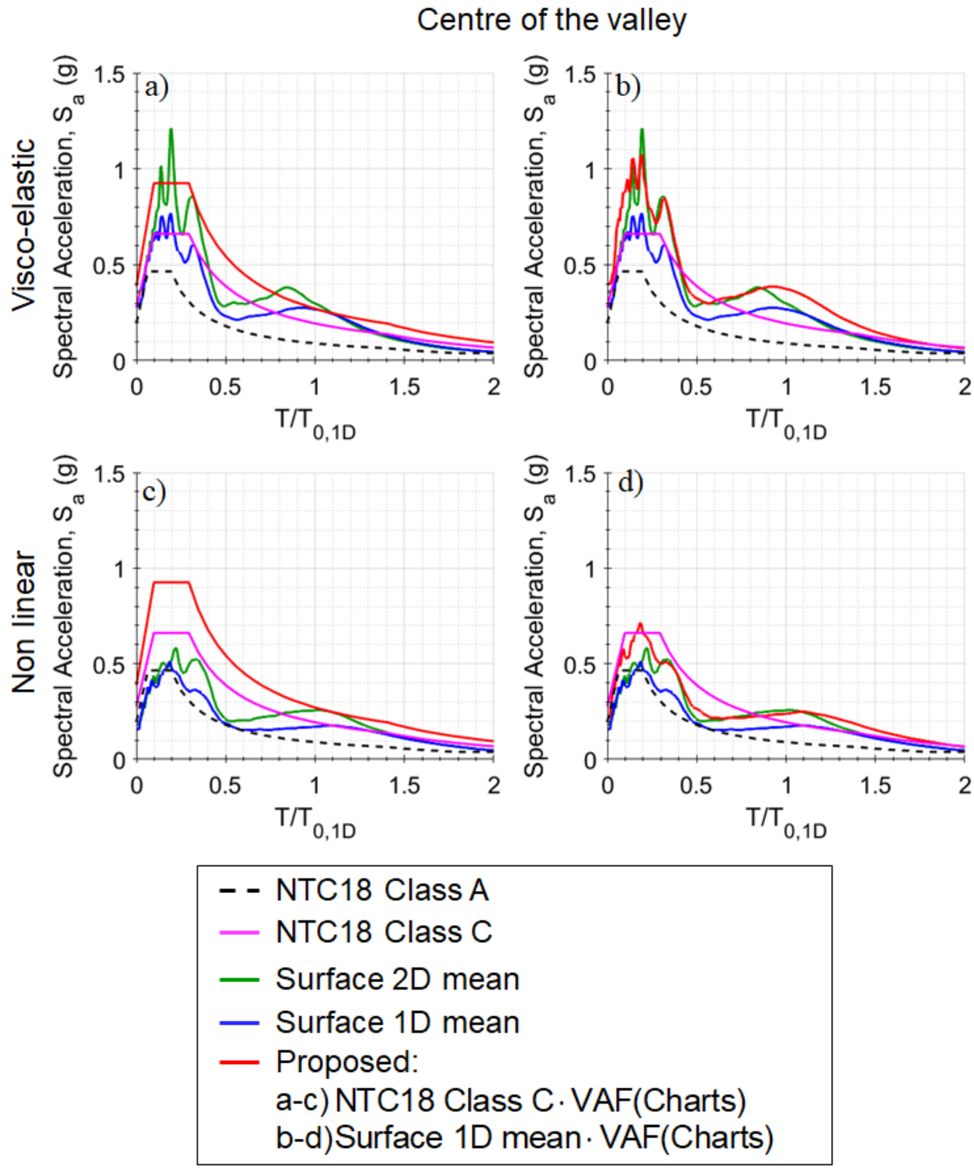

Figure V.3.9 – Spectra obtained from visco-elastic (a, b) or non-linear (c, d) analyses versus those calculated with the simplified (a, c) or standard (b, d) approaches with VAF resulting from the charts, at the centre of Montefranco valley

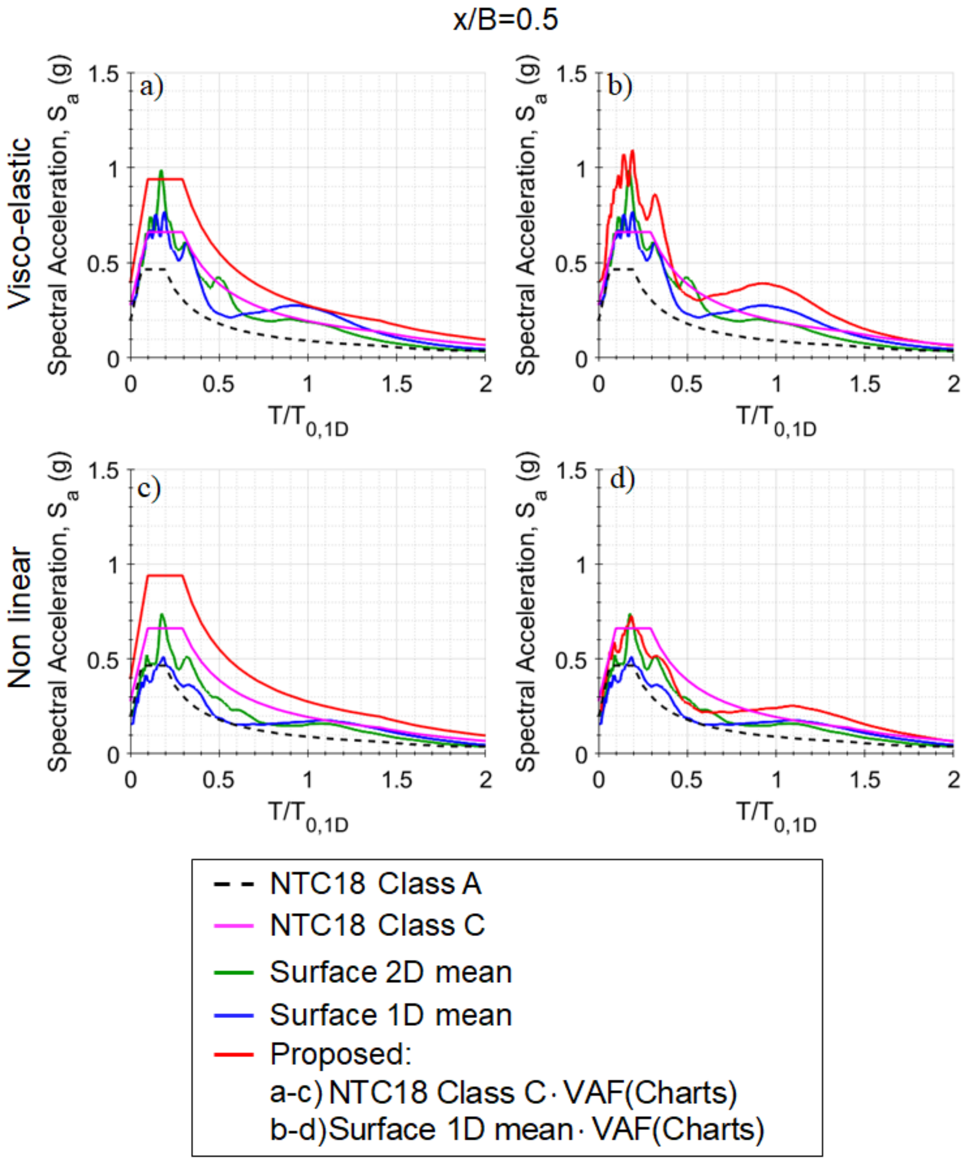

Figure V.3.10 – Spectra obtained from visco-elastic (a, b) or non-linear (c, d) analyses versus those calculated with the simplified (a, c) or standard (b, d) approaches with VAF resulting from the charts, at the position x/B = 0.5 along Montefranco valley

V.3.2 Pretare and Piedilama

Pretare and Piedilama are two hamlets of Arquata del Tronto, located in the same alluvial valley and heavily damaged by the 2016 Central Italy seismic sequence (Figure V.2.3). A seismic microzonation study (Bellaveglia et al., 2018) has been carried out for them following the 2016 events and its results are used to carry out the numerical analyses. In the above-mentioned study, numerous investigations were carried out that allowed to reproduce the geological and geotechnical model of the area. These included a DH at the valley edge of section AA' (Figure V.3.11b) and various HVSR measurements and MASW tests which allowed to obtain the V_S and V_P values to be adopted in the numerical analyses. Table V.3.3 shows the main physical, mechanical and non-linear properties of the soils, while Figure V.3.12 shows the profile of V_S relevant to the depth range of each layer.

Table V.3.3 – Physical, mechanical and non-linear properties of Pretare and Piedilama (modified from Alleanza et al., 2019; Bellaveglia et al., 2018)

Layer	Field test	Soil	Unit weight γ (kN/m^3)	S wave velocity V_S (m/s)	P wave velocity V_P (m/s)	$G(\gamma)/G_0$ and $D(\gamma)$
Fc-q Fc-i_{sup}	MASW	Gravel and Sand	17.66	300	592	Modoni & Gazzellone (2010)
Fc-i_{inf}	DH		18.64	654	2300	
SM_{tf}	DH	Sand and Silt	17.66	332	655	d'Onofrio et al. (2010)
SM_{fd}		Silty Sand	19.62	736	1823	Anh Dan et al. (2001)
$ML_{(tf\text{-}fd)}$	DH	Clayey and Sandy Silt	18.64	564	1648	Ciancimino et al. (2019)
ML_{ec}	MASW	Silt and Clay with Sand	17.66	300	856	
GM	DH	Gravel and Sand	18.64	600	2205	Modoni & Gazzellone (2010)
ALS_{sup} ALS_{inf}	MASW	Weathered B. Bedrock (Flysch)	19.62	770 1300	2829 4777	Visco elastic with D_0=0.5%

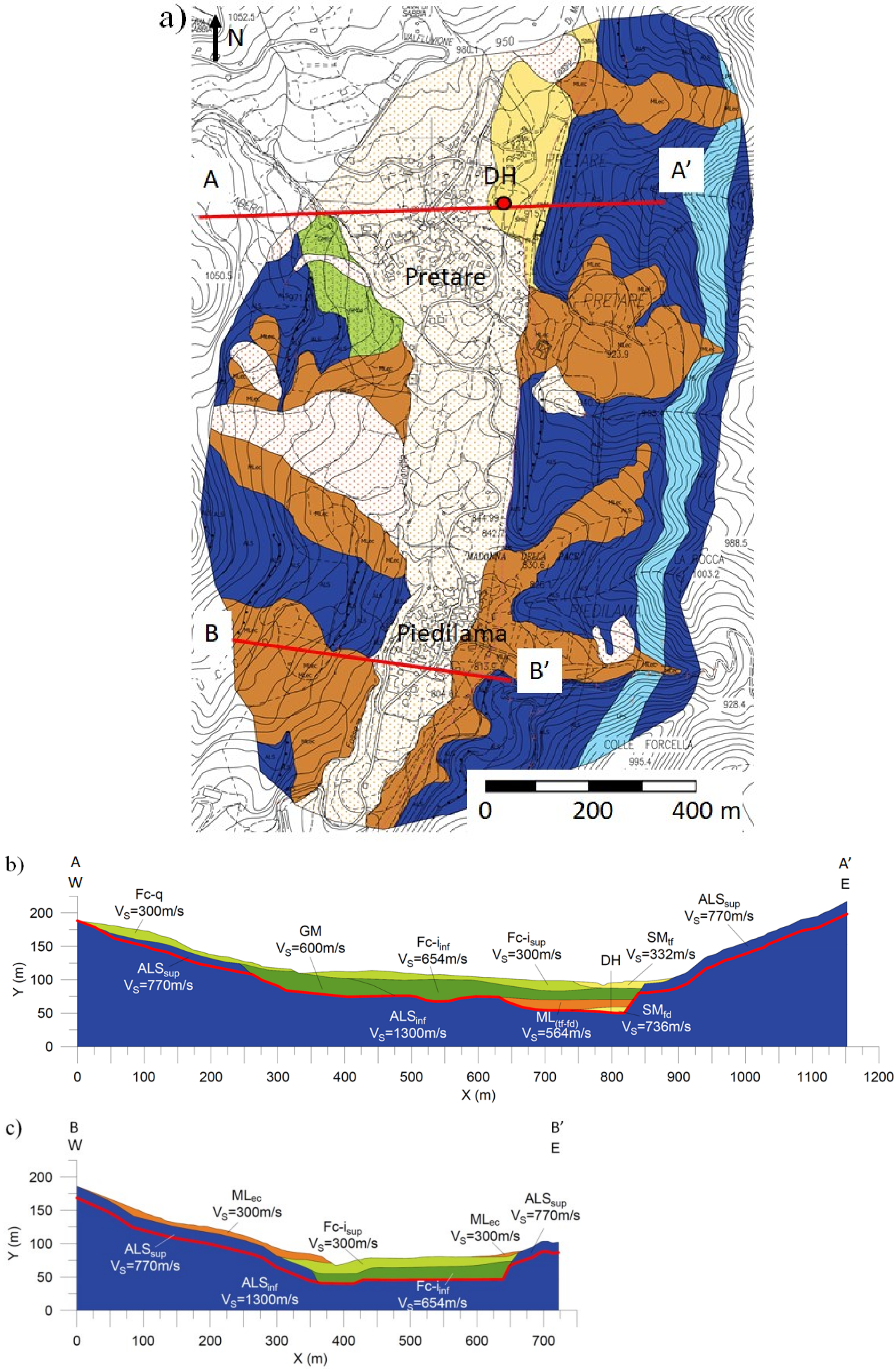

Figure V.3.11 – a) Geolithological map and b) section AA' of Pretare, c) section BB' of Piedilama (modified from Bellaveglia et al., 2018)

Typically, the shear wave velocity, V_S, of the shallower deposits is of the order of 300m/s, while the deeper layers are characterised by a V_S of 600m/s. The shallowest 15m of the outcropping bedrock are affected by weathering with a V_S=770m/s, while the deeper part of the formation is intact and has V_S=1300m/s.

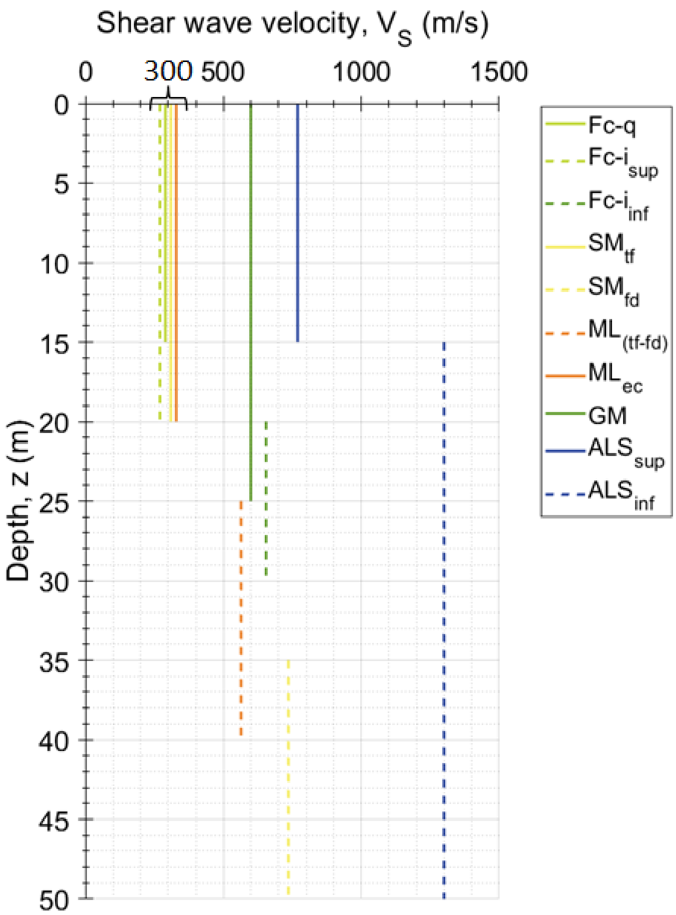

Figure V.3.12 – Profile of V_S adopted for the analysis of Pretare and Piedilama.

The G(γ)/G_0 and D(γ), curves have been assigned to the different soil on the basis of the experimental results of resonant column (RC) and torsional shear (TS) tests carried out on undisturbed samples retrieved from surrounding villages (Ciancimino et al., 2019) or on the basis of literature data on soils with similar grain size distribution (Table V.3.3).

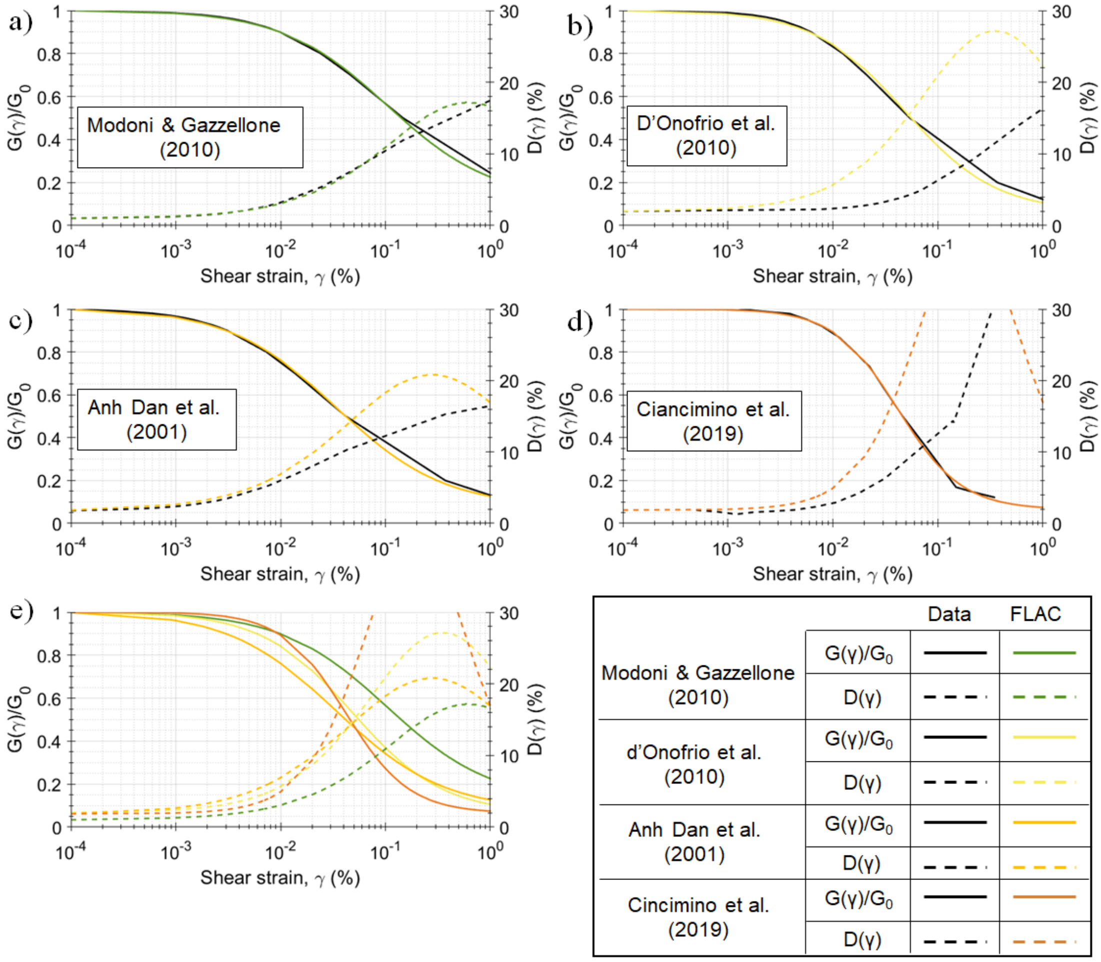

Figure V.3.13 – G(γ)/G₀ and D(γ) curves used for the analysis of Pretare and Piedilama.

Before carrying out the numerical analyses, the proposed charts have been used to estimate the behaviour of the two valleys (Figure V.3.14). The Pretare valley (Section AA') has a half-width of about 300m and a thickness of 45m, while for the Piedilama valley (Section BB') B=185m and H=35m, so that the shape ratio H/B is 0.15 and 0.19, respectively. The $V_{S,eq}$ for the two sections is similar: 575m/s for Pretare and 500m/s for Piedilama, thus the impedance ratio is about 2.5 for both. Both fall at the boundaries of the zone which divides the very shallow valleys from the shallow ones, therefore at the centre of the valley a VAF of 1.05-1.1 is expected for both, while at the edges a higher value is predicted.

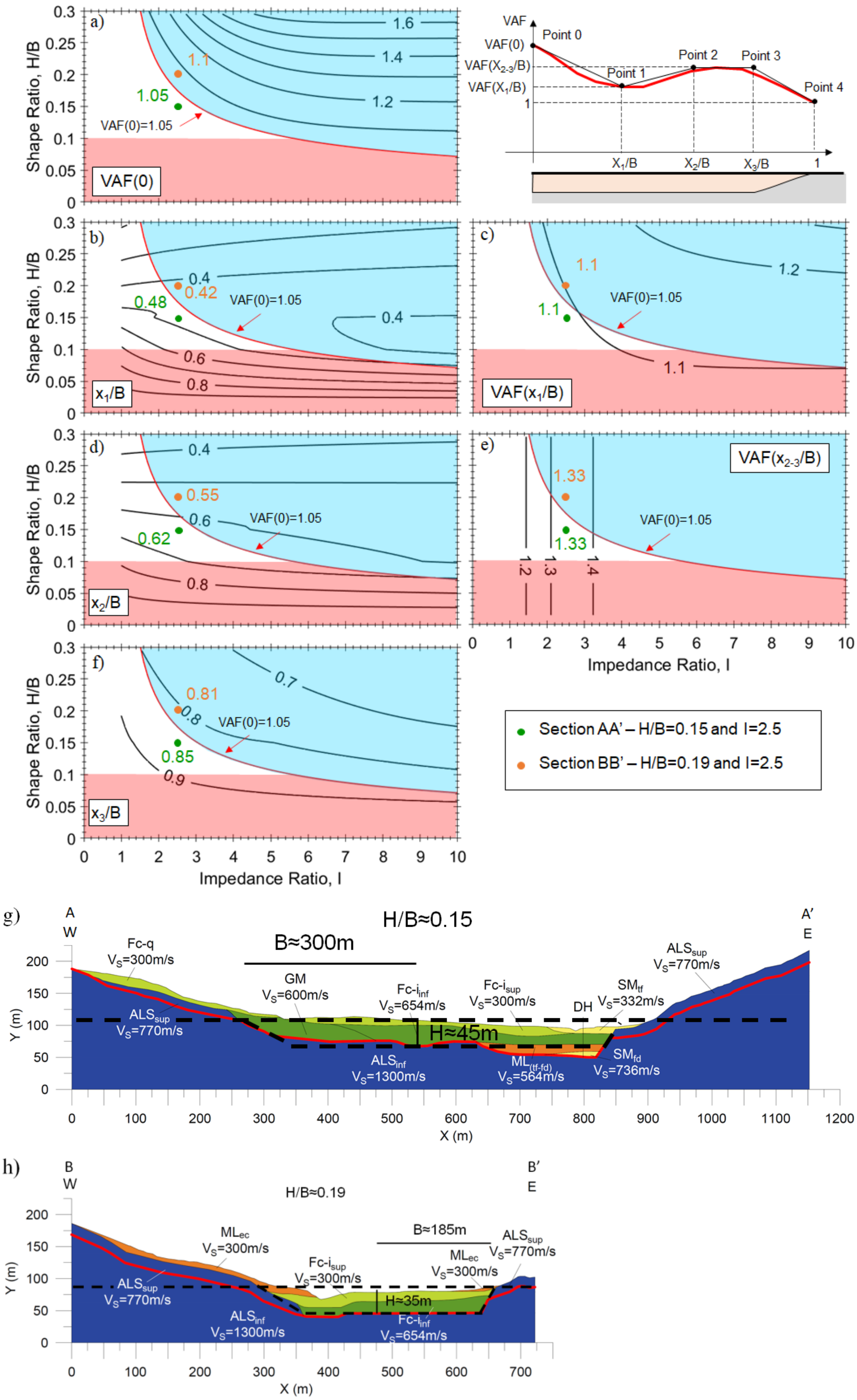

Figure V.3.14 – a-f) Proposed charts to estimate VAF; g,h) schematic valley considered to calculate the VAF for Pretare and Piedilama (black dashed lines).

The reference seismic motion used is composed of 7 accelerograms chosen using Rexel v3.5 (Iervolino et al., 2010), in a way that the mean spectrum is compatible with that provided by the Italian technical standards for subsoil class A and horizontal ground surface. Table V.3.4 shows the main properties of the selected signals, while Figure V.3.15a shows the comparison between the response spectra of the seven selected accelerograms, the mean and the one defined by NTC 2018 for class A. In Figure V.3.15b,c the same spectra are shown but with the periods scaled with respect to $T_{0,1D}$, equal to 0.31s for Pretare and 0.28s for Piedilama.

For both, the predominant periods are lower but close to the resonance ones and therefore both 1D and 2D effects are expected to be considerable.

Table V.3.4 – Main features of the 7 accelerograms selected for Pretare and Piedilama

Earthquake	Date	M_w	Epicentral Distance (km)	Station	Site class	Component
Italia Centrale	30/10/2016	6.5	27.7	Amatrice San Cipriano	A	N-S
Italia Centrale	26/10/2016	5.4	27.9	Poggio Vitellino	A	E-W
Italia Centrale	30/10/2016	6.5	18.6	Accumoli	A	N-S
Italia Centrale	26/10/2016	5.9	10.8	Castelluccio di Norcia	A	E-W
Italia Centrale	26/10/2016	5.9	10.8	Castelluccio di Norcia	A	N-S
Italia Centrale	30/10/2016	6.5	19.2	Montemonaco	A	N-S
Italia Centrale	30/10/2016	6.5	10.5	Avendita PG	A	N-S
	Mean	6.2	17.9			

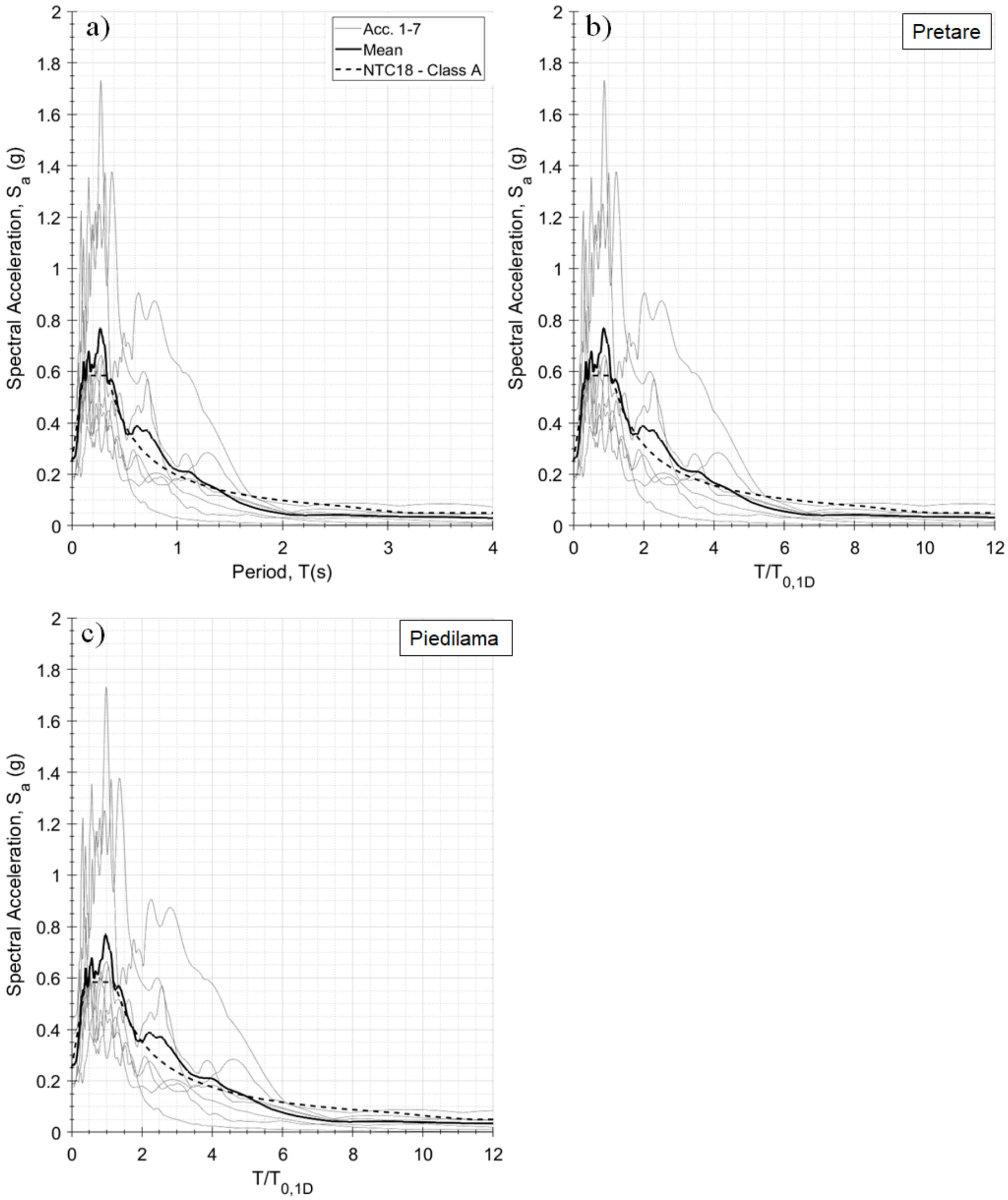

Figure V.3.15 – Comparison between the response spectra of the 7 and mean accelerogram considered, and those obtained with NTC 2018.

Figure V.3.16 shows the VAF calculated by the visco-elastic soil model for the 7 accelerograms, the mean trend and those obtained using the proposed equations and charts, for Pretare. It can be seen that there are two significant peaks at the valley edges, while VAF in the centre is close to unity. The proposed models fail to estimate the location of the maximum VAF and its value. This is due to the fact that the valley has a very complex buried geometry while the proposed VAFs are obtained considering homogeneous trapezoidal valleys.

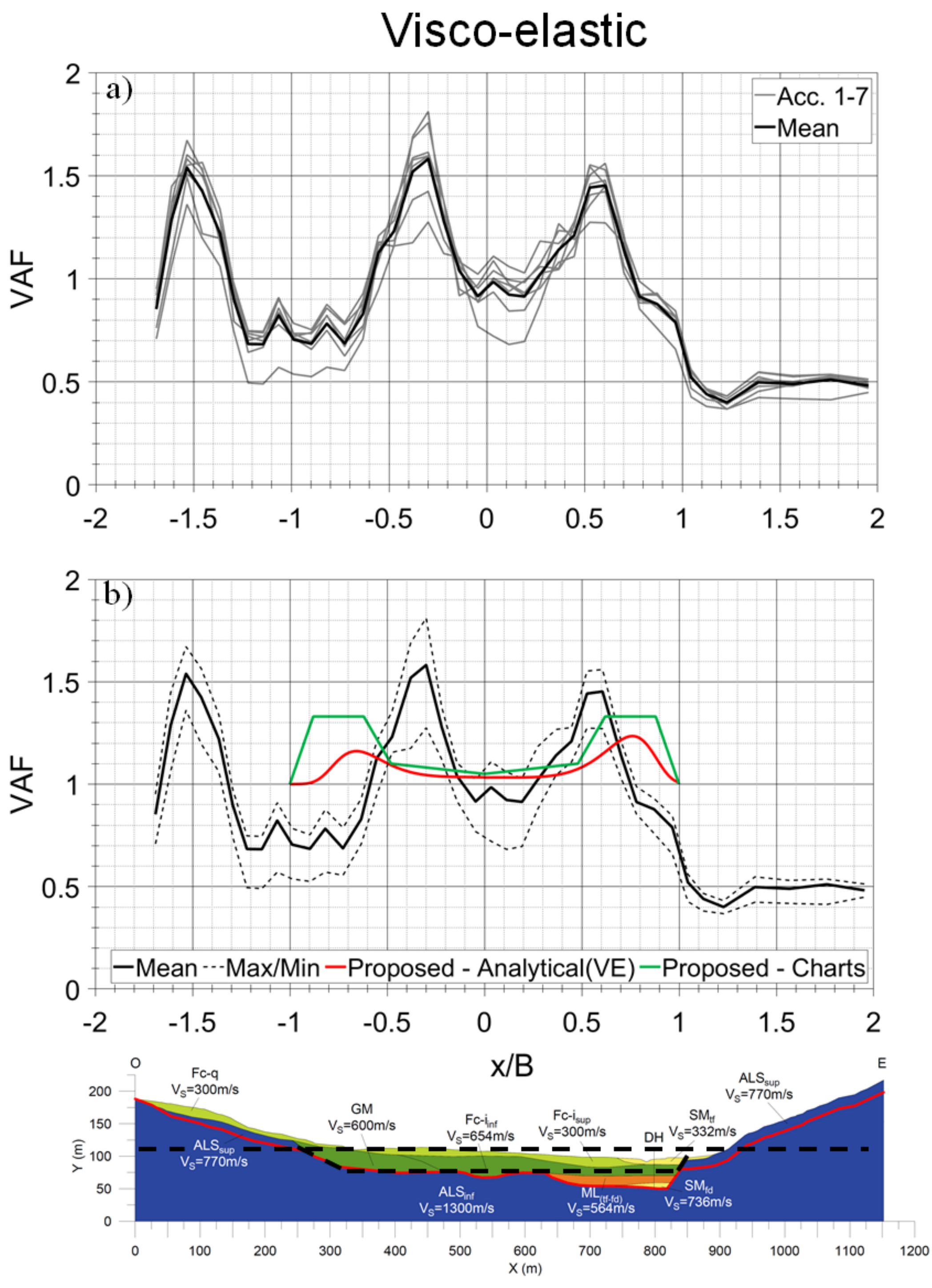

Figure V.3.16 – Comparison between the VAF calculated for the 7 input motions and those proposed in this study, for visco-elastic analysis and section AA' of Pretare.

This is an additional evidence that the 2D motion is strongly influenced by the real geometry of the valley, and therefore the results proposed in this study should be used only in the presence of geometries and properties similar to the ones with which these results are obtained. In this case, the dynamic behaviour of the valley is probably most influenced by the fact that between the superficial and the deep layers of soil there is more or less the same impedance ratio as between the bedrock and these deep deposits. Furthermore, at the right edge (x/B=0.9-1) there is the presence of the inclined weathered bedrock layer which affects the propagation paths of the seismic waves. In addition, between x/B=0.5-1, the stratigraphy is very complex with several changes of material, and there is also an inversion of the V_S profile.

Figure V.3.17 shows the same results considering non-linear soil behaviour. In this case, the calculated VAF is very similar to that resulting from visco-elastic analyses and presents the same trends.

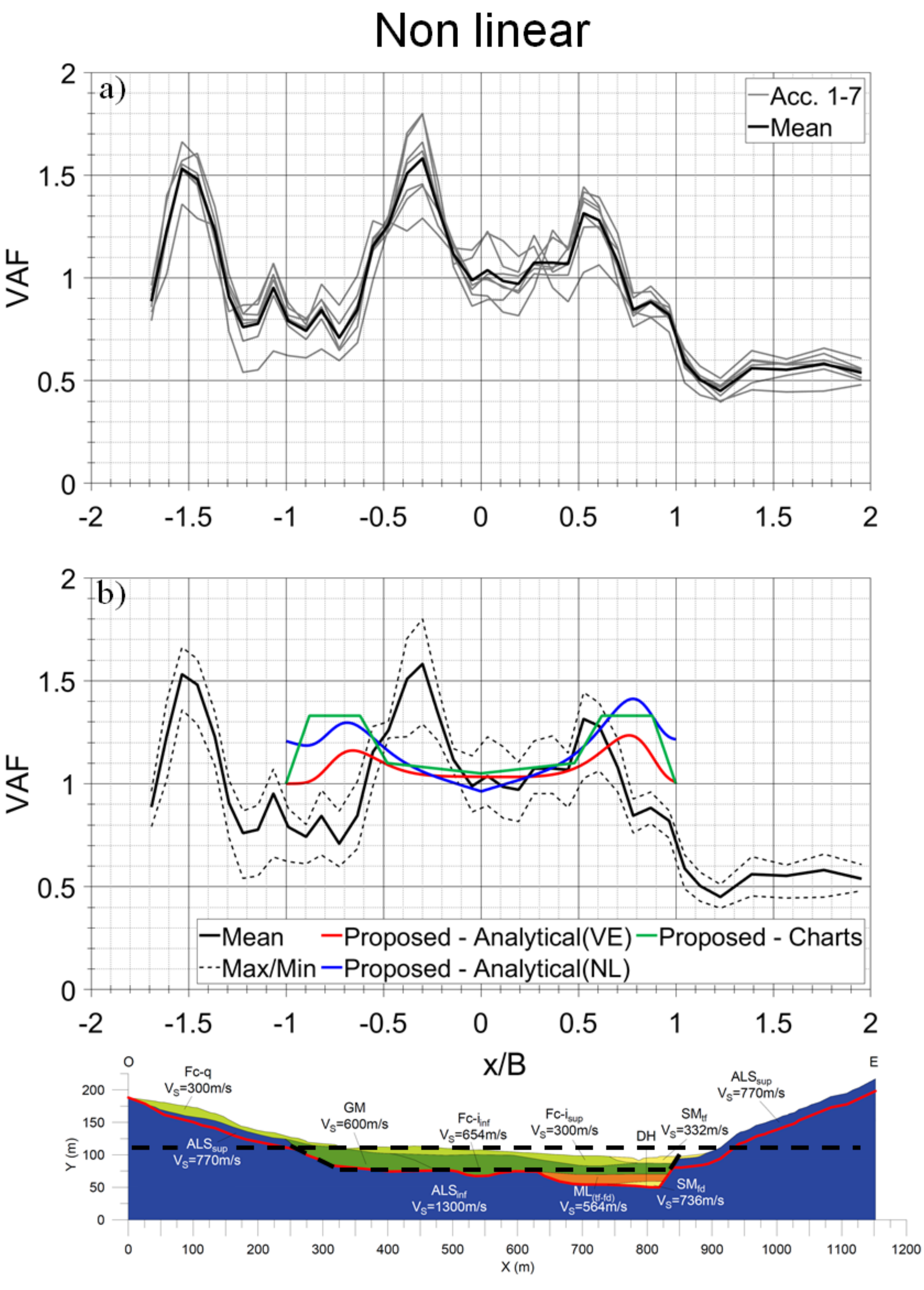

Figure V.3.17 – Comparison between the VAF calculated for the 7 input motions and those proposed in this study, for non-linear analysis and section AA' of Pretare.

Figure V.3.18 shows the comparisons between the mean spectra calculated at the centre of the valley with the 1D analysis (blue line), the 2D analysis (green line), the

NTC 2018 one for classes A and B and that proposed with the two approaches (red line).

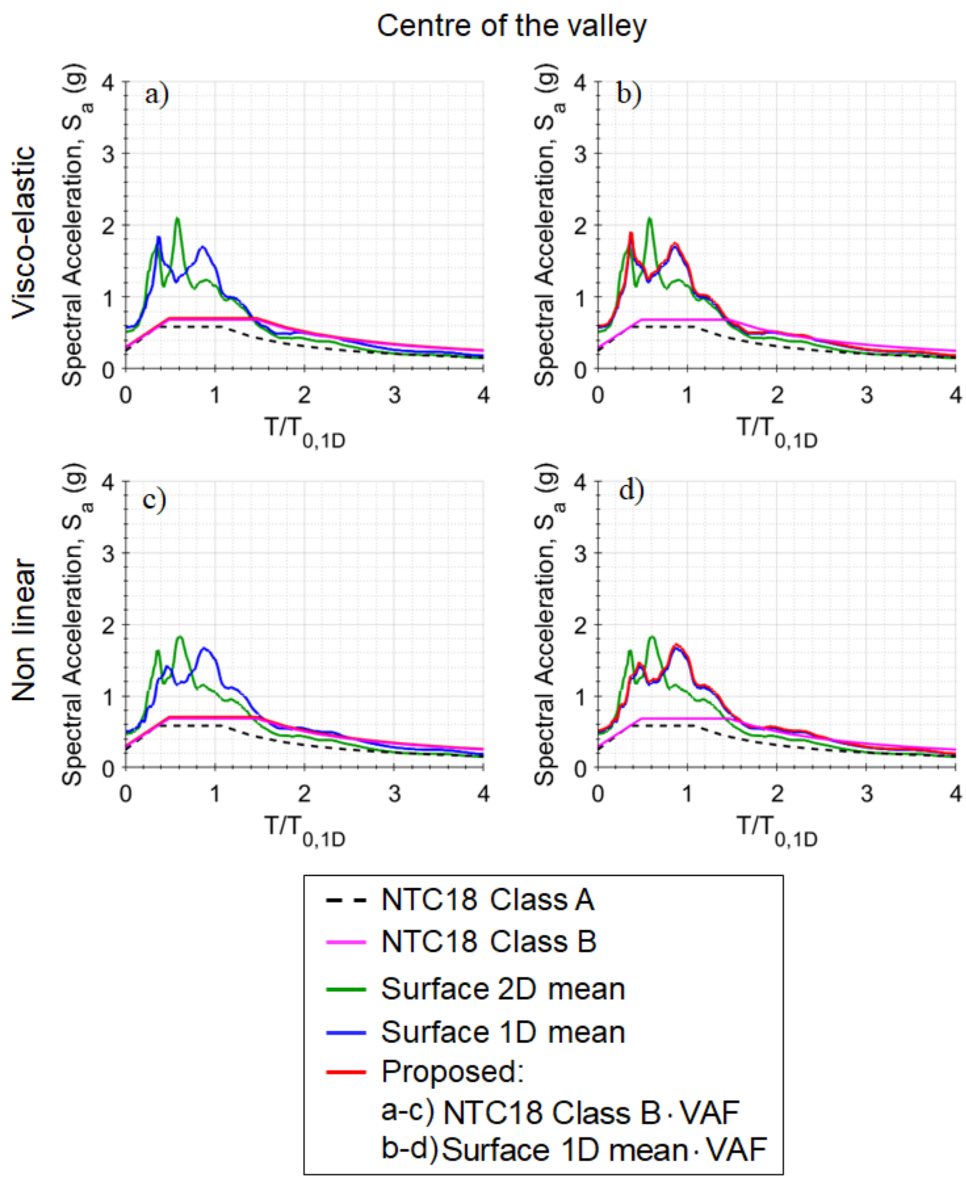

Figure V.3.18 – Spectra obtained from visco-elastic (a, b) or non-linear (c, d) analyses versus those calculated with the simplified (a, c) or standard (b, d) approaches with VAF resulting from Eq. III.5.3, at the centre of Pretare valley.

It should be noted that the VAF at the centre of the valley is almost unitary, thus on average the ratio between the 2D and 1D spectra is also unitary, however this does not imply that they are coincident. Indeed, in this case the two types of analysis show different predominant periods on the surface while the areas of the spectra are on average comparable. This happens for both visco-elastic (Figure V.3.18a,b) and non-linear soil models (Figure V.3.18c,d), and suggests that more research on the VAF still needs to be able to take into account the dependence of the period. Thus, the proposed models with standard approach (red line Figure V.3.18b,d) fail to capture properly the trend of the 2D spectrum because it uniform amplifies the 1D spectrum and does not take into account the variability of the 2D compared to the 1D response with period. Note that in this case the simplified approach (red line in Figure V.3.18a,c) completely misses the prediction.

Figure V.3.19 shows the same comparisons for x/B=-0.3, where the maximum numerical VAF is located. In this case, all the prediction weaknesses outlined above are highlighted, and they are magnified because the predicted VAF is significantly lower than the calculated one.

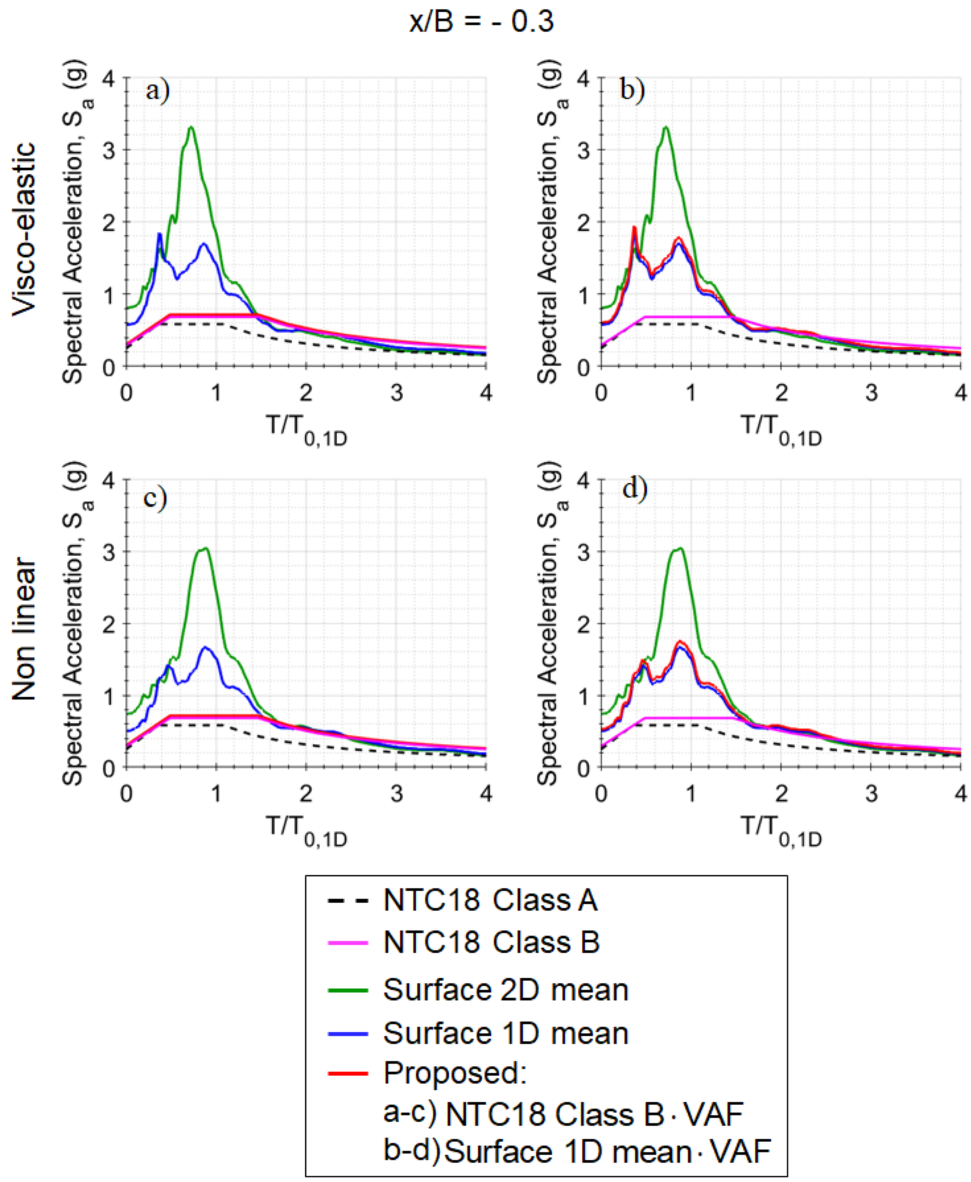

Figure V.3.19 – Spectra obtained from visco-elastic (a, b) or non-linear (c, d) analyses versus those calculated with the simplified (a, c) or standard (b, d) approaches with VAF resulting from Eq. III.5.3, at the position x/B = -0.3 along Pretare valley

Figure V.3.20 and Figure V.3.21 show the same kind of comparisons, but in this case the VAF has been obtained with charts. The predictions do not change significantly, and the same trends as above are found.

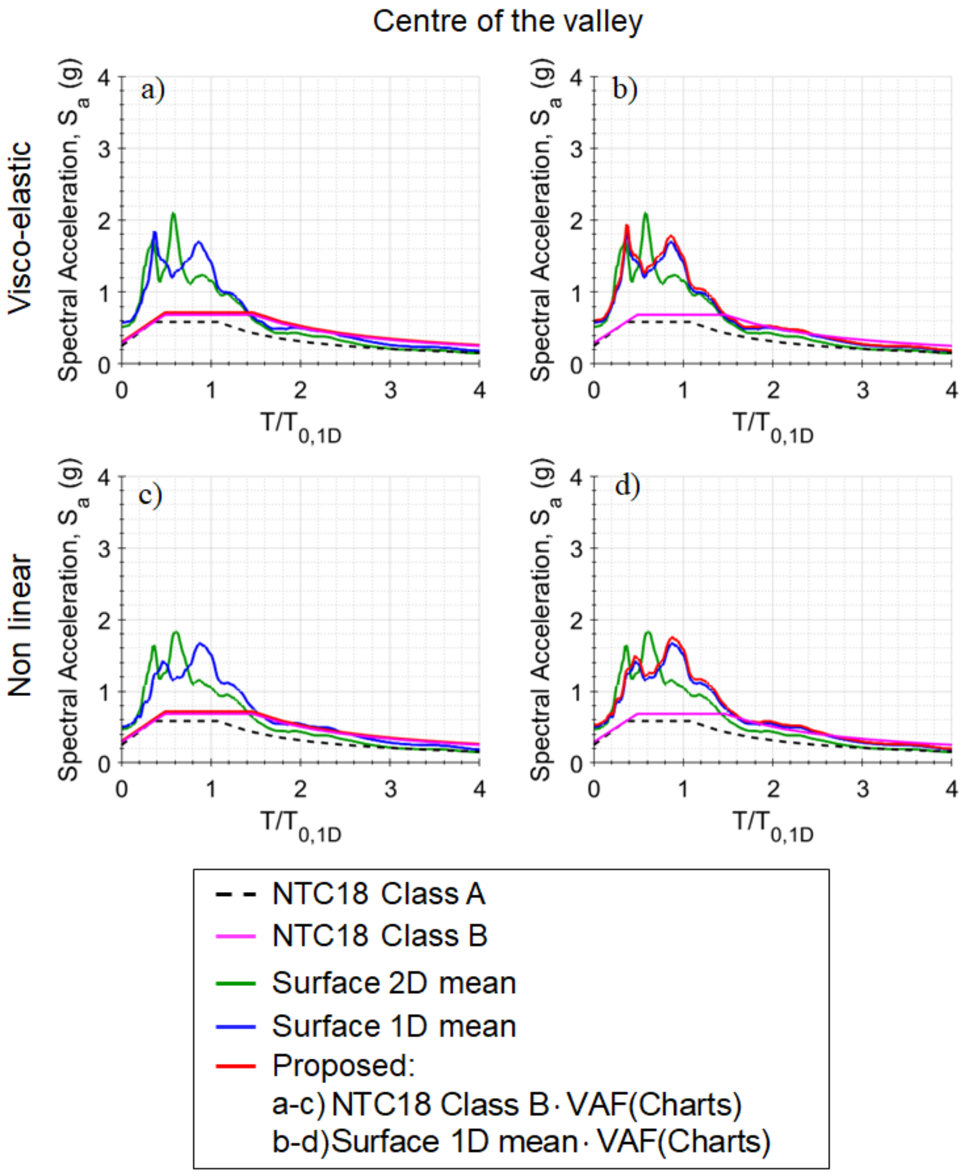

Figure V.3.20 – Spectra obtained from visco-elastic (a, b) or non-linear (c, d) analyses versus those calculated with the simplified (a, c) or standard (b, d) approaches with VAF resulting from charts, at the centre of Pretare valley.

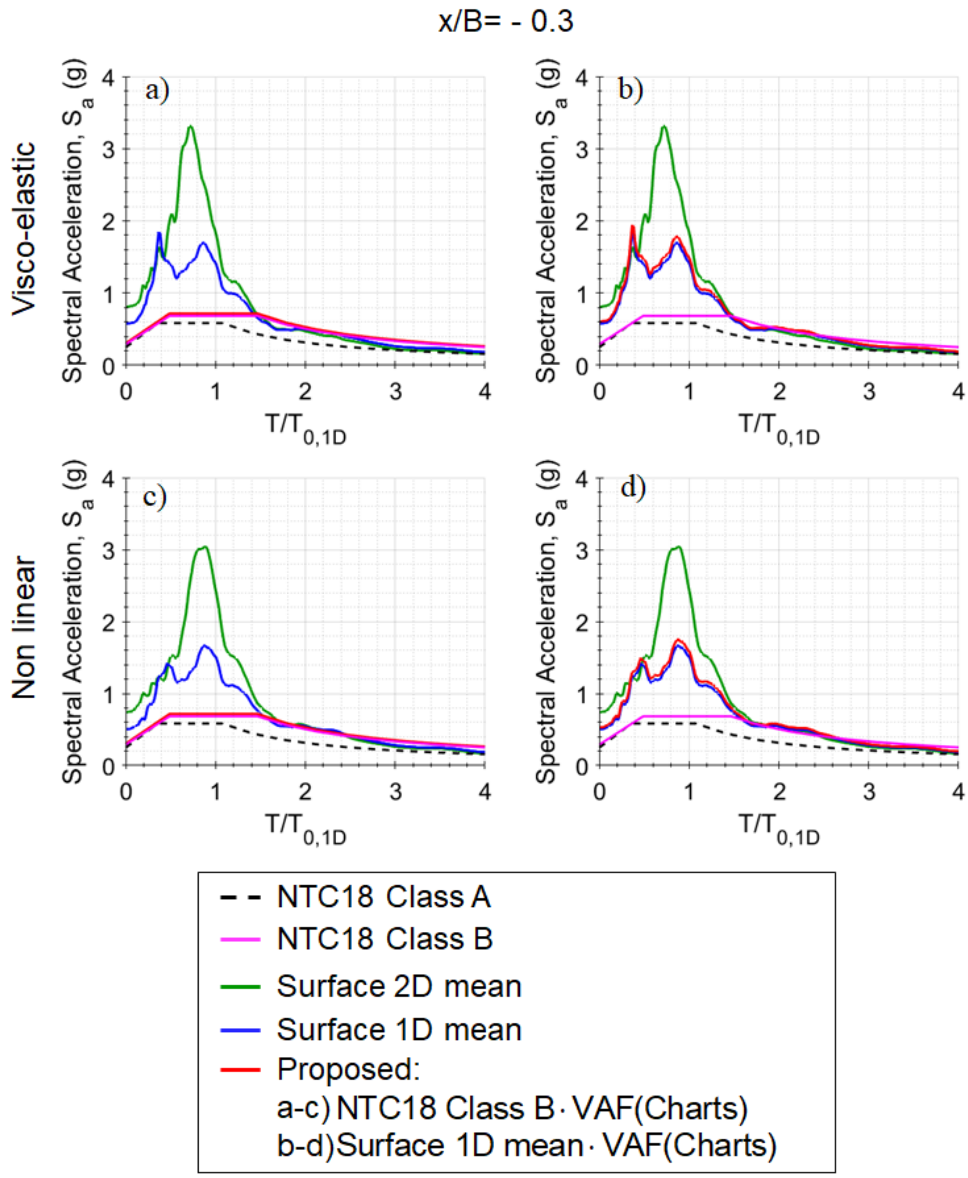

Figure V.3.21 – Spectra obtained from visco-elastic (a, b) or non-linear (c, d) analyses versus those calculated with the simplified (a, c) or standard (b, d) approaches with VAF resulting from charts, at the position x/B = -0.3 along Pretare valley

Figure V.3.22 shows the VAF predicted by visco-elastic analyses for section BB' of Piedilama. In this case, the proposed procedure better predicts the VAF, but it must be noted that at the left edge (x/B=-0.7) that obtained with Eq. III.5.3 (red line) has a lower amplitude, even if the zone of maximum amplification is quite accurately detected. On the other hand, at the right edge (x/B=0.5-1), the combined effects of topography and of the weathered bedrock shift the position of the lateral peak closer to the centre of the valley. The charts well predict VAF at the left edge, while they fail to capture its values at the right edge.

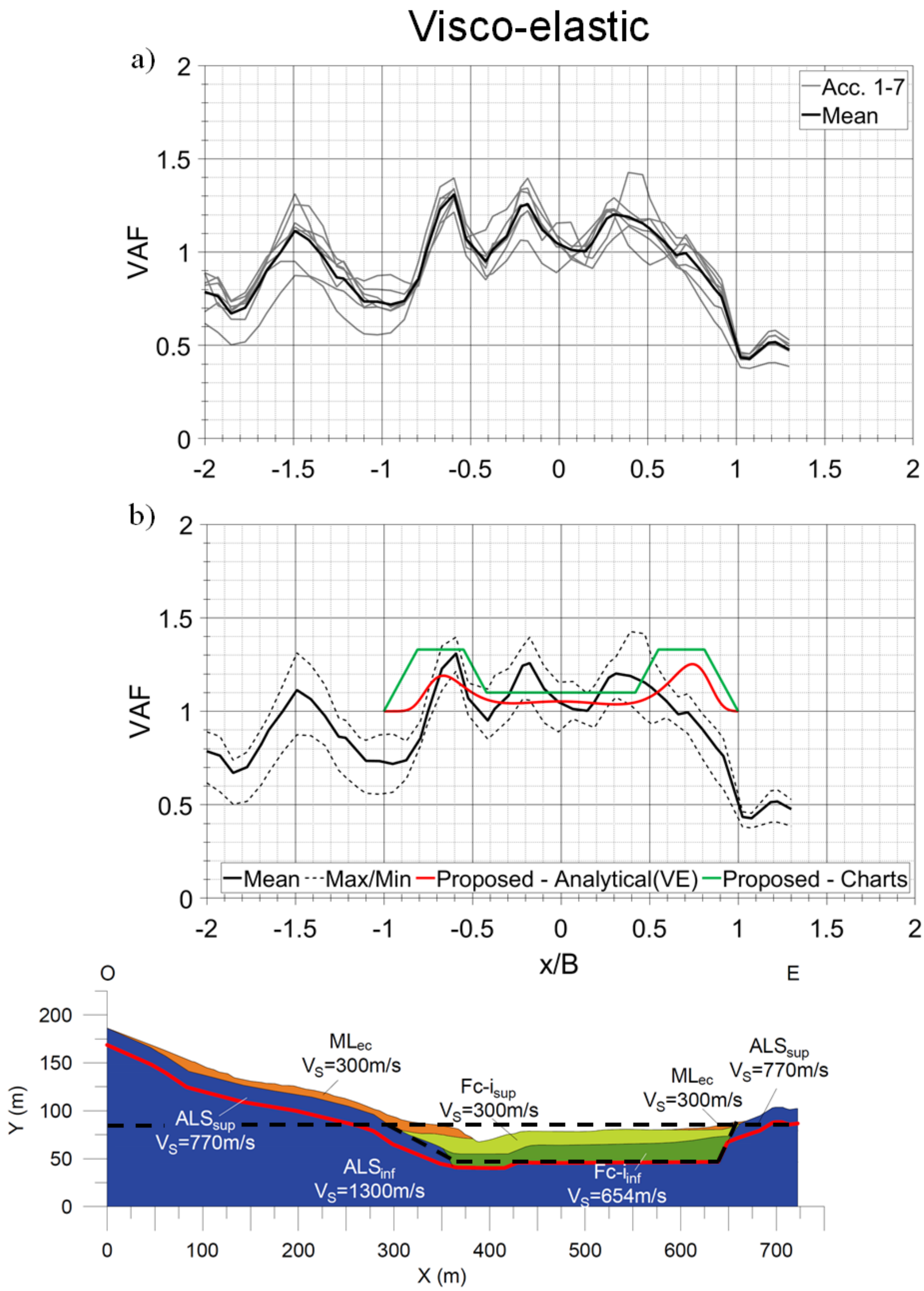

Figure V.3.22 – Comparison between the VAF calculated for the 7 input motions and those proposed in this study, for visco-elastic analysis and section BB' of Piedilama.

The VAF resulting from non-linear analyses (Figure V.3.23) has a lower value; note that the prediction at the left side improves while the right side is still inadequate.

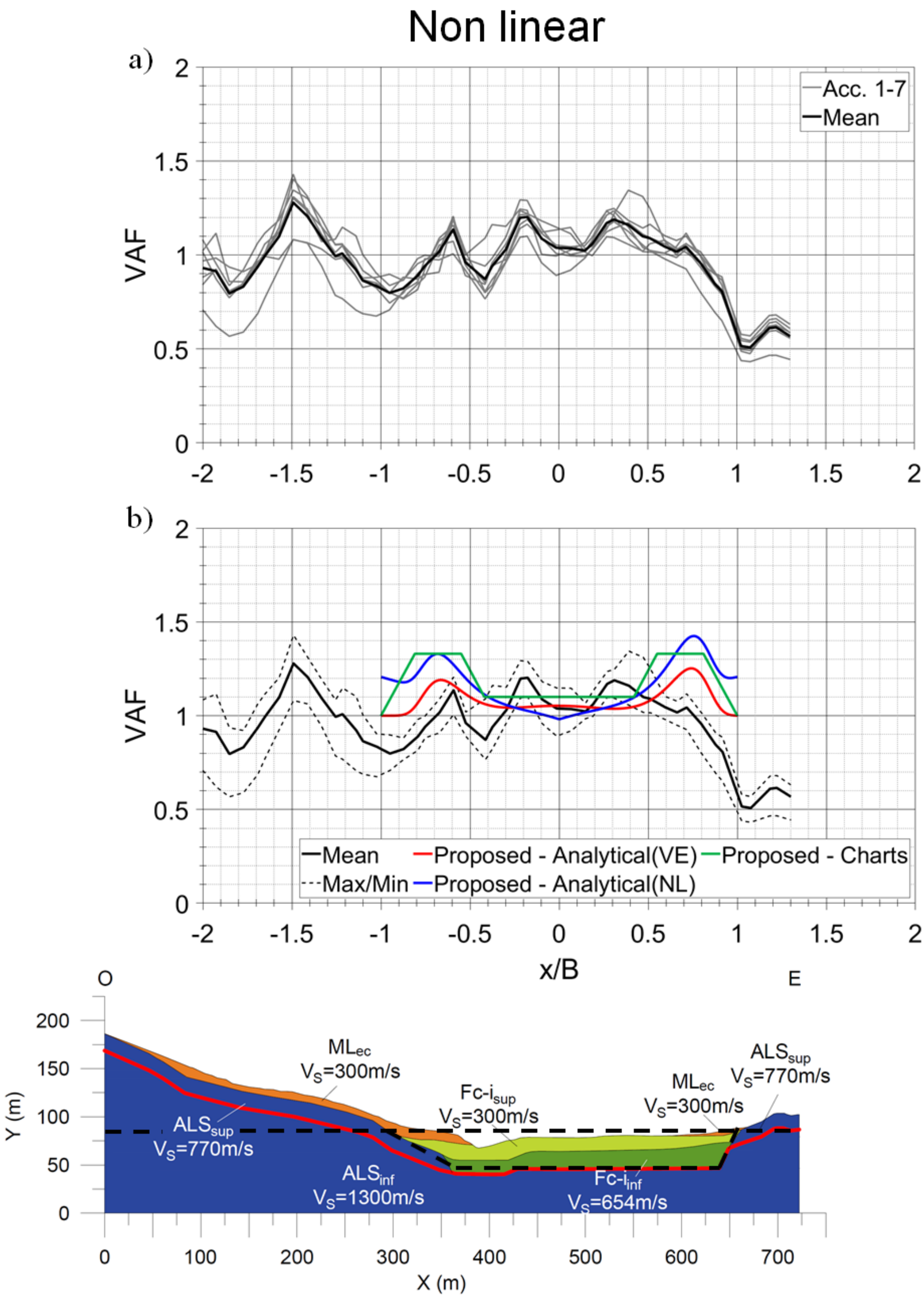

Figure V.3.23 – Comparison between the VAF calculated for the 7 input motions and those proposed in this study, for non linear analysis and section BB' of Piedilama.

Figure V.3.24 shows the comparison between the spectra obtained at the centre of the valley from the different analyses and those estimated with the two approaches proposed. In this case, the 1D spectrum already closely reproduces the 2D one and the prediction improves a bit using standard approach (Figure V.3.24b,d), while that of simplified one (Figure V.3.24a,c) is not so satisfying because it underestimates the amplification.

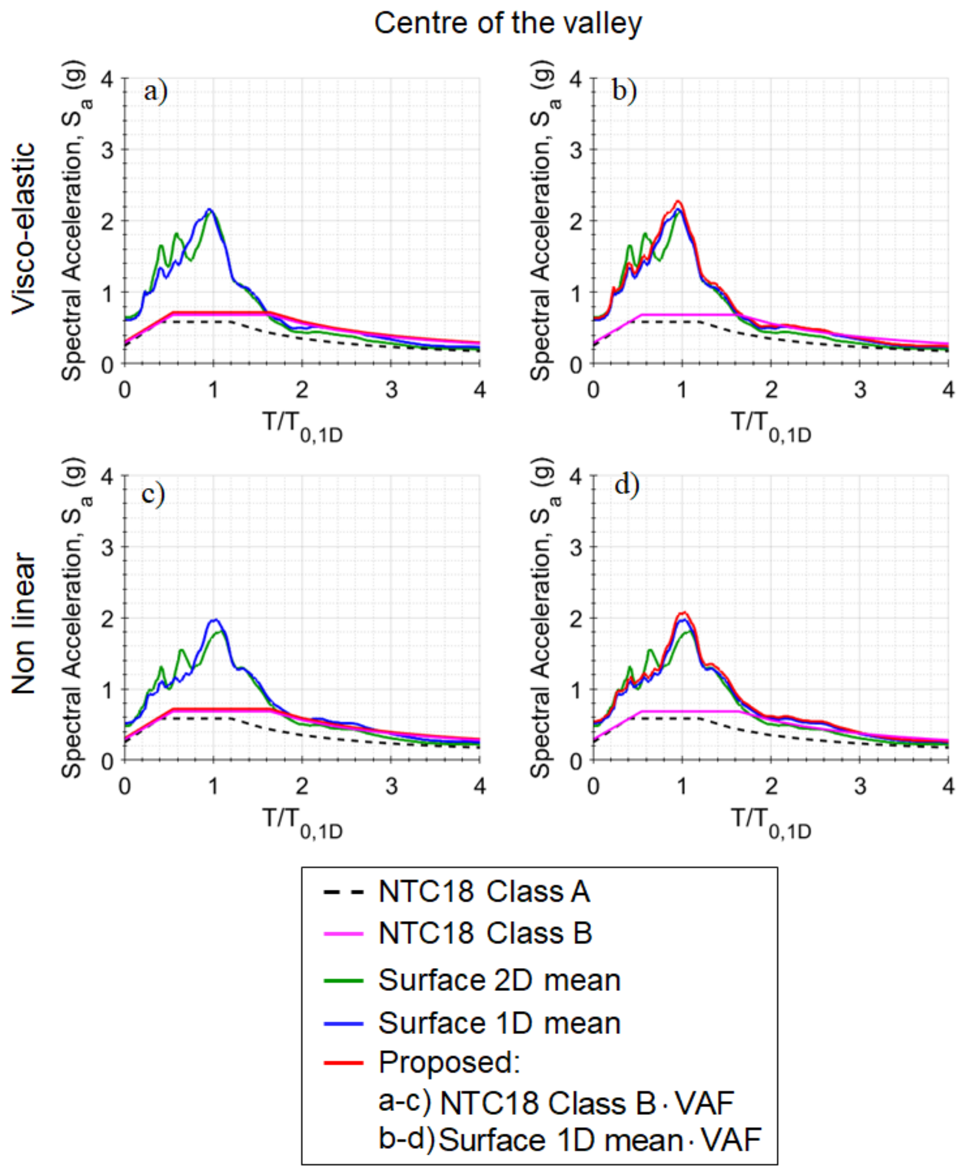

Figure V.3.24 – Spectra obtained from visco-elastic (a, b) or non-linear (c, d) analyses versus those calculated with the simplified (a, c) or standard (b, d) approaches with VAF resulting from Eq. III.5.3, at the centre of Piedilama valley.

Figure V.3.25 shows the same comparisons but for x/B= -0.65, i.e. at the peak of VAF at the left-edge. In this case the simplified approach (Figure V.3.25a,c) is still not satisfying while the standard one (Figure V.3.25b,d) marginally underestimates the results of visco-elastic analyses and lightly overestimates those of non-linear simulations.

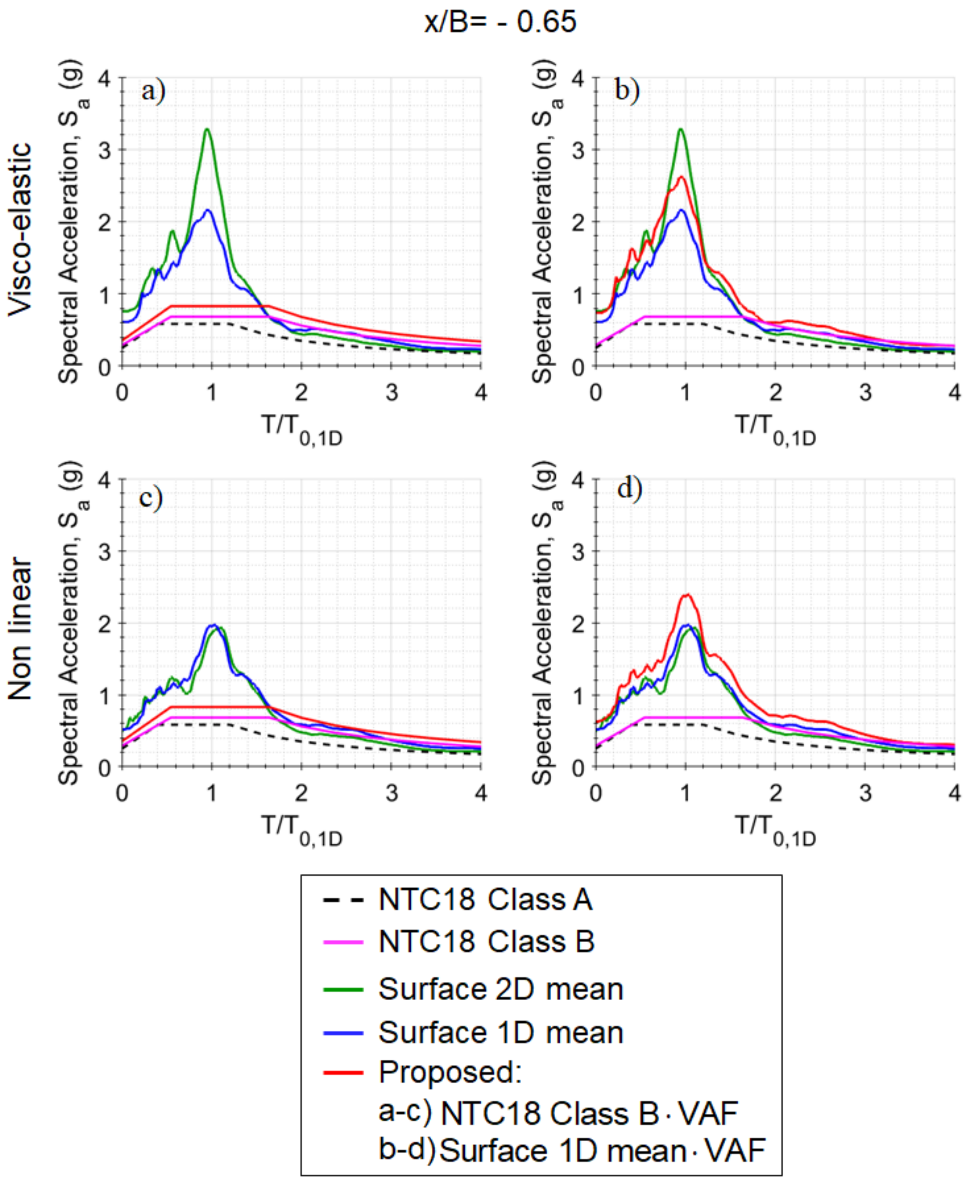

Figure V.3.25 – Spectra obtained from visco-elastic (a, b) or non-linear (c, d) analyses versus those calculated with the simplified (a, c) or standard (b, d) approaches with VAF resulting from Eq. III.5.3, at the position x/B = -0.65 along Piedilama valley

Finally, in Figure V.3.26 and Figure V.3.27 the same comparisons are shown for the valley centre and x/B=-0.65 respectively, but by computing the proposed spectrum with the VAF value obtained from the charts. The prediction does not increase in accuracy and the trends are similar to those obtained using the VAF of Eq. III.5.3.

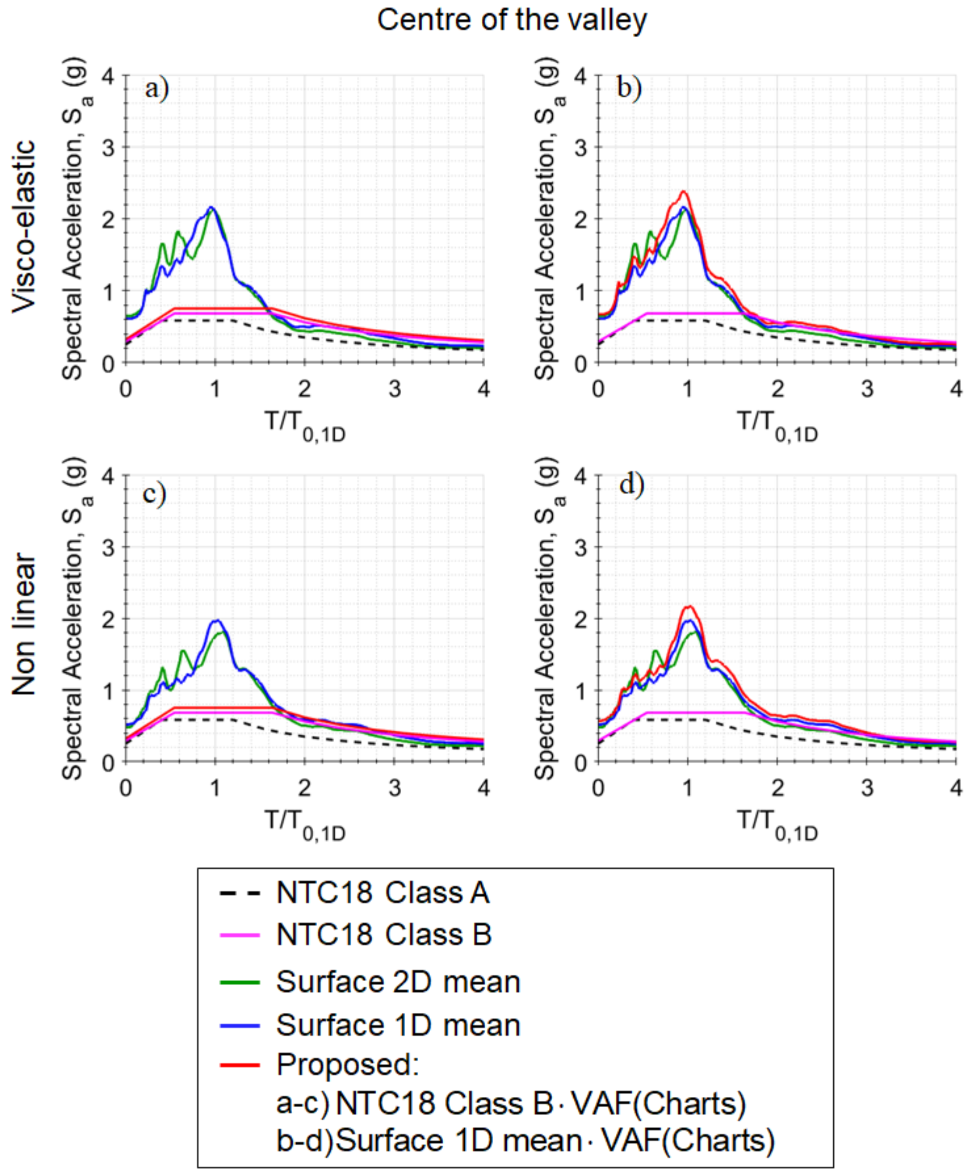

Figure V.3.26 – Spectra obtained from visco-elastic (a, b) or non-linear (c, d) analyses versus those calculated with the simplified (a, c) or standard (b, d) approaches with VAF resulting from charts, at the centre of Piedilama valley.

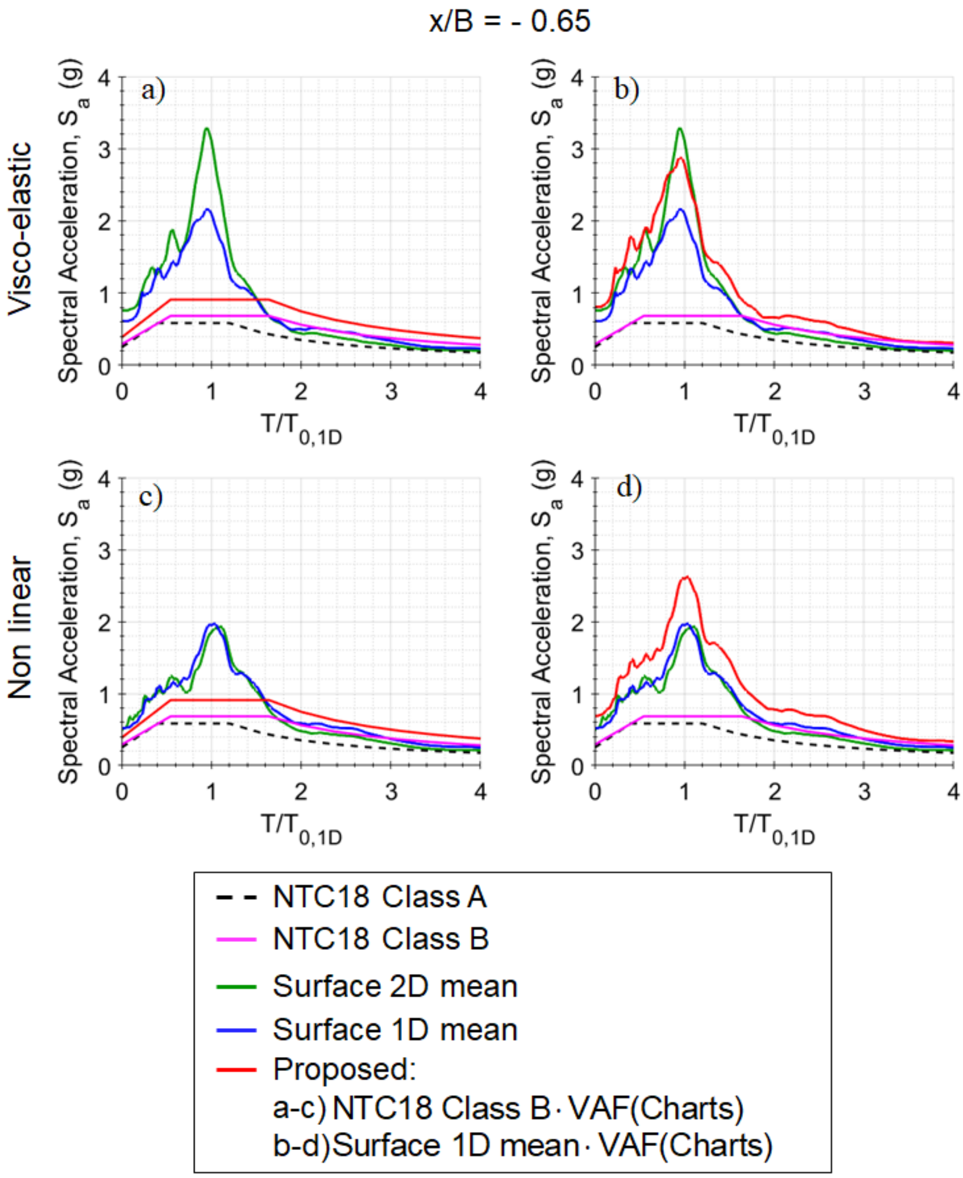

Figure V.3.27 – Spectra obtained from visco-elastic (a, b) or non-linear (c, d) analyses versus those calculated with the simplified (a, c) or standard (b, d) approaches with VAF resulting from charts, at the position x/B = -0.65 along Piedilama valley

VI. CONCLUSIONS AND PERSPECTIVES

The main aim of this study has been to provide a reliable yet simplified method for the evaluation of the complex seismic amplification phenomena in alluvial valleys.

The review of the main relevant literature led to the individuation of the main factors governing the phenomena and to the calibration of the relevant ranges of variability adopted for an extensive parametric study. In this study, valleys with trapezoidal, rectangular and wedge shapes constituted by homogeneous soil with visco-elastic behaviour were subjected to Ricker wavelets input motions with variable dominant frequency. The resulting surface motions were expressed in terms of acceleration time histories and response spectra, and allowed to define a valley amplification factor, VAF, as an index of the 2D morphological effects on the modifications of the response spectrum all along the valley surface, with respect to that predicted by a conventional 1D seismic response analysis. Thereafter, analytical and graphical procedures were proposed to calculate the VAF as a function of the geometric and mechanical parameters of the alluvial soil filling. Considering that most valley deposits in nature are made of deformable and relatively low-aged soils, the simplified assumptions of linear homogeneous soil model were overcome by investigating the effect of non-linearity and inhomogeneity on the seismic response. Finally, a straightforward procedure for taking into account in a simplified way the valley effects on the evaluation of the site-specific response spectra was developed and applied to several case studies.

The first conclusion that can be deduced from this study is that the seismic response of valleys is mainly affected by their geometry, whether trapezoidal or wedge-shaped. In the first case, the motion at the valley centre increases with the shape and the impedance ratios, while it is independent of the edge slope; on the other hand, the maximum amplification at the edges is mainly due to their angle of inclination and to the impedance ratio, while it is independent of the valley shape. The position and size of the zone of maximum amplification depend on all the previous parameters. For the wedge, the VAF is mostly affected by the shape ratio, which defines the value of the slope angle equal to the arctangent of it, and the impedance ratio, typically increasing with them.

The charts allowed the definition of a new class of ‘shallow’ valleys, the ‘very shallow’ ones. These are characterised by a shape ratio such that, whatever the impedance ratio, the ground motion at the centre of the valley is almost one-dimensional, while at the edges it is not. For such valleys, therefore, using in the central zone a response spectrum obtained by means of 1D analyses leads, on average, to underestimating the spectral amplitudes by a maximum of 5-10%.

The evaluation of the effects of non-linearity and inhomogeneity of mechanical properties with depth was pursued by analysing a limited number of valley geometries and soil models. As a matter of fact, the purpose of this study has only been to check the significance of these effects, in order to highlight their main features, and to define a methodology accounting for them, without aiming at providing generalized relationships. Typically, as amplitude and duration of the seismic motion increase, the VAF increases at the edges and decreases at the centre of the valley, compared to the visco-elastic case. This is due to the fact that non-linear effects are such that there is a concentration of shear strain at the valley edge, which causes the 2D motion to change in a different way with respect to the 1D upward S-wave propagation, and therefore their ratio varies with respect to the visco-elastic case. To account for these effects, a method has been proposed for correcting the VAF predictable by the visco-elastic hypothesis, as a function of the maximum expected peak ground acceleration of the horizontal outcropping bedrock.

A possible method for upgrading the technical codes and guidelines to account for valley effects involves two alternative approaches. In the most simplified, the site-specific response spectrum at the surface can be calculated as the product of the reference spectrum, for horizontal outcropping bedrock, and three amplification coefficients that take into account topographic effects, S_T, stratigraphic effects, S_S, and valley effects, VAF. The first two are typically provided by several technical codes (e.g. Eurocode 8, NTC 2018), while the third can be estimated through the equations or charts proposed in this study. The standard approach, instead, requires carrying out a 1D seismic response analysis of the soil column at the valley centre, then multiplying the 1D surface spectrum by the VAF to account for the valley effects. Again, VAF can be calculated by using the same equations or charts.

The application of the proposed VAF equations and charts to the case studies highlighted that the simplified approach always underestimates the response spectrum predicted by accurate numerical simulations. As a matter of fact, the response spectrum provided by the code-conforming simplified procedure, i.e. the product of the reference spectrum by the code-specified S_S, in these cases significantly underestimates the surface motion predicted by 2D finite difference analyses.

Following the standard approach, the prediction depends on how close the real valley is to the ideal cases for which VAF was evaluated: if the valley shape is close enough to the trapezoidal one, the stratigraphy is not very complex and the ground surface is approximately horizontal, the predicted 2D response spectrum is very close to that calculated with numerical analysis. On the other hand, in the case of basins with highly variable geometries and mechanical properties, the prediction is not as accurate. Furthermore, it is seen that the VAF at the valley edge is strongly affected by the actual geometry of the interface between the bedrock and the filling material. Therefore, when it is calculated with analytical formulations, an inadequate estimate of the zone of maximum amplification may take place, whereas this phenomenon is more limited when using charts. Indeed, the latter are obtained in a way that they are independent of the angle of inclination and therefore envelop all possible VAFs. In the centre of the valley, usually VAF is satisfactorily estimated by both analytical expressions and charts. This is due to the fact that, in shallow valleys, the influence at the valley centre of the edge slope is secondary, and the ground motion is mainly ruled by the shape and impedance ratio.

The results of this study allow to identify several issues that can be further explored in the future.

First of all, the results should be extended by taking into account the effects of inhomogeneity and non-linearity, by carrying out a specific and extensive study, able to give information on how to quantify these effects in a more general way.

The effect of the inclination of the outcropping bedrock should also be investigated, in order to overcome the hypothesis of a horizontal ground surface outside the valley.

The results obtained are enough reliable for the so-called ‘shallow valleys’, i.e. those characterised by H/B<0.3. They should be extended to the ‘deep valley’ cases, with a specifically designed parametric study.

The seismic motion at surface is significantly influenced by the true geometry of the valley, hence other shapes - such as sinusoidal or circular - should be investigated. In this way, more general analytical relationships for VAF could be defined, extending those obtained in this study for trapezoidal and wedge-shaped basins.

Finally, the VAF has two major issues. First, for sake of a simple and more practical use, it has been expressed as independent of the frequency content of the reference seismic motion, assuming that it mostly influences the surface seismic motion as predicted by the one-dimensional analysis. Furthermore, VAF is an index of how much, on average, the 2D spectrum is amplified compared to the 1D spectrum. The analysis showed that the former cannot always be obtained by simply increasing the spectral ordinates of the latter. Indeed, the spectrum predicted by 2D numerical simulations and that obtained multiplying by VAF the spectrum resulting from 1D seismic response analysis present differences, that depend on the shape ratio and on the position considered. If the valley is very shallow (H/B<0.1), the two spectra do not differ much at the centre of the valley, while they are not the same at the edges. However, for higher shape ratios, the 2D effects are such that the two spectra are always not close. Therefore, the analytical expressions of the valley amplification coefficients, in this study defined as a function of the impedance ratio and geometrical factors only, should be updated to take these two aspects into account. For example, it might be possible including a functional dependency on the mean frequency of the input motion or on the structural period considered.

References

Aki, K., & Larner, K. L. (1970). *Surface Motion of a Layered Medium Having an Irregular Interface Due to Incedent Plane SH Waves*. Journal of Geophysical Research, 75(5), 933–954.

Alleanza, G. A., & Chiaradonna, A. (2018). *Previsione degli effetti di non linearità dei terreni: confronto tra codici di calcolo per analisi 1D di risposta sismica locale*. VIII IAGIG.

Alleanza, G. A., D'Onofrio, A., Silvestri, F., Catalano, S., Tortorici, G., Chiaradonna, A., de Silva, F., & Romagnoli, G. (2019). *Seismic microzonation of an alluvial valley hit by the 2016 Central Italy earthquake*. Proceedings of 7th International Conference on Earthquake Geotechnical Engineering (VII ICEGE), 1074–1081.

Alleanza, G. A., Chiaradonna, A., Onofrio, A., & Silvestri, F. (2019). *Parametric study on 2D effect on the seismic response of alluvial valleys*. Proceedings of 7th International Conference on Earthquake Geotechnical Engineering (VII ICEGE), 1082–1089.

Anh Dan, L. Q., Koseki, J., & Tatsuoka, F. (2001). *Viscous deformation in triaxial compression of dense well-graded gravels and its model simulation.* Advanced

Laboratory Stress-Strain Testing of Geomaterials (Tatsuoka et al. Eds)., 187–194.

Bard, P. Y. (1982). *Diffracted waves and displacement field over two-dimensional elevated topographies*. Geophysical Journal of the Royal Astronomical Society, 71(3), 731–760. https://doi.org/10.1111/j.1365-246X.1982.tb02795.x

Bard, P. Y., & Bouchon, M. (1980a). *The seismic response of sediment-filled valleys. Part 1. The case of incident SH waves.* Bulletin of the Seismological Society of America, 70(4), 1263–1286.

Bard, P. Y., & Bouchon, M. (1980b). *The seismic response of sediment-filled valleys. Part 2. The case of incident P and SV waves.* Bulletin of the Seismological Society of Americ, 70(5), 1921–1941.

Bard, P. Y., & Bouchon, M. (1985). *The two-dimensional resonance of sediment-filled valleys*. Bulletin of the Seismological Society of Americ, 75(2), 519–541.

Bard, P. Y., & Gariel, J. C. (1986). *Seismic Response of Two-Dimensional Sedimentary Deposits With Large Vertical Velocity Gradients.* Bulletin of the Seismological Society of America, 76(2), 343–366.

Bellaveglia, S., Bistocchi, R. M., & Gattoni, M. (2018). *Microzonazione Sismica di Livello 3 del Comune di Arquata del Tronto ai sensi dell'Ordinanza del Commissario Straordinario n.24 registrata il 15 maggio 2017 al n. 1065*.

Bouckovalas, G. D., & Papadimitriou, A. G. (2005). *Numerical evaluation of slope topography effects on seismic ground motion*. Soil Dynamics and Earthquake Engineering, 25(7), 547–558. https://doi.org/10.1016/j.soildyn.2004.11.008

Brunelli, A., de Silva, F., Piro, A., Parisi, F., Sica, S., Silvestri, F., & Cattari, S. (2021). *Numerical simulation of the seismic response and soil–structure interaction for a monitored masonry school building damaged by the 2016 Central Italy earthquake*. In *Bulletin of Earthquake Engineering* (Vol. 19, Issue 2). Springer Netherlands. https://doi.org/10.1007/s10518-020-00980-3

Brunelli, A., Sivori, D., Cattari, S., Piro, A., de Silva, F., Parisi, F., Sica, S., & Silvestri, F. (2019). *Soil-structure interaction effects on the dynamic behaviour of a masonry school damaged by the 2016–2017 Central Italy earthquake sequence*. Earthquake Geotechnical Engineering for Protection and Development of Environment and Constructions, Silvestri F. and Moraci N. (Eds). Proceedings of the VII International Conference on Earthquake Geotechnical Engineering, 1655–1663.

Chávez-García, F. J., & Faccioli, E. (2000). *Complex site effects and building codes: Making the leap*. Journal of Seismology, 4(1), 23–40. https://doi.org/10.1023/A:1009830201929

Ciancimino, A., Lanzo, G., Alleanza, G. A., Amoroso, S., Bardotti, R., Biondi, G., Cascone, E., Castelli, F., Giulio, A. di, D'Onofrio, A., Foti, S., Lentini, V., Madiai, C., & Vessia, G. (2019). *Dynamic characterization of fine-grained soils* *in central Italy by laboratory testing*. Bulletin of Earthquake Engineering. https://doi.org/10.1007/s10518-019-00611-6

D'Amico, M., Felicetta, C., Russo, E., Sgobba, S., Lanzano, G., Pacor, F., & Luzi, L. (2020). *Italian Accelerometric Archive v 3.1*. Istituto Nazionale Di Geofisica e Vulcanologia, Dipartimento Della Protezione Civile Nazionale. https://doi.org/10.13127/itaca.3.1

Dolce, M., Nicoletti, M., de Sortis, A., Marchesini, S., Spina, D., & Talanas, F. (2017). *Osservatorio sismico delle strutture: the Italian structural seismic monitoring network*. Bulletin of Earthquake Engineering, 15(2), 621–641. https://doi.org/10.1007/s10518-015-9738-x

d'Onofrio, A., Evangelista, L., Landolfi, L., Silvestri, F., Boiero, D., Foti, S., Maraschini, M., & Santucci de Magistris, F. (2010). *Geotechnical characterization of the C.A.S.E. project sites*. Proc. Sustainable Development Strategies for Constructions in Europe and China.

d'Onofrio, A., & Silvestri, F. (2001). *Influence of Micro-Structure on Small-Strain Stiffness and Damping of Fine Grained Soil and Effects on Local Site Response*. International Conferences on Recent Advances in Geotechnical Earthquake Engineering and Soil Dynamics. 15.

Eurocode 8. (2004). *Eurocode 8: Design of structures for earthquake resistance - Part 1: General rules, seismic actions and rules for buildings*. https://doi.org/10.1680/cien.144.6.55.40618

Faralli, L., Gasparri, N., Piccioni, R., & Venanti, L. D. (2018). *Microzonazione Sismica di Livello 3 del Comune di Montefranco ai sensi dell'Ordinanza del Commissario Straordinario n.24 registrata il 15 maggio 2017 al n. 1065*.

Gazetas, G. (1982). *Vibrational characteristics of soil deposits with variable wave velocity*. International Journal for Numerical and Analytical Methods in Geomechanics, 6(1), 1–20. https://doi.org/10.1002/nag.1610060103

Gelagoti, F., Kourkoulis, R., Anastasopoulos, I., Tazoh, T., & Gazetas, G. (2010). *Seismic wave propagation in a very soft alluvial valley: Sensitivity to ground-motion details and soil nonlinearity, and generation of a parasitic vertical component*. Bulletin of the Seismological Society of America, 100(6), 3035–3054. https://doi.org/10.1785/0120100002

Gelagoti, F., Kourkoulis, R., Anastasopoulos, I., & Gazetas, G. (2012). *Nonlinear dimensional analysis of trapezoidal valleys subjected to vertically propagating SV waves*. Bulletin of the Seismological Society of America, 102(3), 999–1017. https://doi.org/10.1785/0120110182

Geli, L., Bard, P. Y., & Jullien, B. (1988). *Effect of Topography on Earthquake Ground Motion: a Review and New Results.* Bulletin of the Seismological Society of America, 78(1), 42–63.

Gutemberg, B. (1957). *Effects of ground on earthquke morion*. Bulletin of the Seismological Society of America, 47(3), 221–250.

Hong, T.-L., & Helmberger, D. v. (1978). *Glorified optics and wave propagation in nonplanar structure*. Bulletin of the Seismological Society of America, 68(5), 1313–1330. http://www.bssaonline.org/content/68/5/1313.short

Idriss, I. M. (1991). *Earthquake ground motions at soft soil sites*. Proceedings of 2nd Int. Conf. on Recent Advances in Geotechnical Earthquake Engineering and Soil Dynamics, 2265–2273.

Iervolino, I., Galasso, C., & Cosenza, E. (2010). *REXEL: Computer aided record selection for code-based seismic structural analysis*. Bulletin of Earthquake Engineering, 8(2), 339–362. https://doi.org/10.1007/s10518-009-9146-1

Itasca Consulting Group. (2016). *FLAC - Fast Lagrangian Analysis of Continua.* Ver. 8.0. Minneapolis. Itasca.

Iyisan, R., & Khanbabazadeh, H. (2013). *A numerical study on the basin edge effect on soil amplification*. Bulletin of Earthquake Engineering, 11(5), 1305–1323. https://doi.org/10.1007/s10518-013-9451-6

Kottke, A. R., & Rathje, E. M. (2008). *Technical manual for Strata*. Report No.: 2008/10. Pacific Earthquake Engineering Research Center, University of California, Berkeley.

Kramer, S. L. (1996). *Geotechnical Earthquake Engineering* (Hall, P., Ed.).

Kuhlemeyer, R. L., & Lysmer, J. (1973). *Finite element method accuracy for wave propagation problems*. Soil Mechanics and Foundations, 99(5), 421–427.

Lanzo, G., & Silvestri, F. (1999). *Risposta sismica locale: Teoria ed esperienze* (Haevelius Edizioni, Ed.).

Lemmi, M., Lolli, O., & Zeni, S. (2017). *Microzonazione Sismica di Livello 3 del Comune di Visso ai sensi dell'Ordinanza del Commissario Straordinario n.24 registrata il 15 maggio 2017 al n. 1065*. https://sisma2016data.it/microzonazione/

Liao, T., Massoudi, N., Mchood, M., Stokoe, K. H., Jung, M. J., & Menq, F. Y. (2013). *Normalized Shear Modulus of Compacted Gravel*. 18th International Conference on Soil Mech Geotech Eng. Challenges and Innovations in Geotechnics, 1535–1538.

Lysmer, J., & Kuhlemeyer, R. L. (1969). *Finite Dynamic Model for Infinite Media*. Journal of the Engineering Mechanics Division, 95(4), 859–877.

MIT 2019. (2019). *Circolare del ministero delle infrastructure e dei trasporti, n.7 del 21 Gennaio 2019: "Istruzioni per l'applicazione dell'aggiornamento delle Norme tecniche per le costruzioni di cui al D.M. 17 gennaio 2018*. Consiglio Superiore Dei Lavori Pubblici. G.U. n.35 Del 11.02.2019.

Modoni, G., & Gazzellone, A. (2010). *Simplified theoretical analysis of the seismic response of artificially compacted gravels*. Proc. of the Vth Int. Conf. on Recent Advance in Geotechnical Earthquake Engineering and Soil Dynamics.

NTC 2018. Ministero delle infrastrutture e dei trasporti. D.M. 17/01/2018. (n.d.). *Aggiornamento delle "Norme tecniche per le costruzioni" (in Italian)*. S.O. n. 8 Alla Gazzetta Ufficiale Della Repubblica Italiana, n. 42 Del 20 Febbraio 2018.

Papadimitriou, A. G. (2019). *An engineering perspective on topography and valley effects on seismic ground motion*. 7th International Conference on Earthquake Geotechnical Engineering.

Phillips, C., & Hashash, Y. M. A. (2009). *Damping formulation for nonlinear 1D site response analyses*. Soil Dynamics and Earthquake Engineering, 29(7), 1143–1158. https://doi.org/10.1016/j.soildyn.2009.01.004

Pitilakis, K., Riga, E., Anastasiadis, A., Fotopoulou, S., & Karafagka, S. (2019). *Towards the revision of EC8: Proposal for an alternative site classification scheme and associated intensity dependent spectral amplification factors*. Soil Dynamics and Earthquake Engineering, 126. https://doi.org/10.1016/j.soildyn.2018.03.030

Rathje, E. M., Abrahamson, N. A., & Bray, J. D. (1998). *Simplified frequency content estimates of earthquake ground motions*. Journal of Geotechnical and Geoenvironmental Engineering, 124(2), 150–159.

Riga, E., Makra, K., & Pitilakis, K. (2016). *Aggravation factors for seismic response of sedimentary basins: A code-oriented parametric study*. Soil Dynamics and Earthquake Engineering, 91, 116–132. https://doi.org/10.1016/j.soildyn.2016.09.048

Riga, E., Makra, K., & Pitilakis, K. (2018). *Investigation of the effects of sediments inhomogeneity and nonlinearity on aggravation factors for sedimentary basins*. Soil Dynamics and Earthquake Engineering, 110, 284–299. https://doi.org/10.1016/j.soildyn.2018.01.016

Rovithis, E. N., Parashakis, H., & Mylonakis, G. E. (2011). *1D harmonic response of layered inhomogeneous soil: Analytical investigation*. Soil Dynamics and Earthquake Engineering, 31(7), 879–890. https://doi.org/10.1016/j.soildyn.2011.01.007

Sanchez-Sesma, F. J. (1990). *Elementary solutions for response of a wedge-shaped medium to incident SH and SV waves*. Bulletin of the Seismological Society of America, 80(3), 737–742. https://doi.org/10.1016/j.foodres.2013.01.036

Seed, H. B., & Idriss, I. M. (1970). *Soil Moduli and Damping Factors for Dynamic Response Analyses*. Report No. EERC 70-10.

The MathWorks Inc. (2021). *Deep Learning Toolbox: User's Guide (R2021b)*. https://it.mathworks.com/help/deeplearning/index.html?s_cid=doc_ftr

Trifunac, M. D. (1971). *Surface motion of a semi-cylindrical alluvial valley for incident plane SH waves*. Bulletin of the Seismological Society of America, 61(6), 1755–1770.

Verrucci, L., Pagliaroli, A., Lanzo, G., di Buccio, F., Biasco, A. P., & Cucci, C. (2022). *Damping formulations for finite difference linear dynamic analyses: Performance and practical recommendations*. Computers and Geotechnics, 142. https://doi.org/10.1016/j.compgeo.2021.104568

Vessia, G., Russo, S., & lo Presti, D. (2011). *A new proposal for the evaluation of the amplification coefficient due to valley effects in the simplified local seismic response analyses*. Rivista Italiana Di Geotecnica, 4, 51–77.

Vucetic, M., & Dobry, R. (1991). *Effect of soil plasticity on cyclic response*. Journal of Geotechnical Engineering, ASCE, 117.

Wong, H. L., & Trifunac, M. D. (1974). *Surface motion of a semi-elliptical hill for incident plane SH waves*. Bulletin of the Seismological Society of Americ, 64(5), 1389–1408. https://doi.org/10.1007/s11589-011-0807-1

Zhu, C., Chávez-García, F. J., Thambiratnam, D., & Gallage, C. (2018). *Quantifying the edge-induced seismic aggravation in shallow basins relative to the 1D SH modelling*. Soil Dynamics and Earthquake Engineering, 115, 402–412. https://doi.org/10.1016/j.soildyn.2018.08.025

Zhu, C., Thambiratnam, D., & Gallage, C. (2018). *Statistical analysis of the additional amplification in deep basins relative to the 1D approach*. Soil Dynamics and Earthquake Engineering, 104, 296–306. https://doi.org/10.1016/j.soildyn.2017.09.003

Zhu, C., & Thambiratnam, D. (2016). *Interaction of geometry and mechanical property of trapezoidal sedimentary basins with incident SH waves*. Bulletin of Earthquake Engineering, 14(11), 2977–3002. https://doi.org/10.1007/s10518-016-9938-z

Zhu, C., Riga, E., Pitilakis, K., Zhang, J., & Thambiratnam, D. (2018). *Seismic Aggravation in Shallow Basins in Addition to One-dimensional Site Amplification*. Journal of Earthquake Engineering, 1–23. https://doi.org/10.1080/13632469.2018.1472679

A. APPENDIX A: CALIBRATION OF VAF RELATIONSHIP FOR TRAPEZOIDAL VALLEY

The variation of VAF along the valley is approximated as the sum of two Gaussian-like functions (Figure A.1), the first one describing the aggravation factor at the valley centre (cyan line) and the second expressing its trend along the edges (red line).

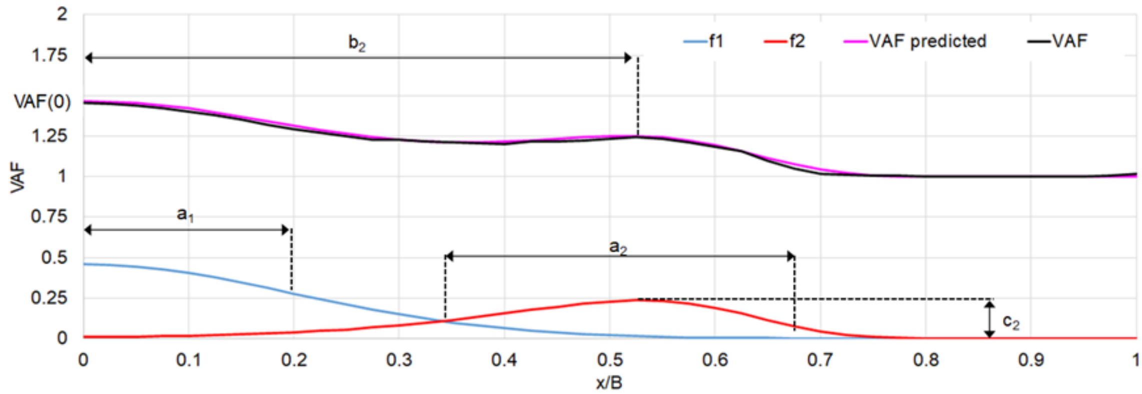

Figure A.1 – VAF model proposed in this study.

The proposed analytical VAF function is then defined as:

$$\mathrm{VAF} = 1 + \left(\mathrm{VAF}(0) - 1\right) \cdot f_1\left(\frac{x}{B}, \frac{H}{B}, I\right) + f_2\left(\frac{x}{B}, \frac{H}{B}, I, \alpha\right) \qquad \text{A.1}$$

where VAF(0) is the amplification computed at the middle of the valley, f_1 and f_2 the functions describing the VAF distributions along the central sector and at the edge, respectively. They can be expressed as:

$$\mathrm{VAF}(0) = 1 + c_0 \cdot \left(1 - \exp\left(-\frac{(I-1)^2}{2 \cdot a_0^2}\right)\right) \quad \text{A.2}$$

$$f_1\left(\frac{x}{B}, \frac{H}{B}, I\right) = \exp\left(-\frac{\left(\frac{x}{B}\right)^2}{2 \cdot a_1^2}\right) \quad \text{A.3}$$

$$f_2\left(\frac{x}{B}, \frac{H}{B}, I, \alpha\right) = c_2 \cdot \exp\left(\frac{\frac{x}{B} - b_2}{a_2} - \exp\left(\frac{\frac{x}{B} - b_2}{a_2}\right)\right) \quad \text{A.4}$$

where c_0, a_0, a_1, a_2, b_2 and c_2 are coefficients defining the Gaussian-like functions. In a preliminary stage they are chosen with engineering judgement to fit the results of the numerical analysis, then their dependency on the geometrical and mechanical properties of the valley is analytically expressed.

Figure A.2 shows the variation of VAF calculated at the centre of the valley, VAF(0), with the impedance ratio for different values of H/B and α. In this and the following figures, the data obtained from the numerical analysis are represented with points and the fitting functions with lines. The marker shape of the points depends on α (e.g. diamond for 90°, circle for 60°, triangle for 45° and star for 30°) while the colour is used to indicate the different H/B values (e.g. red for 0.05, blue for 0.1, cyan for 0.15, green for 0.20 and black for 0.25) and finally the intensity of the colour indicates the impedance contrast (e.g. decreases with I).

VAF(0) is almost unitary for H/B=0.05 and at most equal to 1.1 for H/B=0.1, whatever the value of I and α. For greater shape ratio, however, it depends significantly on the impedance contrast, but it is still independent of α. Furthermore, there is a threshold value of I, which is distinct for each H/B, beyond which VAF(0) is constant.

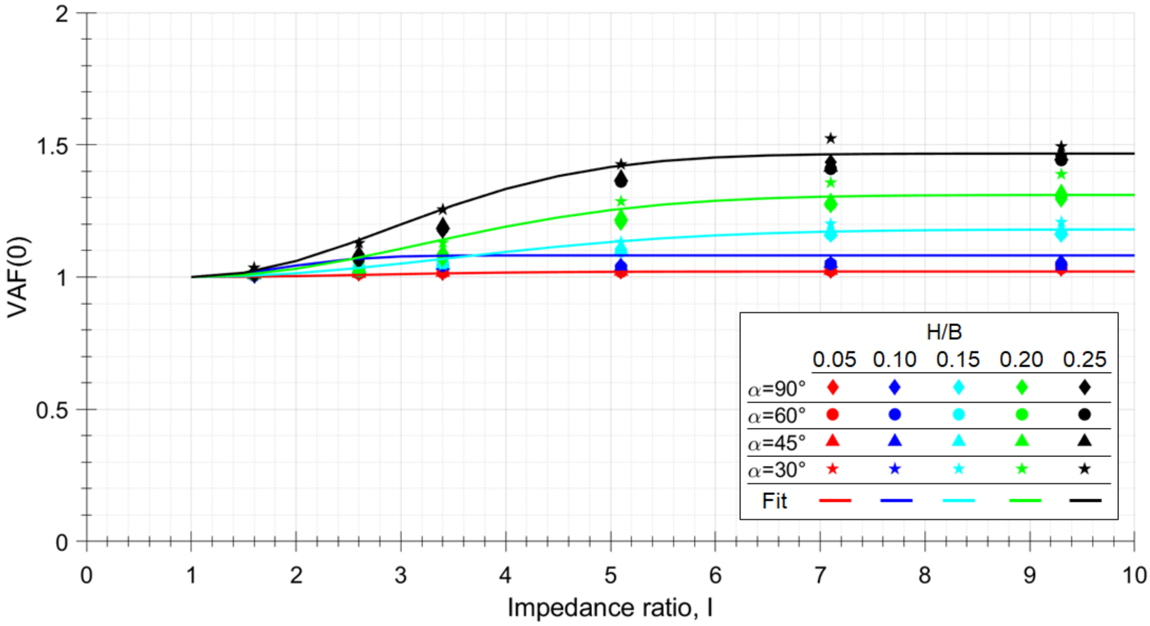

Figure A.2 – VAF calculated at the centre of the valley

Figure A.3 shows the variation of a_0 with H/B for the different angles. It is practically independent of the angle of inclination of the edges, while it strongly depends on the shape ratio. A discontinuity in the trends can be identified for H/B between 0.1 and 0.15, due to the change in the behaviour of the valley. The function that best interpolates the data is therefore a spline, with equation equal to:

$$a_0 = \begin{cases} \frac{H}{B} < 0.10 & 2.463 - 16.509\frac{H}{B} \\ 0.10 \le \frac{H}{B} < 0.15 & 32.838\frac{H}{B} - 2.472 \\ \frac{H}{B} \ge 0.15 & 3.290 - 5.574\frac{H}{B} \end{cases} \qquad \text{A.5}$$

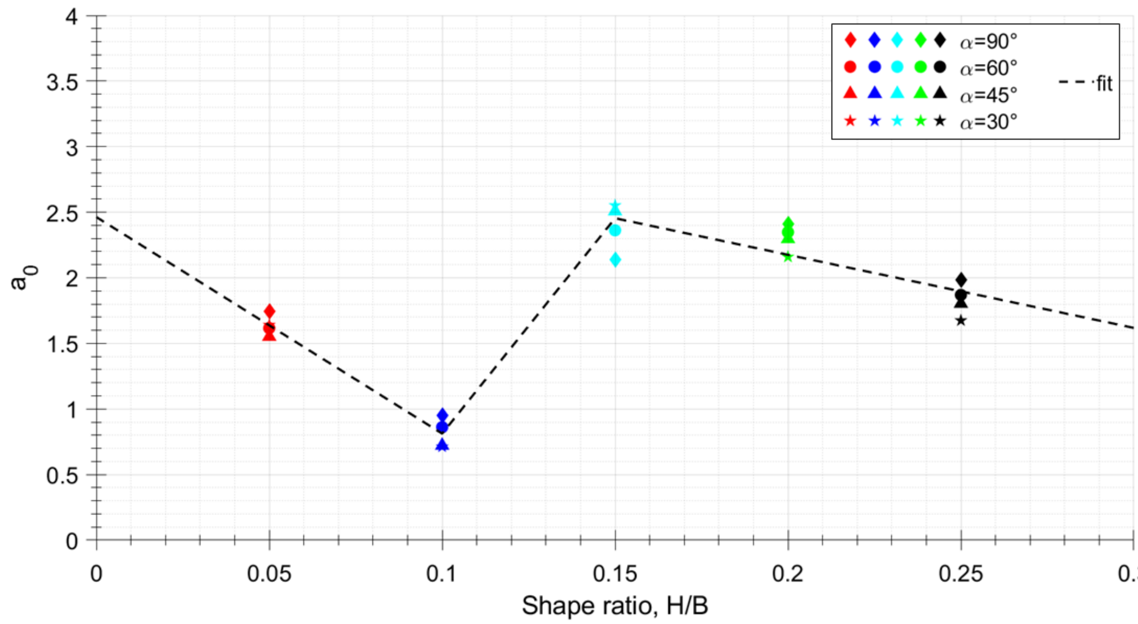

Figure A.3 – Calibration of a_0

The variation of c_0 with H/B is reported in Figure A.4. It increases with the shape ratio and, as a_0, it is independent of the angle. The function that best fits the data is equal to:

$$c_0 = 2.350 \cdot \left(1 - \exp\left(-\frac{\left(\frac{H}{B}\right)^2}{0.282}\right)\right) \qquad \text{A.6}$$

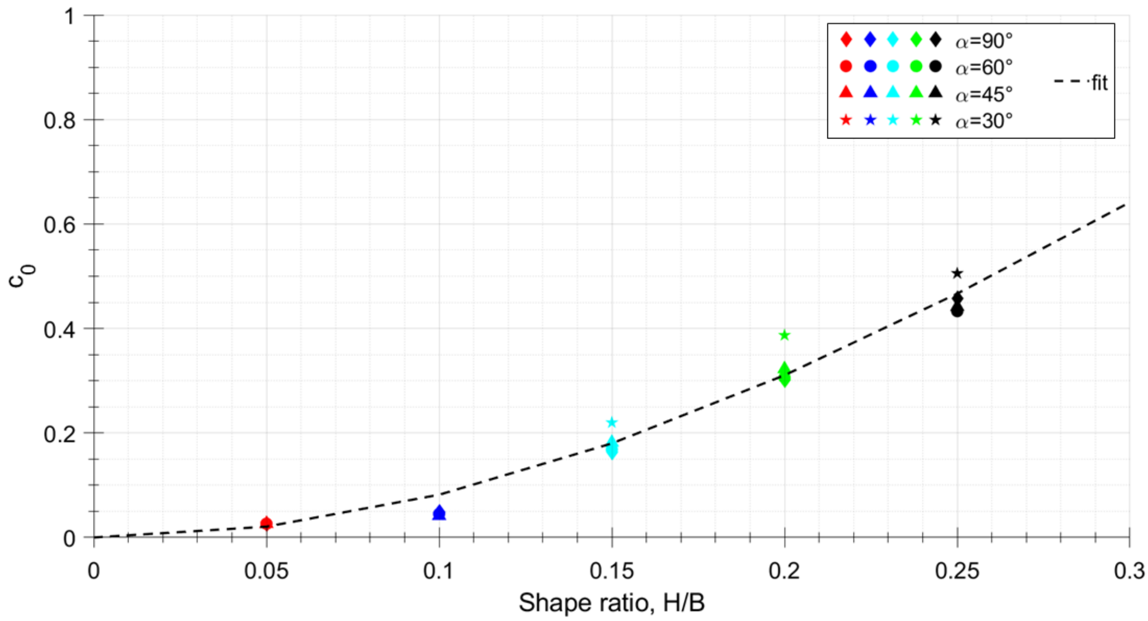

Figure A.4 – Calibration of c_0

Figure A.5a,b show respectively the comparison between the trends of a_0 and c_0 obtained using the Eq. A.5, Eq. A.6 (dashed lines) and the data as the slope of the edge varies. The figures show that the error made by considering a_0 and c_0 independent of α is very low. As a matter of fact, the data are almost constant with the angle and similar to the value obtained with equations.

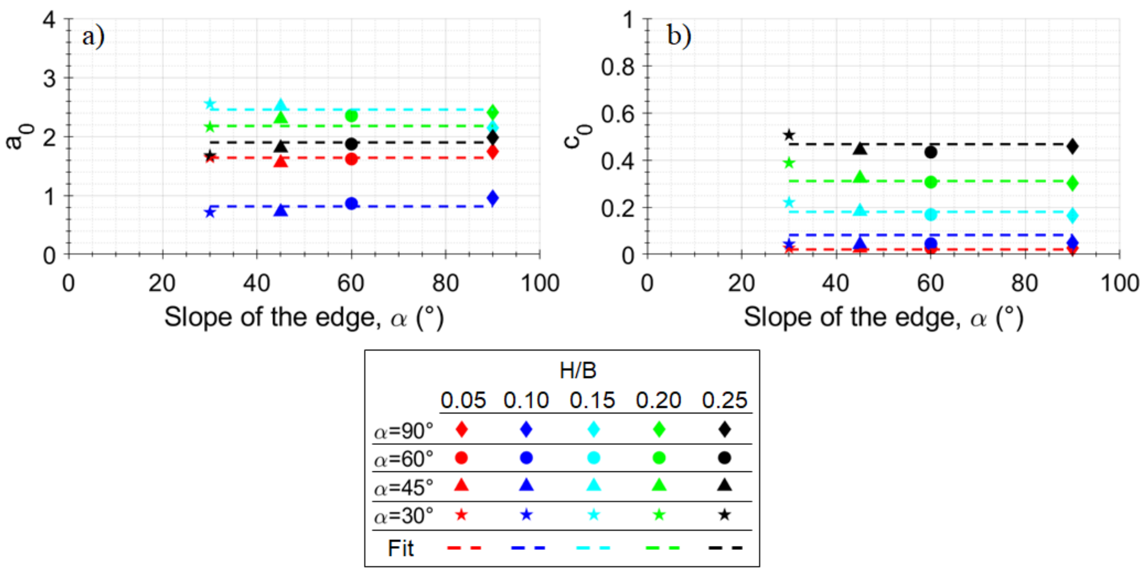

Figure A.5 – Variation of a) a_0 and b) c_0 with the slope of the edge

The function which describes the VAF in the central part of the valley (Eq. A.3) is a Gaussian with standard deviation, a_1, that is independent of α and strongly affected by H/B and less by I. Figure A.6a,b,c show the variation of a_1 with the three key parameters, H/B, I and α respectively. It can be noted that it decreases with a power relation with H/B (Figure A.6a), while it is almost independent of I (Figure A.6b) for H/B<0.1, and increases with I for greater shape ratios. Therefore, a_1 can be defined as (lines in Figure A.6):

$$a_1 = x_1 \cdot \left(\frac{H}{B}\right)^{x_2} + x_3 \qquad \text{A.7}$$

with x_1, x_2 and x_3 parameters which depend on the impedance ratio.

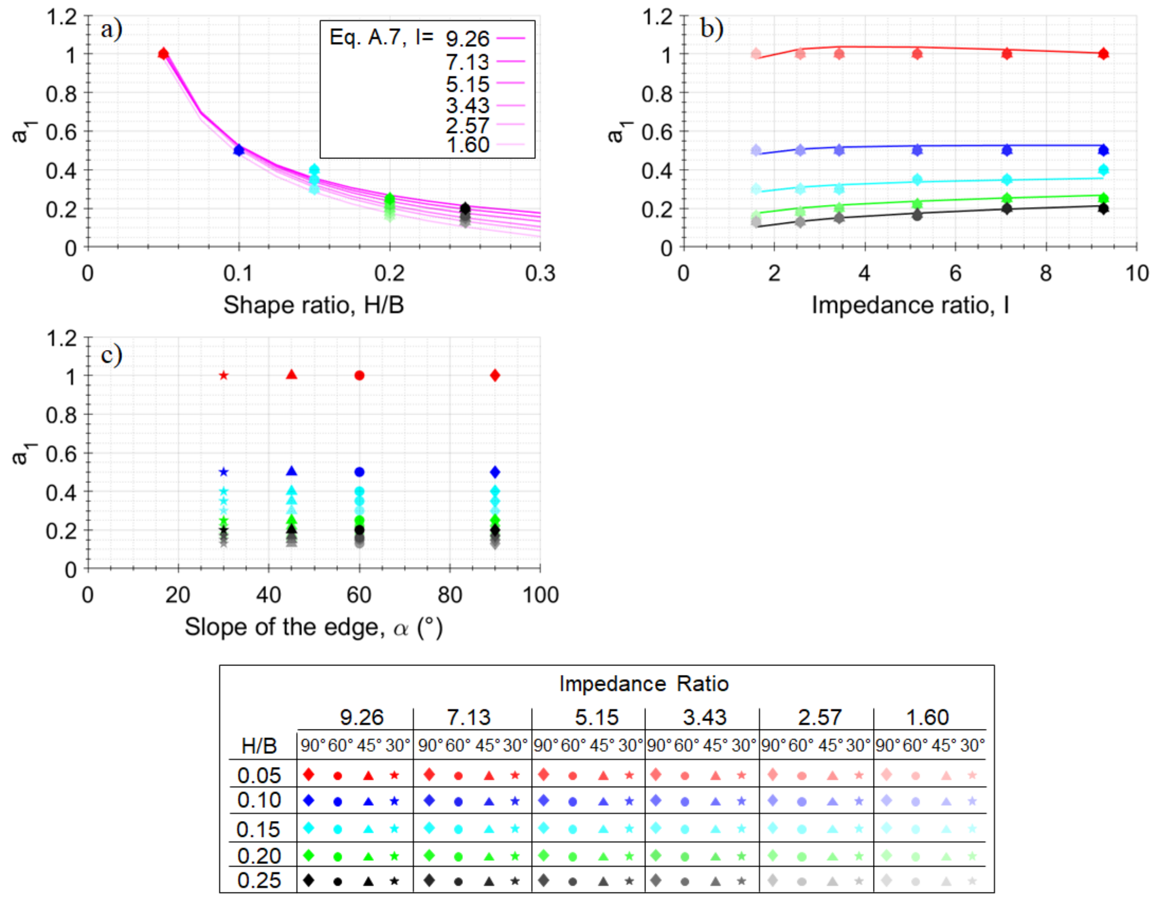

Figure A.6 – Variation of a_1 with a) H/B; b) I; c) α

Figure A.7a,b,c show the variation of x_1, x_2 and x_3 with I, respectively. They can be fitted with power functions of I equal to:

$$x_1 = 0.204 \cdot I^{-0.409} - 0.00998 \tag{A.8}$$

$$x_2 = 0.531 \cdot I^{-0.303} - 1.160 \tag{A.9}$$

$$x_3 = -4.495 \cdot I^{-0.0372} + 4.103 \tag{A.10}$$

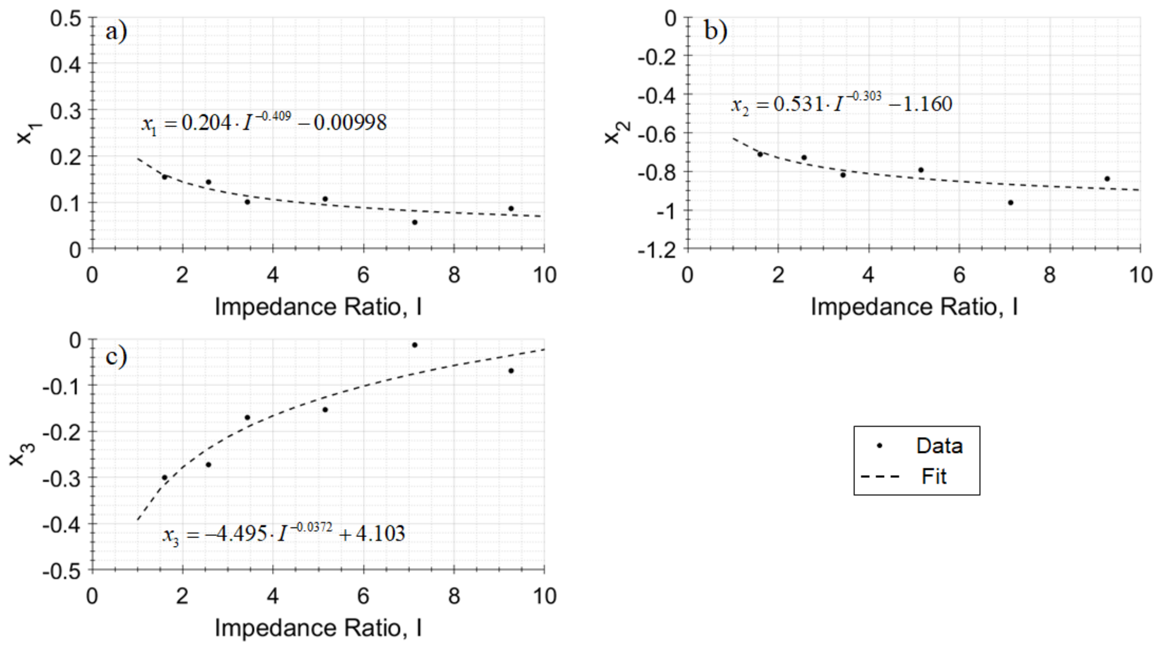

Figure A.7 – Variation of a) x_1; b) x_2; c) x_3 with I

The function f_2 (Eq. A.4), which is representative of the amplification at the valley edge, is obtained by modifying the Probability Density Function, PDF, of the Gumbel distribution, and is defined by 3 parameters (a_2, b_2 and c_2) that can be correlated with the geometry of the valley. The first is a measure of the width of the curves, i.e. the area of the valley where amplifications are maximum, and can be viewed as analogous to the standard deviation of the Gaussian distribution. Instead b_2 is the position across the valley of the maximum of f_2, whose value is proportional to c_2, indeed for $x/B=b_2$ the f_2 is equal to $c_2 \cdot \exp(-1)$.

a_2 is mainly influenced by the impedance ratio (Figure A.8b) and the shape ratio (Figure A.8a), while it is almost independent of the slope angle of the edges (Figure A.8c). In detail, for $H/B<0.15$ it increases with I and H/B, while for greater shape ratios it decreases as I increase and increases with H/B. The function that better fits the data can be written as:

$$a_2 = x_4 + \ln\left(I^{x_5}\right) \qquad \text{A.11}$$

Figure A.8b shows with solid lines the trend of a_2 obtained with Eq. A.11. It can be clearly noticed how it provides a fairly good fit to the data for $H/B<0.1$ and for $H/B>0.2$ while for intermediate values the error increases, however it is limited and is considered reasonable.

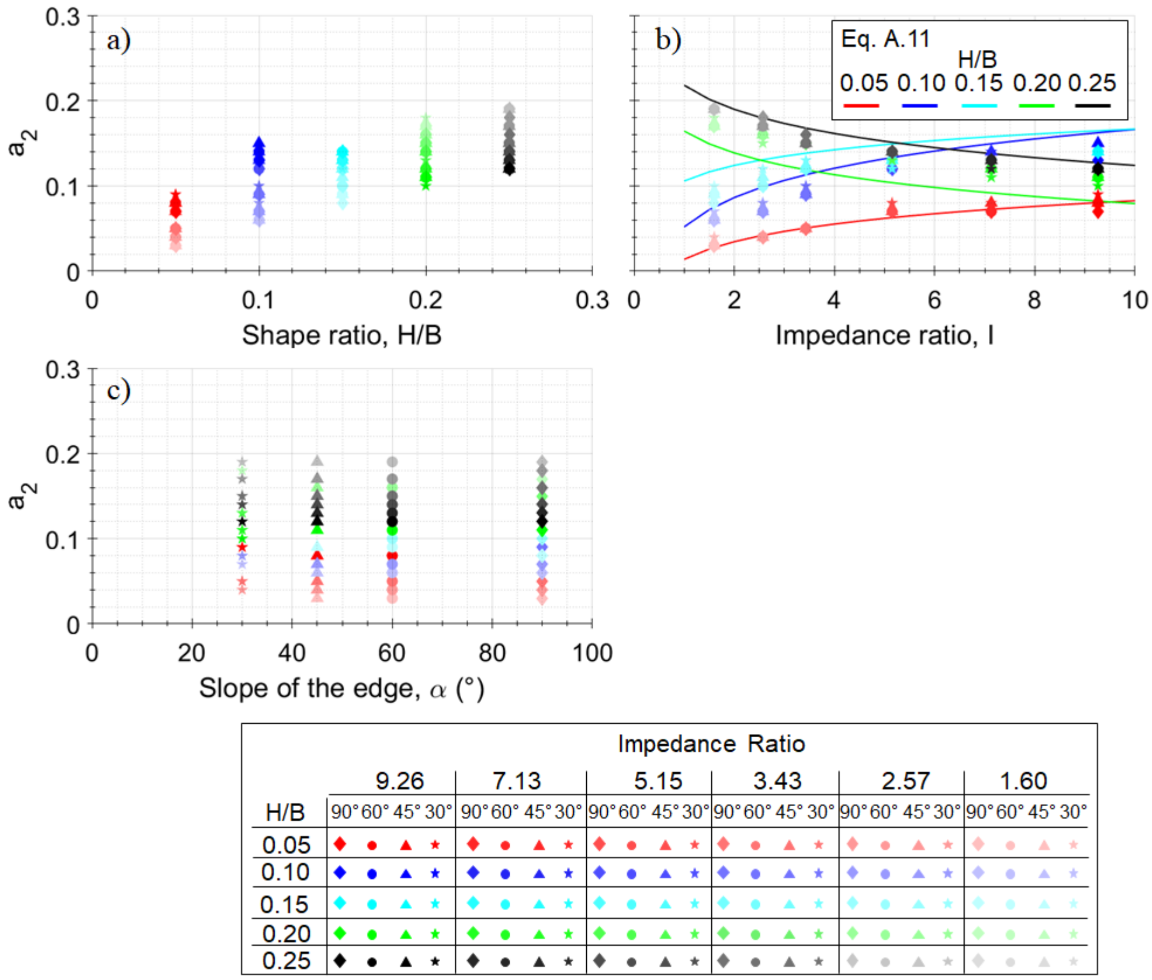

Figure A.8 – Variation of a_2 with a) H/B; b) I; c) α

The trends of x_4 and x_5 with H/B are shown in Figure A.9a,b respectively. The first parameter, that is the value of a_2 obtained for I=1, can be expressed as an exponential function of H/B with equation:

$$x_4 = 0.335 \cdot \left(1 - \exp\left(-\frac{\left(\frac{H}{B}\right)^2}{2 \cdot 0.172^2}\right)\right) \qquad \text{A.12}$$

While x_5 is the exponent of the argument of the logarithm and defines the shape of the function. It is greater than 0 for H/B<0.15 because for such shape ratios a_2 increases with I, while it is less than 0 for deeper valleys because in that case a_2

decreases as I increases. Hence x_5 can be defined by two functions based on the value of H/B:

$$x_5 = \begin{cases} \frac{H}{B} \le 0.15 & -8.567\left(\frac{H}{B}\right)^2 + 1.679\frac{H}{B} - 0.0327 \\ \frac{H}{B} > 0.15 & 1.173 \cdot 10^{-9}\left(\frac{H}{B}\right)^{-9.421} - 0.0414 \end{cases} \qquad \text{A.13}$$

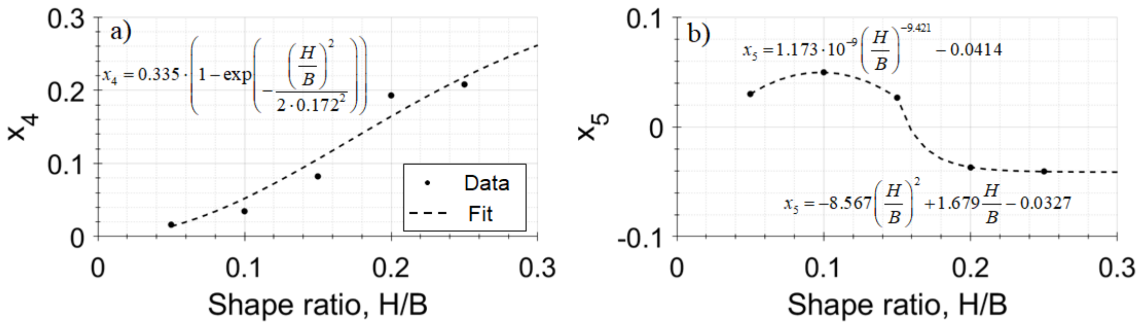

Figure A.9 – Variation of a) x_4; b) x_5 with H/B

Figure A.10a,c,e show the trends of the b_2 with H/B, I and α for all cases, respectively. Since this representation is not able to provide the best insight into which parameters mainly affects b_2, Figure A.10b,d,f show data for only two angles (90° and 30°), H/B (0.05 and 0.25) and I (9.26 and 1.60). They are representative of the general trends of b_2 with the key parameters. In particular, b_2 mainly depends on I, decreasing as its increases. This is due to the fact that as the impedance ratio increases, the zone of maximum amplification moves from the edges towards the centre as described in the previous paragraphs. b_2 is also influenced in a minor way by H/B and α, in detail as the shape ratio increases it decreases, i.e. the maximum amplification moves from the edges towards the valley centre, while it increases with alpha. Therefore, b_2 can be written as:

$$b_2 = x_6 + \ln\left(I^{-x_7}\right) \tag{A.14}$$

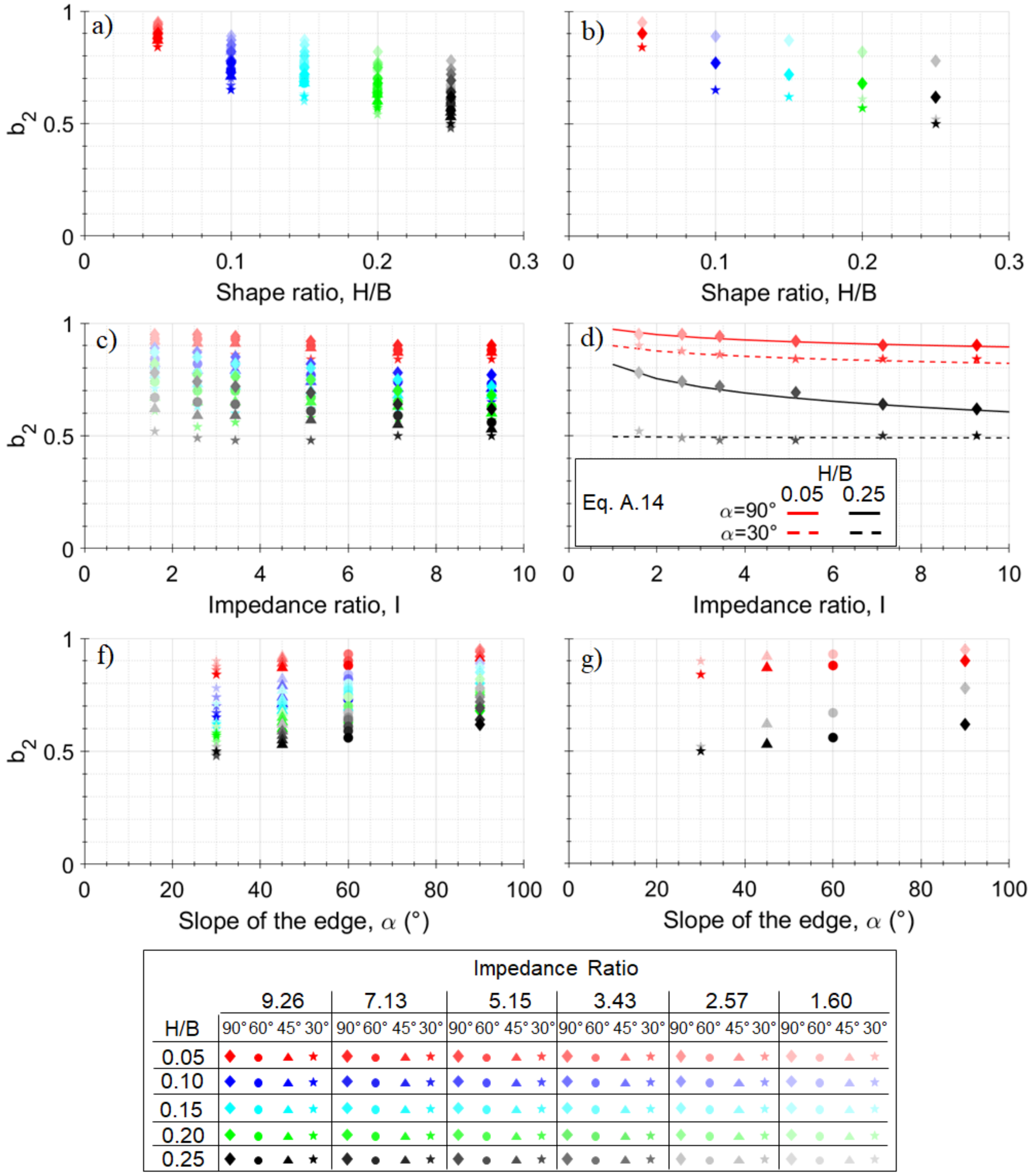

Figure A.10 – Variation of b_2 for all case with a) H/B; c) I; e) α, and b,e,f) only for I=9.26, 1.26, α=90°, 30° and H/B=0.05, 0.25

x_6 and x_7 can be expressed as:

$$x_6 = x_8 + \ln\left(\alpha^{x_9}\right) \tag{A.15}$$

$$x_7 = \begin{cases} \frac{H}{B} < 0.10 & -0.0042 + 0.764\frac{H}{B} \\ \frac{H}{B} \geq 0.10 & x_{10} + \ln\left(\alpha^{x_{11}}\right) \end{cases} \quad \text{A.16}$$

With x_8, x_9, x_{10} and x_{11} equal to:

$$x_8 = 0.967 - 5.849 \cdot \frac{H}{B} \quad \text{A.17}$$

$$x_9 = 0.0097 + 1.127\frac{H}{B} \quad \text{A.18}$$

$$x_{10} = -0.375 \cdot \ln\left(\frac{H}{B}\right) - 0.793 \quad \text{A.19}$$

$$x_{11} = 0.088 \cdot \ln\left(\frac{H}{B}\right) + 0.203 \quad \text{A.20}$$

Figure A.11a,b,c show the trends of x_6, x_8 and x_9, respectively. The first is a logarithmic function of α while the other two parameters vary linearly with H/B. Note that x_6 represents the value of b_2 for I=1 and, coherently with the previous results, it increases with α and decreases as H/B increases.

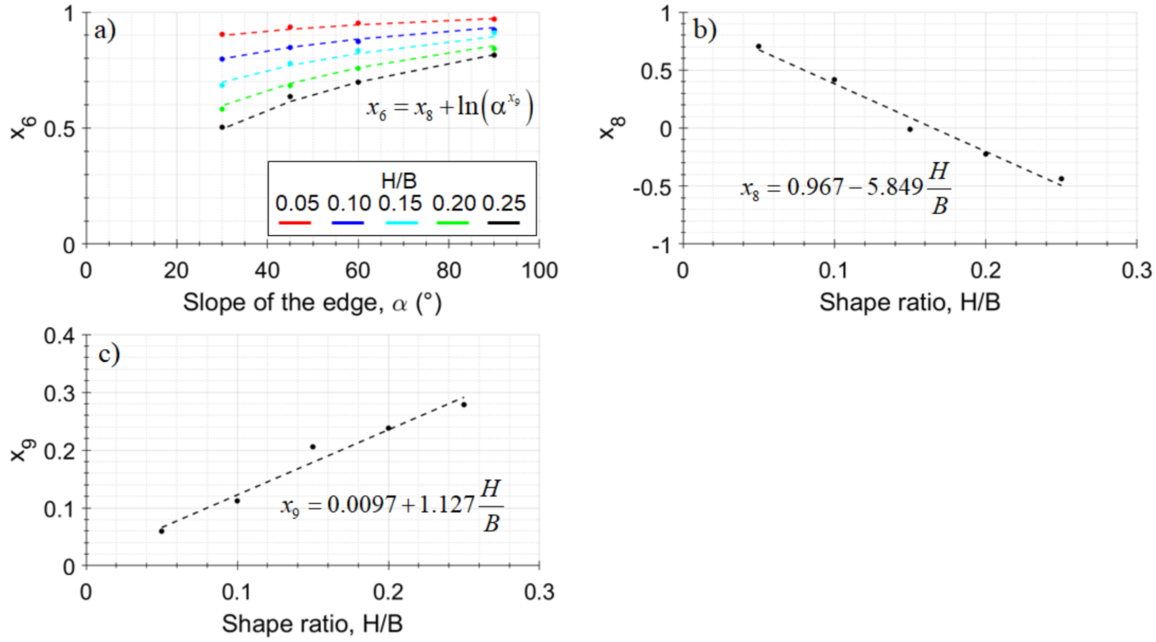

Figure A.11 – Variation of a) x_6 with α; b) x_8 and c) x_9 with H/B.

Figure A.12a,b show the trends of x_7 with H/B and α, respectively. It is linear with H/B and independent of slope angles for H/B<0.1, while for greater shape ratios the trend varies with α, logarithmically decreasing with the angle. Furthermore in Figure A.12c,d the variations of x_{10} and x_{11} with H/B are shown, both parameters are logarithmic functions of H/B however the former decreases with increasing it, whereas the latter increases with the shape ratio.

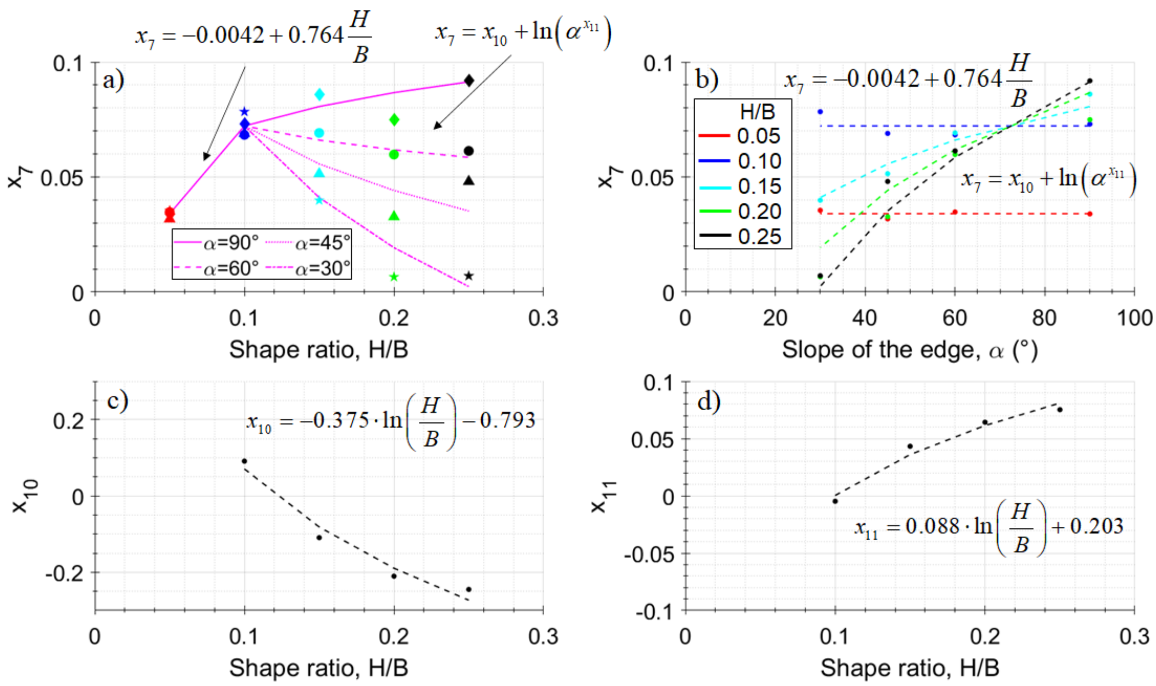

Figure A.12 – Variation of x_7 with a) H/B; b) α; and c) x_{10}; d) x_{11} with H/B

Figure A.13a,b,c show the variations of c_2 with H/B, I and α, respectively. It is independent of the shape ratio, increases with α and is an exponential function of I. In particular, c_2 can be written as:

$$c_2 = x_{12} \cdot \left(1 - \exp\left(-\frac{I^2}{2 \cdot x_{13}^2}\right)\right) \qquad A.21$$

With x_{12} and x_{13} equal to:

$$x_{12} = 0.207 + 0.00919 \cdot \alpha \qquad A.22$$

$$x_{13} = 1.064 + 0.00416 \cdot \alpha \qquad A.23$$

The trend of the latter two parameters is shown in Figure A.14a,b. It is linear with alpha and in particular increases with α.

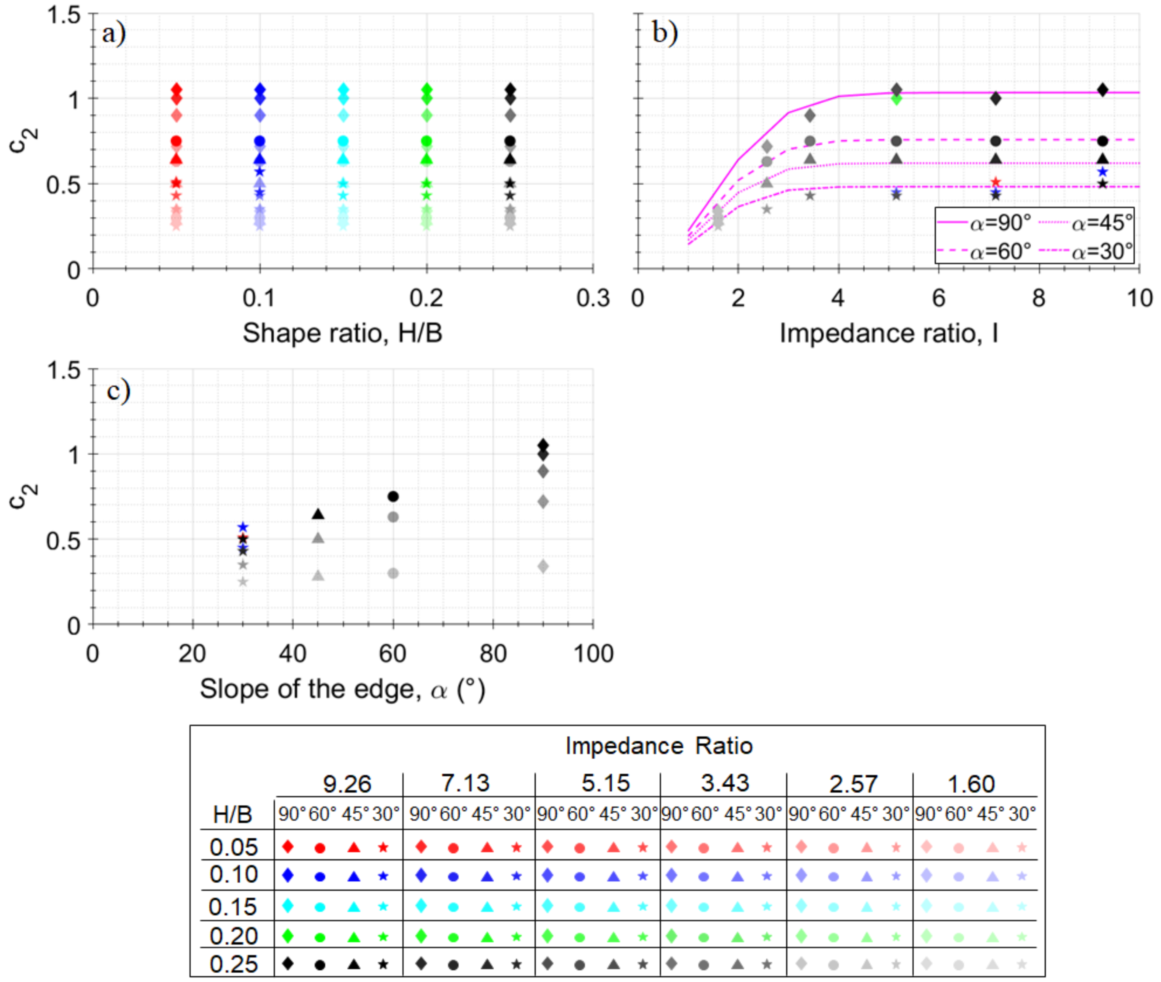

Figure A.13 – Variation of c_2 with a) H/B; b) I; and c) α.

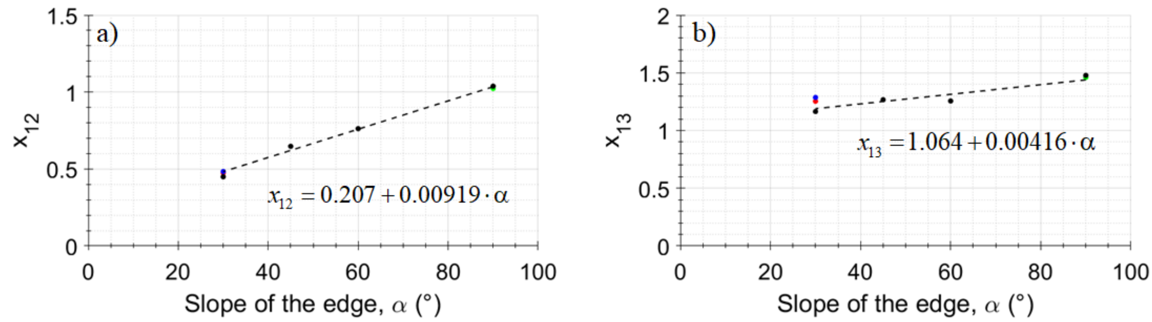

Figure A.14 – Variation of a) x_{12} and b) x_{13} with α

B. APPENDIX B: CALIBRATION OF VAF RELATIONSHIP FOR WEDGE SHAPED VALLEY

The same equation proposed for the trapezoidal basin case has been adopted also for the wedge shape valley (Eq. III.5.3).

$$\mathrm{VAF} = 1 + \left(\mathrm{VAF}(0) - 1\right) \cdot f_1\left(\frac{x}{B}, \frac{H}{B}, I\right) + f_2\left(\frac{x}{B}, \frac{H}{B}, I, \alpha\right) \quad \text{B.1}$$

$$\mathrm{VAF}(0) = 1 + c_0 \cdot \left(1 - \exp\left(-\frac{(I-1)^2}{2 \cdot a_0^2}\right)\right) \quad \text{B.2}$$

The function f_1 and f_2 are set equal to:

$$f_1\left(\frac{x}{B}, \frac{H}{B}, I\right) = c_1 \cdot \exp\left(-\frac{\left(\frac{x}{B}\right)^2}{2 \cdot a_1^2}\right) \quad \text{B.3}$$

$$f_2\left(\frac{x}{B},\frac{H}{B},I,\alpha\right)=c_2\cdot\exp\left(\frac{\frac{x}{B}-b_2}{a_2}-\exp\left(\frac{\frac{x}{B}-b_2}{a_2}\right)\right) \qquad \text{B.4}$$

In the case of the wedge, a_0 and c_0 (Figure B.1) are equal to:

$$a_0=4.202\cdot\exp\left(-13.59\cdot\frac{H}{B}\right)+1.871 \qquad \text{B.5}$$

$$c_0=0.726\cdot\left(1-\exp\left(-\frac{\left(\frac{H}{B}\right)^2}{0.00307}\right)\right) \qquad \text{B.6}$$

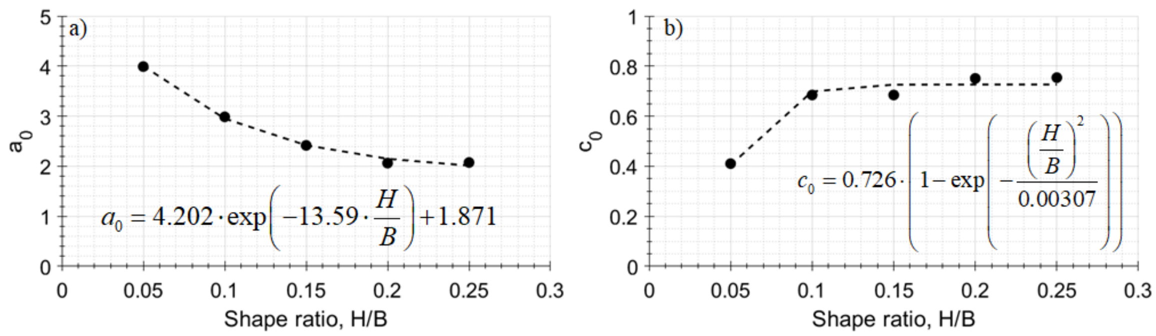

Figure B.1 – Variation of a) a_0 and b) c_0 with the shape ratio

Figure B.2 shows the trends of a_1 and c_1 with H/B, which can be expressed as:

$$a_1=0.0733\cdot\left(\exp\left(5.505\cdot\frac{H}{B}\right)-1\right) \qquad \text{B.7}$$

$$c_1=2.245\cdot\left(\frac{H}{B}\right)^{0.554} \qquad \text{B.8}$$

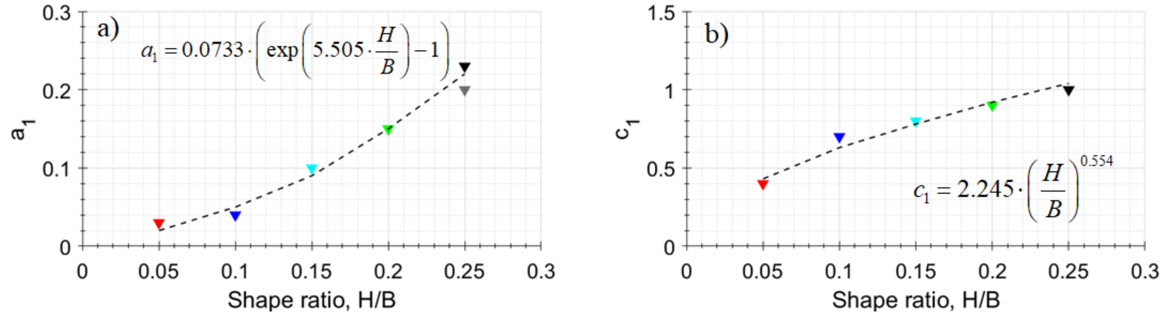

Figure B.2 – Variation of a) a_1 and b) c_1 with H/B

Figure B.3a,b shows the variation of a_2, b_2 with H/B set equal to:

$$a_2 = 0.343 - 0.58 \cdot \frac{H}{B} \tag{B.9}$$

$$b_2 = x_1 + x_2 \cdot \frac{H}{B} \tag{B.10}$$

With x_1 and x_2, shown in Figure B.3c,d, and equal to:

$$x_1 = 0.6161 + 0.0049 \cdot I \tag{B.11}$$

$$x_2 = 0.425 - 1.165 \cdot \exp(-0.512 \cdot I) \tag{B.12}$$

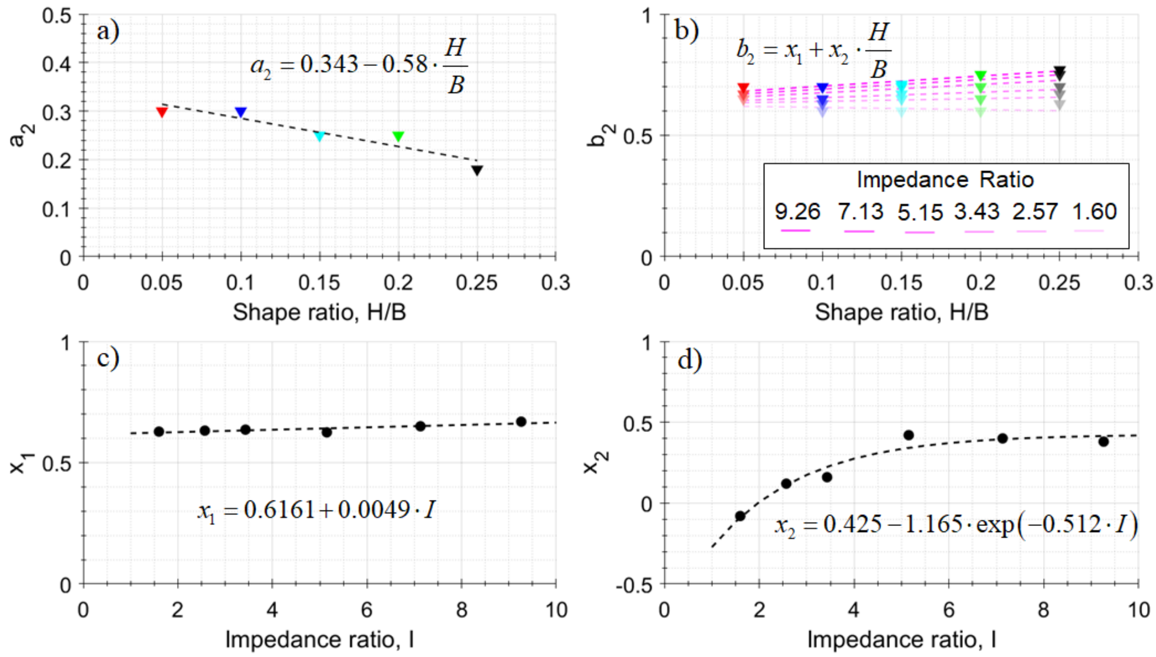

Figure B.3 – Variation of a) a_2, b) b_2 with H/B, and c) x_1, d) x_2 with I

Finally, c_2 (Figure B.4a) is equal to:

$$c_2 = x_3 + x_4 \cdot I \tag{B.13}$$

with x_3 and x_4, shown in Figure B.4b,c, equal to:

$$x_3 = 0.855 \cdot \frac{H}{B} - 0.182 \tag{B.14}$$

$$x_4 = 0.321 - 0.624 \cdot \frac{H}{B} \tag{B.15}$$

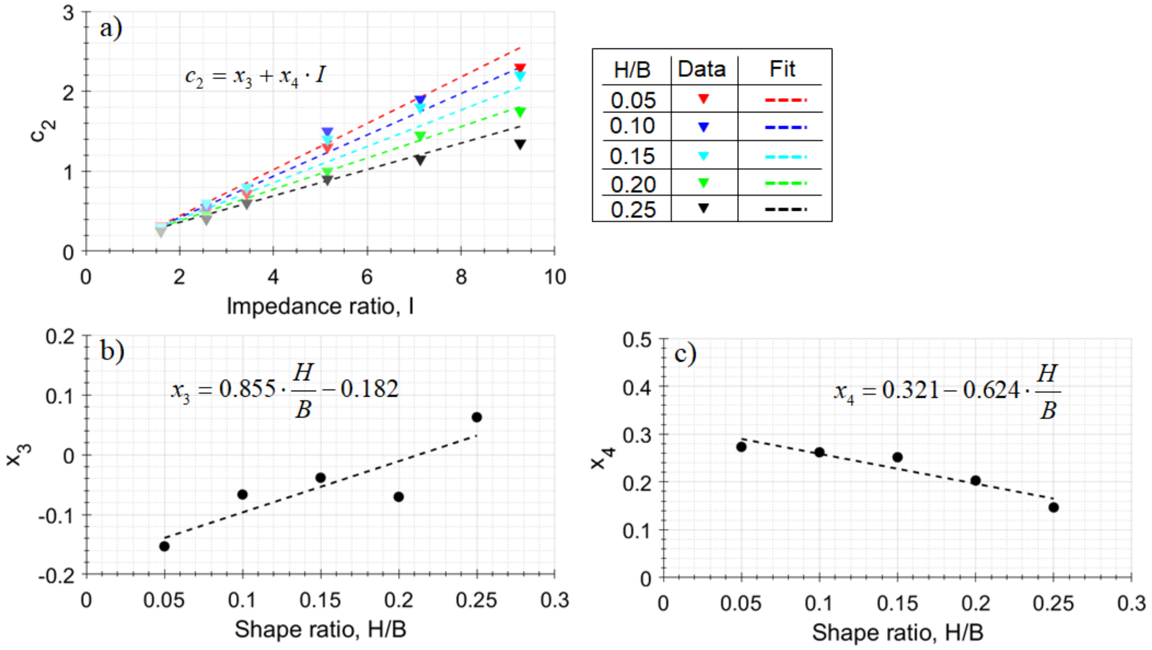

Figure B.4 – Variation of a) c_2 with I and b) x_3, c) x_4 with H/B.